University of Pennsylvania
ScholarlyCommons

Publicly Accessible Penn Dissertations

2021

Manipulating Glass Structure And Properties Through Surface Mediated Equilibrium

Aixi Zhang
University of Pennsylvania

Follow this and additional works at: https://repository.upenn.edu/edissertations

 Part of the Chemical Engineering Commons, Mechanics of Materials Commons, and the Physical Chemistry Commons

Recommended Citation

Zhang, Aixi, "Manipulating Glass Structure And Properties Through Surface Mediated Equilibrium" (2021). *Publicly Accessible Penn Dissertations*. 4084.
https://repository.upenn.edu/edissertations/4084

This paper is posted at ScholarlyCommons. https://repository.upenn.edu/edissertations/4084
For more information, please contact repository@pobox.upenn.edu.

Manipulating Glass Structure And Properties Through Surface Mediated Equilibrium

Abstract

Stable glasses can be made through physical vapor deposition when certain deposition conditions are met. The structure and properties of stable glasses are strongly dependent on the equilibrated surface structure and dynamics during deposition, regulated by surface mediated equilibrium. Hence, studies of surface properties, such as comparing surface relaxation times and surface coordination states with those of the bulk, measuring the length scale over which surface properties can persist into the films, and how these quantities can be altered, become very important in controlling the properties of vapor deposited glasses. This thesis presents several research projects on the effects of molecular structures and deposition conditions on the packing and stability of vapor deposited glasses. To understand the distinct properties of glass surface, indirect experiments on thin film relaxations dynamics were performed. In addition, we have used light and chemical modifications to change the surface structure and dynamics, studying those effects on glass stability. In Chapter 2, amorphous selenium (a-Se) stable glasses were made in dark and under above-bandgap light. Despite their low relative density, a-Se glasses deposited under light exhibited higher kinetic stability compared to the glasses deposited in dark, which is originated from the highly networked structure inherited from the surface structure under light. Chapter 3 is an extended study of Chapter 2 which determined the degree of light facilitated relaxation in a-Se thin films. Chapter 4 demonstrated an extremely long length scale of bulk to thin film transition in a-Se systems compared to what has been found in organic glasses. This extremely long length scale is likely to be related to the increasing density of three/four-coordinated states in a-Se thin films. Chapter 6 resolved the role of intramolecular degrees of freedom on stable glass formation. Especially, the relationship and distinctions between stable glasses optical birefringence and molecular layering were discussed. These observations are connected to the thickness of the mobile surface layer at various deposition conditions, as well as the role of molecular orientation at the top surface. In Chapter 7, we focused on the how intermolecular interaction and micro-phase separation influence stable glass structure and stability.

Degree Type

Dissertation

Degree Name

Doctor of Philosophy (PhD)

Graduate Group

Chemistry

First Advisor

Zahra Fakhraai

Keywords

Amorphous Selenium, Glass Anisotropy, Physical Vapor Deposition, Stable Glass, Surface Mediated Equilibrium

Subject Categories

Chemical Engineering | Mechanics of Materials | Physical Chemistry

This dissertation is available at ScholarlyCommons: https://repository.upenn.edu/edissertations/4084

MANIPULATING GLASS STRUCTURE AND PROPERTIES THROUGH SURFACE MEDIATED EQUILIBRIUM

Aixi Zhang

A DISSERTATION

in

Chemistry

Presented to the Faculties of the University of Pennsylvania

in

Partial Fulfillment of the Requirements for the

Degree of Doctor of Philosophy

2021

Supervisor of Dissertation

_____

Zahra Fakhraai, Associate Professor of Chemistry

Graduate Group Chairperson

_____

Daniel J. Mindiola, Brush Family Professor of Chemistry

Dissertation Committee

Jessica M. Anna, Assistant Professor of Chemistry, Elliman Faculty Fellow

Jeffery G. Saven, Professor of Chemistry

Robert A. Riggleman, Associate Professor of Chemical and Biomolecular Engineering

MANIPULATING GLASS STRUCTURE AND PROPERTIES THROUGH SURFACE MEDIATED EQUILIBRIUM

© COPYRIGHT

2021

Aixi Zhang

This work is licensed under the
Creative Commons Attribution
NonCommercial-ShareAlike 4.0
License

To view a copy of this license, visit

http://creativecommons.org/licenses/by-nc-sa/4.0/us/

ACKNOWLEDGEMENT

I would like to thank everyone who has helped and supported me in the past. It would have been impossible for me to come to where I stand now without you.

First of all, I want to express my great gratitude to my advisor, Prof. Zahra Fakhraai. She is the best advisor in the world, that I could have asked for. Joining her group was the best and wisest decision I made in graduate school. And I really appreciated that she accepted me into her group in my first year. As a PI, Zahra knows when to trust and when to challenge our results. As a mentor, she is caring and thoughtful. But more importantly, as a woman, she taught me the power of will.

Secondly, I would like to thank Prof. Richard Stephens, who sets the standard as a great role model for me as wise and experienced scientist. I admire his talents every time when I saw his sophisticated designs of experiments done decades ago. In the past years, Rich inspired me with his plethora of novel ideas in selenium research and engineering design. His enthusiasm and passion have kept me motivated throughout my PhD.

Next, I want to thank my committee members, Prof. Jessica Anna, Prof. Jeffery Saven, and Prof. Robert Riggleman. I remember the moment when I was challenged on a question about Ellipsometry during my candidacy and how it pushed to better myself from then on. Our annual meeting urged me to think thoroughly about every aspect of my research projects. Your feedback and advice were very valuable for me.

I also had fantastic lab mates in my PhD. I would like to thank Shivajee Govind, for being willing to listen and help all the time; Sarah Wolf, for being a warm and trustworthy friend; Dr. Yi Jin, for being a reliable partner; Alex Moore, for providing us ideas from theoretical insights and for accompanying us going to Brookhaven National Lab, Dr. Haonan Wang, for teaching me everything about Ellipsometry; Dr. Yue Zhang, Dr. Tianyi Liu and Dr. Yi-chih Lin, for getting me to know the basics in the lab. Moreover, I am grateful to

Dr. Ahmad Shamsabadi, Yueli Chen, Dr. Subarna Samanta, Dr. Connor Bilchak, Dr. Chen Li, Melissa Vettelson, Dr. Connor Woods, Youngtae Song, Daniella Levin, Danixa Rodríguez-Meléndez, Omar Ibrahim, Mauricio Alvarez, Murray Skolnick, Wendi Li and Sathya Edamadaka for contributing to the group and making this group an enjoyable and supportive working environment.

I could not have finished my PhD without collaborators. I want to thank Haoqiang Zhao, Gui Gao, Georgia Huang from Dr. Patrick Walsh's group for synthesizing the organic compounds; Dr. Radhe Agarwal and Prof. Jonathan E. Spanier from Drexel University for being helpful in performing X-ray Reflectivity and Ellipsometry measurements; Prof. Paul Heiney for his support in doing X-ray Scattering experiments in-house; Dr. Mikhail Zhernenkov and Dr. Guillaume Freychet at Brookhaven National Lab for their assistance on our sample characterizations; Mr. Harold Borders at Engineering machine shop for his meticulous crafts.

On top of the above-named people, there are mentors and friends who are important to me. I am grateful for my undergraduate research advisor, Prof. Xuefeng Fu, and two of my high school teachers, Jie Gao and Wei Li. I would never think I can pursue a chemistry PhD degree without their encouragement. I am also thankful for my friends in the department: Rui Guo, Wei Weng, Dabin Kim, Tao Li, Dr. Xiujing Xing, Dr. Qinghua Zhao, Dr. Yifan Deng and Shengsong Yang, and outside the department: Chang Liu, Xianyuan Zhao, Yan Cong, Tianyi Feng. Thank you all for being there, with me laughing or crying. I feel so lucky that you have my back.

At last, I want to thank my family, my husband, my mom and dad. Thank you for being understanding and supportive. I am sorry for the moments when I was being stubborn, but you were always patient to wait for me to grow.

The years of 2020 and 2021 are unforgettable, because of the world-wide pandemic. I appreciate everyone who contributed to fighting against the virus and bringing back a

normal life, including health care providers, essential workers, staffs in the university, and people like you.

ABSTRACT

MANIPULATING GLASS STRUCTURE AND PROPERTIES THROUGH SURFACE MEDIATED EQUILIBRIUM

Aixi Zhang

Zahra Fakhraai

Stable glasses can be made through physical vapor deposition when certain deposition conditions are met. The structure and properties of stable glasses are strongly dependent on the equilibrated surface structure and dynamics during deposition, regulated by surface mediated equilibrium. Hence, studies of surface properties, such as comparing surface relaxation times and surface coordination states with those of the bulk, measuring the length scale over which surface properties can persist into the films, and how these quantities can be altered, become very important in controlling the properties of vapor deposited glasses. This thesis presents several research projects on the effects of molecular structures and deposition conditions on the packing and stability of vapor deposited glasses. To understand the distinct properties of glass surface, indirect experiments on thin film relaxations dynamics were performed. In addition, we have used light and chemical modifications to change the surface structure and dynamics, studying those effects on glass stability. In Chapter 2, amorphous selenium (a-Se) stable glasses were made in dark and under above-bandgap light. Despite their low relative density, a-Se glasses deposited under light exhibited higher kinetic stability compared to the glasses deposited in dark, which is originated from the highly networked structure inherited from the surface structure under light. Chapter 3 is an extended study of Chapter 2 which determined the degree of light facilitated relaxation in a-Se thin films. Chapter 4 demonstrated an extremely long length scale of bulk to thin film transition in a-Se systems compared to what has been found in organic glasses. This extremely long length scale is likely to be related to the increasing density of three/four-coordinated states in a-Se thin films. Chapter 6 resolved the role of intramolecular degrees

of freedom on stable glass formation. Especially, the relationship and distinctions between stable glasses optical birefringence and molecular layering were discussed. These observations are connected to the thickness of the mobile surface layer at various deposition conditions, as well as the role of molecular orientation at the top surface. In Chapter 7, we focused on the how intermolecular interaction and micro-phase separation influence stable glass structure and stability.

TABLE OF CONTENTS

LIST OF ILLUSTRATIONS

CHAPTER 1: Introduction

1.1. Glass Theories

1.1.1. Glass Transition

A glass generally refers to a form of amorphous solid that doesn't have long-range ordering. Glassy materials are ubiquitous and have generated a lot of research interests. Compared to crystals, glasses doesn't have grain boundaries and can be easily formed uniformly at large scale[17]. The most ancient glasses are made of silica (SiO_2), which can be produced from sand. More recently, polymers have become substitutes for silicate glasses in some cases because they are lighter and less brittle. Metallic glasses are another important category which are characterized to have superior hardness and corrosion resistance[234]. In addition, small organic molecules are also shown to form glasses. Typically, pharmaceutical solids are required to be produced in amorphous phases to aid their dissolution[245]. Modern technologies utilize molecular organic hole/electron transport materials to make organic light-emitting diodes (OLED), which perform as a new type of digital display[211].

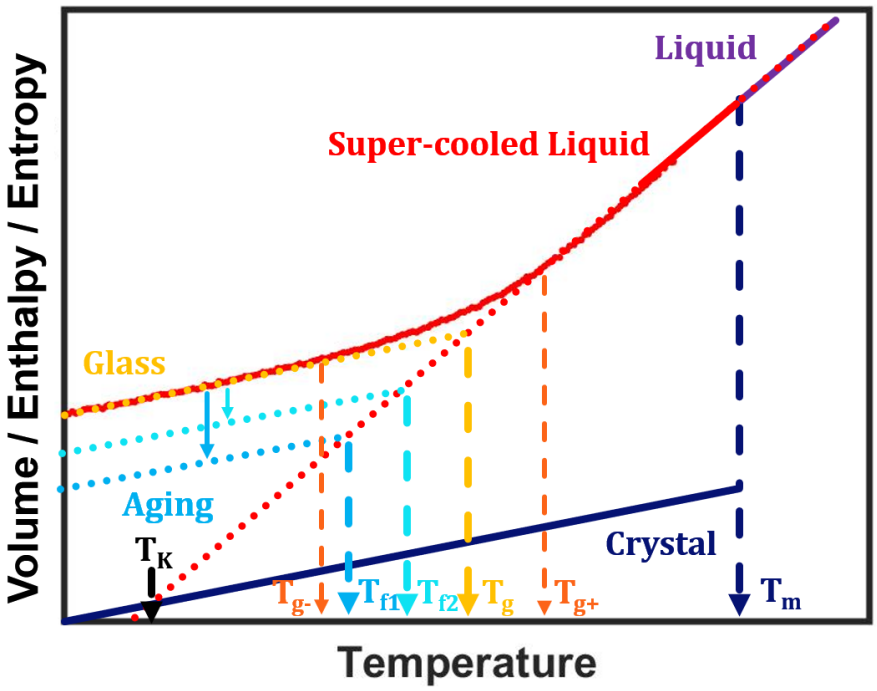

Figure 1.1: Schematic view of volume/enthalpy/entropy of a system as a function of temperature. Liquid (purple), crystal (dark blue), super-cooled liquid (SCL, red) and glass (orange) regimes are colored differently in the graph. Red and orange dotted lines are linear fits to the SCL and glass regimes. Melting point (T_m), glass transition temperature with its upper and lower bound (T_g, T_{g+} and T_{g-}), fictive temperatures (T_{f1} and T_{f2}) for glasses aged to various degrees and the Kauzmann temperature (T_K) are also indicated in the graph.

The most traditional way to make a glass is through cooling[53]. As illustrated by Figure 1.1, when cooled from a liquid, chances are, at the melting point (T_m), a first-order phase transition occurs and the system crystallizes. If the cooling rate is high enough to avoid crystal nucleation and growth, the liquid will stay disordered below T_m, follow the equilibrium line, and enter a super-cooled liquid (SCL) state. As cooling continues, the liquid viscosity will increase dramatically until a point where the molecular motion becomes so slow compared to the timescale of cooling that equilibrium cannot be maintained. At this point, system's properties start deviating from the equilibrium line, and eventually a glass is formed. The temperature at which the glass is formed is named the glass transition

temperature (T_g). Since glass transition happens within a narrow temperature range, conventionally we fit the changes in volume (thickness when measured on films) or enthalpy profile against temperature to lines within the SCL and glass regimes, defining the intersection of these two lines as T_g. To characterize the width of the glass transition, which contains information about the dynamical heterogeneity of the system, we use T_{g+} and T_{g-} to represent the temperatures where the cooling curve deviates from the SCL line and the glass line, respectively. These values represent when the slowest and the fastest regions of the system fall out of equilibrium, respectively.

Because glass transition is a dynamical process, T_g is shown to exhibit a cooling rate dependence. Slower cooling rates allow the molecules to relax more before the dynamics are arrested. As a result, the system will fall out of equilibrium at a lower temperature, giving rise to a lower T_g value. When a T_g value is reported, we typically refer to the value measured at 10 K/min cooling rate, where system's viscosity is estimated to be 10^{12} Pa·s and its structural relaxation time is about $\tau_\alpha \sim$100 s, empirically[117, 157, 2, 190].

Even though glassy materials are kinetically trapped, given a sufficient time, molecular rearrangement can still occur. The process where glass slowly evolves towards equilibrium line below T_g and becomes lower in energy and higher in density, is called physical aging (see Figure 1.1)[30, 257, 154, 203]. Aged glasses can be rejuvenated by annealing above T_g. while a glass is heated, the temperature at which the aged glass volume or enthalpy is equivalent to the extrapolated SCL is defined to be the fictive temperature (T_f), from which we can derive the effective aging time[48, 103]. McKenna *et al.* measured the density and enthalpy change of a 20-millionyear-old Dominican amber relative to the rejuvenated glass, and obtained a 2.1% density increase and 50 J/g enthalpy decrease around 273 K[258].

1.1.2. Glass Fragility

As mentioned above, the viscosity of a glassy systems change rapidly close to T_g. Efforts have been made to measure the temperature dependence of viscosity (η) in a variety of organic and inorganic glassy systems. Two extreme cases were found, when $\log \eta$ is plotted

against T_g/T, network-forming oxides (SiO_2 and GeO_2) typically show a linear Arrhenius relationship[63], while simple atomic alloys, organic molecular liquids, such as *o*-Terphenyl and Solal, as well as many polymers, follow a more curved line which has larger slope around T_g[117]. There are some other species that fall in between these limits[201, 5, 235] (see Figure 1.2). Based on the temperature dependence of η, the materials that have Arrhenius relationship are classified to be "strong" liquids. While others that undergo a more dramatic change in viscosity as temperature changes are called "fragile" liquids.

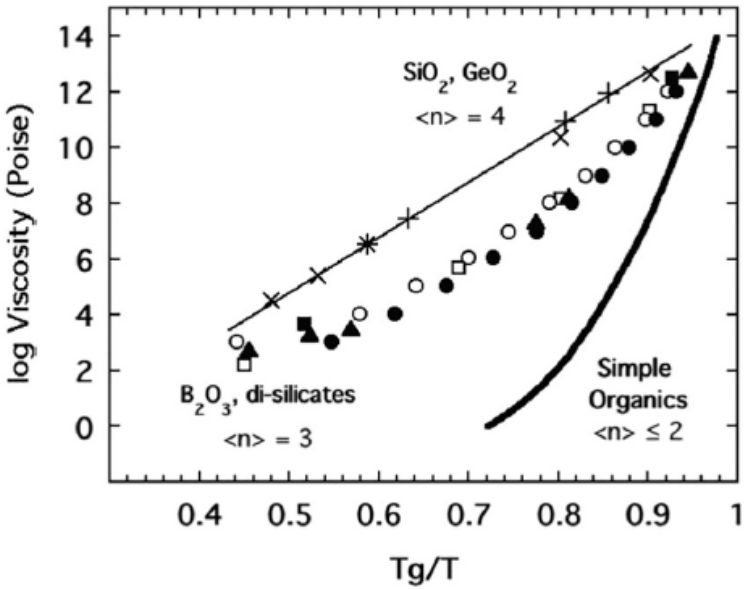

Figure 1.2: Scaled viscosity ($\log \eta$) is plotted against reversed temperature (T_g/T) for SiO_2 (plusses), GeO_2 (crosses), B_2O_3 (triangles), Na_2O-$2SiO_2$ (open squares), K_2O-SiO_2 (closed squares), NBS soda lime silicate (open circles), NBS Lead Silicate (closed circles), and four kinds of simple organic molecular liquids (Salol, ortho-terphenyl, α-phenyl-o-cresol, and tri-α-naphthylbenzene). $\langle n \rangle$ represents the bridging oxygen per polyhedra. Reprinted from reference[201]: D. L. Sidebottom, Fifty years of fragility: A view from the cheap seats, *Journal of Non-Crystalline Solids*, Volume 524, 15 November 2019, 119641, Copyright (2019), with permission from Elsevier.

More quantitatively, the fragility index (m) is defined as the slope of $\log \eta$ (or log(relaxation time), $\log \tau_\alpha$) *vs.* reversed temperature, which is expressed by:

$$m = \lim_{T \to T_g} \frac{\mathrm{d} \log \eta(T_g/T)}{\mathrm{d}(T_g/T)} \simeq \frac{\mathrm{d} \log \tau_\alpha(T_g/T)}{\mathrm{d}(T_g/T)}, \tag{1.1}$$

firstly put forward by Angell *et al.*[5, 19, 3]. This second relationship is derived from an empirical estimation of viscosity from viscoelastic relaxation time, $\eta \approx \tau_\alpha G_\infty$, where G_∞ is the infinite frequency shear modulus[19, 201]. Strong liquids have smaller m values compared to fragile liquids.

Earlier researchers have investigated the relationship between a liquid' fragility and its structure[235, 202], distribution in structural relaxation[19], vibrational dynamics below T_g[190] and excess configurational entropy[137]. Strong glass forming materials generally consist of highly-constrained networked structures, which sense little to no disturbance upon small topological change[235, 202]. Some rigid polymers and those form hydrogen bonds are shown to be strong liquids too[5, 87]. As for more fragile liquids, including molecular glasses, they mainly interacts through weak van der Waal interactions. Therefore their structures are more easily altered. As temperature increases above T_g, fragile liquid's viscosity will reduce dramatically. According to Adam-Gibbs's model[50], which will be introduced in section 1.1.3, the accessible conformations for fragile liquids will increase much more rapidly than strong liquids when a few constrains are released, resulting in a rise in their configurational entropy. While more experimental investigations are needed to understand the exact connections between the effects mentioned above, it seems there are strong correlations between liquid fragility, topology, structural relaxation and configurational entropy.

In addition to the fragility index (m), more conveniently, we use the apparent activation energy (E_a) at T_g to describe the height of the activation barrier for structural relaxation. When considering a small temperature range close to T_g, we can approximate glass relaxation to a single-barrier activation process, where:

$$E_a = \lim_{T \to T_g} k_B \frac{\mathrm{d} \ln \tau_\alpha(1/T)}{\mathrm{d}(1/T)}. \tag{1.2}$$

k_B is the Boltzmann's constant; A is a fitting parameter. The relationship between E_a and m is: $E_a = \ln(10) \cdot m k_B T_g$. Strong liquids have smaller E_a which show almost no temperature dependence. While for fragile liquids, E_a will increase upon cooling. Over a

broader temperature range, rather than a simple exponent, Vogel-Tammann-Fulcher (VFT) equation is generally used to describe the temperature dependence of relaxation time (or viscosity), which is written as[229, 65, 215]:

$$\tau_\alpha = A \exp \frac{E_a}{k_B(T - T_0)}. \tag{1.3}$$

As you may notice from the expression, VFT equation encounters a singularity at $T = T_0$, which does not have explicit physical meaning. However, Chandler and Garrahan demonstrated the temperature dependence of fragile liquid relaxation time, τ, (or viscosity, η) could also collapse onto one uniform parabola form with no singular behavior at any finite temperature:

$$\log(\frac{\tau}{\tau_o}) = J^2 \left(\frac{1}{T} - \frac{1}{T_o}\right)^2, T < T_o, \tag{1.4}$$

where T_o is the onset temperature, above which the system relaxation has very weak temperature dependence, and J is a material dependent quantity[55, 56].

1.1.3. Glass Transition Theories

Glass transition is not a true first or second-order thermodynamical phase transition. Thermodynamically, it shows continuous change in volume and entropy, the first order derivatives of Gibbs free energy, but has apparent discontinuities in specific heat and isothermal compressibility, the second order derivatives of Gibbs free energy, when temperature goes through T_g. In addition, from a dynamic point of view, recent studies found that glass transition is featured by having dynamic heterogeneity[178], where fast and slow relaxation (active and inactive phase) can coexist spatially and temporally[33, 86].

Thus far, numerous models and theories have been proposed to explain the nature of glass transition, including free volume theory[108], Adam-Gibbs model[50], random first order transition theory[20, 131], mode coupling theory[230, 175], dynamical facilitation[105, 163, 185] and kinetic constrained models[68, 142, 180].

Based on the thermodynamic interpretation of glass transition, a critical paradox that

has not been resolved is the so-called Kauzmann entropy crisis. As denoted in Figure 1.1, because the liquid entropy decays faster than the crystal entropy as it is cooled, at a temperature T_K (Kauzmann temperature), which is not far below T_g, the liquid line will intersect with the crystal line[99]. If the trend continues, below T_K, the entropy of the liquid will become smaller than that of the crystal and will reach zero above 0 K, which is a violation of the third law of thermodynamics. However, dynamic facilitation theory can avoid the Kauzmann temperature by taking particle activity as a measurement instead of thermodynamic quantities[185]. Other theories predict the existence of a real thermodynamical phase transition close to, or at T_K, to avoid this crisis[50, 131, 20]. It is also possible that the SCL would curve to a lower slope to circumvent T_K without any transitions[161, 144].

1.1.4. Potential Energy Landscape of Glass Forming Systems

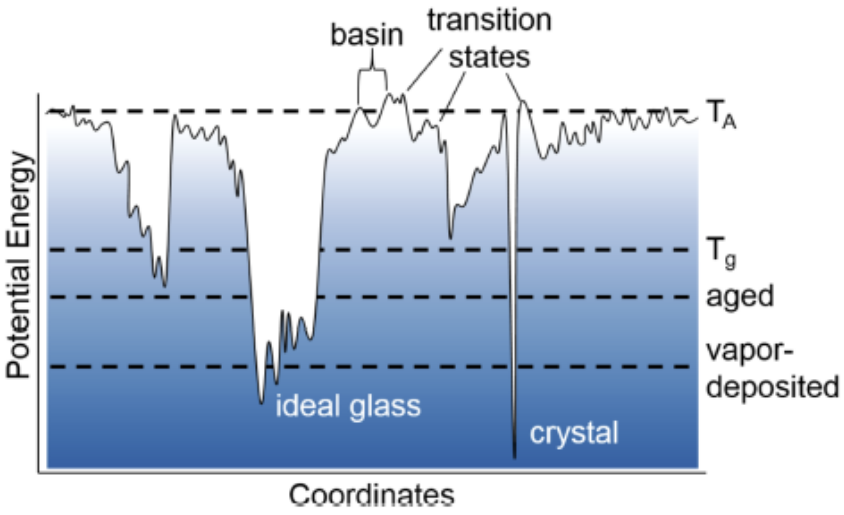

Figure 1.3: A schematic drawing of potential energy plotted against the particle coordination for glass forming systems. T_A is the temperature at which non-Arrhenius dynamics start to show up; T_g is the glass transition temperature. "Aged", "vapor-deposited", "ideal glass" and "crystal" indicates where their corresponding energy cross with the potential energy landscape. Reprinted from reference[52]:M. D. Ediger, Perspective: Highly Stable Vapor-deposited Glasses, *The Journal of Chemical Physics*, Volume 147, 1 December 2017, 210901, Copyright (2017), with the permission of AIP Publishing.

Because of the complexity of the glass transition and its dynamical nature, the potential energy landscape (PEL) of glass forming systems are featured with widely distributed local minima from where non-Arrhenius dynamics are first observed to places close to the potential energy of crystals. A schematic drawing of the glass potential energy landscape is shown in Figure 1.3. Within the SCL region, the system is able to hope over different local minima via activated hops. However, as the temperature goes down, the system becomes inergodic and equilibrium cannot be maintained[31], eventually landing in a configuration associated with a certain energy.

There is a concept of "ideal glass" which has the closest energy towards a crystal. It represent a nearly perfect amorphous packing with a configuration entropy of zero ($S_c = 0$). It is not yet clear whether an ideal glass state exists and if so, how it can be produced. Efforts have been made both in simulations[109] and experiments[15, 119, 120]. The answers to these questions are correlated with the resolution of the Kauzmann entropy crisis, and are as such important.

1.2. Enhanced Surface Dynamics on Glassy Materials

1.2.1. Fast Surface Diffusion

Surface diffusion being introduced here specifically refers to the lateral translational motion of the surface particles (see Figure 1.4 for the schematic plot). According to the Mullins's theory, there are four mechanisms accounting for the flattening of features on a solid surface: viscous flow, evaporation-condensation (in a closed system), volume diffusion and surface diffusion[151]. As a result, when a sinusoidal surface gratings is flattened, the decay constant (K) is made up of four components that come from the four mechanisms, respectively, and each of them has a different dependence on the sinusoidal spacial frequency ($q = 2\pi/\lambda$, where λ is the grating wavelength).

Therefore, surface grating decay experiments are generally used to measure and characterize the surface diffusivity, by differentiating different flattening mechanisms according to the

power law dependence of the decay constant on q. Previous research on both polymers and molecular glasses have found that when annealing temperature was lower than a threshold (usually close to T_g), the flattening of surface grating would be dominated by the surface diffusion[250, 259, 246], signified by a $K \propto q^4$ relationship, from which the surface diffusion coefficient can be derived. A more recent work containing a variety of organic molecules established a relationship between the molecular size and the surface diffusion coefficient (see Figure 1.5)[124]. The deeper a molecule penetrates into the surface at equilibrium, the slower it diffuses. The observation here indicates the existence of gradients in surface mobility, which will be discussed in section 1.2.3. Besides the surface grating decay experiments, 2D-diffusion induced by introducing rod-like particles onto the surface has also been used to measure the surface diffusion coefficient and showed similar results[255]. Taking advantage of the 2D-diffusion method, which doesn't require above-T_g-annealing, the surface diffusion of aged glasses[253, 24], stable glasses (which will be introduced in section 1.3)[253], and thin films (whose relaxation can be much faster than bulk films)[252] can be measured. It turned out that their surface diffusion all behave very similarly with Arrhenius temperature dependence, equivalent to the values at the surface of liquid quenched bulk glasses. This indicates that the fast surface diffusion is decoupled from the dynamics of the rest of the film.

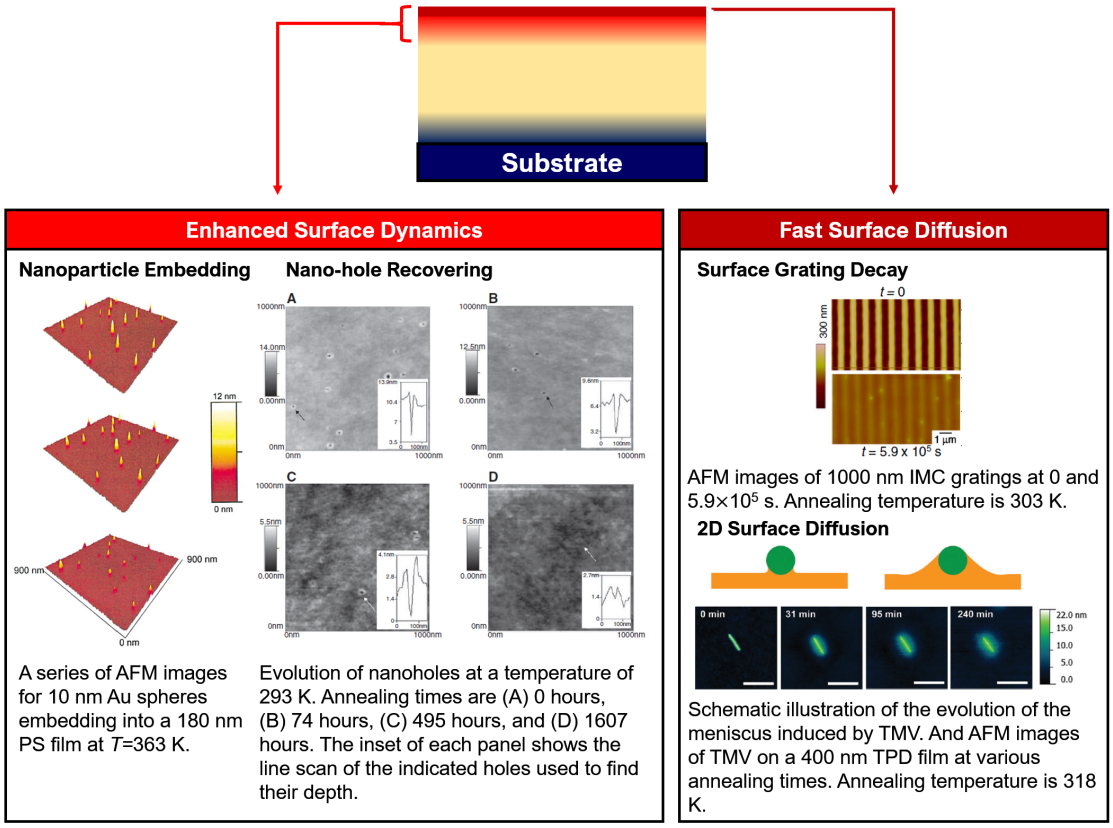

Figure 1.4: Distinguishment between fast surface diffusion and enhanced surface dynamics, with the methods used in meausuring. Nanoparticle embedding part is reprinted from reference[219]: J. H. Teichroeb and J. A. Forrest, Direct imaging of nanoparticle embedding to probe viscoelasticity of polymer surfaces, *Physical Review Letters*, Volume 91, 3 July 2003, 016104, Copyright (2003), with the permission of The American Physical Society. Nano-hole recovering part is reprinted from reference[61]: Z. Fakhraai and J. A. Forrest, Measuring the surface dynamics of glassy polymers, *Science*, Volume 319, Issue 5863, 01 Feb 2008, 600-604, Copyright (2008), with the permission of The American Association for the Advancement of Science. Surface grating decay part is reprinted from reference[259]: L. Zhu, C. W. Brian, S. F. Swallen, P. T. Straus, M. D. Ediger and L. Yu, Surface self-diffusion of an organic glass, *Physical Review Letters*, Volume 106, 24 June 2011, 256103, Copyright (2011), with the permission of The American Physical Society. 2D surface diffusion part is reprinted from reference[255]: Y. Zhang, R. Potter, W. Zhang and Z. Fakhraai, Using tobacco mosaic virus to probe enhanced surface diffusion of molecular glasses, *Soft Matter*, Volume 12, 14 Oct 2016, 9115-9120, Copyright (2016), with the permission of The Royal Society of Chemistry.

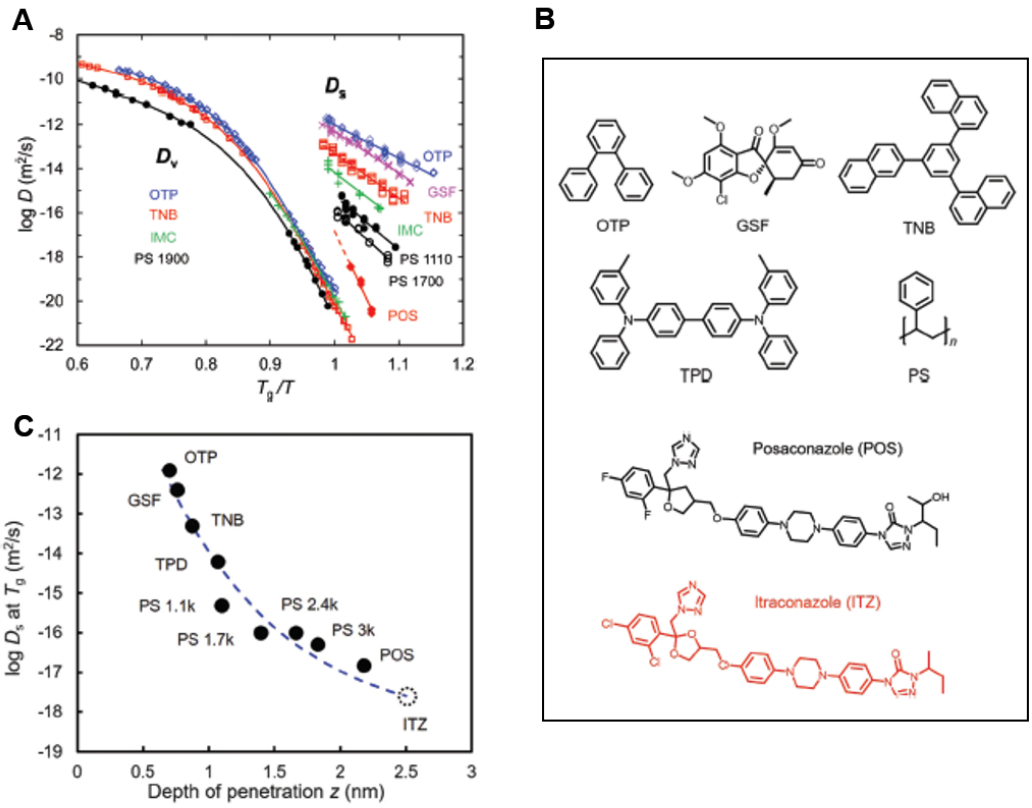

Figure 1.5: (A) Scaled surface diffusion coefficient (D_s) and bulk diffusion coefficient (D_v) for a collection of molecules shown in (B). (B) Chemical structures of the molecules plotted in this figure. (C) A master curve between log (D_s) and the penetration depth of the molecules in (B). Reprinted from reference[124]: Y. Li, W. Zhang, C. Bishop, C. Huang, M. D. Ediger and L. Yu, Surface diffusion in glasses of rod-like molecules posaconazole and itraconazole: Effect of interfacial molecular alignment and bulk penetration, *Soft Matter*, Volume 16, 22 May 2020, 5062-5070, Copyright (2020), with the permission of The Royal Society of Chemistry.

When the grating decay method was applied to metallic glasses, they were also seen to have fast surface diffusion[26, 27]. However, the magnitudes of enhancement relative to the bulk depends on the specific components[217, 34, 7] and are generally found to be smaller than the magnitudes of enhancement observed on organic molecular glass surfaces[187, 27, 12]. Through molecular dynamics simulations, it was identified that surface energy and the missing bonds of the surface atoms are responsible for the fast surface diffusion on metallic glasses[7, 6]. The formation of alloy clusters may in turn inhibit the atom diffusion[25].

1.2.2. Enhanced Surface and Thin Film Relaxation Dynamics

The fast surface diffusion in section 1.2.1 specifically characterizes the mobility of the immediate glass surface. In addition to that, enhanced surface dynamics within a certain range close to the surface are also reported. The surface relaxation times of polymers and their molecular weight dependence were mainly studied through fluorescence probes[77, 54, 160], nanoparticle embedding experiments[92, 168] and hole recovery experiments[60] (see Figure 1.4 for the schematic plot). Similar methods can be applied to molecular glasses as well[43]. Computer simulations[226, 199, 18] have also shown results supporting the idea of enhanced surface dynamics on glassy materials, below just the immediate free surface.

As the film thickness is reduced, the surface portion will become more and more dominant. Enhanced surface dynamics have significantly facilitated the thin film relaxations. Previous report on the dewetting of N,N'-Bis(3-methylphenyl)-N,N'-diphenylbenzidine (TPD) molecular glass shows that the evolution in film morphology could happen below T_g for films below 30 nm[254]. When there are no strong substrate interactions, glass transition temperatures of thin films are measured to be lower than the bulk value, with a smaller activation energy[101, 70]. The expansion coefficient[101, 237] and indices of refraction[90] are shown to increase as film thickness decreases, while the viscosity[239], physical aging rate[166] and elastic modulus[222] decreases with decreasing film thickness.

Fast surface diffusion and enhanced surface dynamics are two separate concepts, as indicated in Figure 1.4. In some systems they are correlated. However, for polymers that are characterized to have enhanced surface dynamics[60, 92, 168], their surface diffusion are relatively low compared to most molecular glasses[60, 124], because part of their long chain are anchored within the slow dynamics region below the free surface. Measurements directly on surface diffusion and thin film relaxation result in different dependence on temperature[252]. There are also glasses that don't show fast surface diffusion but have enhanced surface relaxation[188]. Plenty of investigations have already suggested that surface diffusion and thin film relaxation time (τ_α) are decoupled.

Nevertheless, a common feature exhibited by fast surface diffusion and enhanced surface dynamics for fragile liquids is that both of them have relatively weak temperature dependence which follows Arrhenius relationship[259, 167, 43], as oppose to the bulk relaxation which depends strongly on temperature and follows the VFT equation. It is important to study the enhanced surface dynamics on glassy materials because it plays a key role in maintaining their physical properties. The surface crystal growth rate is found to be proportional to surface diffusion coefficient[246]. Surface initiated degradation[238] and transformation[214] can generally cause material failure. In section 1.3.3, we are going to introduce how fast surface relaxation facilitates the formation of stable glasses, which is the main research subject of this thesis.

1.2.3. The Gradient of Dynamics of the Surface Mobile Region

As introduced above, the bulk viscosity of a glassy material reaches 10^{12} Pa·s (τ_{alpha} ~100 s) at T_g. And both the viscosity and structural relaxation times could increase by approximately one order of magnitude upon every 5 K reduction in temperature. However, at the free surface, the surface dynamics can be 4 - 6 orders of magnitudes faster than the bulk dynamics and are shown to depend only weakly on temperature (1 decade in relaxation time $\sim$ 40 K temperature change). The distinction between surface and bulk relaxation times can be more pronounced at temperatures below T_g. Considering the significant distinctions between surface and bulk dynamics, it is necessary to investigate how the gradient of mobility looks like in between, and how deep the effects of enhanced surface dynamics penetrate. In Figure 1.5, the organic glass surface diffusivity is shown to be related to the penetration depth of the organic molecules[124]. Moreover, in earlier publications from our group, we found a simple 2-layer (or 3-layer including the interface with substrate) model containing a constant interfacial layer thickness cannot fit the apparent activation energy change with film thickness well[254, 256]. Both experimental results above suggest that there is a continuous decay in molecule mobility (relaxation) from the free surface, instead of an abrupt change. Some computational studies also provide evidences to support the existence of a dynamics gradient[135, 78]. Additionally, this gradient of dynamics in the surface mobile re-

gion is shown to be strongly dependent on film thickness and temperature[124, 256, 78, 237].

A lot of research have been done with a focus on determine the length scale of fast surface dynamics. Through nanoparticle embedding experiments, people estimated a 3 - 9 nm liquid-like layer at the free surface close to T_g[196, 167]. By mixing a small amount of fluorescence probe into polystyrene thin films and monitoring the fluorescence decay, the thickness of the surface mobile layer was measured to be $\sim$7 nm at T_g, decreasing with decreasing temperature[160], and became $\sim$1 nm at 0.9 T_g. A neutron scattering experiment based on molecule diffusivity gave similar results[213].

On the other hand, macroscopic T_g measurements on thin films can be used as an indication of how much their relaxation is enhanced. If fast surface dynamic persists in the main part of a film, we should expect it to stay on the extrapolated SCL line longer and have a smaller T_g. Indeed, a significant reduction in T_g for polymer films thinner than 40 - 60 nm has been observed in multiple systems[104, 101, 70, 54, 67]. The mid-point of thin film to bulk transition generally occurs $\sim$ 30 nm. Similar length scale is seen on molecular glasses too[256].

A more intriguing discovery is the separation between enhanced surface dynamics and substrate effect. When there is a favored interaction between the molecule and substrate, two distinct T_gs might be observed and they become separated more in thin films, suggesting a divergence in relaxation dynamics within a 16 nm film[71]. Details discussion on substrate effect will not be elaborated here. However, it worth bringing into attention that the competition between substrate effect and enhanced surface dynamics will largely influence thin film behaviors.

1.3. Stable Glass

1.3.1. Physical Vapor Deposition and the Discovery of Stable Glass

Physical vapor deposition (PVD) is a commonly used thin film manufacturing method. During PVD, samples are heated to evaporate or sputtered onto substrates inside super

high vacuum chambers. Uniform amorphous films can generally be formed through PVD. In 2007, Ediger's group reported a discovery of a highly stable glass using PVD method, by performing the deposition under controlled substrate temperature and rate[213]. The glasses they made were characterized to have higher density, lower enthalpy and better kinetic stability compared to liquid quenched glasses (LQs). Because of their extraordinary stability, they are named "stable glasses" (SGs).

As mentioned above, deposition temperature (T_{dep}) and rate (r) are two main factors that control the glass stability. Vast investigations have been conducted to understand the influence of these two factors. For most organic glasses, the maximum stability is usually observed up around T_{dep} = 0.8 - 0.85 T_g[102, 41, 128, 172, 249], except for those which have strong inter-molecular interactions[118]. As for the deposition rate, lower r will yield more stable glasses[103, 132, 22]. A detailed explanation on the influence of T_{dep} and r will be provided in section 1.3.2.

Since their discovery, SGs have drawn a lot of research interest because of their improved thermodynamic and kinetic stability measured by Differential Scanning Calorimetry (DSC)[213, 103, 172] ,X-ray Reflectivity[213] and *in situ* Ellipsometry[41, 128]. In addition, SGs are characterized to be mechanically stronger[62, 223, 218] and have better resistance toward degradation[169, 170], crystallization[182] and gas/liquid permeation[47, 206]. Up to now, more than 50 organic molecules have been reported to form SGs when deposited under certain conditions[52]. Metallic amorphous materials[249, 132] and low molecular weight narrow distributed polymers[171] and colloidal glasses[28] are shown to form SGs as well.

More significantly, the discovery of SGs has potentially opened up a new way to study the concept of "ideal glass" and resolve the aforementioned Kauzmann Entropy Crisis. Rather than performing aging experiments that take incredible amount of time, through PVD, it has become to access the equilibrium state as close as 2 K away from the predicted Kauzmann temperature in ethylbenzene and toluene systems. Interestingly, no anomalies indicative of potential phase transitions has been observed in these systems[15, 119, 120].

If the extrapolation continues to hold, T_K will be reached and the configurational entropy S_c will diminish to 0 in a liquid. To avoid that, it is suggested that very likely a phase transition will occur within several Kelvins above T_K, either to an ideal glass or to crystals.

1.3.2. Surface Mediated Equilibration and Stable Glass Formation

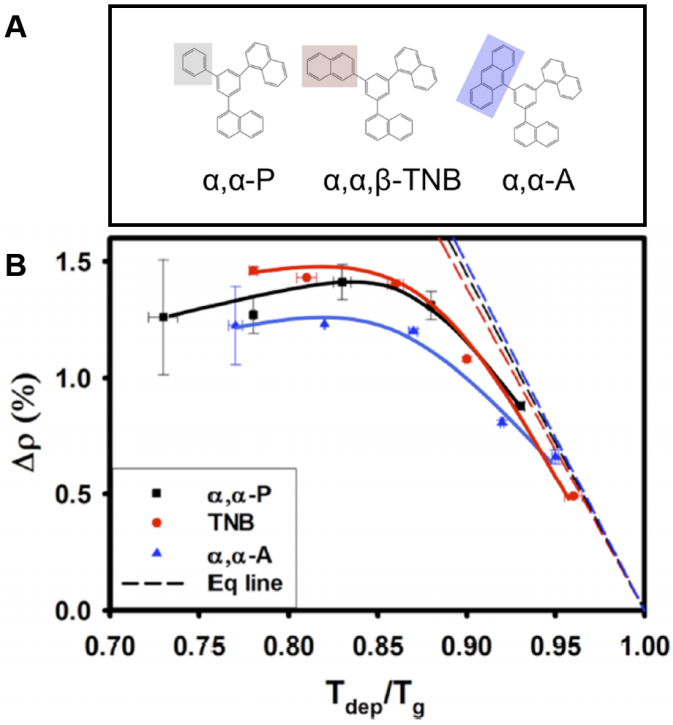

Figure 1.6: (A) Molecular structures of the molecules shown in (B). (B) Temperature dependence of PVD glass relative density ($\Delta\rho$) for α,α-P, α,α,β-TNB and α,α-A. Dashed lines are the equilibrium lines for each molecule assuming the density upper bound for PVD glasses is defined by the extrapolated SCL line. Reprinted from reference[128]: T. Liu, K. Cheng, E. Salami-Ranjbaran, F. Gao, C. Li, X. Tong, Y. Lin, Y. Zhang, W. Zhang, L. Klinge, P. J. Walsh and Z. Fakhraai, The effect of chemical structure on the stability of physical vapor deposited glasses of 1,3,5-triarylbenzene, *Journal of Chemical Physics*, Volume 143(8), 28 August 2015, 084506, Copyright (2015), with the permission of AIP Publishing.

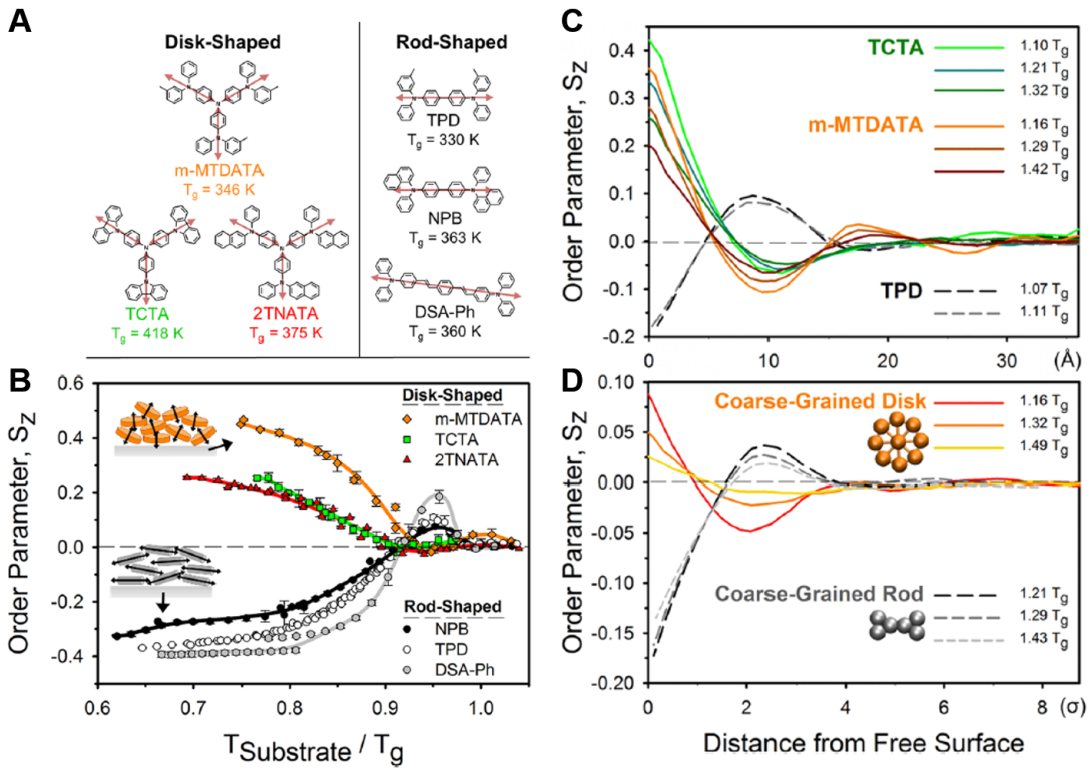

Figure 1.7: (A) Molecular structures of the molecules shown in (B)&(C). (B) Experimental order parameter (S_z) as a function of T_{dep} calculated from ellipsometry or UV-Vis experiments for a variety of rod-shaped and disk shaped molecules. (C)/(D) Order parameter (S_z) obtained from atomistic/coarse-grained simulations as a function of distance from the free surface of the corresponding equilibrium liquids for selected molecules. Reprinted from reference[233]: D. M. Walters, L. Antony, J. J. de Pablo and M. D. Ediger, Influence of molecular shape on the thermal stability and molecular orientation of vapor-Deposited organic semiconductors, *The Journal of Physical Chemistry Letters*, Volume 8(14), 5 July 2017, 3380-3386, Copyright (2017), with the permission of American Chemical Society. This is an unofficial adaptation of an article that appeared in an ACS publication. ACS has not endorsed the content of this adaptation or the context of its use.

Surface Mediated Equilibration (SME) has been proposed to account for the formation of stable glasses[133, 18], with fast surface dynamics, which is introduced in section 1.2, being its basis. It is understood that during the deposition process, molecules on top of the surface will have certain mobility and lower activation energy that allows them to accommodate themselves with a energy favored state before they are deeply buried[213, 205, 225, 52]. This is equivalent to a fast aging/slow cooling process, which occurs on the surface of deposited

films during PVD, resulting in a more stable glass that exists at a lower state on the PEL.

Because of the existence of dynamics gradients in the surface mobile region, besides the diffusion and relaxation of the very top layer molecules, molecular motions that happened below the surface within its dynamics gradient layer are of critical importance. Evidences are provided that significant structural rearrangement could occur under the immediate surface and it plays a role in controlling PVD glass stability and packing[148]. An *in situ* dielectric measurement indicated that a thin layer of molecules with a thickness of several nanometers would undergo an aging process that lasted a couple of minutes toward equilibrium when deposition was finished[220].

If we look at any T_{dep} dependence of PVD glass stability, we observe a curve with a single maximum as T_{dep} decreases from T_g[102, 213, 128, 249]. Taking PVD glass relative density as an example, we see the density of PVD glass follow the equilibrium line defined by their extrapolated SCL line at high T_{dep} and start to deviate as T_{dep} is further decreasing. After going through a maximum, the density becomes smaller (Figure 1.6[128]). In the high T_{dep} regime, before the maximum density is achieved, surface molecules have sufficient mobility to arrange themselves before their dynamics are arrested. The driving force towards equilibrium is the main limitation that defines the ultimate density of the glasses in this regime. However, As T_{dep} is further reduced, surface relaxation times become larger and the thickness of the dynamics gradient region will shrink. In this regime, stability is compromised due to high kinetic barriers for rearrangement. The maximum relative density is achieved at the T_{dep} where a balance is met between the thermodynamic driving force and kinetic barriers.

Deposition rate (r) is another variable that affects PVD glass stability[103, 37, 132]. Lower r provides more time for the molecules to accommodate. Therefore, PVD glass stability will increase and the T_{dep} giving the maximum stability will decrease as r decreases[22]. Because the surface relaxation time of metallic glasses is generally longer than that of organic glasses[26, 246, 132], similar extent of stability in metallic glasses will require adopting lower

deposition rates[132]. Moreover, in molecular systems with strong/preferred inter-molecular interactions, such as hydrogen bonding[224, 118] or micro-structure aggregation[148], a shift of the T_{dep} for maximum stability towards T_g and a reduction in its value are observed due to the constrain on surface mobility[35, 36].

SME can also be used when understanding the SG structure and anisotropy. Since SGs are formed under kinetically arrested conditions through a single-direction growth method, they are usually characterized to have optical birefringence[242, 39, 42, 200, 233, 156, 143] and packing anisotropy[75, 42, 76, 233, 72, 10, 236, 207]. As can be seen in Figure 1.7, the order parameter (S_z) of PVD glasses exhibit a strong T_{dep} dependence for disk-shaped and rod-shaped molecules. By comparing the experimental result with simulations, it has been concluded that the PVD glass packing is actually inherited from the equilibrium liquid structure of each molecule at the free surface[233]. Under low T_{dep}, the thickness of surface mobility gradient is relatively small and the as-deposited glass packing will only reflect the preferred molecular orientation at the very top layer of the equilibrium liquid, which is oriented due to the flat surface constraint. However, as T_{dep} becomes higher (or at lower deposition rates), a larger surface mobility gradient will facilitate the PVD glass to adopt an averaged structure of a thicker layer on the surface of the equilibrium liquid[133, 75, 42], resulting in orientation normal to the surface, or ultimately isotropic configuration[148].

1.4. Summary

In this dissertation, I will discuss my graduate work on manipulating SG packing and properties by changing deposition conditions, nature of the deposited compound and modifying the molecules' chemical structure. The properties I am mainly focused on are the SG relative density, kinetic stability (onset temperature of transformation), optical birefringence, and structural anisotropy. By looking at different vapor deposited systems, we demonstrate the importance of surface mediated equilibrium and how subtle surface relaxation can control the deposited glass packing and properties.

In Chapter 2, I studied the SGs formed by a chalcogenide atom, selenium, under different

deposition conditions. Especially, light, for the first time, has been introduced into deposition process. A polyamorphic state of amorphous selenium (a-Se) with extraordinary kinetic stability was formed by depositing under light. In Chapter 3, light-induced fluidity in a-Se thin films was measured quantitatively by dewetting experiments. And the deviating behaviors of a-Se thin films compared to bulk films are discussed further in Chapter 4. Chapter 5 presents work on the influence of intra-moleculer degrees of freedom on PVD glass stability and anisotropy. In this chapter, I illustrated in details how intra-molecular relaxation, molecular shape, surface diffusion, and gradients of surface dynamics are involved in the formation and structure of SGs. At last, Chapter 6 shows the effect of inter-molecular interactions, investigating molecules containing fluorocarbon tails with various lengths. The experimental data are compared and validated by simulations.

CHAPTER 2: Polyamorphism of Vapor-deposited Amorphous Selenium in Response to Light

This chapter is reproduced with permission from reference[248]: A. Zhang, Y. Jin, T. Liu, R. B. Stephens, Z. Fakhraai, Polyamorphism of vapor-deposited amorphous selenium in response to light, *Proceedings of the National Academy of Sciences of the United States of America*, Volume 117(39), 29 September 2020, 24076-24081, Copyright (2020), National Academy of Sciences.

2.1. Abstract

In the past decade, a lot of work has been done on organic stable glasses (SGs). It was understood that enhanced surface mobility is critical in producing SGs. Only a few inorganic systems have been studied so far in terms of their ability to form SGs and the variables that controls their stability. In this chapter, we discuss about the SG formation of an inorganic glass, amorphous selenium (a-Se) and its response to light.

A-Se has a complicated molecular structure with over-coordinated defects and dangling bonds. Moreover, its structure and the dynamics of the surface can be altered when exposed to above-bandgap light. Here, we investigate the effect of light on the properties of vapor-deposited a-Se glasses at a range of substrate temperatures and deposition rates. We demonstrate that deposition both under white light illumination and in dark results in thermally and kinetically stable glasses. Compared to glasses deposited in dark, stable a-Se glasses formed under white light have reduced thermal stability, as measured by lower density change, but show significantly improved kinetic stability, measured as higher onset temperature for transformation. While light induces enhanced mobility that penetrates deep into the surface, resulting in lower density during vapor-deposition, it also acts to form more networked structures at the surface, which results in a state that is kinetically more stable with larger optical birefringence. We demonstrate that the structure formed during deposition with light is a state that is not accessible through liquid quenching, aging, or

vapor deposition in dark, indicating the formation of a unique amorphous solid state.

2.2. Introduction

Physical vapor deposition (PVD) is a widely used method to prepare amorphous thin films. Over the past decade, a variety of systems have been shown to form stable glasses (SGs) when prepared through PVD with the substrate temperature (deposition temperature, T_{dep}) held below the glass transition temperature (T_g) of the material[213, 103, 41, 172, 118, 128, 249, 132]. SGs have improved thermal[213, 128, 103, 232] and kinetic stabilities[41, 183, 172, 249, 132] compared to liquid quenched (LQ) glasses, resembling glasses aged for hundreds or millions of years. SGs are also shown to have anisotropic packing that depends on the deposition conditions and molecular structure[183, 243, 42, 129].

It is understood that SG formation is a result of surface-mediated equilibration (SME) due to enhanced mobility near the glass surface [118, 246, 132, 18, 148, 188, 42]. When T_{dep} is held below T_g, at slow deposition rates ($\sim$ 0.2 nm/s for most organic glasses), the surface region has sufficient mobility[253] to reach more energetically favored states before molecules are buried deeper into dynamically arrested states. The stability of a PVD glass thus strongly depends on T_{dep}[102, 41, 128, 172, 249] and the deposition rate[103, 132, 22]. SME also influences the structure of a PVD glass and its birefringence, which are inherited from the equilibrium states at the free surface of the glass[233, 9] and the layers directly below the free surface[148, 42].

A few inorganic glasses have also been shown to produce stable and/or anisotropic glasses upon PVD[195, 249, 132, 150]. However the enhanced surface mobility in these systems appears to be less pronounced[26, 246, 132, 12]. Thus, in order to achieve a similar extent of stability, lower deposition rates are required[132]. In both organic and inorganic systems, besides the T_{dep} and deposition rate, few factors are available to control the degree of enhanced surface mobility and its penetration depth[118].

A-Se is an exception, where above-bandgap light can strongly affect its surface structure and

dynamics, therefore potentially the SME process. A-Se is of interest because it is useful in applications such as digital X-ray detection[177] due to its outstanding X-ray cross section. Extensive studies on a-Se structure[240, 191, 136] indicate that it is primarily made of disordered Se_n helical chains with some coordination defects and vast inter-chain non-bonding interactions. Viscoelasticity measurements indicate that the temperature dependence of creep compliance in a-Se close to its T_g is very similar to a polystyrene system with $M_w \sim 12000$ close to its respective T_g. Thus the chain length of a-Se is estimated to be around 230 atoms/chain around T_g[16]. It is also estimated that the a-Se has more three- and four-fold-coordination sites at its free surface[191]. A-Se has a low bandgap, $\sim$2 eV[177], allowing its structure to be altered by white light. The light-induced behavior of a-Se has been thoroughly investigated using various techniques[111, 112]. The electrons excited by above-bandgap irradiation[112] increase the system's coordination number[111, 251], facilitate bond rearrangements[112] and valence alternations. As a result, a-Se chains exhibit extra fluidity under illumination. The penetration depth of light-induced effects is estimated to be $\sim$ 50 nm to 1000 nm below the surface, depending on light conditions (See Figure 2.12B). While the free drift time of light generated electrons/holes is estimated to be on the order of 10^{-6} to 10^{-4} s within the temperature range of our experiment[79].

Here we study how light-induced changes in Se surface dynamics and structure can affect the SME process and, in turn, the formation of a-Se SGs. We demonstrate that SGs produced under white light illumination (lit) and in dark are structurally distinct and cannot be simply transformed into one another. When lit, highly networked and kinetically stable SGs are produced that cannot be otherwise made through physical aging of any length of time, representing a region in the energy landscape that was previously inaccessible. This is a unique demonstration of polyamorphism in an atomically simple structure, which is achieved through manipulation of the surface structure and dynamics using light.

2.3. Experimental Details

2.3.1. Material and Film Preparation

Selenium lumps (purity 99.999%) were purchased from Goodfellow Corporation and used directly. The bulk glass transition temperature (T_g) of a-Se wes determined by differential scanning calorimetry (DSC, Model Q2000 from TA Instruments). 9 mg selenium lump was sealed in a DSC aluminum pan with hermetic lid (TA Instrument) and heated from 273 K to 523 K at 10K/min, followed by cooling to 273 K at the same rate. This measurement was repeated using the same parameters on the same sample. T_g was calculated by averaging the onset and the offset of the glass transition upon cooling, and determined to be 306±1 K (Figure 2.1).

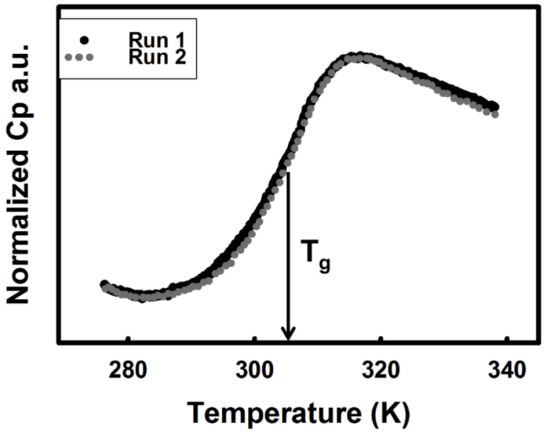

Figure 2.1: Differential scanning calorimetry measurements showing the heat capacity (C_p, arbitrary units) of a-Se as a function of temperature at a 10 K/min cooling rate. T_g is determined to be 306±1 K. Two independent cooling rates are shown.

A-Se films of approximately 2000±100 nm thickness (or 3000±100 nm thickness when the deposition rate was 4 nm/s) were deposited on Boron doped Si substrates with a native oxide layer of $\sim$ 1 nm (Virginia Semiconductor Inc.) in a custom vacuum chamber, as what is described in our previous publication[128]. The base pressure of the chamber was $\sim 1 \times 10^{-7}$ torr. The temperature of the copper sample holder, which is attached to the inner side of a top aluminum flange, was controlled by an thermoelectric cooler

outside the flange. Temperature of the aluminum flange was read through a thermistor temperature sensor (Oven Industries Inc., TR91-170). The thermoelectric module was cooled using a Polyscience water chiller (Model 9102) which contains ethylene glycol-water mixture (ethylene glycol:water = 50:50 wt%). The set up provides a deposition temperature range of 255 K< T_{dep} <400 K. The deposition temperature (T_{dep}) reported in this paper are based on a linear extrapolation from a previous calibration, using calibration standards reported previously[128], which compensate for the temperature difference between the copper sample holder and the aluminum flange. The deposition rate was monitored using a quartz crystal microbalance (Sycon Instrument STM-1) mounted beside the copper sample holder. An aluminum oxide crucible filled with selenium lumps was placed in a tungsten heating basket. By controlling the power input to the basket, the deposition rate was controlled within the range of 0.02 - 4 nm/s. Deposition rate was generally stabilized before 5% of the film was deposited (10% for films deposited at 4 nm/s). Stabilization at higher deposition rates were more challenging and thus the results are not reported here.

Illumination during deposition was introduced by a white LED light (Thorlabs LEDWE-15, Epoxy-Encased White Light LED, see Figure 2.12A for emission spectrum[221]). Optical power at the substrate position was measured to be 1.0±0.5 mW/cm^2 with COHERENT FIELDMATE optical power meter and PM10 PowerMax probe.

Upon finishing the deposition, a-Se films were kept inside the chamber for ∼1 hour either at T_{dep}, when the T_{dep} was below 273 K, or at 273 K, when the T_{dep} was above 273 K, before they were transferred from the deposition chamber onto the ellipsometer stage (J. A. Woollam, Model M-2000 V). This was done to ensure that the evaporation source was adequately cooled before the chamber was exposed to the ambient atmosphere. To prevent the effect of ambient light, which affects a-Se properties, a 660 nm deep red LED (ABI GR-PAR38-12W-DR) light was used as the lab's lighting source when the films were handled and transferred.

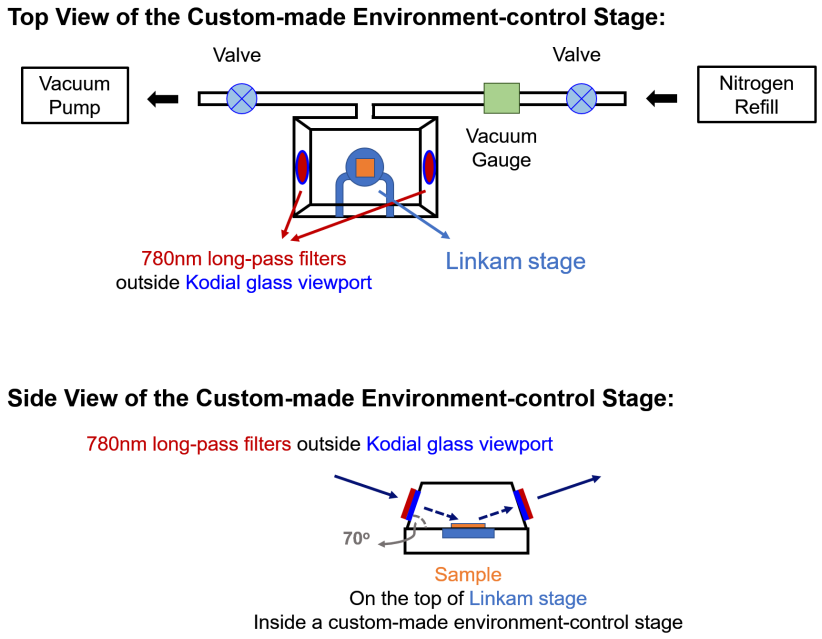

Figure 2.2: A schematic drawing of the custom-made environment-control stage for ellipsometry measurements.

2.3.2. in situ Ellipsometry Transformation to Determine Film Stability

Ellipsometry measurements were carried out at 70° incident angle under nitrogen atmosphere in a custom-made environment-control stage (Figure 2.2). This was done in order to prevent water condensation during the heating and cooling cycles at temperatures below the dew point of water, which was required for this study. The chamber was connected on one side to an Edwards XDS5 Dry Vacuum Pump and on the other side to a nitrogen cylinder. Vacuum level were measured using a thermal conductivity gauge (Kurt J. Lesker 275i Convection Vacuum Gauge Module) placed in-line of the stage. The stage was equipped with a Linkam temperature-control module (Linkam THMS350V) used to control temperature of the sample during transformations. The viewports on both sides of the stage were made up of Kodial glass (Kurt J. Lesker QF16-075-VP) and form 70° angle with the sample's reflection plane.

To block the ellipsometer's incident light above the a-Se bandgap (650 nm determined by

ellipsometer fitting, see Figure 2.11C), a 780 nm long-pass filters was placed outside each viewport (Figure 2.2), unless otherwise stated.

Within 30 min after removing each sample from the deposition chamber, the sample was placed on the vacuum Linkam stage using a thermally conductive paste (Custom Thermoelectric Arctic Alumina Thermal Compound) and the stage was sealed. The chamber was then pumped down to ∼100 mtorr and refilled with nitrogen gas. This procedure was repeated 3 times to remove residual water, before filling the stage with nitrogen back to 1 atm. The sample was then cooled under nitrogen to 253 K, heated to 323 K (or 333 K when measuring T_{onset}) at 10 K/min and held isothermally for 20 min. The transformation from as-deposited stable glass (SG) to liquid-quenched glass (LQ) was typically completed within the 20 min hold at 323 K (Figure 2.3B). The sample was then cooled back to 253 K at 10 K/min to measure the T_g, density change ($\Delta\rho$), and fictive temperature (T_f), as shown in Figure 2.4.

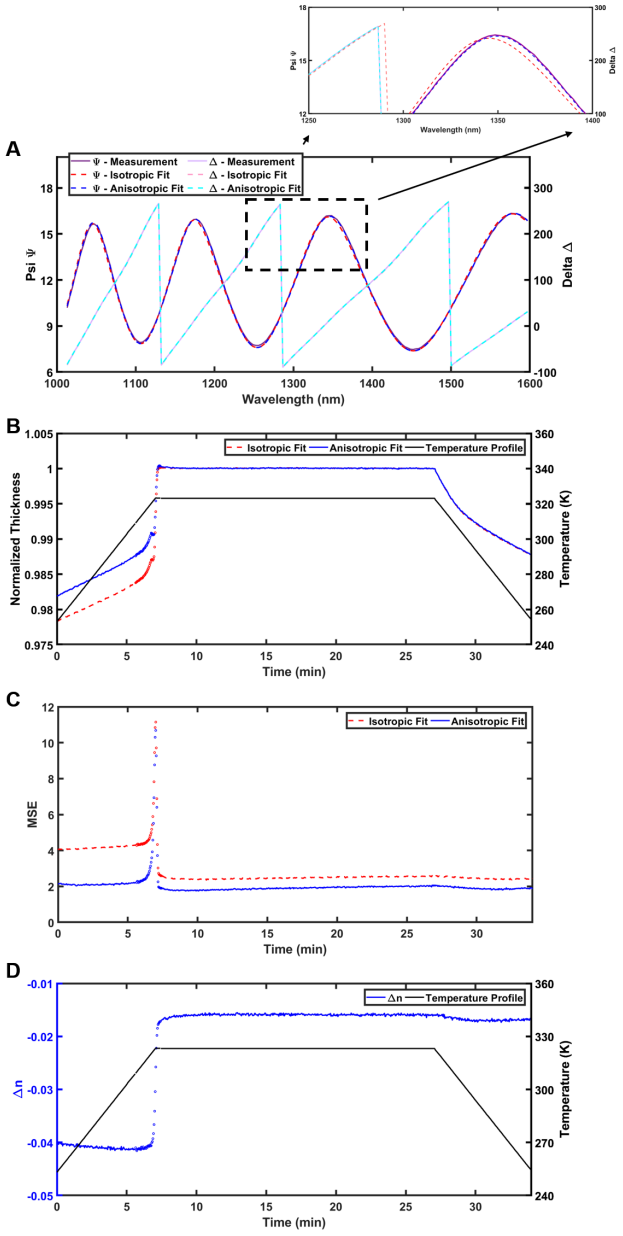

Figure 2.3: (A) Spectroscopic ellipsometry angles $\Psi(\lambda)$ and $\Delta(\lambda)$ vs. wavelength for a 2 μm-thick a-Se SG film (T_{dep} = 262±1 K, 0.2±0.02 nm/s, dark). Isotropic and anisotropic Cauchy model fits are plotted. The image on the top right corner is a zoomed in image between the wavelength of 1250 nm to 1400 nm to amplify the difference between isotropic and anisotropic fitting. (B) Normalized thicknesses of the same a-Se film derived from isotropic and anisotropic Cauchy models as a function of time as the temperature is ramped through transformation. Thickness is normalized by the thickness of the super-cooled liquid at 323 K. (C) Mean squared error (MSE) of the isotropic and ansiotropic Cauchy model fits to the experimental $\Psi(\lambda)$ and $\Delta(\lambda)$ values. (D) Difference in refractive index ($\Delta n = n_z$ - n_{xy}) of the sample when it is fitted with anisotropic Cauchy model.

During the temperature ramp, Spectroscopic Ellipsometer variables Ψ (amplitude change) and Δ (phase change) were recorded every 2.4 s with zone averaging. Ψ and Δ relate to the ratio of R_p to R_s, where R_p represents the reflection coefficient of light parallel to the plane of incidence and R_s refers to the reflection coefficient of light perpendicular to it:

$$\frac{R_p}{R_s} = \tan\Psi \exp(i\Delta)$$

Since light above bandgap is blocked by a filter, the ellipsometric angles were fitted to a transparent Cauchy model in the wavelength range between 1000 nm to 1600 nm to obtain the transparent index of refraction, as well as film thickness. Correction for window effects originated from the Kodial glass viewports was also applied during the fitting. When needed, a wavelength-independent out of plane optical birefringence was also included as:

$$\begin{aligned} n &= A + \frac{B}{\lambda^2} \\ \Delta n(\lambda) &= n_z - n_{xy} = A_z - A_{xy} \end{aligned}$$

Fitting parameters used are: A, B, dZA (when needed, dZA = A_z - A_{xy}), film thickness and roughness. Roughness is fitted as an analogy to a low-index layer which has 50% material and 50% void.

Figure 2.3 shows the quality of fitting of the as deposited data to both isotropic ($\Delta n = 0$) and anisotropic Cauchy fits as well as the evaluated normalized thickness and fitting error for both models as the temeprature is ramped through transformation. It can be clearly seen that anisotropic model fitting agrees better with the experimental Ψ and Δ (Figure 2.3A). It also gives smaller mean squared error (Figure 2.3C). The normalized thickness of SG derived from anisotropic Cauchy model is larger than the thickness obtained from the isotropic Cauchy model. As such, using an isotropic fit would overestimate the stability of a given sample. After the film is transformed into the supercooled liquid (SCL), the two models report much smaller difference in values for the film thickness as a function of

temperature because the film is almost isotropic at this point and the fitted birefringence becomes smaller. We note that sometimes a small birefringence remains in the LQ glass due to the stress induced by the expansion coefficient mismatch between the glass and the silicon substrate upon cooling from temperature above T_g[40].

We note that there is a large MSE error during the transformation for both models. This is likely due to the transformation growth fronts moving into the film and as such making the index of refraction more inhomogeneous[40]. The values of the index in this regime are unreliable and are marked differently in the figures containing transformation data.

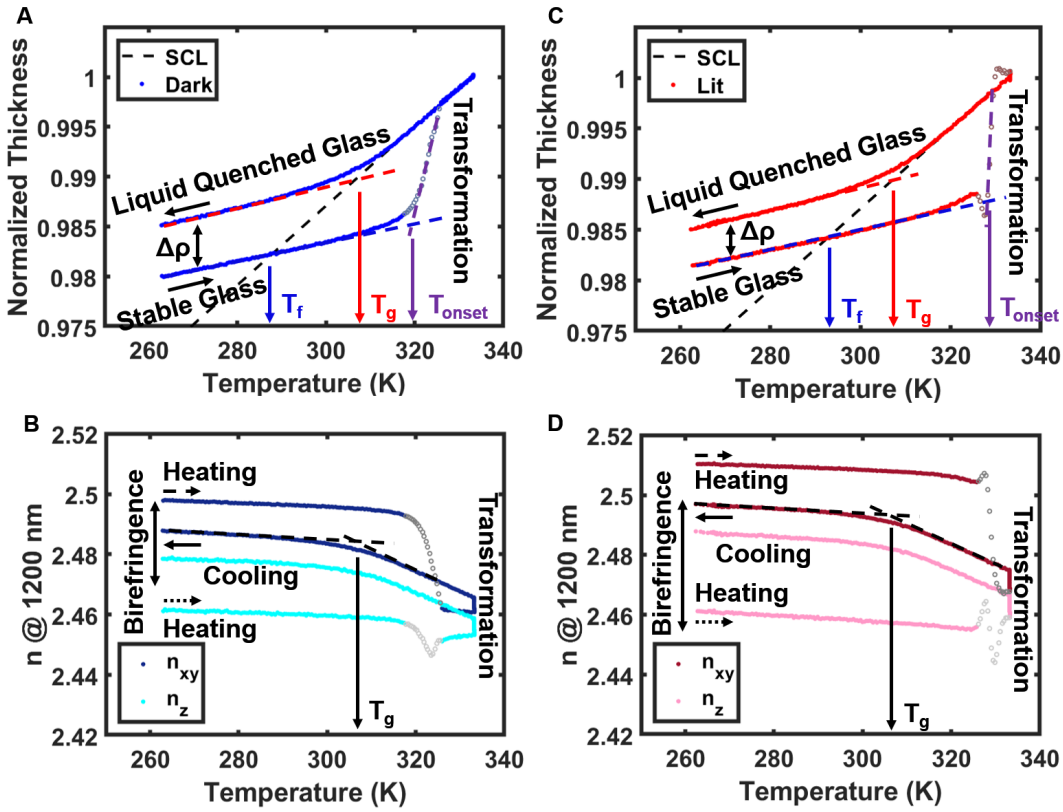

Figure 2.4: (A) Normalized thickness as a function of temperature for a 2 μm-thick a-Se film deposited at T_{dep} = 262±1 K ($0.86T_g$), with a deposition rate of 0.2±0.02 nm/s in dark. The as-deposited film was heated from 253 K to 333 K and held isothermally for 20 min, then cooled back to 253 K, transforming into LQ glass state. The heating/cooling rates were 10 K/min. Arrows show how T_g, T_f, T_{onset}, and $\Delta\rho$ are determined. Black, red, and blue purple dashed lines are linear fits to the SCL, LQ, SG and transforming regions, respectively. (B) In-plane (n_{xy}) and out-of-plane (n_z) refractive index as a function of temperature for the film as (A). Arrows show the directions of heating and cooling for n_{xy} and n_z. (C) Normalized thickness as a function of temperature for a 2 μm-thick a-Se film deposited at T_{dep} = 262±1 K ($0.86T_g$), with a deposition rate of 0.2±0.02 nm/s under white light. The film is treated in the same way as what is described in (A). (D) In-plane (n_{xy}) and out-of-plane (n_z) refractive index as a function of temperature for the same film as (C). Unfilled symbols in all graphs represent the regime where the ellipsometry fits are unreliable due to the transformation growth fronts.

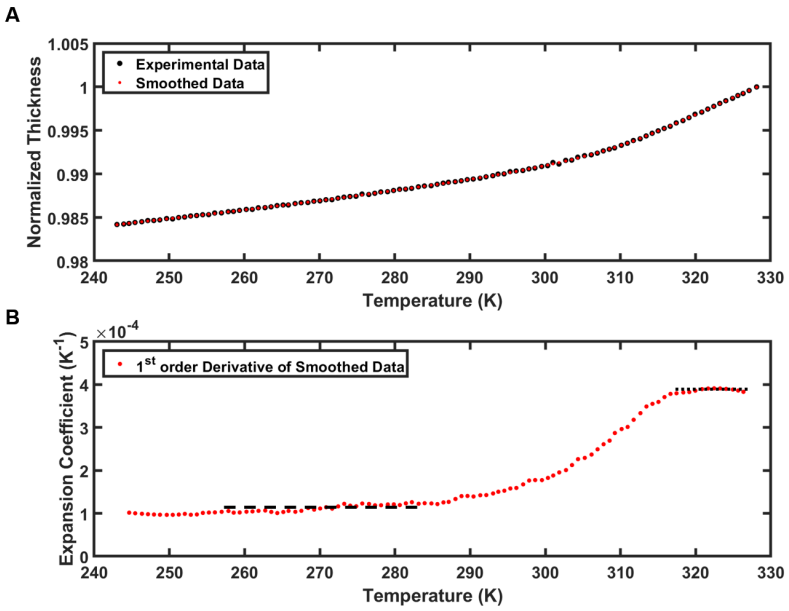

Figure 2.5: (A) Normalized thickness as a function of temperature for a 2 μm-thick a-Se measured upon cooling. Data was smoothed using 3^{rd} order Savitzky-Golay filter in Matlab with a frame length of 10% for the entire data set. (B) Expansion coefficient as a function of temperature, calculated to be the 1^{st} order derivative of the smoothed data in (A). The black dotted line indicates the region used to fit to obtain the SCL expansion coefficient and the dashed line is the corresponding regions for the LQ region.

Density increase ($\Delta\rho$) of the as-deposited glass was determined by comparing the normalized thickness of the as-deposited SG with the transformed LQ glass at 273 K. The fictive temperature (T_f) was defined by the intersection between the extrapolated super-cooled liquid (SCL) line and the heating expansion line of the stable glass (SG). T_f values below T_g and positive $\Delta\rho$ values are indicative of thermal stability of as-deposited films. The kinetic stability was evaluated through measurements of the onset temperature of transformation (T_{onset}). As indicated in Figure 2.4A&C, SG and LQ Glass regimes are fitted linearly from 253 K to 283 K; while SCL regime is fitted from 318 K to 323 K. By averaging more than 10 individual cooling curves, a-Se LQ glass expansion coefficient was determined

to be $(1.0 \pm 0.1) \times 10^{-4}$ K^{-1} and SCL expansion coefficient was measured to be $(3.9 \pm 0.1) \times 10^{-4}$ K^{-1}. These two values were fixed and used in every calculation of density increase and fictive temperature in the manuscript. The glass transition temperature (T_g) measured by fitting ellipsometer data with the method described above is 304±1 K. The SCL expansion coefficient determined here is reasonably close to the values reported in previous publications, which were $(3.55 \pm 0.01) \times 10^{-4}$ K^{-1}[134] and 4.82×10^{-4} K^{-1}[51]. On the other hand, our LQ glass expansion coefficient is slightly lower than what they reported, which are $(1.40 \pm 0.01) \times 10^{-4}$ K^{-1}[134] and 1.64×10^{-4} K^{-1}[51]. This is because the temperature range used in this manuscript to determine the expansion coefficient (253 K - 283 K) is lower than the temperature range used by Dzhalilov and Rzaev (283 K - 293 K), and we find that in the latter range a-Se has not yet fully vitrified and its expansion coefficient continues to decrease as we further decrease the temperature. The glass transition is fully completed and a plateau in the expansion coefficient is reached only when the temperature is decreased below 285 K (Figure 2.5).

2.4. Result and Discussion

2.4.1. The Structure and Stability of Vapor-deposited a-Se Films Prepared in Dark and Lit

A-Se films were deposited in both lit and dark conditions at a range of T_{dep} and deposition rates, as detailed in the Experimental Details section. In the accessible range of T_{dep} in this study, all as-deposited films, both in dark and lit conditions, showed higher density and lower T_f than the LQ glass, indicating that thermally stable glasses were formed (Figure 2.6A&B). As seen in Figure 2.6A&B, as the T_{dep} is decreased, $\Delta\rho$ is increased and T_f is decreased along the extrapolated SCL line (dashed line in Figure 2.6A&B), reaching a maximum around $T_{dep} \sim 0.86T_g$. This maximum in stability is a result of competition between the rate of SME, which decreases with decreasing temperature, and the depth of the equilibrium state, which increases with decreasing temperature. This behavior is consistent with SG formation in other organic[102, 213, 128] and inorganic glasses[249]. It

is an indirect indication that the surface mobility in both lit and dark conditions is enhanced compared to the bulk dynamics.

However, the measured fractional density increase ($\Delta\rho$) of a-Se, both in lit and dark conditions, is generally lower than typically observed in molecular SGs. In molecular SGs, within the T_{dep} range of 0.9 $T_g < T_{dep} < T_g$, near-equilibrium states are obtained with densities close to that of the extrapolated SCL values ($\Delta\rho_{max} \sim$ 1.2% - 1.8%)[41, 128]. In a-Se, even when T_{dep} is only slightly lower than T_g, density increase remains noticeably smaller ($\Delta\rho_{max} \sim 0.5\%$) and T_f stays well-above the corresponding SCL values (Figure 2.6A&B), indicating that in a-Se other kinetic barriers hinder the system's ability to achieve near-equilibrium states.

To understand this apparent kinetic trap, we note that when a-Se oligomers (predominately Se_5 to Se_7[174]) arrive at the surface, they bond rapidly, within 10^{-6}-10^{-4} s[79], to form longer polymer chains, whose equilibrium chain length can be approximately 200 atoms/chain. The polymeric nature of the chain can increase the barriers for relaxation and limit the packing efficiency of a-Se glass during SME. The interaction between the short incoming chains can also potentially slow down the surface mobility and reduce the depth of mobile region, analogous to what has been observed in molecular SGs with strong intermolecular interactions[36, 118, 148].

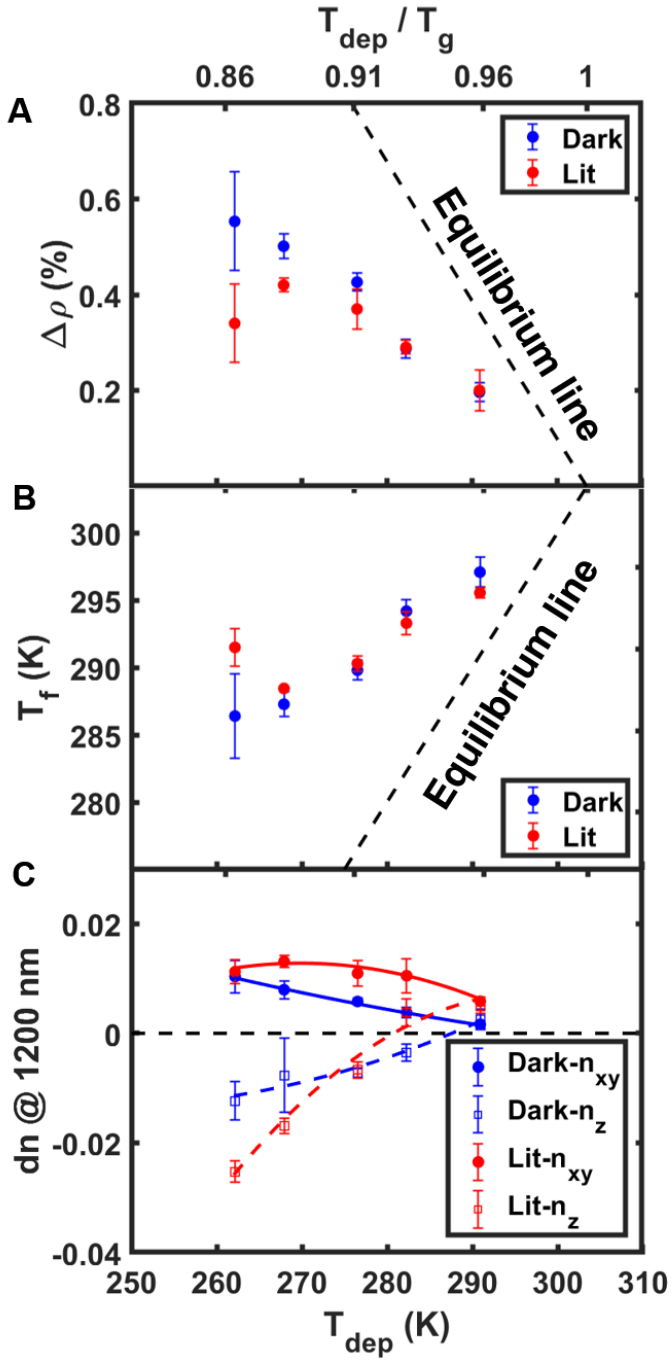

Figure 2.6: (A) Relative density, $\Delta\rho$, of a-Se films deposited in dark (blue) and lit (red) conditions vs. T_{dep}, at a deposition rate of 0.2±0.02 nm/s. (B) Fictive temperature, T_f, of a-Se films deposited in dark (blue) and lit (red) conditions vs. T_{dep}. The black dashed lines in (A) and (B) are the extrapolated equilibrium values. (C) In-plane (n_{xy}) and out-of-plane (n_z) change in the index of refraction of lit (red) and dark (blue) SG films vs. T_{dep}. Lines are guides for the eye. Error bars are based on multiple independent experiments.

An indirect evidence for the polymeric nature of a-Se on its packing is the emergence of optical birefringence, despite a-Se's atomic nature. All as-deposited films, both in lit and dark conditions, show negative optical birefringence (Figure 2.6C) with larger values of the in-plane index of refraction (n_{xy}) compared to the out of plane index (n_z). The optical birefringence disappears upon heating above T_g and subsequent cooling to the LQ state. The negative optical birefringence ($n_{xy} > n_z$) is an indirect indication that chains are primarily aligned horizontally and thus the packing is more frustrated normal to the surface. It is notable that n_z is even smaller than the LQ index, implying that the average atomic distances normal to the film's plane are even larger than the LQ state. These effects become stronger at lower T_{dep} and under the lit conditions, explaining the lower density of lit samples at low T_{dep}. This is likely due to the fact that during lit deposition more networks are formed at the free surface, further prohibiting the SME process. We note that the signatures of this anisotropic packing seem not resoluble by our in-house Grazing Incidence Wide Angle X-ray Scattering (GIWAXS) instrument (Xenocx Xeuss 2.0, more details in Supplementary Information section). However the values measured using ellipsometery are systematically beyond the resolution of SE (typically, $\Delta n \sim 0.005$). Optical birefringence is also observed in molecular SGs. The effect have been attributed to either molecular orientation[39, 75], which is analogous to the in-plane orientation of polymeric chains in a-Se, or layering, which typically results in positive birefringence[129] as well as a distinct layering peak in GIWAXS measurements[75, 9], but it is not observed in our GISAXS experiments (Figure 2.14).

2.4.2. Extraordinary Kinetic Stability of Films Deposited with Light

Despite their thermal stability measured as lower $\Delta\rho$ (Figure 2.6A) at low T_{dep}, lit samples show extraordinary kinetic stability compared to the dark samples. For example, an a-Se Film deposited at $0.86T_g$, 0.2 nm/s and heated at 10 K/min, has an onset of transformation temperature of $T_{onset} = 328\pm2$ K under lit conditions (Figure 2.4C), which is 9 K higher than the $T_{onset} = 319 \pm 2$ K for deposition in dark (Figure 2.4A) and 22 K higher than T_g. This same film, has a density increase of $\Delta\rho = 0.34 \pm 0.08\%$ deposited lit as opposed

to $\Delta\rho = 0.55 \pm 0.08\%$ when deposited in dark, indicating relatively lower thermal stability. This observation is in contrast with most organic SGs whose thermal and kinetic stabilities are generally positively correlated[232, 41]. To understand the origin of this phenomenon, we focus on the unique surface structure of a-Se and how it is affected by light.

Similar to other chalcogenide glasses, a-Se glasses exhibit photo-induced structural rearrangement. Upon illumination with above-bandgap light, a-Se undergoes a volume increase[91, 82] and anisotropic crystallization[164]. Detailed examination using various techniques show an increase in the average coordination number under illumination with an emergence of more three- and four-fold coordinated pairs[111, 113]. Simulations also show more bond breaking with excited electrons and structural topological changes[251]. Given the high absorption coefficient ($\sim 10^4$ - 10^5 cm^{-1}) of above bandgap light, these effects are expected to penetrate somewhere between 50 nm to 1000 nm into the film's surface[80] (Figure 2.12) and are thus not of significant importance in bulk LQ a-Se glasses. However, the increase in volume and coordination number, as well as increased surface mobility can significantly affect the properties of the PVD glass through SME. We note that we do not observe any evidence of surface crystallization in this study in GIWAXS and AFM measurements (Figures 2.13 and 2.14).

The effects of light on the surface mobility and structure is indeed indirectly observed when we compare the properties of lit and dark SGs. Lower $\Delta\rho$ and n_z (Figure 2.6A&C) indicate larger volume at the surface region of lit a-Se films, which templates the structure of the SG film as the atoms are dynamically arrested upon further deposition. A higher fraction of highly coordinated networked structure can also explain the improved kinetic stability of lit samples. Breaking the covalently bonded networks likely requires heating to a higher temperature than is required to transform a molecular SG with Van der Waals interactions.

We note that the states obtained during lit deposition cannot be obtained by a physical aging process of a liquid-quenched glass. While aging can potentially increase the network density[45], that should be reasonably similar to the degree of network formation obtained

during PVD in dark conditions. The density of the networks in lit condition is typically only affected at the surface region for aging while lit. As such, the propagation of this higher network density throughout the film is only possible by PVD while lit. This templating of the structure through the free surface is analogous to the birefringence in molecular glasses that are templated by the orientation of molecules by the surface, except that here this is achieved by actively altering the free surface state using light.

2.4.3. Deposition Rate Dependence of Film Stability

The complicated structure of a-Se either with or without illumination also affects the dependence of their thermal and kinetic stability on the deposition rate in non-trivial ways. Figure 2.7 shows the dependence of $\Delta\rho$, T_f and T_{onset} of a-Se SGs deposited both in lit and dark conditions vs. deposition rate. Focusing first on samples deposited in dark, in the deposition rate range of 0.02 nm/s to 4 nm/s accessible to this study, the density slightly increases and the fictive temperature decreases with decreasing deposition rate, which is expected given the kinetic nature of the SME process. However, decreasing the deposition rate by 2 orders of magnitude from 2 nm/s to 0.02 nm/s only elevates $\Delta\rho$ by $\sim$0.3% and lowers T_f by $\sim$8 K. More surprisingly, T_{onset} is more or less unaffected by the deposition rate in this range. This is in contrast with molecular SGs where the deposition rate has a more significant impact on both the thermal and kinetic stability[103] of SGs. Similarly, while lower surface mobility of metallic glasses results in lower relative thermal stability in these systems[26, 246, 132], limited existing data shows significant increase of T_{onset} when the deposition rate is decreased[132].

The limits in density increase upon reducing the deposition rate implies that there are significant kinetic barriers towards further equilibration during PVD, which is consistent with the packing frustrations due to network formation limiting the density gain. This is also consistent with nearly constant T_{onset} as observed in Figure 2.7C. Indeed we expect a large drop of T_{onset} upon further increase of deposition rate, which appears as a slight decrease of T_{onset} at 4 K/min deposition, but our current set up does not allow faster

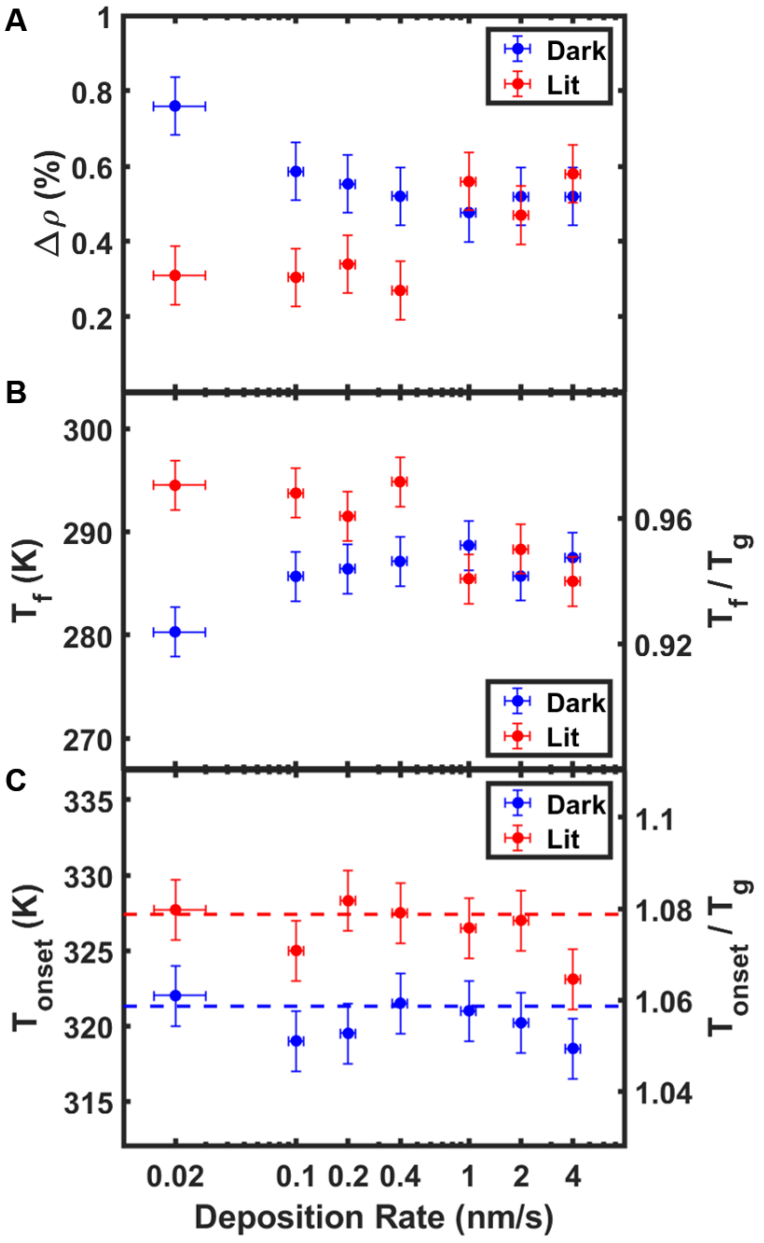

Figure 2.7: (A)/(B)/(C) $\Delta\rho/T_f/T_{onset}$ vs. deposition rate of a-Se films deposited in dark (blue) and lit (red). All films were deposited at 262±1 K ($0.86T_g$). Error bars are averaged over all data points.

depositions to probe this hypothesis.

In lit conditions, at low deposition rates $\Delta\rho$ is significantly lower than films deposited in dark. However, there is a surprisingly sharp improvement at a deposition rate between 0.4 - 1 nm/s above which, lit and dark depositions yield films with similar $\Delta\rho$ (Figure 2.7A). Interestingly, the kinetic stability remains enhanced in lit conditions even at these rates, indicating that the enhanced network structure persists at higher deposition rates. Given the network formation only requires a very short time compared to the timescale of our accessible deposition rate and the insensitivity of T_{onset} to the deposition rate, we do not expect the effective molecular weight of lit samples to be widely different at various deposition rates, except perhaps at the highest rate here where T_{onset} starts decreasing for both dark and lit samples, indicating lower kinetic stability. As such, it is not clear how the increased density is achieved despite the kinetic barriers introduced by network formation.

One possible explanation for this trend is that during the time of deposition, light induces mobility in the bulk of the film, resulting in partial transformation. Previous studies have demonstrated photo-induced bond extension and volume expansion of LQ a-Se under irradiation[91, 82]. It has also been previously demonstrated that in molecular SGs, light induced change in the molecular configuration can lead to transformation of the as-deposited SGs[169]. Depositions at rates slower than 0.4 nm/s take several hours to yield a 2-micron-thick film while depositions faster than 1 nm/s are completed within 30 min. During longer depositions, a-Se films could have partially transformed, resulting in increased thickness, which is measured as an effectively lower $\Delta\rho$. Figure 2.8A shows that indeed when a sample deposited in dark is exposed to white light, it partially transforms. However, this transformation is limited, being 0.3% volume increase within 3 hours, which indicates that the top $\sim$1100$\pm$200 nm of the film has been transformed. This is consistent with the estimated penetration depth of light into the film's surface (50 nm - 1000 nm, Figure 2.12B)[80]. However, as detailed below, this explanation is not consistent with other aspects of this phenomenon.

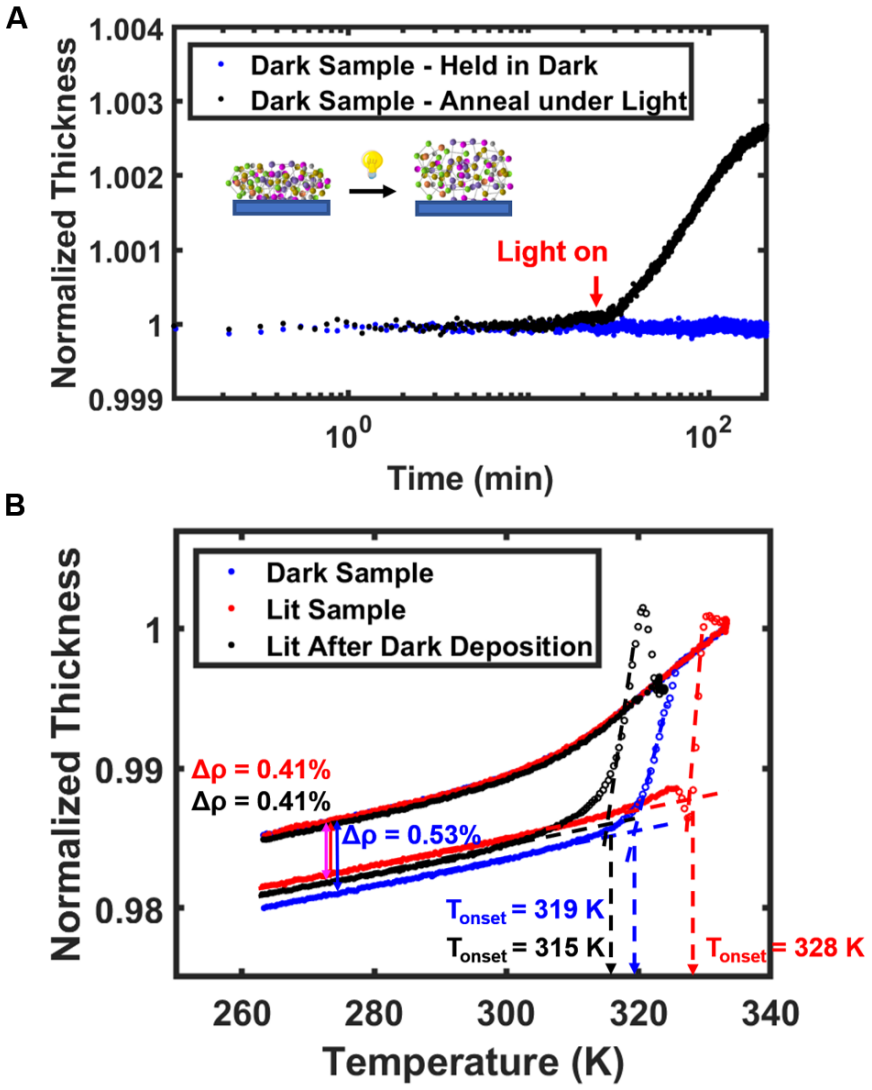

Figure 2.8: (A)Thickness of 2μm a-Se films held at 260 K in dark (dark blue) and white light (black) conditions after deposition in dark. The light intensity was ∼3 mW. Both films were deposited in dark at T_{dep}= 262±1 K (0.86T_g) and 0.2±0.02 nm/s rate. The red arrow indicates the beginning of illumination. The inset is a schematic image of the film expanding under light. (B) Comparison between samples deposited under dark and held in dark (blue), deposited under dark and exposed to light for 3 hours (black), and deposited under light (red) for a duration of 3 hours of deposition. All samples were deposited at T_{dep}= 262±1 K (0.86T_g) and 0.2±0.02 nm/s rate.

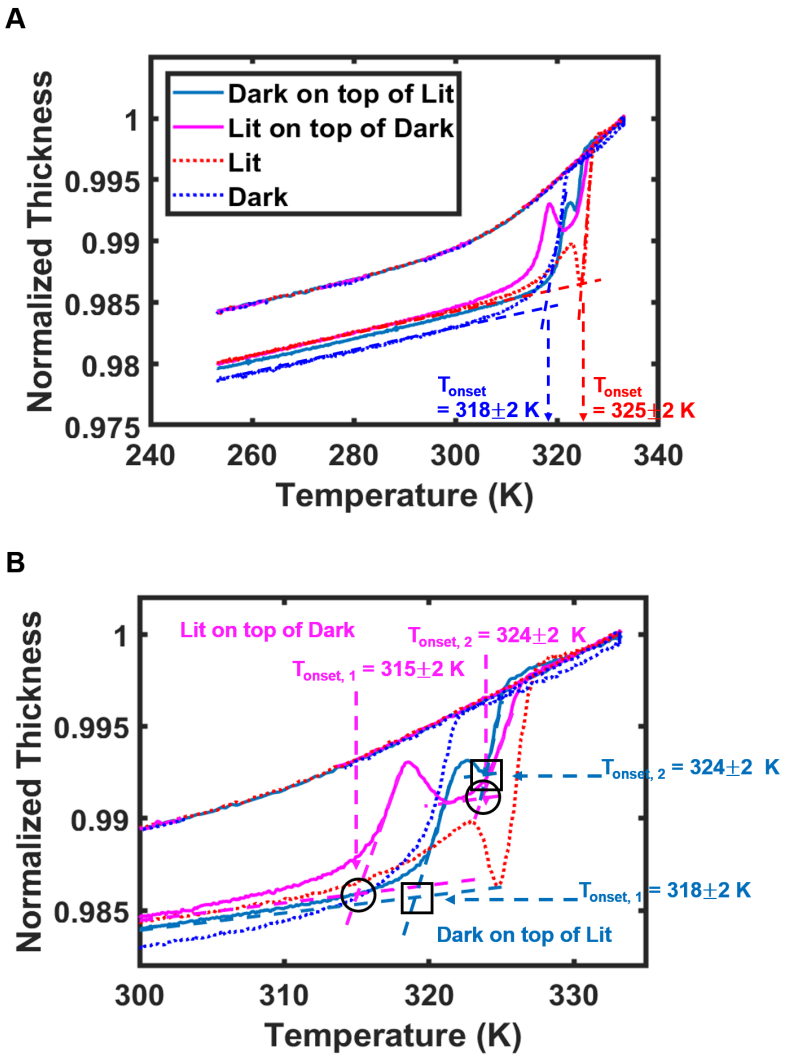

Figure 2.9: (A) Normalized thickness as a function of temperature for 2 μm a-Se films deposited in dark (blue), lit (red), in dark for 2μm then lit for 2μm (magenta) and lit for 2μm and then in dark for 2μm (dark blue). T_{dep} for all samples was 262±1 K (0.86T_g) and deposition rate was 0.2±0.02 nm/s. All samples were transformed with the same procedure as described in text for SGs, except that the heating and cooling rates were 3 K/min. (B) Same data plotted in the transformation region.

When the kinetic stability of a lit film is compared with a sample deposited in dark and held under white light for the same duration of 3 hours, the two samples have similar densities, but starkly different kinetic stability. The film illuminated after deposition is kinetically less stable than the lit sample and even the film deposited in dark (Figure 2.8B). Illumination after deposition has reduced the apparent kinetic stability of the film. However, illumination during deposition is generating a uniquely networked structure with higher kinetic stability. Despite of its partial volume recovery, the structure is locked in a network that can only be transformed upon heating. To further demonstrate that these two films are distinct, we deposited films that were illuminated either for the first half of the deposition or the second half of the deposition (Figure 2.9).

As can be seen from Figure 2.9A, T_{onset} are measured to be 318±2 K and 325±2 K for the dark and lit samples respectively. However, it is clear from Figure 2.9A&B, the other two samples that are deposited in in dark(lit) then lit(dark) consecutively each show two distinct onset values: $T_{onset,1}$ = 315±2 K and $T_{onset,2}$ = 324±2 K for the sample deposited dark and then lit, and $T_{onset,1}$ = 318±2 K and $T_{onset,2}$ = 324±2 K for the sample deposited lit and then dark. It can be seen that, $T_{onset,1}$ for the sample deposited dark and then lit is lower than $T_{onset,1}$ for the sample deposited lit and then dark, which suggests two things: first, being exposed to light can make the dark layer transform partially, giving a lower $T_{onset,1}$; second, since the sample deposited under light has the highest T_{onset} while light illumination on dark sample renders a lower T_{onset} layer, this extra kinetic stability cannot be simply explained by light exposure. It must be an effect of above-bandgap light during the deposition process.

2.4.4. Polyamorphism of Amorphous Selenium

Given the data shown in Figure 2.7C and 2.9, we can frame the process of lit deposition as follows; the thickness of the surface region which plays a role in the SME process is significantly larger in lit samples, 50-1100 nm based on Figure 2.8A and literature[80]. This region also has increased specific volume, resulting in a reduced $\Delta\rho$ of the SGs deposited

lit, as their structure is templated by the free surface. When this sample is heated in dark, the protocol adopted in this paper, it transforms into the SCL state that corresponds to the dark a-Se, with lower specific volume, resulting in lower apparent thermal stability. However, as shown in Supplementary Information, Figure 2.16, when the transformation is performed under above-bandgap light (without long-pass filters during ellipsometery) a new super-cooled liquid state is observed with larger specific volume than the ordinary, dark SCL. This state is a metastable state which will eventually become the ordinary SCL when all the excess bonds are broken upon further heating and removal of the above-bandgap light. It is important to note that this new SCL state and its corresponding SG states with their distinct excess specific volume and highly networked structures are not accessible in bulk a-Se, as they can only be achieved in the region affected by light, which is limited to the surface. This is evident when SGs deposited in dark are transformed in light and do not show this level of excess expansion (Supplementary Information, Figure 2.16B). An intriguing aspect of these observations is that the gradients of the mobility of the free surface region appear to depend on the deposition rate (Figure 2.7), with potentially a smaller thickness at higher deposition rates, indicating longer structural relaxation times for the volume expansion of these highly networked states, which is the only way to rationalize higher density at higher deposition rates.

These observations suggest that a-Se deposited in dark or lit conditions produces distinct polyamorphous solid states with a barrier between them, as schematically shown in Figure 2.10. A corresponding polyamorphic super-cooled liquid state likely exists for the lit structure, but its properties need to be characterized more carefully. This state is likely stable in thin (50-1000nm) a-Se films and future studies focused on thin films can likely characterize its properties. Polyamorphism has been previously observed in phosphorous[98], water[147], as well as other organic[115, 179] and inorganic compounds[192, 198]. It has recently been shown that polyamorphism can be observed in PVD glasses produced under different deposition conditions, with stable liquid states above T_g [179]. Here, polyamorphism is achieved through the modification of the near-surface region of a-Se, which results in simultaneous

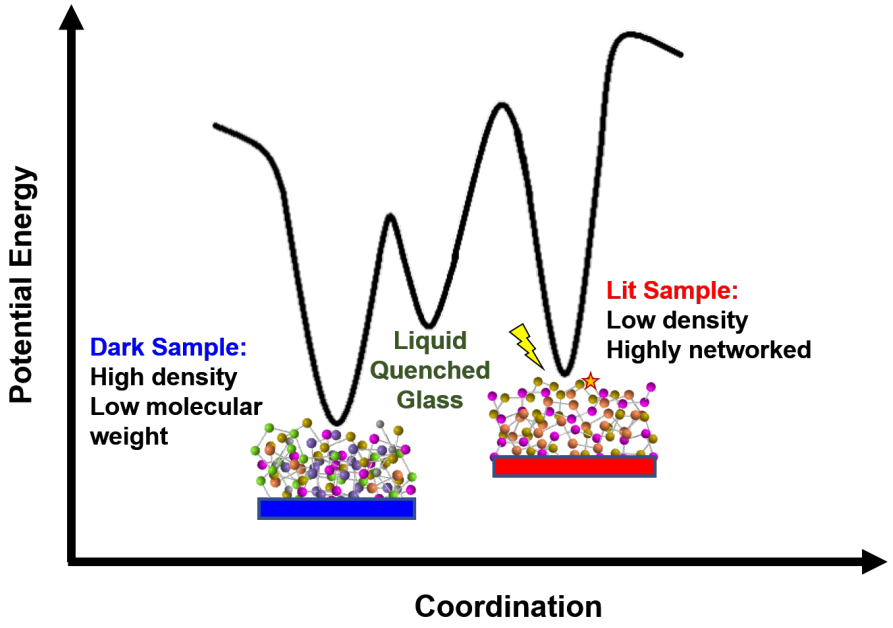

Figure 2.10: A schematic drawing for part of a-Se potential energy landscape. Dark sample and Lit sample locate at different local minima on potential energy landscape. Dark sample has lower potential energy and lower energy barrier to transform to LQ glass.

changes in the network structure and the density of the PVD glass. The distinct structure obtained under light is inaccessible through liquid-quenching and can only be transformed into the low-networked state upon heating above T_g, indicating significant barrier between these two states. Illumination after deposition does not enable access to this part of the energy landscape and results in further transformation (Figure 2.8B). It is worth nothing that a-Se shares some common features of other polyamorphic systems, such as distinct structural change and directional bonding[97, 198], which typically signify polyamorphism.

2.5. Summary and Outlook

In this study, we have prepared a-Se SGs through PVD both in dark and under white light illumination (lit) conditions. We demonstrate that when above-bandgap light is applied during vapor deposition, the kinetic stability of a-Se SGs is significantly improved despite their larger relative specific volume (lower thermal stability) compared to the corresponding SGs deposited in dark. However, when films deposited in dark are exposed to light after

deposition, they show both lower density and reduced kinetic stability. We attribute these results to the changes in structure and dynamics of a-Se surface when illuminated by above-bandgap light. With light, more networked structures are produced on the constantly revitalizing surface. The resulting high-molecular weight structure on one hand frustrates the packing and on the other hand, requires higher temperatures to break. We show there is strong evidence the packing produced under these conditions is an amorphous state that is not accessible through aging or vapor deposition in dark, and as such, is a distinct polyamorphic solid state. The corresponding state of these structures can likely be identified and studied in a-Se thin films.

A key aspect that enables access to these unique states is the increased thickness of the surface region (estimated to be 50 nm-1000 nm) while illuminated, as well as the distinct surface structure due to production of free electrons. To our knowledge, this is the first application of light to manipulate the surface-mediated equilibration process, to produce distinct stable glass structures. In addition to T_{dep} and deposition rate, for light-sensitive materials, surface illumination can affect the dynamics, the length scale and gradients of the mobility, as well as the structure of the liquid at the free surface, producing distinct packings. In a-Se, based on the light penetration depth, the first 50 nm of a-Se films during lit deposition likely has much faster dynamics than the other 1000 nm region of the surface. Future work should focus on controlling the light intensity, wavelength (which can control the absorption depth and mobility gradients), as well as film thickness, to understand exact the role of light. Designing corresponding organic molecules with light sensitive functional groups will be beneficial as well in terms of expanding these studies to other systems and exploring the detailed structure of as-deposited SGs. We expect the implementation of other experimental techniques such as Raman and IR spectrum to be helpful to resolve these fine structures.

2.6. Supplementary Information

2.6.1. Ellipsometry Determination on Amorphous Selenium Bandgap

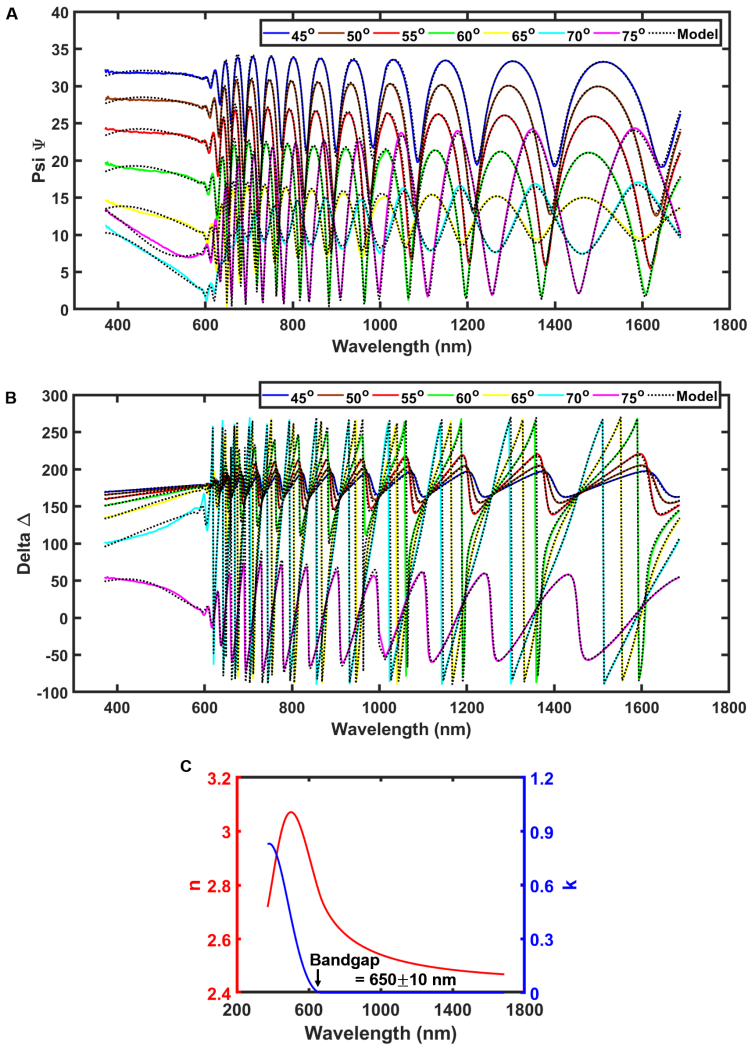

Figure 2.11: (A) Ψ (solid lines) measured using spectroscopy ellipsometry along with the model used to fit the results (dotted lines) for a 2 μm-thick a-Se LQ glass film. Different colors show various angles of measurements from 45° to 75° at 5° intervals. (B) Δ (solid lines) measured using spectroscopy ellipsometry along with the model used to fit the results (dotted lines) for a 2 μm-thick a-Se LQ glass film. Different colors show various angles of measurements from 45° to 75° at 5° intervals. The model is fitted simultaneously to data at all angles. (C) The real (n) and imaginary (k) parts of refractive index of the same sample as a function of wavelength. A bandgap of 650±10 nm is labeled on the graph.

Spectroscopy ellipsometry was performed using a J. A. Woollam M-2000V instrument. Full wavelength (from 370 nm to 1700 nm) ellipsometer angles Ψ (amplitude change) and Δ (phase change) were collected in multi-reflection-angle from 45° to 75° at 5° intervals on an approximately 2 μm-thick liquid-quenched (LQ) a-Se film. CompleteEase (J.A. Woollam Company) was used to fit the ellipsometry angles Ψ and Δ. A three-layer model which consists of a silicon substrate, a 1-nm-thick silicon oxide layer, and a selenium layer was applied to fit the data. The selenium layer was fitted using an isotropic Kramers–Kronig consistent absorptive model with one Tauc-Lorentz oscillator located at 2.63 eV. The Kramers–Kronig equation specifically defines the relationship between the real part (n) and imaginary part (k) of the refractive index ($\widetilde{n} = n + ik$), and ensures the conservation of energy[85]. Figure 2.11 shows the fitting and resulted refractive index values. The bandgap of a-Se is subsequently determined using the imaginary part of refractive index, k, which is proportional to the extinction coefficient, to be 650±10 nm.

2.6.2. LEDWE-15 Emission Spectrum and a Estimation of the White Light Penetration Depth

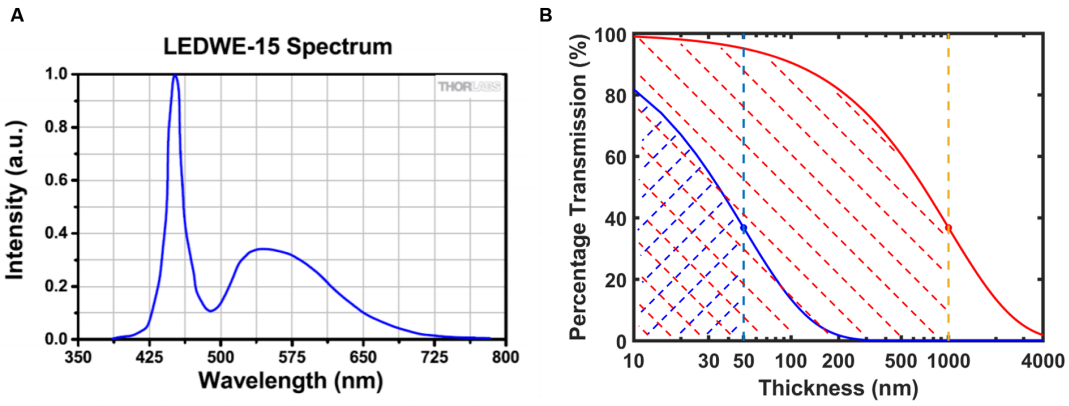

Figure 2.12: (A) Emission spectrum of Thorlabs LEDWE-15 LED bulb that is used inside deposition chamber[221]. (B) Percentage transmission of white light through a-Se film. In this estimation, absorption coefficient is taken to be 2×10^5 cm^{-1} around 440 nm (blue line) and 10^4 cm^{-1} around 620 nm (red line)[80]. Percentage transmission (PT) is calculated with: PT $= \exp(\alpha \cdot l)$, where l is the depth of penetration. The inflection points of the two lines are at 50 nm and 1000 nm respectively. Thus the penetration depth of white light is estimated to be between 50 nm to 1000 nm.

The emission spectrum of the white LED used inside deposition chamber is depicted in Figure 2.12A. Then the light penetration depth was estimated based on a-Se absorption coefficient at two representative wavelengths. Based on the inflection points of the two curves in Figure 2.12B, white light can possibly penetrates 50 nm to 1000 nm into a-Se films. We note that this is quite a large range and the actual depth should depend on the specific light source that is used and the light intensity.

2.6.3. Atomic Force Microscopy Characterization

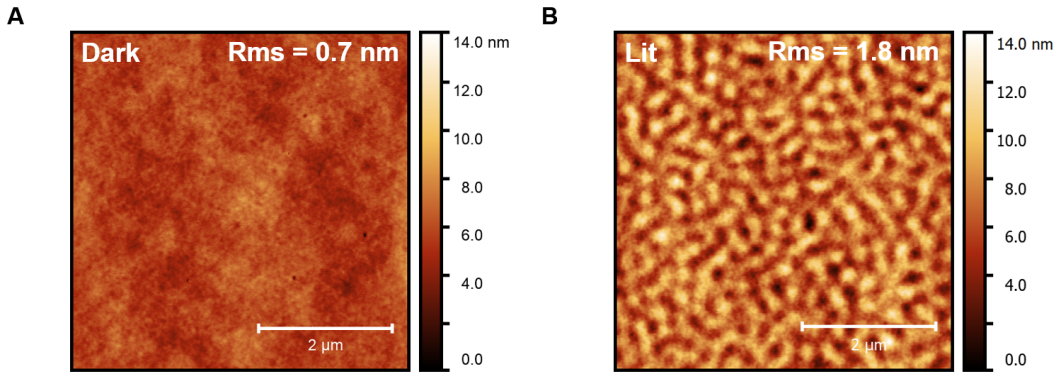

Figure 2.13: (A) Atomic Force Microscope (AFM) topography image of the surface of a 2 μm-thick a-Se film deposited at $T_{dep} = 262\pm1$ K ($0.86T_g$), with a deposition rate of 0.2±0.02 nm/s in the dark. Grain wise mean square roughness (RMS) is measured to be 0.7±0.2 nm. (B) AFM topology image of a 2 μm-thick a-Se film deposited at $T_{dep} = 262\pm1$ K ($0.86T_g$), with a deposition rate of 0.2±0.02 nm/s under white light illumination. It has larger roughness than films deposited in dark, with a RMS to be 1.8±0.2 nm.

Atomic Force Microscope (AFM) measurement is conducted using Agilent Technologies AFM (Model N9610A) with a XY-Z closed loop scanner (Model N9524B) under room temperature in a vibration-isolating cabinet. Sample mounting and topography scanning are done in dark except for a 632 nm laser which is necessary for AFM measurement. The time it takes to finish each measurement is less than 1 hour. There is no significant change of the sample observed during measurement.

2.6.4. Grazing Incidence Wide Angle X-ray Scattering Characterization

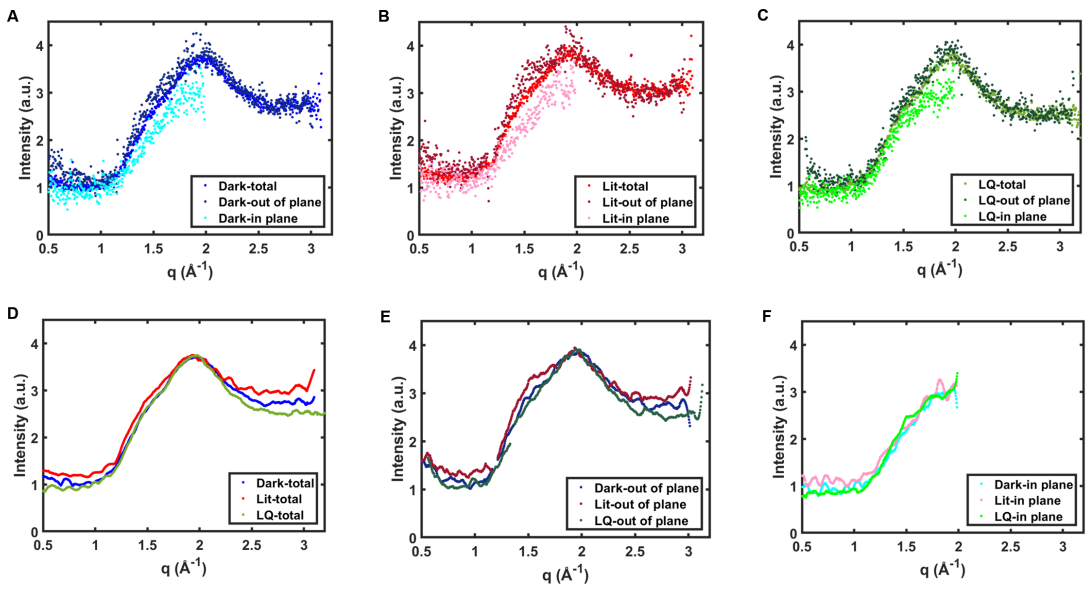

Figure 2.14: (A) Grazing Incidence Wide Angle X-ray Scattering (GIWAXS) intensity (I(q), arbitrary unit) as a function of scattering vector (q) for a 2 μm-thick a-Se film deposited at T_{dep} = 262±1 K ($0.86T_g$), with a deposition rate of 0.2±0.02 nm/s in the dark. (A) GIWAXS intensity (I(q), arbitrary unit) as a function of scattering vector (q) for a 2 μm-thick a-Se film deposited at T_{dep} = 262±1 K ($0.86T_g$), with a deposition rate of 0.2±0.02 nm/s under white light illumination. (C) GIWAXS intensity (I(q), arbitrary unit) as a function of scattering vector (q) for a transformed liquid quenched glass (LQ). (D), (E), (F) are the same data as (A), (B), (C), but smoothed using a 3^{rd} order unweighted least-squares regression with a window size of 31. Total (D), out of plane (E), and in plane (F) scattering intensities are compared separately. Here, total means the intensity is integrated from all azimuthal angles through 0° - 180°; out of plane is the integration of azimuthal angles from 60° - 120°; while in plane intensity is integrated from 0° - 30° and 150° - 180°, where 0° is set parallel to the substrate.

Grazing Incidence Wide Angle X-ray Scattering (GIWAXS) is conducted with Xeuss 2.0 X-ray Scattering Machine from Xenocs with a copper source and a incident angle of 0.22° under room temperature. Unnecessary light is avoided. Acquisition time is 90 min and there is no significant change of the sample observed during measurement.

2.6.5. Fragility and Determination of Estimated Aging Time

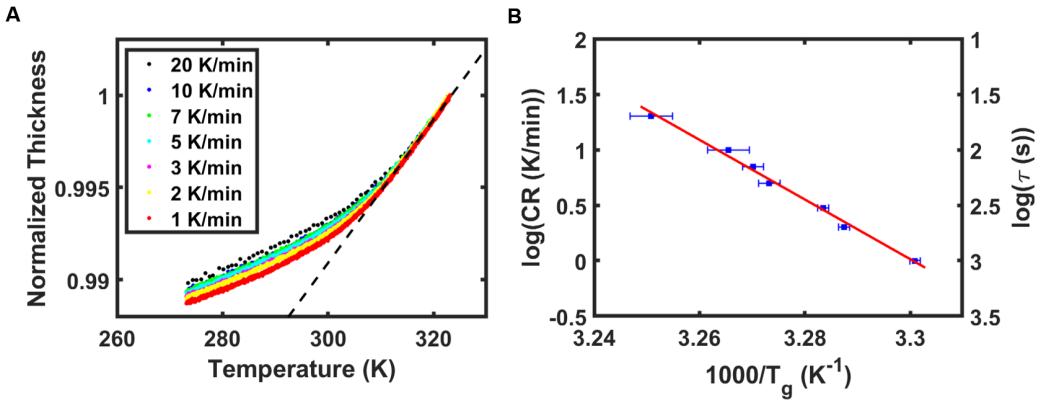

Figure 2.15: (A) Cooling rate dependent T_g measurements (CR-T_g) for a 2 μm-thick a-Se film. Normalized thickness is plotted vs. temperature at different cooling rate ranging from 20 K/min to 1 K/min. The dashed line indicates the SCL line. (B) Log of cooling rate (left axis) and estimated relaxation time (τ, right axis) vs. $1000/T_g$ based on the data shown in (A). τ is estimated by assuming that 100 s relaxation time corresponds to 10 K/min cooling rate at T_g. The solid line is the best linear fit to the data.

The Dynamical fragility (m), a measure used to show how strongly the dynamics of a glass deviates from Arrhenius behavior around T_g, is defined with the equation[3, 4]:

$$m = \left.\frac{\partial(\log \tau)}{\partial(T_g/T)}\right|_{T=T_g}$$

Fragility of selenium has been measured through enthalpy relaxation[210, 134]and viscosity measurements[193, 74] to be ranging from 46 to 64. Using the fragility reported above, the estimated years of aging for the most stable glass in this study, deposited at T_{dep} = 262±1 K ($0.86T_g$) with a deposition rate of 0.2±0.02 nm/s in dark, is around 2 to 28 days.

We have also performed cooling rate dependent T_g measurement ($\mathrm{CRT_g}$, Figure 2.15) in the cooling rate range of 1 K/min to 20 K/min, where the thickness change of a 2 μm-thick sample was monitored on the Linkam module in our custom-made environment-control stage on ellipsometer during cooling ramps of different rates. The rates of heating/cooling are precisely controlled by a Linkam T95-PE controller with a LNP95 liquid nitrogen pump.

Spectroscopic ellipsometer data was collected during heating and cooling. An isotropic Cauchy model described before was used to fit the data within the wavelength range of 1000 nm to 1600 nm. Heating rates here are fixed to be 10 K/min while we vary the cooling rates. This experiment was completed with the 780 nm long-pass filters mounted on the windows of the custom-made environment-control stage introduced before under vacuum. Relaxation time, τ, is empirically estimated by assuming a 100 s relaxation time corresponds to 10 K/min cooling rate at T_g[127]. The relationship between the can be written as:

$$\frac{\tau}{second} \times \frac{CR}{K/min} \approx 1000$$

roughly.

Based on this data, the fragility of a 2000 nm thick film of a-Se supported on Si substrate is measured to be 88. Thus, the estimated aging time of our most stable glass state is $\sim$4 years. Direct aging experiments on LQ 2000 nm film of a-Se, aged at 260 K for 33 days shows a modest density gain of 0.1%, which is consistent with the fragility value reported here.

2.6.6. Discussion on SGs Transformed Without Filters

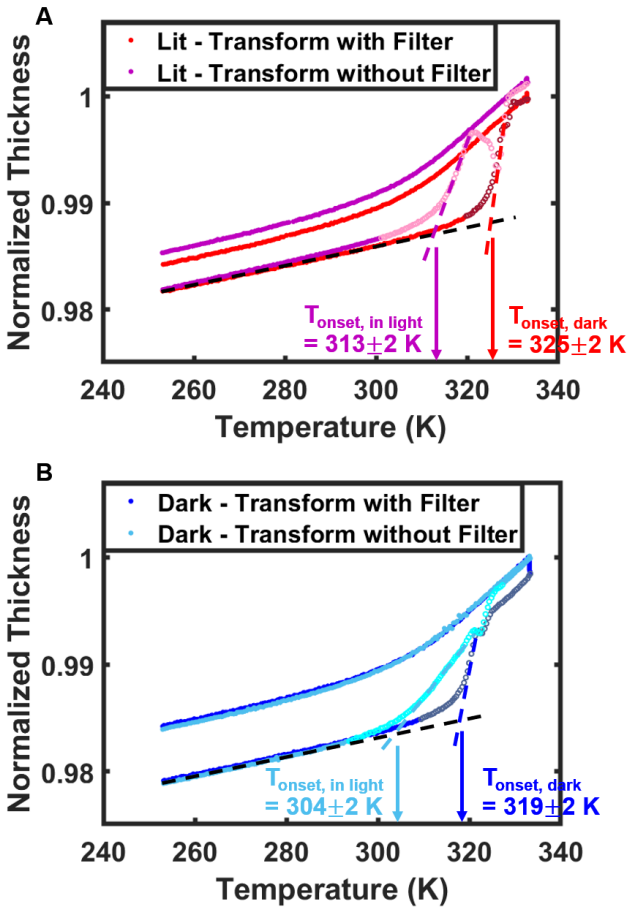

Figure 2.16: (A) Normalized thickness as a function of temperature for 2 μm a-Se films deposited under light at 262±1 K ($0.86T_g$) with a deposition rate of 0.2±0.02 nm/s. One sample is transformed with the 780 nm long-pass filters mounted outside the custom-made environment-control stage viewports (red, transformed dark); the other one is transformed without (purple, transformed in light). The sample transformed with filters is normalized with the thickness of its own SCL at 333 K. The other samples is normalized assuming that its SG had the same initial density given that the two samples were produced in the same batch of deposition and thus had identical initial conditions. (B) Comparison of 2 μm a-Se films deposited in dark at 262±1 K ($0.86T_g$) with a deposition rate of 0.2±0.02 nm/s. One is transformed with the filters (dark blue, transformed dark) while the other one sample is transformed without (light blue, transformed in light). Both transformation curves were normalized with their corresponding thickness of SCL at 333 K. Heating and cooling rates for all four samples were 10 K/min. Unfilled symbols in all graphs represent the regime where the ellipsometry fits are unreliable due to the transformation growth fronts.

As can be seen in Figure 2.16B, for dark samples, regardless of whether the transformation is done with or without ellipsometer filters that block above-bandgap light (transformed in light or dark), they give very similar density change. One noticeable difference is that when transformed without filters, the sample shows lower T_{onset} because light facilitates faster rearrangement at lower temperatures ($T_{onset,inlight}$ = 304±2 K compared to $T_{onset,dark}$= 319±2 K). However, as for the lit samples shown in Figure 2.16A, when we normalize the two transformation curves assuming that the SGs have the same density (which it to say they are both normalized to the dark SCL at 333 K), we notice in additional to having a lower T_{onset} ($T_{onset,inlight}$= 313±2 K compared to $T_{onset,dark}$= 325±2 K) when transformed in light, lit sample also transforms into a SCL state with higher normalized thickness (larger specific volume) than the equilibrium SCL in dark. As such, the sample shows an apparently higher density change. This is a meta stable state as we do not observe this degree of volume expansion when a LQ glass is exposed to light, or when the SG deposited in dark is transformed in light as seen in Figure 2.16B. The result from this comparison between SGs transformed with and without filters indicate that it is possible that lit samples transform to a different SCL state than dark samples when exposed to above-bandgap light and thus have a meta-stable SCL state that is not accessible otherwise. This is an evidence of the existence of two distinct polyamorphic liquid states, one of which is meta-stable and is only accessible when a-Se glasses is both deposited and transformed under light.

2.7. Acknowledgments

This work was funded by NSF-MRSEC DMR-1720530. I acknowledge the use of the Dual Source and Environmental X-ray Scattering facility operated by the Laboratory for Research on the Structure of Matter at the University of Pennsylvania (NSF-MRSEC DMR-1720530) and Prof. Paul Heiney. The equipment purchase was made possible by an NSF MRI grant (17-25969), an ARO DURIP grant (W911NF-17-1-0282), and the University of Pennsylvania. Special thank is given to Prof. Zahra Fakhraai, Prof. Richard B. Stephens and Dr. Tianyi Liu for their valuable guidance and ideas on performing research.

CHAPTER 3: Quantitative Determination of Light Facilitated Dewetting on Amorphous Selenium Thin Films

3.1. Abstract

Thin film of glasses are shown to have properties that deviate from their bulk counterparts. When supported films are thinner than a certain threshold, substrate interaction from the solid-glass interface and enhanced surface dynamics from the air-glass interface will start to play essential roles in the films' properties. The study of thin film dynamics has drawn significant interest because of their important applications in coatings and photo/electronic devices. The main subject studied here, amorphous selenium (a-Se), is a metallic glass that can be used as a high-field photon sensor. Despite its high efficiency in photon detecting, a-Se is shown to have limited stability and degrading performance upon bandgap light irradiation. It is essential to understand the effect of light on a-Se thin films, particularly in a quantified way. In this work, light-induced dynamics on a-Se thin films are measured via isothermal dewetting experiments under microscope and compared with the results collected in dark. Since the dewetting of a-Se on silicon substrate satisfies the criteria for non-slip dewetting conditions, the dewetting velocity can be directly related to film viscosity. We demonstrate that a-Se thin film with thickness up to 250 nm viscosity can be significantly reduced when white light illumination is present with a smaller activation energy for relaxation. The length scale of light-facilitated dynamics enhancement is strongly correlated with the light intensity.

3.2. Introduction

The properties of glassy thin films have been under extensive investigation to understand the role of substrate effects and enhance surface dynamics. Various experimental[101, 70, 54, 239, 166, 222, 194, 254, 29, 125] and simulation results[197, 226, 138, 199] have demonstrated strongly deviating behaviors of thin films compared to their bulk counterparts. For polymeric materials, it was shown that the glass transition temperatures (T_g)[101, 70, 54],

film viscosity[239], physical aging rate[166], and elastic modulus[222] could change significantly as films become thinner than a certain threshold, which usually happens around 30 to 60 nm depending on the system as well as the characterization technique used. A few studies that are focused on molecular glasses gave similar results[194, 254, 29]. In molecular glasses, the bulk to thin film transition also appears to occur around 30 nm, which is very close to the transition points seen in polymeric systems. However, whether this length scale persists in inorganic glasses remains unclear, since their building blocks and grain sizes are smaller than organic glasses[125]. It is meaningful to study the fast surface length scale in inorganic glasses from both fundamental science and industrial application's points of view.

The inorganic glass chosen here is amorphous selenium (a-Se), which is a well-known chalcogenide glass. A-Se is mainly made up of long polymeric chains with chain length ∼200 atoms/chain[79]. The usage of a-Se based photon detectors can be dated back to the 1950s[96], when they were known to produce avalanche multiplication which increased photon conversion gain dramatically[84]. Nevertheless, general studies on a-Se were mostly focused on thick films[114, 177, 95, 96] with thicknesses ranging from 10^1 to 10^3 microns. Only a few studies have been performed on the photo-response of a-Se thin films (∼1 micron)[121, 122, 123]. Recent publications showed that a-Se thin films could exhibit better kinetic stability compared to thick a-Se films, with smaller external electrical field required to give rise to rapid response to photons[123].

Even though a-Se thin films have remarkable performance as a photon detector, the structure and properties of a-Se can be easily altered by above-bandgap (bandgap ∼2.15 eV[121]) light exposure[165, 69, 82, 1]. How light affects a-Se dynamics is not well understood so far. Evidences were shown that Valence Alternation Pairs (VAP, $2C_1^0 \longrightarrow C_3^+ + C_1^-$, where C stands for a chalcogenide atom, its subscript corresponds to the coordination number and its superscript is the charge state) can be generated when a-Se is exposed to above-bandgap light[110, 112], which can potentially facilitate the unentanglement of Se chains. But to our knowledge, the magnitude of enhancement in relaxation has not been measured quan-

titatively so far. Due to a-Se's strong absorption within the visible light region[80], a-Se thin films become a better subject when studying the effect of light on a-Se's relaxation dynamics and viscosity, compared to several tens of microns thick pieces, because smaller light intensity is required for a-Se thin films to exhibit properties different from their dark measurements and the penetration depth of light is limited to about a micron in general cases.

In spite of the importance and advantages of studying the properties of a-Se thin films, thin film viscosity measurements, particularly for films less than 500 nm in thickness, are tricky, given that the general parallel plate rheometry measurements are not applicable. In polymeric systems, thin film viscosity has been studied qualitatively by measuring the relaxation of a trace amount of fluorescent probes mixed in the matrix[160, 159] or indirectly by evaluating the glass transition temperature(T_g) obtained through various methods[67, 104, 101, 70, 54, 58, 158, 231]. A more quantitative way was developed by O'Connell and McKenna *et al.* in 2005, which could provide the dynamical modulus values by monitoring the biaxial membrane inflation (bubble inflation) under uniform pressures[153]. Moreover, the stress-strain responses and viscoelastic properties of thin films have also been measured by uniaxial tensile tester[106, 81, 14] and thermal wrinkling methods[32, 209, 208].

Dewetting (hole growth) experiments have also been used to determine the thin film viscosity[184, 44, 247, 227, 141, 140]. However, a clear relationship between dewetting velocity (front moving rate) and film viscosity can only be defined under certain circumstances[184, 44, 247]. Non-slip dewetting is one of the special cases, where the gradient of dewetting velocity in the longitudinal direction decays to zero at the substrate place. When non-slip dewetting condition is met, the driving force of dewetting, which comes from imbalanced interfacial tensions, and the viscous dissipation within the dewetting wedge will reach a balance. The velocity of moving contact line (v_{dewet}) stays a constant at prolonged time, which can be used as a justification criteria. Under non-slip dewetting condition, for low molecular weight polymeric systems, it can be proved that the film viscosity (η) is inversely proportional to

v_{dewet}[176].

In this work, the viscosity of a-Se thin films are measured and compared using isothermal dewetting experiments. The dewetting of a-Se on Si substrate obey non-slip dewetting condition. Therefore, the film viscosity can be quantitatively determined from v_{dewet} and compared under different film thickness, dewetting temperature, and light conditions. When fitted to an Arrhenius function, the activation energy of dewetting are derived. Our results show that a 50 nm a-Se thin film has roughly the same relaxation activation energy as bulk a-Se measured by parallel plate rheometry measurements[16]. Nevertheless, when the experiments are conducted under light, the activation energy for a-Se thin film dewetting can be reduced by more than a half, suggesting that the relaxation process of a-Se thin film can be significantly altered by visible light.

3.3. Experimental Details

3.3.1. Material and Film Preparation

Selenium lumps (purity 99.999%) were purchased from Goodfellow Corp. and used directly. The same deposition chamber was used as described in section 2.3.1. A-Se thin films with thicknesses between 50 to 250 nm were deposited on Boron doped Silicon substrates (Virginia Semiconductor Inc., with a $\sim$ 1 nm native oxide layer on top). To avoid dewetting, deposition temperatures were kept at 259$\pm$1 K, the lowest accessible deposition temperature (T_{dep}) in this setup. A-Se films of thicknesses between 50 to 250 nm did not appear to be dewetted upon deposition, as measured by Atomic Force Microscopy (AFM, Agilent Technologies Model 5420, examples of as deposited and annealed 50 nm films, the thinnest films studied in this manuscript, are shown in Figure 3.9). Deposition rates (r) were controlled $r \sim 0.2$ nm/s. Given the ramp-up stage at the beginning of deposition and the slow-down stage at the end when the heating source was turned off, $r \sim 0.2$ nm/s only reflects an averaged deposition rate. The immediate r during deposition is ranging from 0 to 0.3 nm/s. We note that the variations in r do not affect the experiments performed here, because all films were annealed at 323 K for 10 min (T_g+17 K, a-Se T_g was determined to

be T_g = 306±1 K through DSC), to remove their thermal history and erase the effect of inconstant deposition rates, before they were used for the isothermal microscope dewetting experiments.

3.3.2. Isothermal Dewetting Experiment Performed Under Microscope

Isothermal dewetting experiments of a-Se thin films were performed using Olympus BX51 Microscope. Micron-size holes, visible in the microscope, were nucleated by annealing a-Se samples at higher temperatures after they were transformed into ordinary liquid quenched glasses. The designated annealing temperature were 331 K for 50 nm films, 336 - 338 K for films with thickness ≥ 100 nm. The general annealing time was ∼10 min, but it was adjusted based on the film thickness and the size of nucleated holes. After the dewetted holes had been generated and had grown to micron-size, the films were quenched to 298 K at 10 K/min cooling rate, ready for the following isothermal dewetting experiments at various temperatures. All annealing were performed on Linkam THMS600 thermal stage in the absence of ambient light. Because white light exposure can affect a-Se properties[248], annealing in dark ensured similar initial conditions for experiments. A 660 nm deep red LED (ABI GR-PAR38-12W-DR) light was used in the lab as the lighting source during sample handling from deposition to mounting on the microscope.

Sample dewetting temperatures were maintained using a Linkam PE100 Thermoelectric stage placed on top of microscope sample plate, with a T95 Controller. Because the position of the temperature sensor was slightly away from the sample location and the contact between Linkam PE100 stage and the microscope sample plate was close enough to facilitate heat dissipation, there was a discrepancy between the temperature setpoint on the Linkam controller, and the actual temperature of the sample. A calibration of the sample temperature was conducted with an external thermister and the results can be found in Supplementary Information section (Figure 3.8).

Images of a single area, containing several initially dewetted holes were taken at 1 - 1.5 h time intervals during dewetting experiments in reflection mode using Olympus DP72 camera,

which was controlled by cellSens software (Olympus). The magnification of the microscope was fixed at 100x (objective lens) and the resolution was set at 1360×1024 pixels. The size of each pixel under these hardware conditions was measured to be $(64.5\ nm)^2$, which was used to convert the number of pixels to actual dewetted area, using a TGX11 calibration gratings (MikroMasch). The stacks of images taken during experiments were subsequently analyzed by Fiji the software (Version 1.52p). For the convenience of analysis, individual round-shaped dewetting hole were chosen when extrapolating the dewetted area and the radius of each dewetted hole (R) was approximate to:

$$R(nm) = \sqrt{\frac{N}{\pi}} \times 64.5, \tag{3.5}$$

where N is the number of pixels measured in a hole. An example of the image analysis process is shown in Figure 3.1.

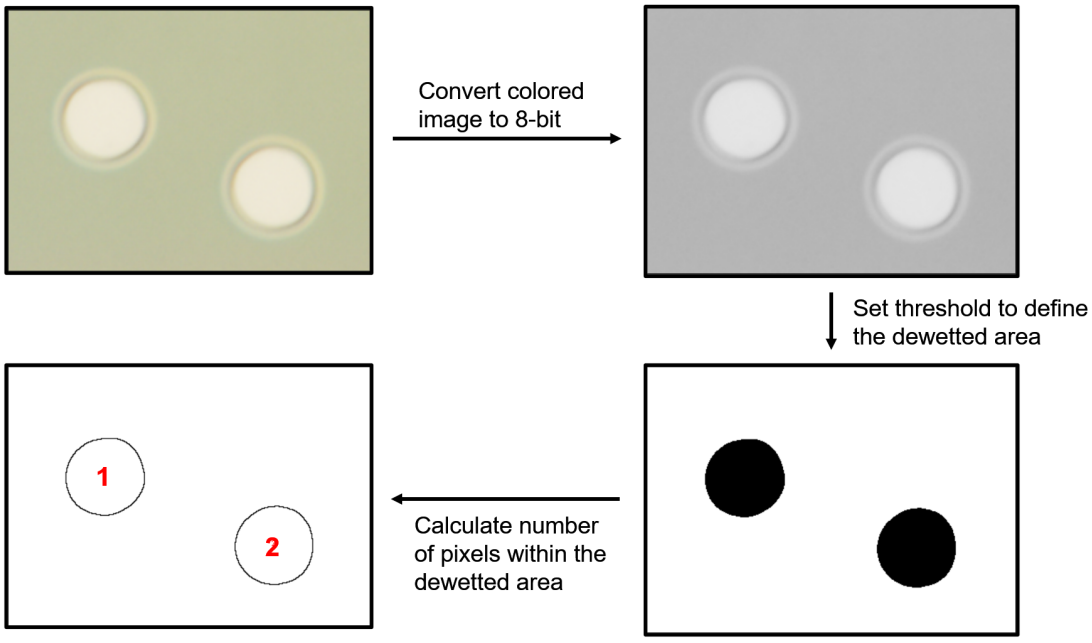

Figure 3.1: An example of the microscope image analysis of the hole size for thin film dewetting experiments.

The light conditions during the dewetting experiments were controlled by adjusting the

intensity or filtering the white light illumination of the microscope lamphouse (U-LH100L-3-7, 12V/100W Halogen Lamphouse). When full intensity was used, the light intensity at the sample position was measured to be 1.5±0.2 mW/cm^2 with COHERENT FIELDMATE optical power meter and a PM10 PowerMax probe. The microscope light was kept on continuously during light-exposure-experiments. The dark-experiments (no light exposure) were carried out with the light mostly kept off, except for when images were taken, where it was passed through a FGL665 long-pass filter (Thorlabs), before reaching the sample. The filter blocked light with wavelength below 665 nm. Since the bandgap of a-Se has been determined to be ∼650 nm (Chapter 2 Figure 2.11C), this filter can block nearly all above-bandgap light that could be absorbed by a-Se. After each image was taken, microscope light was turned off immediately, as such the effect of lighting when taking an image during dark-experiments should be negligible in these conditions.

3.4. Result and Discussion

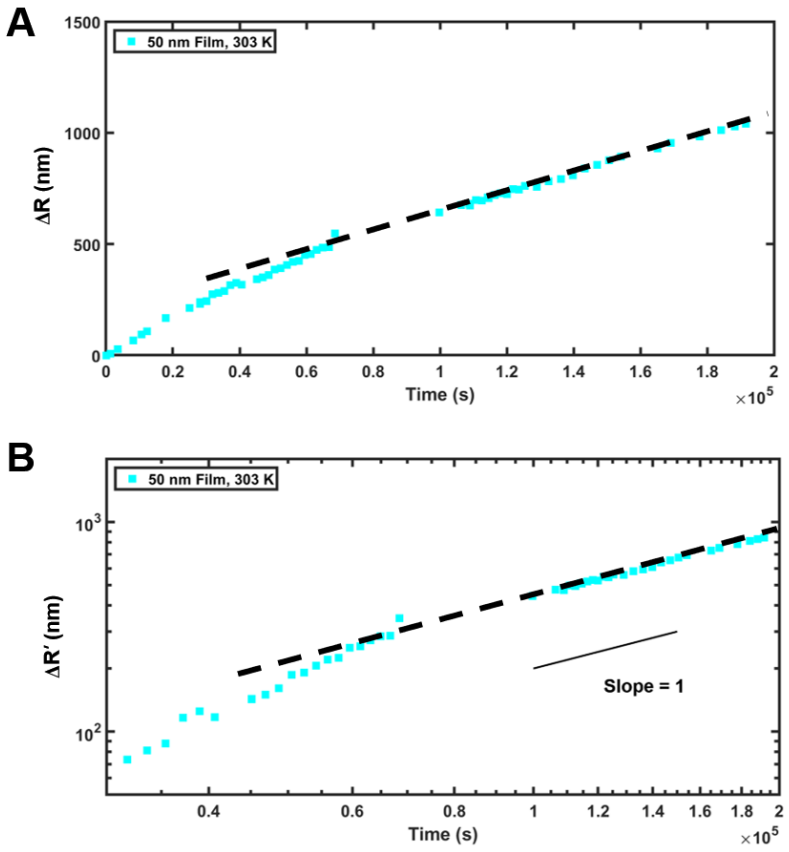

Figure 3.2: (A) Growth of a single dewetted hole's radius, R, *vs.* time. Dewetting is performed on a 50 nm a-Se film at 303 K under light, showing a constant front moving rate. (B) log-log plot of the same set of data set shown in (A). The solid and dashed lines both show slopes of 1, which confirms the non-slip dewetting condition.

As can be seen from Figure 3.2A, the radius of a dewetted hole increases at a constant rate (v_{dewet}) after an initial time ~60000s, with a slope of 1 in Figure 3.2A, indicating linear dewetting. All a-Se thin films dewetting measurements reported in this manuscript, with or without exposure to light, show linear dewetting, signified by non-slip dewetting.

3.4.1. Dewetting of a-Se 50 nm Films in Dark

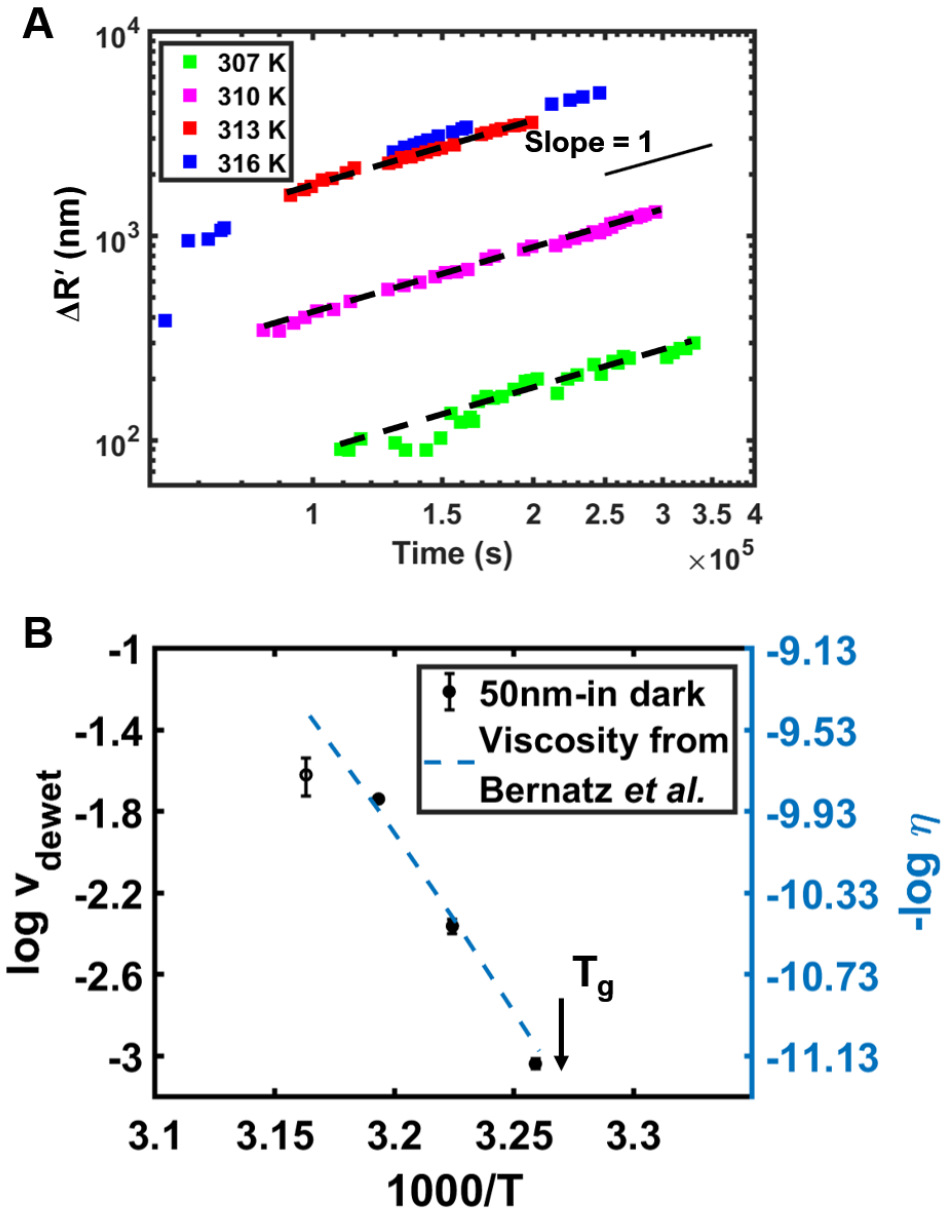

Figure 3.3: (A) The radius, R, of single holes *vs.* time for 50 nm a-Se films dewetted at different dewetting temperatures, T. Solid black line shows slope of 1. Dashed lines are fits to the data. (B) v_{dewet} *vs.* $1000/T_{dewet}$ obtained from data in (A) (black squares). The empty marker was collected at the highest dewetting temperature (316 K), where non-slip dewetting conditions no longer apply within our experimental time frame. A-Se bulk viscosity obtained from parallel plate rheometry measurements[16] is plotted with a dashed line on the right y axis in the figure. Error bars are defined by multiple experiments of various dewetting holes. A-Se T_g is indicated on the graph by a black arrow.

Isothermal dewetting experiments were first performed on 50 nm a-Se films in dark. As shown in Figure 3.3A, except for the profile collected at 316 K, which didn't appear to have a constant v_{dewet} in the experimental window, dewetting of 50 nm a-Se films at temperatures above T_g obeyed non-slip dewetting condition, and the film viscosity (η) can be derived from:

$$\eta \propto \gamma_L / v_{dewet} \cdot \theta_{equ}^3, \tag{3.6}$$

where γ_L stands for the liquid-air interfacial tension and θ_{equ} is the equilibrium contact angle between a-Se and the Si substrate. When $\log v_{dewet}$ is plotted against $1000/T$ and compared with previously reported $-\log \eta$[16] in Figure 3.3B, within the temperature range of our experiments, the activation energy (E_a) derived from $\frac{\mathrm{d}\log v_{dewet}}{\mathrm{d}(1000/T)}$ is similar as $\frac{\mathrm{d}\log \eta}{\mathrm{d}(1000/T)}$, suggesting a 50 nm a-Se film behaves like bulk a-Se. The relationship between v_{dewet} and η is calculated to be: $\log(\frac{\eta}{\mathrm{Pa{\cdot}s}} \cdot \frac{v_{dewet}}{\mathrm{nm/s}}) = 8.1 \pm 0.2$. We were not able to performed dewetting experiments on thinner a-Se films because of the difficulties in nucleating isolated dewetted holes on a-Se films thinner than 50 nm.

The viscoelatic properties of freestanding a-Se thin films down to a thickness of 60 nm were also measured by McKenna *et al.* using bubble inflation method[244]. They concluded that the viscoelastic response of a-Se thin films shows Arrhenius behavior with a smaller dynamic fragility (m) and E_a compared with the bulk results obtained from macroscopic recoverable creep and compliance measurements, which is in contrast with our observation above. A difference between our experiments and the data in reference [244] is that they were testing the viscoelatic properties on freestanding a-Se films, while our experiments were conducted on films supported by Si substrates. Freestanding films are subject to the confinement effects from both interfaces. while supported films have substrate interaction on one side. It is possible that we will see a reduction in m if we could do dewetting experiments on thinner films.

3.4.2. Dewetting of a-Se Thin Films Under Light

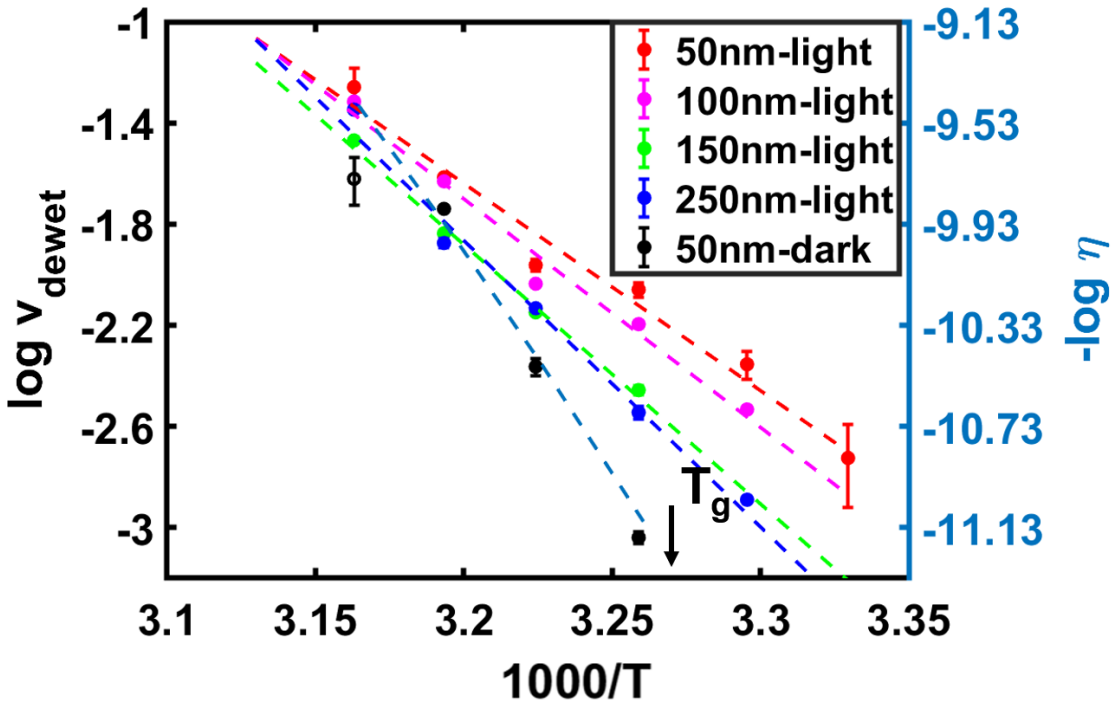

Figure 3.4: v_{dewet} *vs.* $1000/T$ for a-Se thin films with different thicknesses. Results for dewetting both in dark and light are shown. Error bars are defined by multiple experiments. Dashed lines (dash-dotted line for the dark result) are Arrhenius fits to experimental data. A-Se T_g is indicated on the graph by a black arrow.

When dewetting of a 50 nm a-Se films are performed under white light (full light intensity from the microscope lamphouse), a large increase in v_{dewet} (Figure 3.4) is observed. Additionally, the E_a for dewetting of a 50 nm a-Se film under light is reduced to less than a half ($E_{a,50nm,light}$ = 157±16 kJ/mol *vs.* $E_{a,50nm,dark}$ = 328±30 kJ/mol), indicating light activated relaxation enhancement and a reduction in film viscosity. The effect of white light can be observed in a-Se films as thick as 250 nm too. As can be seen from Figure 3.4, $E_{a,250nm,ligh}$ = 217±23 kJ/mol is still lower than $E_{a,50nm,dark}$, suggesting a faster relaxation than bulk dynamics in these systems.

The acceleration in thin film relaxation in polymeric systems has been attributed to fast

surface dynamics[77, 160, 92, 60]. However, from the thin film experiments conducted in dark, we note that the fast surface dynamics on a-Se[12] does not seem to play an important role in controlling the 50 nm a-Se films' relaxation, while a large relaxation enhancement is observed under light for much thicker films. This is due to the VAP formed under light exposure, which can break Se-Se bonds, effectively reduce the molecular weight, remove entanglements, and facilitate a-Se structural relaxation. This effect is known as photo-induced fluidity[216] in chalcogenide glasses. On the other hand, the recombination of charged sites can result in the segment exchange, and the formation of three/four-coordinated defect sites[111], which may inhibit further relaxation. By comparing the E_a calculated from experiments performed in dark and under light, we can conclude that the light assisted unentanglement is the reason why thick a-Se films can relax faster under light than thinner films in dark. The formation of three/four-coordinated defect sites does not seem to slow down the film's dynamics, because they can be easily swapped to two-coordinated sites through charge transfer to release the constraints[112, 113].

3.4.3. Light Facilitated Dewetting in a-Se

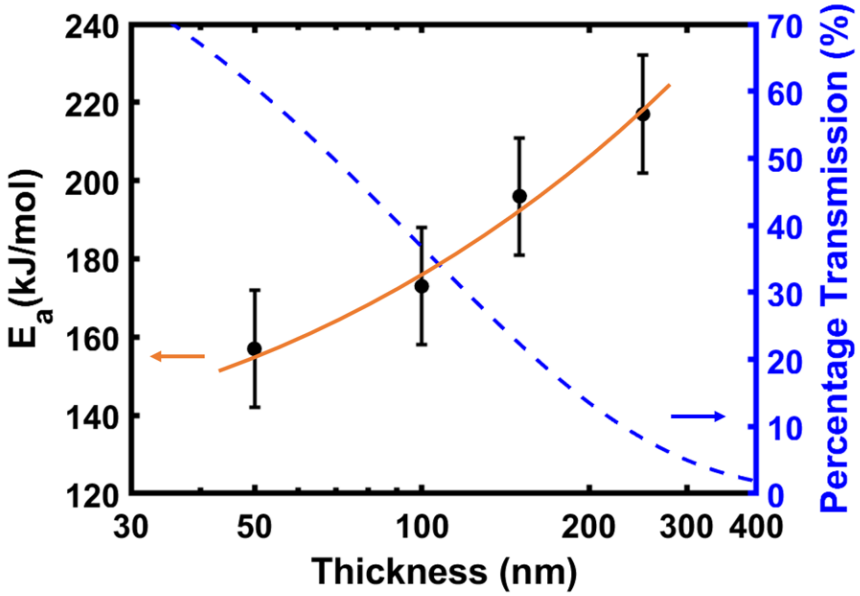

Figure 3.5: Left y axis: apparent activation energy for a-Se thin film dewetting (E_a) *vs.* film thickness (black dots, orange solid line is a guidance to the eye). Right y axis: the percentage of light that can be transmitted after penetrating through the film (blue dashed line). The absorption coefficient for a-Se (α_{Se}) used to estimate these values is 10^5 cm^{-1}.

As can be seen from Figure 3.4, the E_a calculated for a-Se dewetting under light decreases with increasing film thickness. It has been reported that a-Se has strong absorption in the visible light region, with an absorption coefficient (α_{Se}) of $\alpha_{Se} \sim 2 \times 10^5$ cm^{-1} around $\lambda =$ 440 nm and 10^4 cm^{-1} around $\lambda = 620$ nm[80]. For simplicity, we use $\alpha_{Se} \sim 10^5$ to estimate the percentage of light that can penetrate a-Se films at certain thicknesses, given the surface illumination geometry of our experiments. Plotting E_a and percentage transmission against a-Se film thickness on the same figure (Figure 3.5), we notice a clear negative correlation, which suggests semi-quantitatively that the degree of enhanced dynamics in a-Se thin films depends on the number of photons absorbed. Moreover, when experiments are performed with half of the initial light intensity, under the same temperature, we see a reduction of v_{dewet} (Figure 3.6). The negative correlation in Figure 3.5 and the light intensity dependent v_{dewet} help confirm that the light facilitated dewetting observed here is mainly due to

the VAP generated by photon activation, which reduces entanglements in these films and therefor the film viscosity.

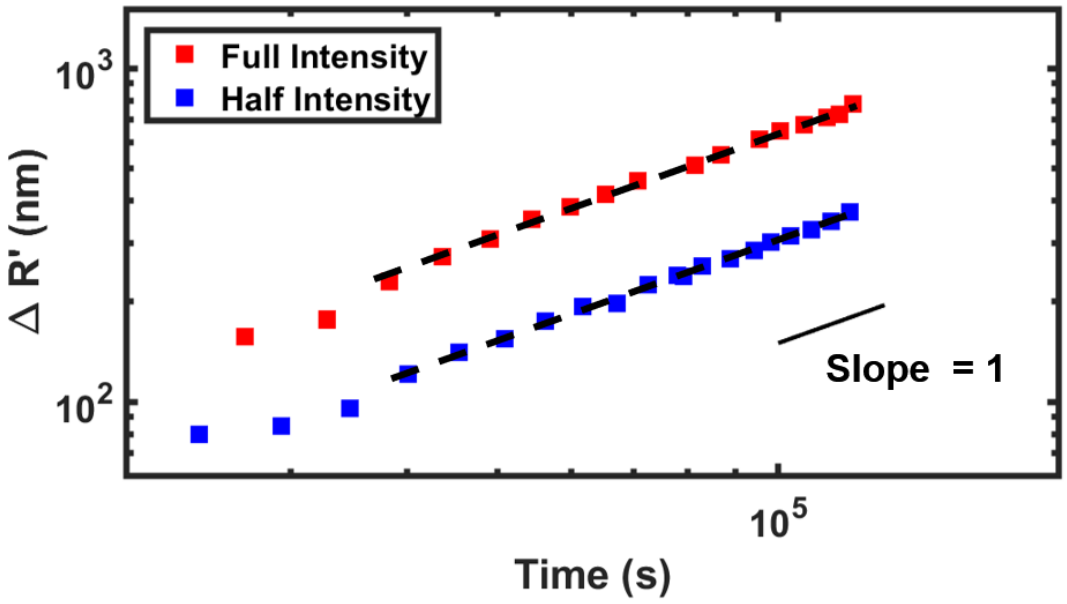

Figure 3.6: Single holes radius, R, *vs.* time for 100 nm a-Se film dewetted at 307 K with full light intensity (red, 1.5±0.2 mW/cm^2) and half light intensity (blue, 0.7±0.2 mW/cm^2). Dashed black lines are fits to data. Solid black line shows slope of 1.

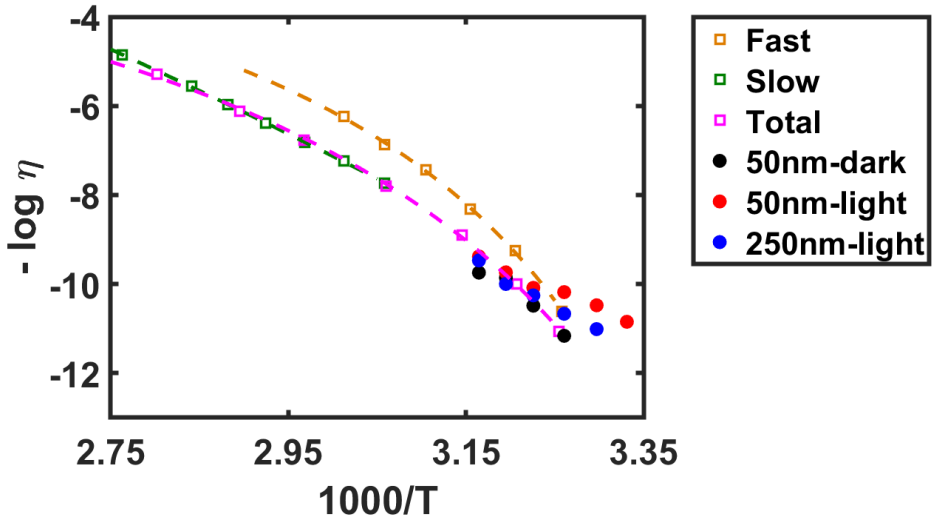

Figure 3.7: -log η *vs.* 1000/T for 50 nm a-Se films dewetting in dark (black), 50 nm (red) and 250 nm (dark blue) a-Se films dewetting under light. -log η is calculated from log v_{dewet} with a single shift factor as described in the text. In addition, data from literature: the contributions of the slow (green) and fast (orange) relaxation components in a-Se total viscosity (magenta) *vs.* 1000/T, are plotted. Dashed lines are VFT fits to data. Reprinted from reference[261]:W. Zhu, B. G. Aitken, S. Sen, Observation of a dynamical crossover in the shear relaxation processes in supercooled selenium near the glass transition, *The Journal of Chemical Physics*, Volume 150, Issue 9, 7 March 2019, 094502, Copyright (2019), with the permission of AIP Publishing.

The relaxation of a-Se close to T_g was found to consists of two components: a slow relaxation which is controlled by the Se–Se bond scission and renewal dynamics and a fast cooperative process which can be attributed to the normal Se chain segmental motions[260, 261]. Using a modified Maxwell model, a-Se viscosity can be written as $\eta \approx \tau_s G_s + \tau_f G_f$, where the $\tau_{s(f)}$ and $G_{s(f)}$ stand for the relaxation time and plateau shear moduli of the slow (s) and fast (f) relaxation processes. In reference [261], it was estimated that $G_s \sim 10^{6.2}$ and $G_f \sim 10^9$. Within the low viscosity regime between $\eta \sim 10^5 - 10^9$ Pa·s, a-Se's viscosity is dominated by the slow process, and the fast process plays a more and more important role as η increases from $\sim 10^9 - 10^{12}$ Pa·s[261].

However, when overlapping the viscosity of a-Se thin films calculated from the dewetting experiments, as what is established in Figure 3.4, with the fast/slow and total viscosity

contributions reported in reference [261] (Figure 3.7), we found that the apparent viscosity of a 50 nm a-Se film is lower than the boundary set by the fast segmental relaxation in bulk a-Se, which indicates that the effect of above-bandgap light is not only expediting the slow relaxation process by prompting Se chain breaking, but also accelerating a-Se segmental motions significantly by cutting the chains shorter and reducing their effective molecular weight. A comparable result was found when polymers viscosity became smaller with decreasing molecular weight[181, 38].

Also, in Figure 3.7, it is shown that the temperature dependence of viscosity switched from a Vogel-Tammann-Fulcher (VFT) relationship in bulk a-Se measurements to an Arrhenius relationship in a-Se thin film experiments conducted in light. The Arrhenius behavior between viscosity (or relaxation times) and temperature is usually seen in ultra-thin organic films[239, 254]. Lateral surface diffusion is also shown to have Arrhenius temperature dependence[255, 250]. The a-Se thin films being Arrhenius-like under light suggests that their activation process and potential energy landscape are likely to be altered by photons absorbed, becoming more "surface-like". Another observation we want to make in Figure 3.7 is the convergence of a-Se thin film viscosity around $T^* \sim 315$ K (T_g+9 K), below which temperature the acceleration of dewetting under light appears to be more prominent. Similar crossover between bulk and thin film dynamics was seen in polymers as well[70, 59]. It was proposed that T^* is an onset of surface dynamics, which requires further investigation.

3.5. Summary and Outlook

Here we presented our work on qualitatively determining the viscosity and light-induced fluidity in a-Se thin films, using isothermal dewetting experiments under microscope. A 50 nm a-Se film on Si substrate behaves bulk-like dynamics. However, when white light is applied during the experiments, a-Se films' mobility can be largely improved. A 250 nm a-Se films shows a smaller viscosity under light than a 50 nm a-Se film in dark. The light-induced fluidity in a-Se has been attributed to Se-Se bond breaking, reducing in effective molecular weight and the subsequently prompted chain relaxation, facilitated by the

formation of Valence Alternation Pairs when light is absorbed. The negative correlation between the dewetting activation energy and the degree of light transmission into the film also demonstrates the importance of lighting conditions in a-Se dynamics. A higher light intensity could potentially activate much thicker a-Se films. Thus, ideally, the dynamics of a-Se films can be finely tuned by changing the external light intensity, which is an important consideration when using a-Se as a photoelectronic devices.

Future investigation should be focused on tuning the light properties, such as intensity and wavelength, to see how a-Se respond to various energy levels and how deep into the film light can have an affect on. From the thin film point of view, it will be beneficial to extend these experiments to thinner films, in order to study the bulk to thin film transition length scale in inorganic glasses, which is beyond the scope of this work. These studies are essential in reconciling the mismatch between different experiments conducted under various (probably underestimated) lighting conditions[210, 134, 193, 74] and better understanding of a-Se properties when used as photon detectors.

3.6. Supplementary Information

3.6.1. Sample Dewetting Temperature Calibration

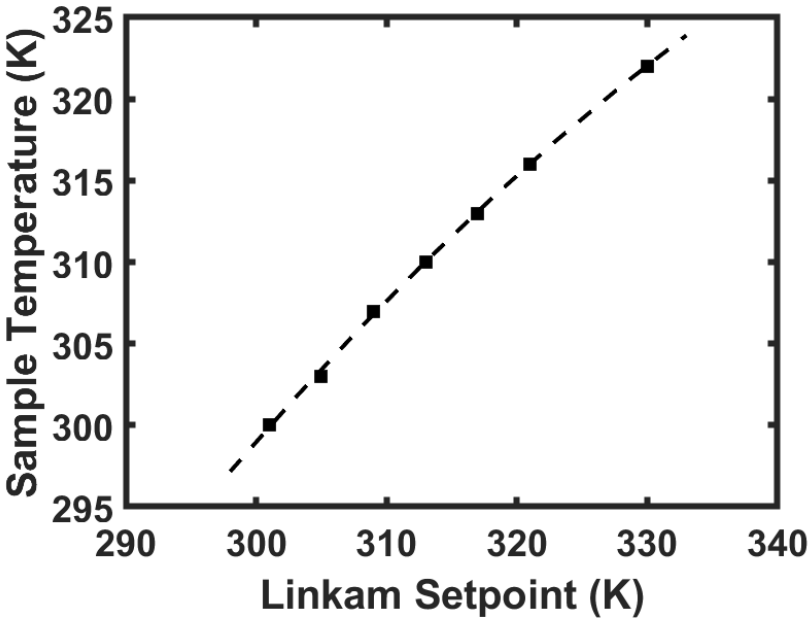

Figure 3.8: Correlation plot between the actual sample dewetting temperature and the set-point on Linkam T95 Controller (black squares). Dashed line is the second order polynomial fit to experimental data.

The actual temperature of samples annealed on Linkam PE100 Thermoelectric stage was calibrated using a separate thermistor (Oven Industries Inc., TR91-170). Temperatures read by the thermistor were recorded after at least 2 hours annealing at the designated setpoint. The results were further confirmed with melting point standards in the range of 320 - 322 K (Benzophenone, Sigma Aldrich) and summarized in Figure 3.8.

3.6.2. As-deposited and Annealed Morphology of 50 nm a-Se Thin Films

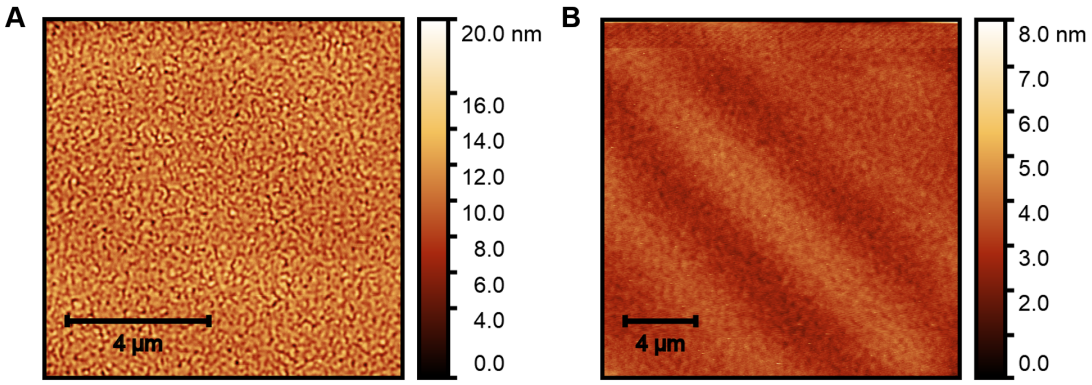

Figure 3.9: Surface morphology of 50 nm a-Se (A) as-deposited ($T_{dep} = 259 \pm 1$ K) and (B) annealed ($T_{anneal} = 323 \pm 1$ K for 10 min) films measured using AFM.

3.7. Acknowledgments

I thank Danixa Rodríguez-Melendez from the University of Puerto Rico at Cayey for performing the preliminary experiments as an undergraduate student, and Prof. Zahra Fakhraai and Prof. Richard B. Stephens for their guidance.

CHAPTER 4: Thermal Properties of Amorphous Selenium Thin Films

4.1. Abstract

In this chapter, I will discuss the thermal properties of a-Se thin films. In particular I will focus on how the expansion coefficients (α) of a-Se thin films become different from the bulk value over a ∼200 nm length scale, and aim to explain these anomalous observations. A-Se α in both super-cooled-liquid (SCL) and glass regions (α_{SCL} and α_{SCL}) are measured to increase with decreasing film thickness or cooling rate, especially for the films thinner than 200 nm. This ∼200 nm length scale is much larger than what were measured on polymeric and organic molecular materials (∼30 to 80 nm). We attribute this extremely large length scale to the intrinsic elastic properties of a-Se as a chalcogenide glass and the difference in atomic bonding structures when comparing a-Se thin films with the bulk.

4.2. Introduction

Previous investigations have demonstrated the thin film properties of polymeric, organic molecular, and inorganic glasses are different from their bulk behaviors. Viscosity[239], physical aging rate[166], elastic modulus[222] and glass transition temperature[101, 70, 54] of thin films can be significantly influenced by their interfacial properties, geometry and confinement effects. Extensive researches have been conducted on polymeric and organic molecular glasses, with their critical thickness from which films properties deviate compared to bulk measured to be around 30 to 80 nm, based on the nature of the materials and the experimental method used. However, similar phenomena in inorganic glasses have been rarely explored as such, the length scale where bulk to thin film transition occurs in inorganic glasses remains an open question.

A few studies have also explored the film thickness dependence of expansion coefficients (α)[204, 237, 107, 116, 13, 71]. But there was no consensus made so far. Some demonstrated no change in α, regardless of the variation in film thickness[107, 116], substrate interaction[126] or cooling rate[13, 71]; while others concluded an increasing α with de-

creasing film thickness[104, 204, 237]. The thermal expansion of a system was shown to become different after physical aging[100, 155] or when the samples were made in specific ways, such as physical vapor deposition[128], which suggests α may be correlated with the molecular packing and relaxation times.

From a theoretical point of view, based on the Elastically Collective Nonlinear Langevin Equation (ECNLE) theory, structural relaxations within a dense liquid involve both local and collective motions, with two distinct but inter-related activation barriers corresponded to them[145, 146]. In particular, the longer range collective motion requires elastic fluctuation, which is thus related to the elastic shear modulus of the material. When it comes to thin films, interfacial effects have to be considered. A position dependent correction needs to be applied to the activation barriers[162, 189]. Recent results show the hard surface at the substrate has an effect too. Thinner films have larger suppression in the value of both local and elastic activation barriers, which account for enhanced dynamics in thin films. The length scale over which thin film properties deviate from the bulk should be related to the local cage size, which could be derived from the system's structural factor (radial distribution function), and the material's elasticity. The experimental observation that the perturbed length scale at polymer-polymer interface being related to the polymer's elastic modulus[11, 66] is in agreement with the ECNLE theory prediction.

The cooling rate dependence of a-Se α was predicted by computer simulation before and has been validated by experiments[139, 73, 149]. In this work, we measured the α variance not only with cooling rates, but also with film thickness. It was shown that the α of a-Se thin films became larger when either the cooling rate or film thickness was reduced. A $\sim$200 nm length scale, at which the bulk to thin film transition occurs, was detected. Taking advantage of this extremely large length scale, we took X-ray Reflectivity and Ellipsometry measurements on a-Se films thinner than 200 nm, aiming to reveal the differences in atomic packings between a-Se thin films and the bulk, as well as understand the reason behind this large length scale.

4.3. Experimental Details

4.3.1. Material and Film Preparation

Selenium films were deposited in the deposition chamber introduced in section 2.3.1 and annealed at 323 K for at least 20 min before use, to make sure all experiments were done on liquid quenched glasses.

4.3.2. In situ Ellipsometry Measurements to Calculate a-Se Expansion Coefficients

In situ Ellipsometry measurements were conducted by integrating a Linkam temperature-control module (THMS350V) with J. A. Woollam Spectroscopic Ellipsometry (SE, Model M-2000 V). SE angles $\Psi(\lambda)$ and $\Delta(\lambda)$ were collected every 2.4 s with zone averaging at a fixed 70° angle while a film was going through programmed temperature ramps on the Linkam stage. Generally, a 10 K/min heating rate was used and the cooling rates were allowed to vary between 20 K/min to 2 K/min. The temperature range of heating and cooling was 253 to 323 K. Since a-Se's bandgap was determined to be ∼650 nm (Figure2.11), to minimize the effect of light on our results, samples were handled in dark and covered with light-blocking materials after they were mounted on the Linkam stage, except for two viewports that were equipped with 780 nm long-pass filters, allowing below-bandgap ellipsometer light to pass through. Basically, above-bandgap light was avoided during our *in situ* ellipsometry measurements when determining a-Se expansion coefficients (α).

Measurements were conducted under vacuum using a custom-made environment-control stage (Figure 2.2) as described in section 2.3.2, as well as under N_2 flow in low humidity environments without vacuum. Because a correction to the window effects from the Kodial glass viewports had to be applied when fitting the data collected under vacuum, ambient pressure measurements were done to confirm our observations were not originated from any error introduced by fitting the window effects. There was no apparent difference between the data collected under these two conditions. Most data reported in this chapter were

collected under N_2 flow in low humidity environments and no obvious water accumulation was detected.

To extrapolate thickness and α information from *in situ* measurements, SE angles $\Psi(\lambda)$ and $\Delta(\lambda)$ were fitted to an isotropic transparent Cauchy model within the wavelength range between 1000 to 1600 nm:

$$n = A + \frac{B}{\lambda^2}. \tag{4.7}$$

When the film thickness was above 300 nm, A, B, film thickness, and roughness were used as fitting parameters. When the films were thinner than 300 nm, fitting to film roughness was omitted to avoid over-fitting. The choice of parameters to fit was shown to have some influence on the exact value of α, especially for the films thinner than 300 nm, but it didn't change the overall qualitative conclusions we presented here. No distinct optical anisotropy was observed in annealed a-Se films.

Expansion coefficients (α) of a-Se super-cooled liquid (α_{SCL}) and Glass (α_{GL}) regions were measured during cooling ramps. A-Se film thicknesses were normalized to their thicknesses at the highest annealing temperature (323 K) before they were fitted linearly between 313 to 323 K and 260 to 280 K to calculate the α_{SCL} and α_{SCL}. As can be seen from Figure 4.1B, the first derivative of normalized thickness reached plateau values within the temperature ranges we chose to fit the data.

4.3.3. X-ray Reflectivity Measurements

X-ray Reflectivity (XRR) measurements were conducted on a-Se films with various thicknesses using Rigaku SmartLab X-ray diffractometer. 2θ angle were scanned between 0.4002° to 4.0002° at 0.1° intervals. Cu K_α line was used as X-ray beam source. The thickest sample measured by XRR was ∼130 nm. Samples thicker than 150 nm didn't yield clear fringes, due to increasing film thickness and surface roughness. XRR experiments were performed to compare the density of a-Se films at various thicknesses. For a single component thin films, the critical angle in XRR (θ_c), above which total external reflection happens, can be

related to the films density (ρ) by:

$$\theta_c = \sqrt{\frac{r_0 \lambda^2}{\pi} N_A \frac{(Z + f')}{A} \cdot \rho} \tag{4.8}$$

where θ_c is a small angle. In the equation, r_0 stands for the Bohr atomic radius, λ is the X-ray beam wavelength, N_A is the Avogadros number, Z represents the number of electrons per atom, f' is the dispersion part of a complex atom form factor in X-ray absorption edge, and A stands for the atomic weight[241]. Given that all other quantities are constants in a-Se, the change in its ρ will be reflected by θ_c in the way $\theta_c \propto \sqrt{\rho}$.

4.3.4. UV Spectroscopic Ellipsometry Characterization

A-Se complex index of refraction ($\widetilde{n} = n + ik$) was obtained by doing SE measurements using UV-Visible-IR light with a wavelength span of 250 nm to 1000 nm (J. A. Woollam). Samples were measured at 5 reflection angles between 55° to 75° at 5° intervals. The fitting model that was used to fit the SE angles $\Psi(\lambda)$ and $\Delta(\lambda)$ contains 3 layers: a silicon substrate, a 1-nm-thick SiO_2 which accounts for the native oxide layer on silicon substrate, and an isotropic absorptive layer that stands for the a-Se film. The third layer for a-Se consist of two Tauc-Lorentz oscillators located at ∼2.0 eV and 4.1 eV, respectively. Its complex index of refraction obeyed Kramers–Kronig relationship. The results of fitting for a-Se films of various thicknesses can be found in Figure 4.5.

4.4. Result and Discussion

4.4.1. Deviating Behaviors of a-Se Thin Films Expansion Coefficients

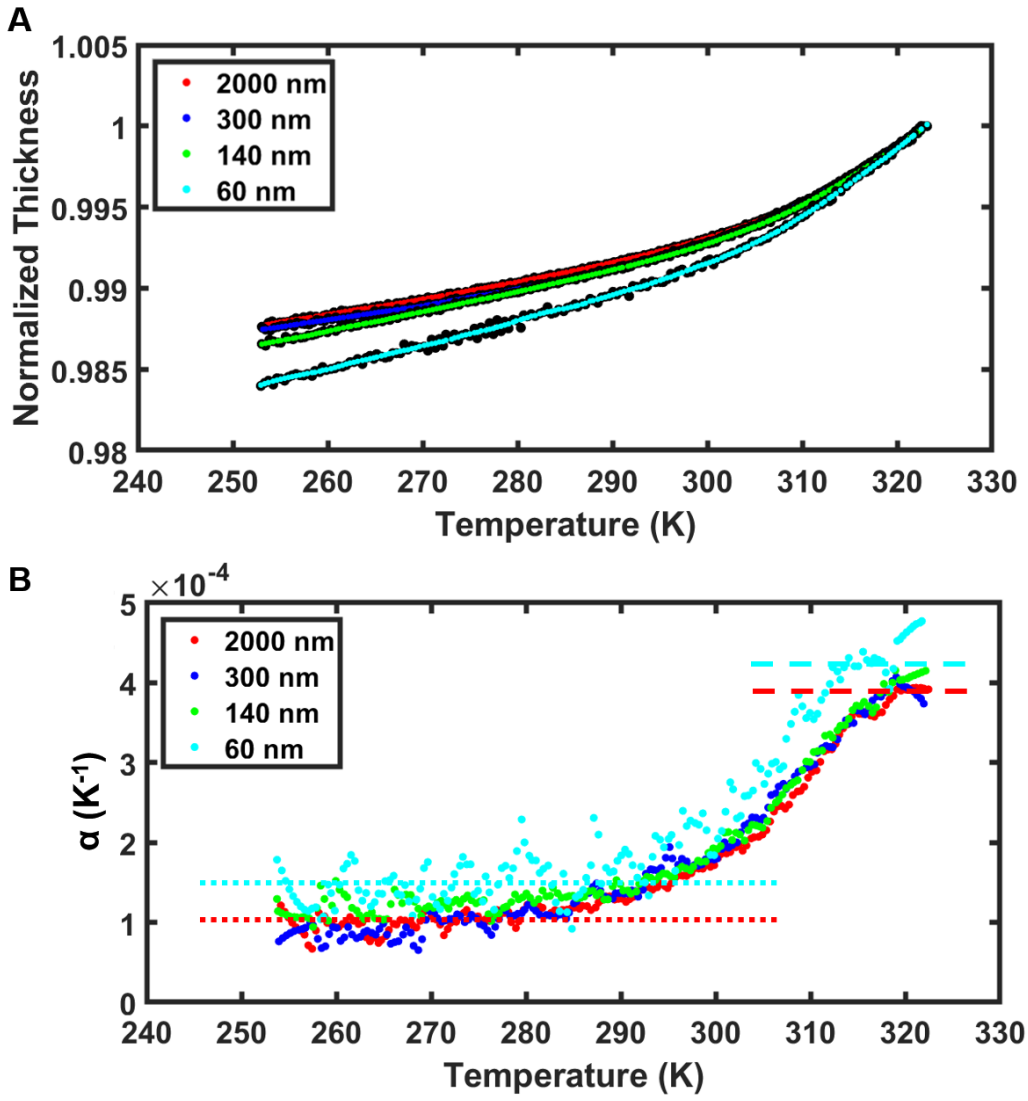

Figure 4.1: (A) Normalized thickness *vs.* temperature for a-Se films of various thicknesses. Cooling rate was 10 K/min. Black dots are raw data collected from *in situ* SE for films of various thicknesses. Colored Data were the smoothed data of black dots using 3^{rd} order Savitzky-Golay filter in Matlab with a frame length of 10% for the entire data set. (B) α calculated as the 1^{st} order derivative of the smoothed data in (A) *vs.* temperature. Dashed and dotted lines are guidance to the eye where the α_{SCL} and α_{SCL} for 60 nm (cyan) and 2000 nm (red) a-Se films' α reach a plateau. It is seen that 60 nm a-Se films have higher α_{SCL} and α_{SCL} than the 2000 nm a-Se films.

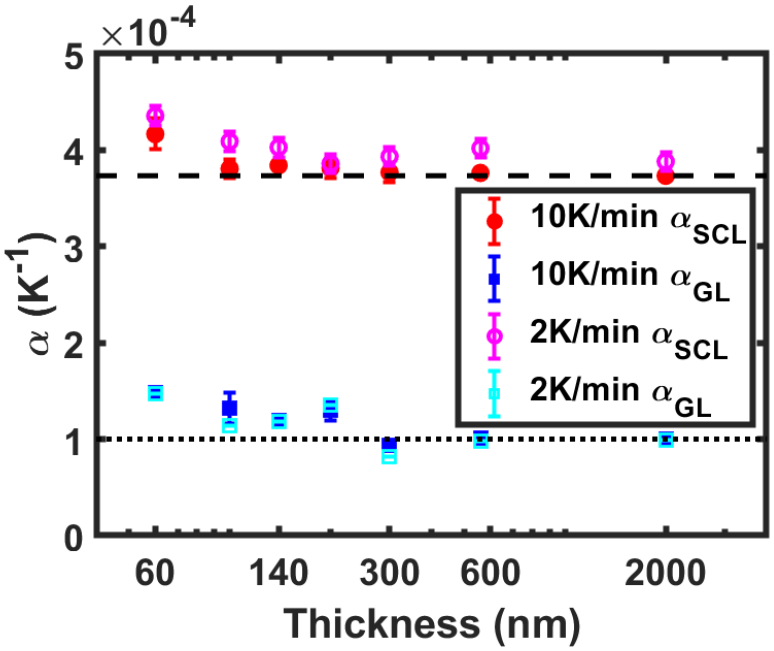

Figure 4.2: Expansion coefficients in SCL (α_{SCL}) and glass regions (α_{GL}) *vs.* film thickness. Results of 10 K/min (solid symbols) and 2 K/min (empty symbols) cooling rates are shown in the figure. Dashed and dotted lines indicate the α_{SCL} and α_{GL} for 2000 nm (bulk) films cooled at 10 K/min.

Several thickness profiles collected during cooling were shown in Figure 4.1A for a-Se films of different thicknesses. The α of them were calculated as the slope of the linear fits to their SCL and GL regions, whose temperature ranges were determined by the plateaued parts of the first order derivative of smoothed data (Figure 4.1B). It can be seen clearly from Figure 4.2A that when a-Se films become thinner than ~200 nm, their α_{SCL} and α_{GL} both start to increase with decreasing film thickness, with α_{GL} being more sensitive to thickness by showing a larger length scale over which the deviation α happens.

Similar changes in α were reported on polymeric thin films before. However, the length scale measured in polymers is around 20 to 60 nm, regardless of their molecular weight or the interfacial interaction with substrates[204, 237]. Nothing as large as a ~200 nm perturbed length scale was reported previously. The reason for this extremely long length scale in a-Se will be discussed more in the next section.

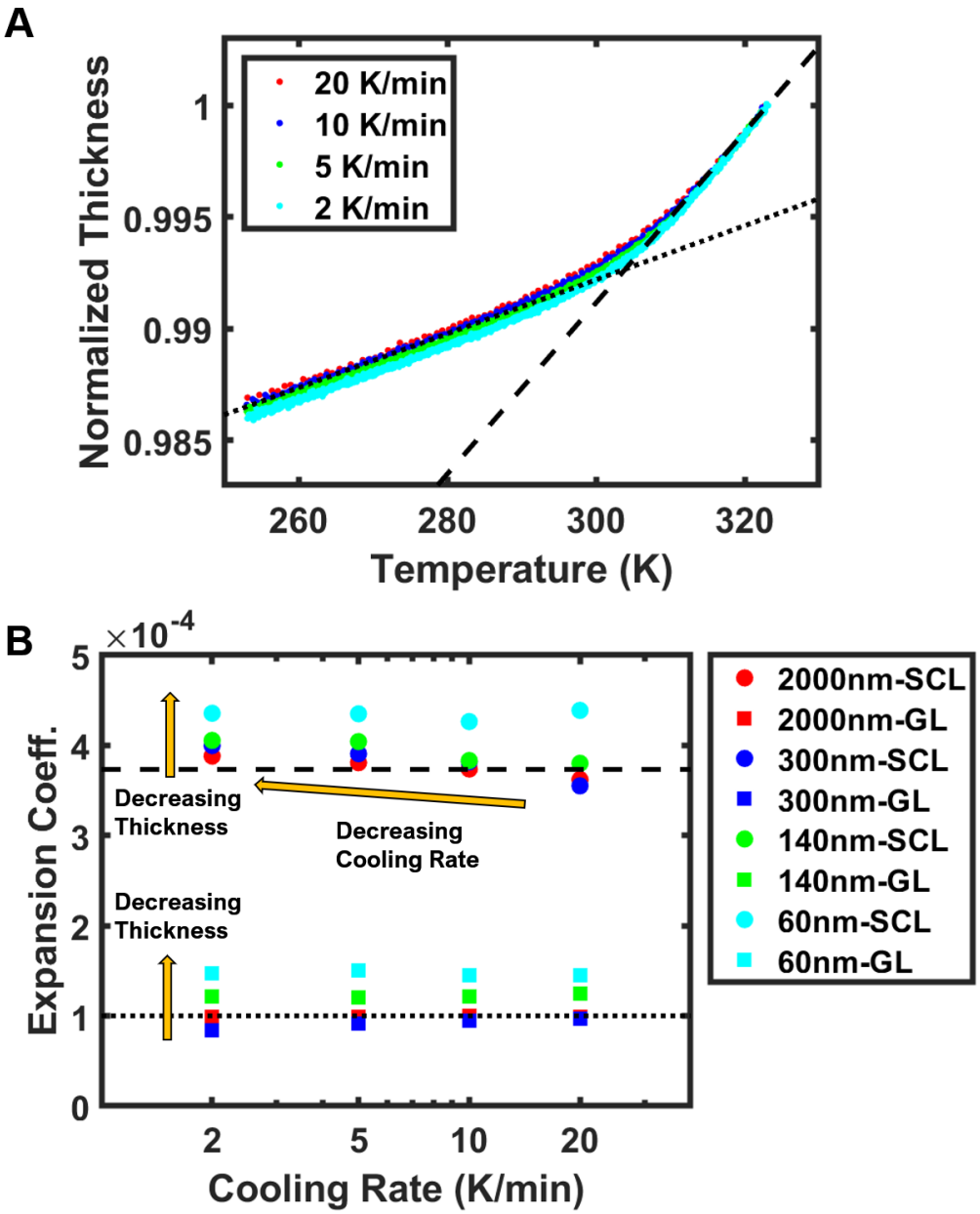

Figure 4.3: (A) Normalized thickness *vs.* temperature for 140 nm a-Se films cooled at various cooling rates ranging from 20 K/min to 2 K/min. Dashed and dotted lines are the fittings to the SCL and GL regions at 10 K/min cooling rate. (B) A-Se α *vs.* cooling rate for films with different thicknesses. Dashed and dotted lines indicate the α_{SCL} and α_{GL} for a 2000 nm (bulk) cooled at 10 K/min.

The cooling rate dependence of α was also measured and the results were plotted in Figure 4.3. Two distinct trends were seen from Figure 4.3B. In terms of the α_{GL}, it is less perturbed

by the cooling rate than film thickness. However, as for α_{SCL}, it increase with either decreasing cooling rate or film thickness. The influence of cooling rate is seemed to be the most prominent in films around 300 nm.

4.4.2. Difference in Packings Between a-Se Thin Films and the Bulk

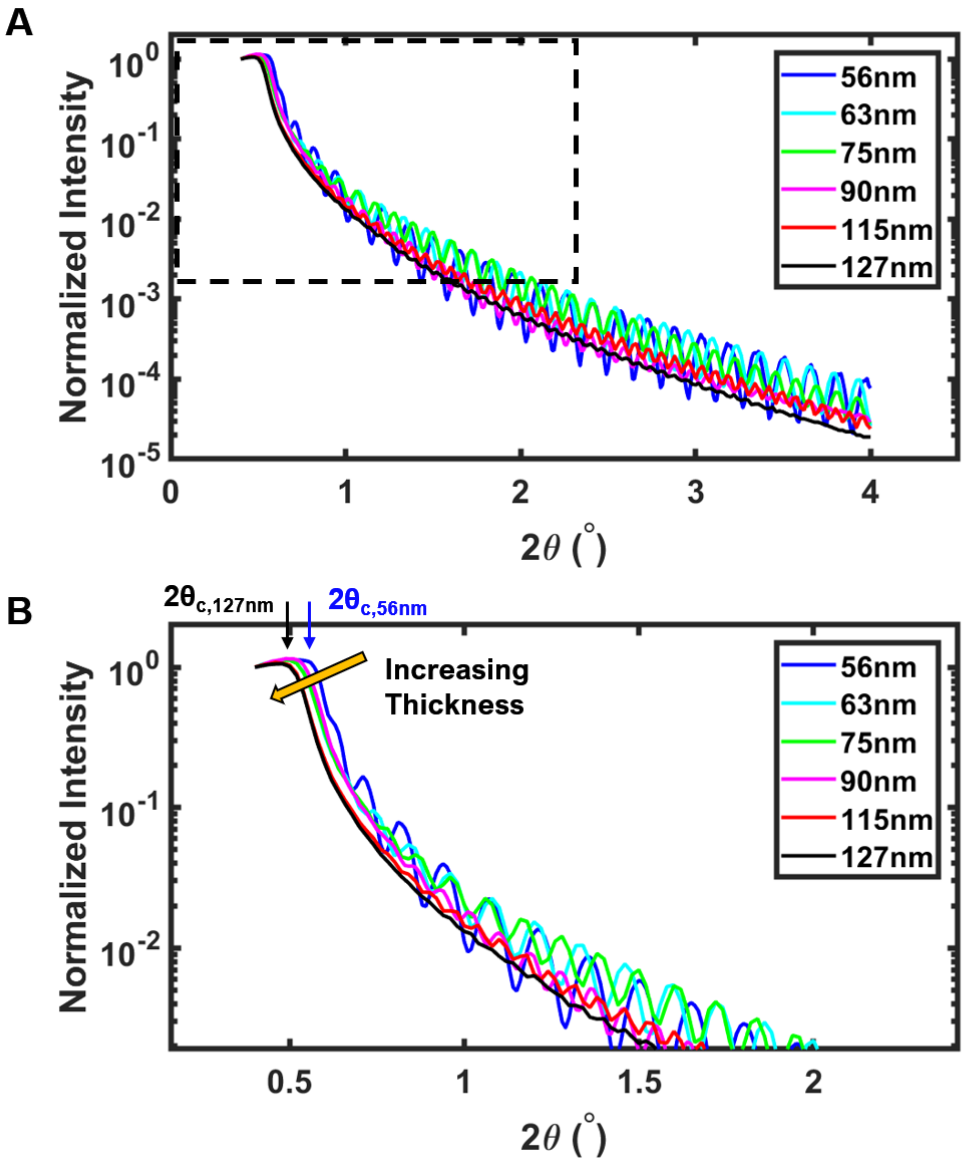

Figure 4.4: (A) X-ray Reflectivity data on a-Se films with various thicknesses. The part in black box is zoomed in in (B). The position of critical angles (θ_c) were pointed out for 56 nm and 127 nm a-Se films.

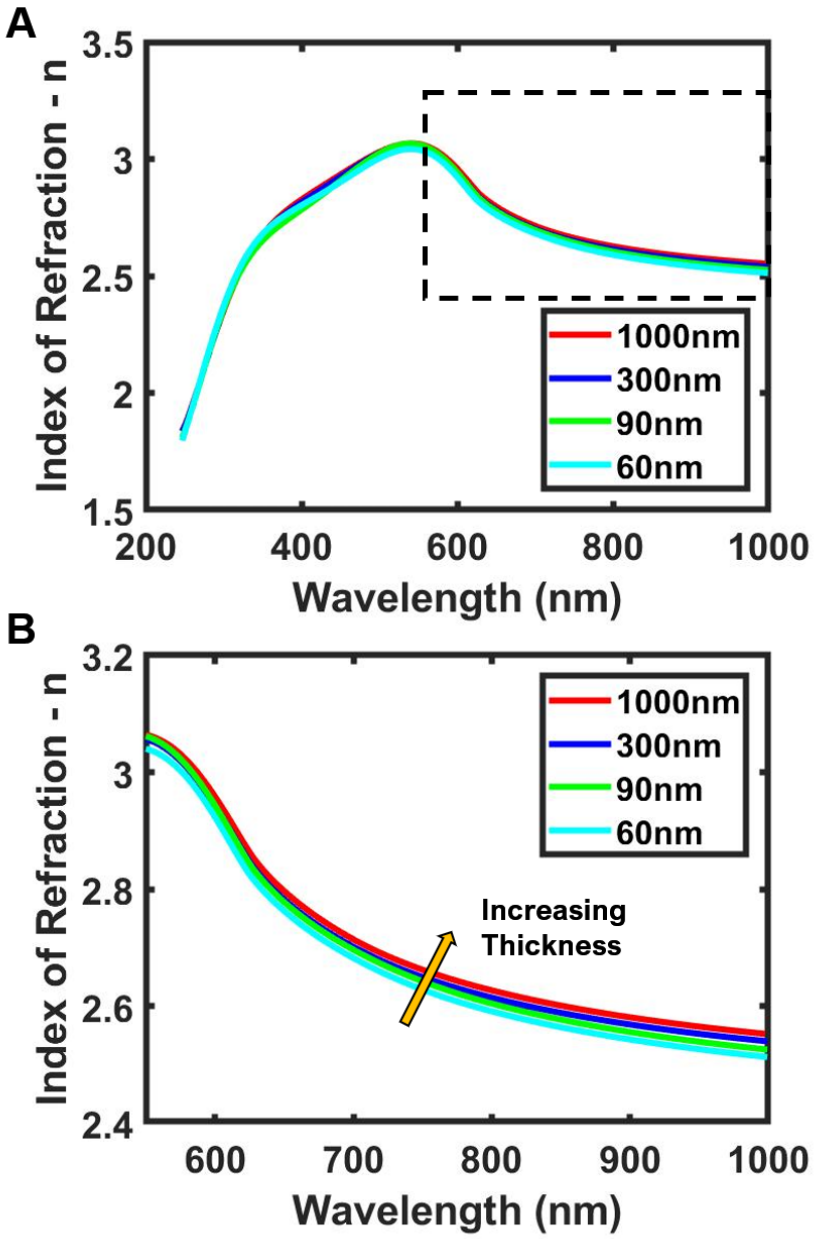

Figure 4.5: (A) Real part index of refraction collected on a-Se films with various thicknesses. Ellipsometric Ψ and Δ were fitted with an isotropic Kramers–Kronig consistent absorptive model, from which the complex refractive index ($\widetilde{n} = n + ik$) was derived and the real part, n, was plotted in the figure. The part in black box is zoomed in in (B).

X-ray Reflectivity (XRR) experiments were used to compare the atomic density of a-Se thin films. As introduced in the Experimental Details section, the critical angle (θ_c) in XRR is

related to the density of an atomic film (ρ) through: $\theta_c \propto \sqrt{\rho}$. From Figure 4.4, we noticed a decreasing trend in θ_c with increasing film thickness, which suggests a larger atomic density in 56 nm a-Se films than 127 nm a-Se films. However, as can be seen in Figure 4.5, the complex index of refraction ($\widetilde{n} = n + ik$) obtained by fitting Ellipsometry data collected over 250 nm to 1000 nm wavelength range shows contradictory results, with thicker films having higher index of refraction, which presumably correspond to higher packing density. We note that both XRR and Ellipsometry have their own uncertainties in determining density and index of refraction. XRR is more accurate in measuring thinner films, while Ellipsometry is better at fitting thicker films. Nevertheless, the results here indicate the atomic packing within a-Se film changes with thickness gradually, though we are not sure in which way the film density becomes.

Earlier work by Scopigno *et al.* demonstrates that the surface (top ~5 nm) of a-Se contains more three/four-coodinated defects than the bulk[191]. Due to the modification of bonding structure, from a 1D chain-like to 2D plane or 3D network-like, they inferred that the surface strain can be more readily conveyed to the bulk with the higher coordinated packings. Here we postulate the extremely long length scale we observed from which a-Se bulk to thin film transition occurs is due to the higher percentage density of over-coordinated Se defected states in thin films, which results in a longer-ranged elastic response. Detailed relationships between this higher coordinated structure and thin films density and index of refraction will require more investigations in the future.

Lattice stiffness and bonding anharmonicity can jointly determine the thermal α of a material[89]. Alternation of the bonding structure can be an important reason why the α of a-Se thin films are deviating from the bulk. Moreover, the change in α with cooling rate may be a combined result of fast aging (increase in effective molecular weight) and alternation in packing happened close to T_g, with the process being easier in SCL region than in deep GL state. This accounts for why we see α_{SCL} depend more strongly on cooling rate than α_{GL}. A throughout aging experiment and subsequent structural characterization

may be helpful in distinguishing the two effects.

4.5. Summary and Outlook

The expansion coefficients (α) of a-Se films were measured to become larger than 2000 nm bulk films when they are thinner than ~200 nm, which is quite large a length scale compared to what has been seen in organic polymeric systems. We attribute this extremely long length scale to the change in a-Se thin film bonding structures which contains more three/four-coodinated defected states than the bulk. The higher density of networked structures in a-Se thin films facilitates a longer range elastic responds during structural relaxations than polymers and organic glasses. Meanwhile, it also gives rise to the change of α and atomic packing of a-Se thin films. More direct measurements on the change in a-Se bonding structure with thickness using Extended X-ray Absorption Fine Structure (EXAFS) or Raman are needed to understand our observations fully.

4.6. Acknowledgments

I wants to thank Dr. Radhe Agarwal and Prof. Jonathan E. Spanier for their help in Ellipsometry and X-ray Reflectivity measurements, Prof. Richard B. Stephens and Prof. Zahra Fakhraai for their guidance.

CHAPTER 5: Influence of Intra-molecular Degrees of Freedom on the Amorphous Structure of Stable Glasses

This chapter is reproduced from a manuscript in preparation.

5.1. Abstract

Physical vapor deposited (PVD) stable glasses (SGs) have been extensively studied in recent years with a focus on understanding the effect of molecular shape and inter-molecular interactions on the properties exhibited by these systems. In this chapter, we demonstrate how subtle changes in intra-molecular degrees of freedom can dramatically affect the surface relaxation, and in turn, the packing and stability of PVD glasses.

It has been recognized that Surface Mediate Equilibration (SME) is a key mechanism that controls SG packing and molecular alignment. Molecules with different shapes and functional groups pack and relax differently at the immediate free surface region. Relaxation in layers adjacent to the free surface has been shown to reduce structural anisotropy and enhance SG stability. However, little is understood on the role of intra-molecular degrees of freedom in the structure and relaxation at the free surface and the depth of surface mobility gradients. In this work, SGs formed by two structurally similar molecules, 9-(3,5-di(naphthalen-1-yl)phenyl)anthracene (α,α-A) and 9-(3,5-di(naphthalen-1-yl)phenyl)-phenanthrene (α,α-Phen) are compared. The only difference between these two molecules lies in the intra-molecular relaxation barrier of the anthracene (-A) substituent compared to phenanthrene (-Phen). Spectroscopic Ellipsomtetry and Grazing Incidence Wide-angle X-ray Scattering (GIWAXS) characterizations of the SGs produced by these molecules demonstrate that while the chemical structure of the two molecules are very similar, their properties differ significantly when the deposition temperature (T_{dep}) is varied. Close to the glass transition temperature (T_g), α,α-Phen, with lower rotational barrier of the -Phen substituent, makes more isotropic SGs with reduced molecular layering, while at lower T_{dep}, it can orient along the free surface, producing strongly anisotropic as well as significantly

less stable glasses. We demonstrate that the loss of configurational entropy in α,α-A due to the intra-molecular rotational frustration increases its barriers for surface relaxation and reduces the depth of surface mobility gradients, explaining its increased layering and reduced orientational anisotropy. By analyzing the data presented here and previous works on molecular PVD glasses, we provide a possible mechanism for the formation of layering within a certain range of deposition temperature.

5.2. Introduction

Stable Glasses (SGs) are produced by physical vapor deposition (PVD) at relatively slow deposition rates onto substrates held below the glass transition temperature (T_g) of the material[213, 103, 128, 172, 118]. Since their discovery[213], organic SGs have drawn a lot of research interest because of their improved density[39, 128] and thermal stability[213, 103, 232, 172, 173] that is analogous to highly-aged liquid quenched glasses (LQs). In addition to the extraordinary physical properties of SGs, vapor-deposited glasses also exhibit various degrees of optical birefringence[242, 39, 42, 200, 233, 156, 143], magnetic anisotropy[83] and structural anisotropy[49, 46, 75, 76, 233, 10, 236, 207, 129] which depend on the molecular shape and deposition conditions. It is essential to understand the interplay between structural anisotropy and glass stability, as molecular structure and deposition conditions are varied, because it is critical in determining the optical[242, 152, 236], mechanical[62, 223, 218] , and electronic[57, 8] properties of organic thin films in applications such as coatings and functional devices.

The structural anisotropy of PVD glasses can be originated from two factors, orientational ordering of the molecules, inherited from the free surface, and layering in the direction normal to the surface, due to deposition geometry. For orientational ordering, Bagchi *et al.* reported a generic "face-on" packing for both rod-like and disc-like molecules when deposited around $0.8T_g$, despite their dramatically different chemical structures[10]. As the deposition temperature (T_{dep}) increases toward T_g, this generic packing becomes weaker. Especially for rod-like molecules, their "face-on" packing at low T_{dep} will transition into an out-of-plane

liquid-crystal like structure when T_{dep} is around $0.95T_g$[233]. In other work, deposition closer to T_g or at slower deposition rates (r_{dep}) has been shown to result in isotropic packing for shorter molecules[22]. Surface Mediated Equilibration (SME) can provide insight into these observations. Surface boundary conditions can dictate in-plane orientation at the immediate free surface, while the layer below can take out-of-plane orientation[42, 148] or become isotropic when relaxation is sufficiently fast. During PVD, molecules on the surface are able to optimize their configuration regarding to their equilibrated liquid (EL) structure[133, 18, 9] as long as enhanced surface relaxation (or diffusion) is allowed at a given T_{dep} and r_{dep}. Even though enhanced surface relaxation is observed almost ubiquitously on SG formers and have a much weaker temperature dependence compared to the glass bulk relaxation[246, 253, 212, 188], the depth of surface mobility gradients is shown to be strongly dependent on T which decreases sharply as T is decreased[160, 220]. A few efforts have been made to estimate the depth of surface mobility gradient. Using fluorescence probes, the surface gradient thickness in freestanding polystyrene was estimated to be $\sim$7 nm around T_g and reduce to $\sim$1 nm around $0.9T_g$[160]. A recent work on 2-methyltetrahydrofuran organic glass derived a 2.5 nm surface mobility gradient at $0.82T_g$[220]. Combining the experimental results, simulated EL structures and analysis on the depth of surface mobility gradient, it can be concluded that when T_{dep} is close to T_g and r_{dep} is sufficiently slow, a large depth of surface mobility gradient results in the structure of SGs being an averaged form of a thick layer in EL, therefore, the as-deposited glasses appear to be isotropic. While as T_{dep} is further decreased, fewer layers of molecules on the surface will have sufficient mobility and the SGs structure will be determined by the molecular orientation of a thinner surface layer in EL[133, 75, 42, 23].

The phenomenon of molecular layering in SGs was firstly proposed by Fakhraai group[129] in a sphere-shaped molecular system, α,α-A. By identifying the correlation between the index of refraction in the out-of-plane direction and the density of SGs, as well as direct photoilluminescence experiments showing isotropic dipole orientation, they concluded that the improvement in density of α,α-A SGs mainly comes from its layered packing. The

fact that layering exists in sphere-shaped molecular SGs indicates it is a separate effect from molecular orientation, which is more widely investigated. Thus, investigations on the origin of layering in PVD glass and the factors controlling its intensity are essential in understanding SG formation.

Two methods have been generally used to measure the SGs' optical birefringence and structural anisotropy: Spectroscopic Ellipsometry (SE)[243, 40] and Grazing Incidence Wide-angle X-ray Scattering (GIWAXS)[75, 21, 10, 22], besides Infrared[93] and photoilluminescence[64] spectrum. SE can provide information on the difference between the in-plane and out-of-plane index of refraction through proper anisotropic modeling. In GIWAXS, distinctive peaks are predominated observed in either xy or z direction, when a particular packing orientation is preferred. The scattering features typically used to quantify the orientational order parameter is a broad peak that corresponds to the inter-molecular distancing[75, 21, 10] in the glass state. Besides the broad peaks, within a certain range of T_{dep}, a separate and sharper peak, localized at a lower q, can be observed in z direction, in various molecular SG systems, including rod-like, and even sphere-like molecules[49, 75, 9]. Because the length scale corresponds to this peak is similar to the size of deposited molecules, the aforementioned peak has recently been attributed to molecular layering.

Here, to understand the relationship between molecular structure and SGs packing, we focus on the role of intra-molecular relaxation. Two molecules, 9-(3,5-di(naphthalen-1-yl)phenyl)anthracene (α,α-A) and 9-(3,5-di(naphthalen-1-yl)phenyl)phenanthrene (α,α-Phen), with similar chemical formula and molecular weights are designed and synthesized. The difference between the two molecules is in the substituent on the 3,5-di(naphthalen-1-yl)benzene (diarylbenzene) moiety, where an anthracene (-A) group in α,α-A is replaced by a phenanthrene (-Phen) group in α,α-Phen. This simple replacement of one substituent results in a significant decrease of the rotation barrier for the Phen–diarylbenzene bond compared to the A–diarylbenzene bond (Figure 5.7A and more details in the Experimental Details section), resulting in differences in the intra-molecular relaxation between the two

molecules, as well as a change in the equilibrium shape from a spherical (α, α-A) to an ellipsoidal (α, α-Phen) one. This small change in the intra-molecular relaxation barrier, has a surprisingly large effect on the stability, density, optical birefringence, and the tendency of the molecules to form layered structures, during PVD, with larger distinctions at low deposition temperatures. We demonstrate that these differences are originated in the orientation and mobility of the molecules at the free surface, and the thickness of the mobile layer as a function of T_{dep}.

5.3. Experimental Details

5.3.1. Materials and Film Preparation

The two molecules used in this study, 9-(3,5-di(naphthalen-1-yl)phenyl)anthracene (α, α-A) and 9-(3,5-di(naphthalen-1-yl)phenyl)phenanthrene (α, α-Phen) were synthesized using Suzuki cross-coupling as detailed in our previous publication[127] and Supplementary Information. Organic films with thicknesses of 24 nm, ∼150-240 nm and ∼1 micron were thermally vapor deposited in a custom-built high vacuum chamber[188] at a deposition rate of 2 $\mathring{A}$/s. The basic description of the custom-built ultra-high vacuum deposition chamber can be found in reference[188, 94]. The base pressure of the chamber was maintained at $\sim 2 \times 10^{-7}$ Torr.

Most data presented here were collected on temperature gradient (T-grad) samples, which were made through deposition on a silicon substrate held between two independently temperature-controlled stages as detailed below and in previous publication [94](See Figure 5.1).

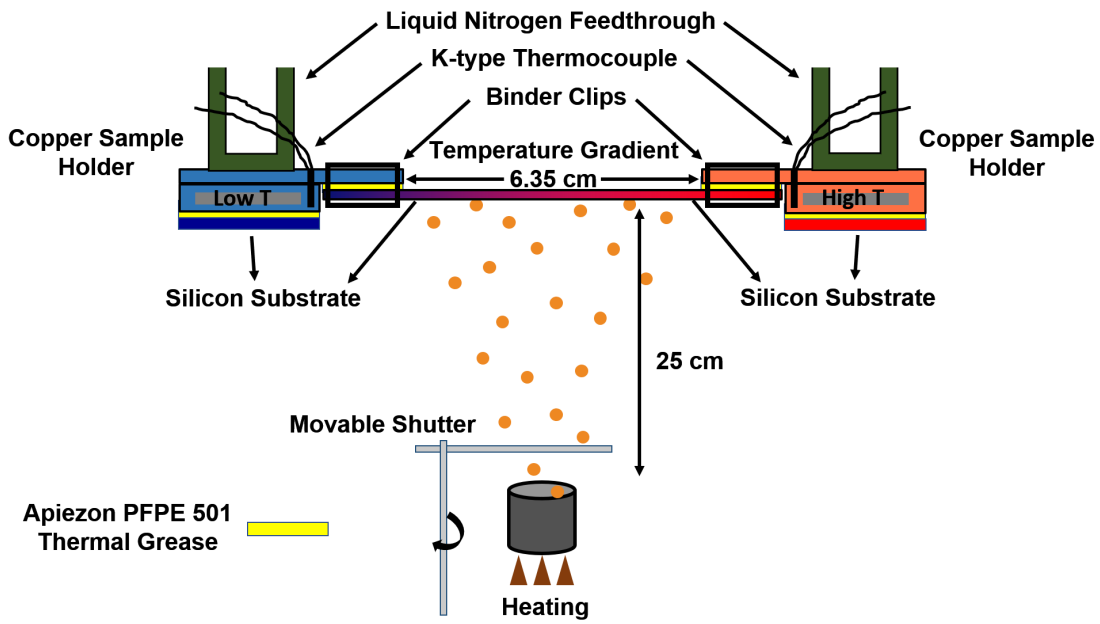

Figure 5.1: A schematic drawing of the custom-built T-grad setup inside the high vacuum deposition chamber for thermal vapor-deposition. The typical size of the silicon wafers used to make T-grad samples was ∼8.5 cm×2.0 cm, with 6.35 cm suspended between the two temperature-controlled copper stages and ∼1 cm clipped on each side. We assume the temperature gradient starts from the edge of each stage where the Si substrate is no longer attached to copper.

Before each deposition, the compound of interest (α,α-A or α,α-Phen) was premelted in a vacuum oven (Fisherbrand Isotemp Model 281A) under low vacuum (∼1 kPa). The premelting temperature was ∼543 K for α,α-A (melting point $T_{m,A} = 508\pm2$ K) and ∼483 K for α,α-Phen ($T_{m,Phen} = 448\pm2$ K), respectively. The melting points were determined by differential scanning calorimetry (DSC, TA instruments Q2000). After premelting, the glassy compounds were loaded onto a 1-cc alumina crucible (Kurt J. Lesker Co.) and placed into a tungsten basket at the bottom of the chamber. By heating the tungsten basket (and the alumina crucible) using an external power source (TDK-Lambda GEN 8-90U), the compounds were vapor-deposited onto Si substrates that were mounted on a temperature-controlled sample stage[94]. Deposition rate, r_{dep}, was monitored using a quartz crystal microbalance (QCM, Inficon STM-2). A movable shutter placed about 2 cm above the crucible was used to make sure the r_{dep} was stabilized at 2±0.2 $\AA$/s before the deposition

begun. This r_{dep} was maintained throughout each deposition.

Boron doped silicon substrates with a native oxide layer of ∼1 nm (Virginia Semiconductor Inc.) were adhered to the copper sample stages with Apiezon PFPE 501 Thermal Grease (silicone-free, ultra-high vacuum). When T-grad setup was used, a pair of binder clips were used to make sure the thermal contact between Si substrate and the copper sample stage were well-maintained in the presence of heat flow. The temperature of copper sample holders were controlled individually using Omega Platinum Series microprocessor-based PID controllers (CN16DPT-330) and measured with K-type thermocouples (Omega Engineering). Cooling of these substrates were facilitated by liquid nitrogen feed-throughs welded onto the copper sample holders (a schematic drawing is shown in Figure 5.1).

Upon finishing deposition, the hot-side of the T-grad sample was quenched rapidly and the cold-side was heated to room temperature. Samples were removed and measured by SE or placed in a freezer within one hour after deposition, for other characterizations.

5.3.2. Calculation of Temperature at Each Individual Point on the T-grad Samples

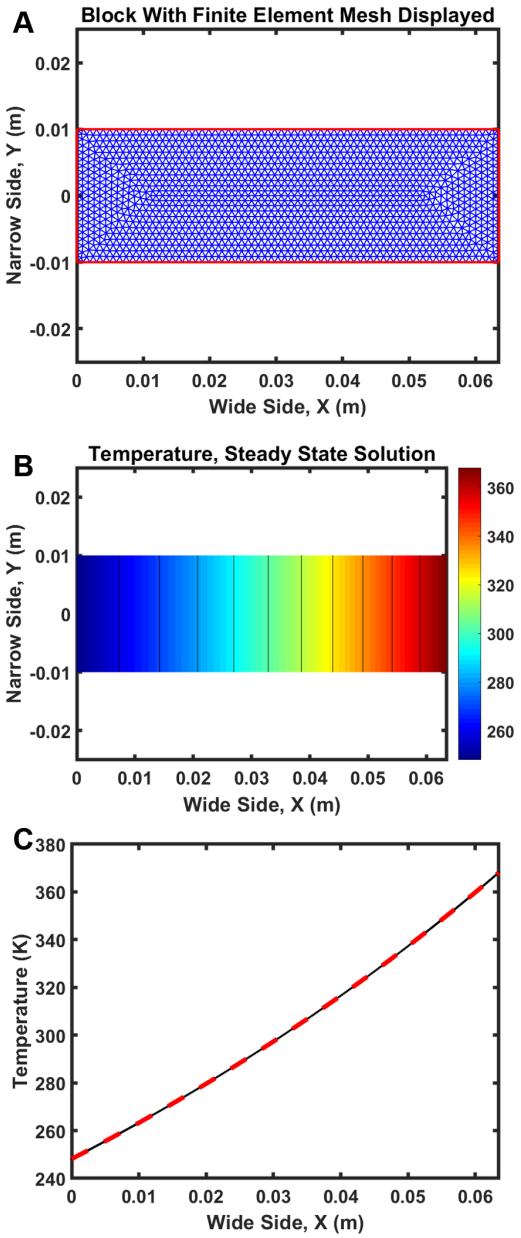

Figure 5.2: (A) Meshes created for solving the partial differential equation numerically. (B) Steady state solution for the temperature distribution on a gradient sample. (C) Temperature profile along the X axis (black dots) and a third-order polynomial function (red dashed line) obtained by fitting the meshed result.

The temperature at a given point along the temperature gradient can be determined by solving the partial differential equation of the Fourier's law:

$$\boldsymbol{q}(\boldsymbol{x}) = -k(T)\boldsymbol{\nabla}T(\boldsymbol{x}).$$

Here, $\boldsymbol{x}$ is the coordinate along the T-grad sample; $\boldsymbol{q}(\boldsymbol{x})$ is the heat flow at that point and $T(\boldsymbol{x})$ is the temperature. The thermal conductivity of silicon ($k(T)$) is a function of temperature and is given by[228]:

$$\log k(T) = 2.177 + 88.24 \times T^{-1} - 0.001033 \times T + 2.716 \times 10^{-7} \times T^2.$$

Given the simple geometry of the T-grad samples, we can assume that the temperature gradient is only formed along the long axis of the sample (x direction). Therefore a simplified one dimensional equation can be used to model the gradient. When steady state is met, $\boldsymbol{q}(\boldsymbol{x})$ is a constant. Given the boundary condition of the two facing narrow sides having fixed known temperatures, the partial differential equation can be solved numerically. A geometry with the same dimension as the suspended part of the Si substrate was created using a Matlab script, and the two narrow edges were assigned to have a temperature equivalent to the setpoint of the temperature controller on each side. Then this geometry was meshed and numerically solved. Figure 5.2 shows an example of the meshed geometry and the solution for temperature distribution. The meshed result along X was then fitted into a one-dimension third-order polynomial and the temperature at each individual point was calculated from there.

Previous reports involving temperature gradient setups either utilized a supportive bridge under the glass substrate[62] or performed corrections to the end point temperature[41] due to the imperfect thermal contact. In our setup, no correction to the endpoint temperatures were applied. Extensive calibration experiments, reported in our previous publication[94] and performed for this study (see Supplementary Information Figure 5.16), show that the

difference between the temperature at the end of the silicon wafer and the copper is $|\Delta T| \leq \pm 4$ K, which is within the error of determining the location, considering a 120 K gradient was generated over 6.35 cm distance. When taking this error into account, the results agree well with depositions on substrates with temepratures maintained at a single T_{dep} value across the T-gradient sample, as shown in our previous publication[94].

5.3.3. Spectroscopic Ellipsometry Characterization

The relative density change ($\Delta\rho$) and birefringence index of refraction of α,α-A and α,α-Phen PVD glasses were measured by Spectroscopic Ellipsometry (SE, J. A. Woollam M-2000V) on the same day of deposition. The data was obtained by mapping each T-grad sample on a 3×32 grid, facilitated by an automatic translation stage on the SE. The distances between datapoints on both directions were 0.2 cm. At each point, ellipsometeric angles Ψ (amplitude change) and Δ (phase change) were collected on the the spectral wavelength range of 370 nm$< \lambda <$1700 nm at various reflection angles between 65° to 75° at 5° intervals. Since most PVD films are optically birefringent, the SE data was fitted to a transparent anisotropic Cauchy model written as:

$$\begin{aligned} n_{xy} &= A_{xy} + \frac{B}{\lambda^2} \\ n_z &= A_z + \frac{B}{\lambda^2} \\ dZA &= n_z - n_{xy} = A_z - A_{xy} \end{aligned}$$

in the wavelength range of 550 nm $< \lambda <$1700 nm. Here n_{xy} and n_z are the in-plane and out-of-plane indices of refraction, respectively and A_{xy}, A_z, and B are the Cauchy fit parameters. The film thickness, h, was also used as an independent fitting parameter.

Due to the limitations of the sample size for our heating stage (Linkam temperature-controller, THMS600), after the first full SE scan , the as-deposited T-grad samples were split into three pieces, each about 2.8 cm in length from the wide side. Each sample was subject to a thermal ramp individually to transform the film into the lquid-quenched (LQ)

state. Before and after each transformation cycle, multi-angle SE mapping was performed at room temperature (298 K) on the same set of grid coordinates, and the data was fitted as described above. The thermal transformation cycle consists of three steps: heating the sample to 393 K from 298 K, annealing it at 393 K for 30 min, and cooling it back to 298 K. The heating and cooling rates were kept at 10 K/min. During every transformation cycle, *in-situ* SE measurements were performed at a single point on the sample, while recording Ψ and Δ at 2.4 s intervals with zone averaging, to make sure the samples were fully transformed at the end of the annealing period (thickness reaches a plateau at 393 K). After each thermal cycle, $\Delta\rho$ was calculated for each grid point by comparing the *ex-situ* values of thickness obtained at the same grid coordinates before and after the transformation. An example of the data collected is shown in main text Figure 5.3. Generally, three data points were collected at the same T_{dep} (along the narrow direction, Y) and the data was averaged to improve accuracy.

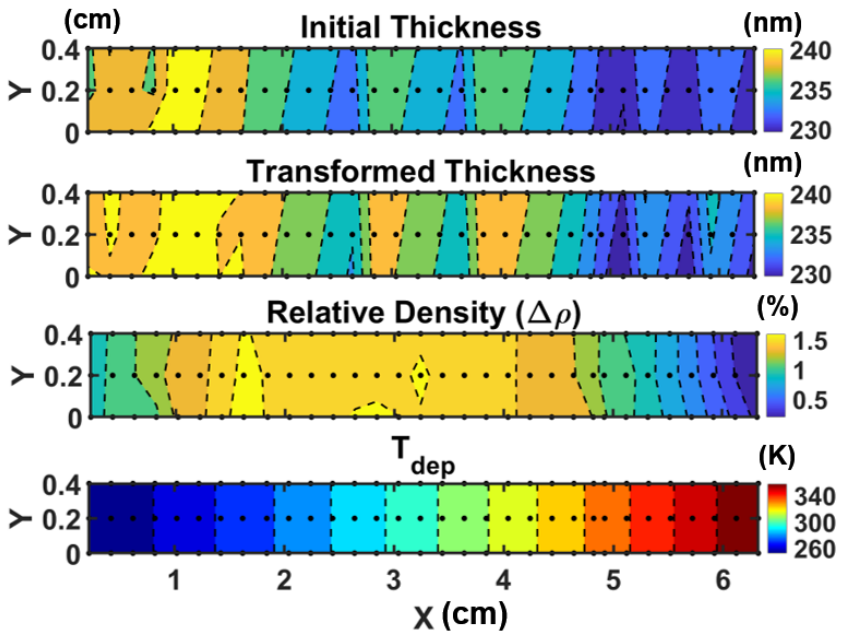

Figure 5.3: From top to bottom, contour plots of the initial thickness of as-deposited film, the thickness of the transformed LQ glass, calculated relative density ($\Delta\rho$) based on this set of data, and T_{dep} for a ~240 nm α,α-A T-grad sample. Black dots on the graphs indicate the coordinates where SE measurements were taken.

The $\Delta\rho$ and indices of refraction data reported here, are the averaged values collected from several independent sets of PVD depositions. Because the coordinates and the corresponded T_{dep}s where obtained from samples with various T-grad ranges, the data measured on different samples were put into bins with a width of 4 K each, in the deposition range of 250 K< T_{dep} <366 K. The averaged $\Delta\rho$ and indices of refraction with standard error were calculated within each bin.

5.3.4. Grazing Incidence Wide-angle X-ray Scattering (GIWAXS) Measurement

Grazing Incidence Wide Angle X-ray Scattering (GIWAXS) was mainly conducted using a Xeuss 2.0 X-ray Scattering Machine (Xenocs). The x-ray incident angle was set at 0.2°. Examples of the 2D GIWAXS spectrum and integrated in-plane and out-of-plane scattering intensity are shown in Figure 5.4&5.5. Typically, 16 evenly-distributed points were measured on each T-grad sample at room temperature. Data displayed in Figure 5.11C are the averaged values between two independent 1 μm samples, and the vertical error bars show the standard error. The horizontal error bars for defining T_{dep} were obtained as described in section 5.3.2.

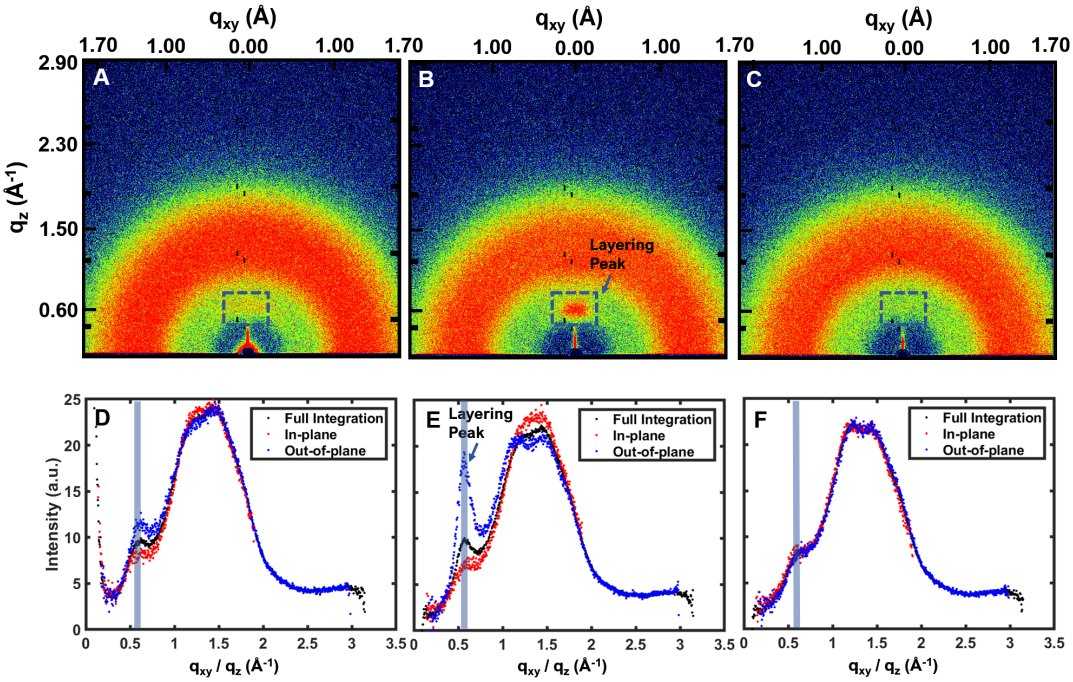

Figure 5.4: (A)/(B)/(C) 2D GIWAXS patterns for a 1 μm thick films of α,α-A deposited at T_{dep}=251 K/298 K/365 K, respectively. (D)/(E)/(F) Full (black), in-plane (q_{xy}, red) and out-of-plane (q_z, blue) integration of the scattering intensity for the data displayed in (A)/(B)/(C). For full integration, the intensity was radially integrated at all angles between 0° to 180°. For q_{xy}, the integration was performed between 0° to 30° and 150° to 180°, and for q_z, the integration was performed between 60° to 120°. (A) - (F) show the location of the layering peak, which is observed more prominently at T_{dep}=298 K in (B) and (E).

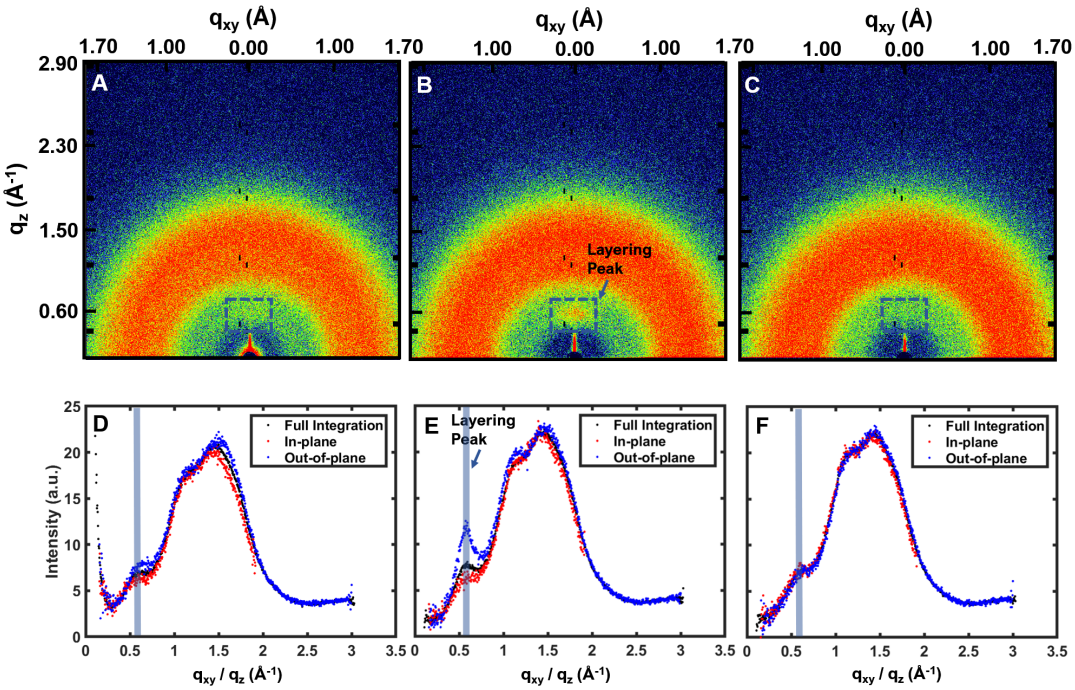

Figure 5.5: ((A)/(B)/(C) 2D GIWAXS patterns for a 1 μm thick film of α,α-Phen deposited at T_{dep}=251 K/298 K/365 K, respectively. (D)/(E)/(F) Full (black), in-plane (q_{xy}, red) and out-of-plane (q_z, blue) integration of the scattering intensity for the data displayed in (A)/(B)/(C). For full integration, the intensity was radially integrated at all angles between 0° to 180°. For q_{xy}, the integration was performed between 0° to 30° and 150° to 180°, and for q_z, the integration was performed between 60° to 120°. (A) - (F) show the location of the layering peak, which is observed more prominently at T_{dep}=298 K in (B) and (E).

5.3.5. Dewetting Experiments Conducted Using Atomic Force Microscopy

Dewetting experiments on α,α-A and α,α-Phen thin films were conducted using Atomic Force Microscope (Agilent Technologies 5420 AFM) with a XY-Z closed-loop scanner (Model N9524B). The initial morphology was measured at room temperature (298 K). The samples were then heated to the target annealing temperature using a custom thermoelectric setup (Custom Thermoelectric modules and Oven Industries temperature controller) and annealed isothermally. After 90 min, heating was turned off and the samples were left to cool back to room temperature. The final morphology was collected within 10 min after the heating

was turned off.

5.3.6. Using Density Functional Theory to Calculate Rotation Barriers

Density Functional Theory (DFT) calculations were carried out using Gaussian in WebMO with B3LYP functional and 6-31G(d) basis. First, the geometries of single molecule of α,α-A and α,α-Phen were optimized. As can be seen from Figure 5.6A&C, the optimized dihedral angles is -89.8° for the anthracene-3,5-di(naphthalen-1-yl)benzene (A-diarylbenzene) bond and -56.6° for the Phen-diarylbenzene bond, respectively. As scuh, α,α-A is more spherical in shape, while α,α-Phen is ellipsoidial in shape. The size of α,α-A is estimated to be $\sim$1.2 nm in all directions. For α,α-Phen, the molecule's short axis is $\sim$1.2 nm while its long axis is $\sim$1.4 nm (Figure 5.6B&D).

Once equilibrium geometries were identified, a coordinate scan on the dihedral angle of the A-diarylbenzene/Phen-diarylbenzene bond was performed in the range of -180° to 180° to estimate the rotational barrier of the bond. To do this, the anthracene/phenanthrene moiety was rotated by a certain degree. Then molecule's geometry was optimized under the constrain of a fixed dihedral angle, and the energy was calculated. A 10° interval was chosen at first and away from the barrier. A 1° interval was used close to the energy barrier, to better map the behavior.

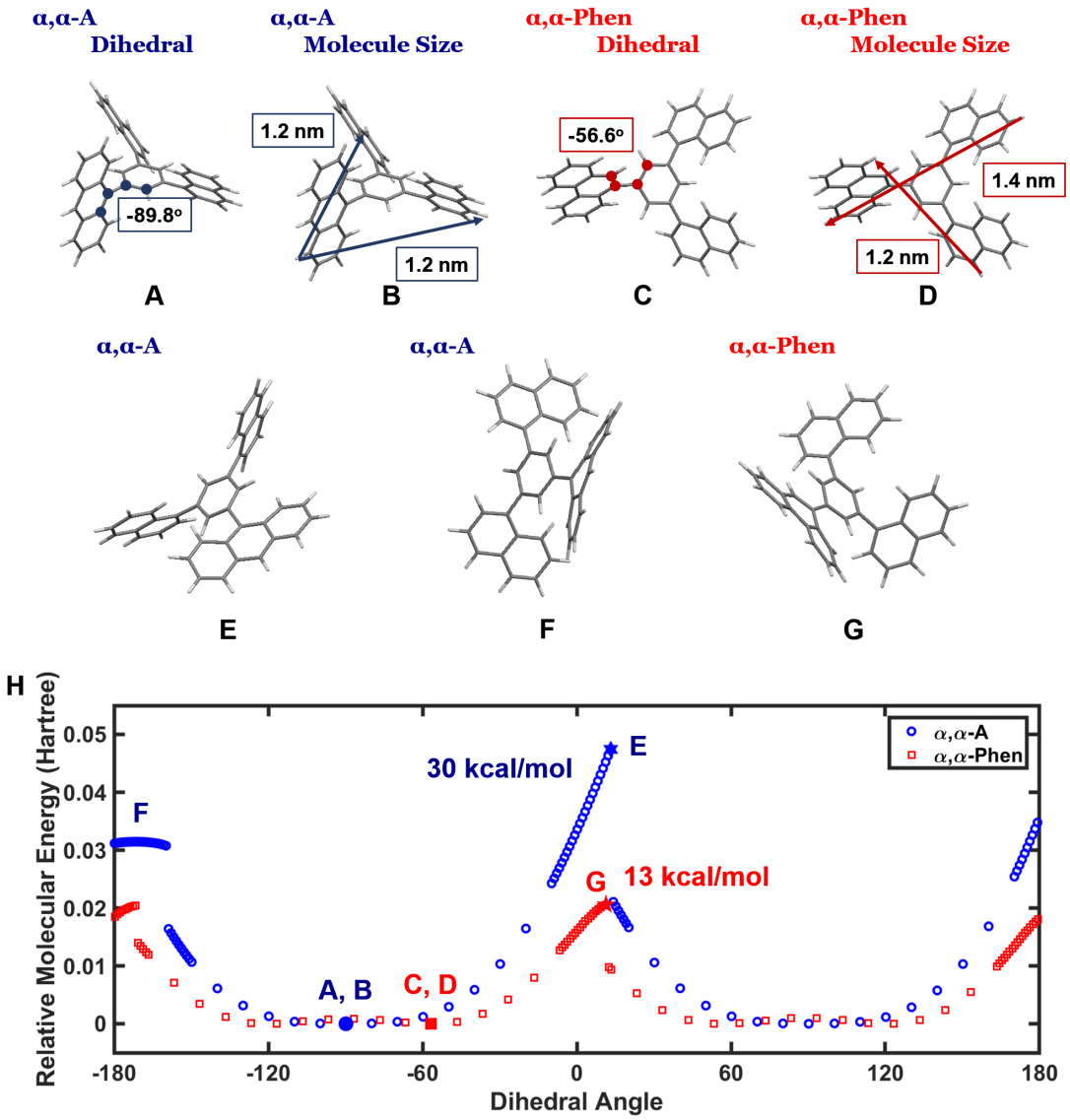

Figure 5.6: (A)-(G) Molecular geometries for α,α-A/α,α-Phen molecules on the potential energy landscape. (A) and (B) are the optimized α,α-A structure with the dihedral angle -89.8°. The arrow shows the approximate molecular size of 1.2 nm. (C) and (D) are the optimized α,α-Phen structure, with the diherdral angle -56.6°. The arrows show the molecular size at two different directions to be 1.2 nm and 1.4 nm (E) is the maximum energy site for α,α-A, with a dihedral angle of 13.2°. (F) is a distorted geometry showing how the barrier is overcome by the bending of the anthracene moity at the dihedral angle of -179.8°. (G) is the maximum energy site for α,α-Phen, at the dihedral angle 11.4°. (H) Relative molecular energy compared to the optimized value, vs. the dihedral angle for α,α-A (blue) and α,α-Phen (red). The letters A-G indicated on the graph show the locations corresponding to the molecular geometries shown in (A)-(G).

It can be seen from Figure 5.6H that the highest molecular energy is obtained when the dihedral angle is 13.2° for α,α-A and 11.4° for α,α-Phen. the discontinuation in energy when the barrier is overcome can be attributed to the accumulating constrains as the moiety rotates and a sudden relaxation when the constrain is released. If the coordinate scan is done in the opposite direction (decreasing values of the diherdral angle at each step), this overshoot will be observed at -13.2° or -11.4°, respectively (hysteresis). This asymmetry can also be seen in α,α-A barriers around 180° approaching from the two directions, for a similar reason that the initial geometries are different compared to the geometry optimized out of equilibrium. When the coordinate scan is performed between -150° to 170°, the molecule will be optimized to a distorted geometry shown in Figure 5.6F. This distorted geometry is unlikely to be adopted because the immediate energy as this molecule is forced to turn into this distorted state is initially ∼73 kcal/mol relative to the optimized molecular energy. This is much higher than the energy required to go through the other transition geometry around 0° (Figure 5.6E). For α,α-Phen molecule, the energy changes between going through ∼0° and ∼180° barriers are quite similar. To draw a conclusion from these DFT calculation, if we look at the transition ∼0°, from the discrete stepped energy calculation, the rotation barrier of the A-diarylbenzene bond is estimated to be ∼30 kcal/mol, while the barrier is only ∼13 kcal/mol for the Phen-diarylbenzene bond. We note that this is not a strict calculation for transition state energy, but it sets the lower bound for the rotational barrier and is adequate to be used as a rough estimation.

Another information we can get from Figure 5.6H is that α,α-Phen molecule has a energy basin flatter than α,α-A, which allows it to have more possible configurations during equilibration. This higher configurational entropy in α,α-Phen compared to α,α-Phen makes it easier relax at the free surface at low T_{dep}s.

5.4. Result and Discussion

5.4.1. Relative Density and Optical Birefringence of α,α-A and α,α-Phen PVD Glasses

The structures of the two molecules, α,α-A and α,α-Phen, are shown in Figure 5.7A, along with the estimated dihedral rotational barriers for the -A (30 kcal/mol) and -Phen (13 kcal/mol) substituents. These barriers were calculated using density functional theory. Figure 5.7B shows a representative transformation curve of as-deposited films of each molecule obtained using spectroscopic ellipsometry (SE). SE was performed *in-situ* as the samples were heated above T_g and cooled back to room temperature to evaluate the T_g and the relative density ($\Delta\rho$) of the as-deposited SGs compared to the LQ Glasses. As can be seen from the cooling curves, the T_gs of the two molecules are slightly different, with $T_{g,A}$ = 364±1 K and $T_{g,Phen}$ = 366±1 K. For both compounds, deposition at $T_{dep} \sim 0.83T_g$ resulted in a similar $\Delta\rho$ of $\Delta\rho = 1.5 \pm 0.1\%$ compared to the LQG.

High throughput temperature gradient (T-grad) samples of α,α-A and α,α-Phen SGs were produced by independently controlling the temperature at the two ends of a silicon substrate. The temperatures at the two ends were T_{cold} = 248 K and T_{hot} = 368 K respectively, producing a 120 K gradient along a 6.35 cm length of a rectangular silicon substrate.

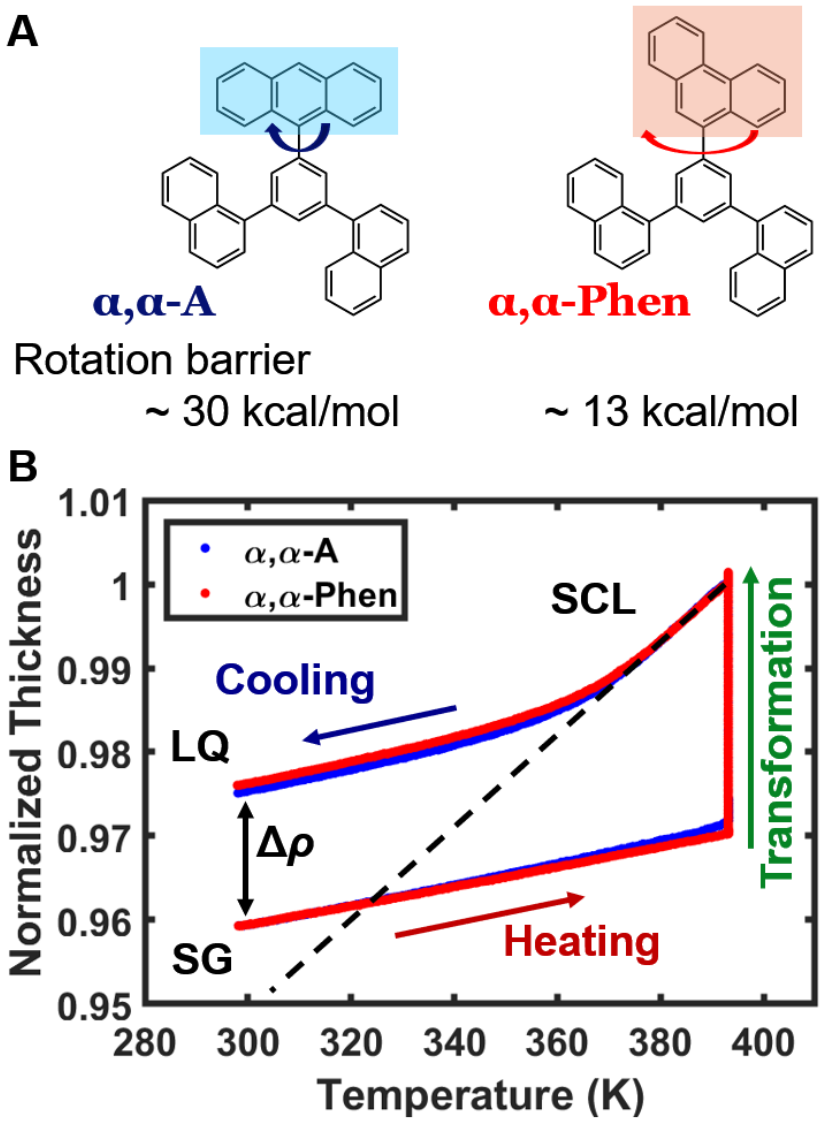

Figure 5.7: (A) Chemical structures of α,α-A (left) and α,α-Phen (right) molecules. The two molecules have different barriers to diherdral rotation, estimated to be 30 kcal/mol for α,α-A and 13 kcal/mol α,α-Phen, respectively based on DFT calculations. (B) Normalized thickness vs. temperature for transformation curves of ~240 nm films of α,α-A (blue) and α,α-Phen (red) SGs deposited at T_{dep} ~$0.83T_g$ (T_{dep} = 301±2 K for α,α-A and T_{dep} = 303±2 K for α,α-Phen, respectively). As-deposited films were heated from 298 K to 393 K and held isothermally for 30 min, to reach SCL, then cooled to 298 K, transforming into the LQG. The heating/cooling rates were 10 K/min. The relative density increase ($\Delta\rho$, shown with black arrow) was evaluated at 298 K and is $\Delta\rho \sim 1.5\pm0.1\%$ for both molecules. The T_gs were determined to be $T_{g,A} = 364 \pm 1$ K for α,α-A and $T_{g,Phen} = 366 \pm 1$ K for α,α-Phen, respectively.

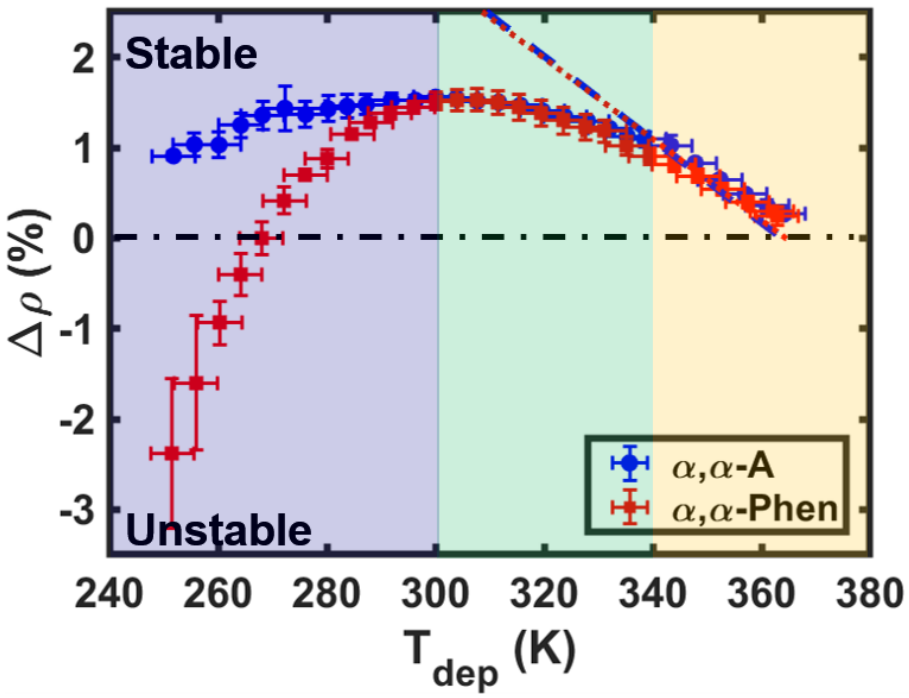

Figure 5.8: Relative density ($\Delta\rho$) of as-deposited α,α-A (blue circles) and α,α-Phen (red squares) films vs. T_{dep} for T-grad samples. Dashed and dotted lines are the extrapolated SCL equilibrium lines for α,α-A (blue) and α,α-Phen (red) respectively. The error bars are calculated as explained in Experimental Details section. The colors highlight the three distinct regimes of behavior as discussed in the text.

What can be seen from Figure 5.8 are the $\Delta\rho$ obtained from SE on α,α-A and α,α-Phen PVD glasses at various T_{dep}. For both α,α-A and α,α-Phen, $\Delta\rho$ follow the extrapolated SCL equilibrium lines, within the range of error when determining T_{dep} (as described in section 5.3.2 and 5.6.2), for 340 $K < T_{dep} < T_g$ (orange region), producing SGs with similar degrees of stability. As T_{dep} is further decreased below 340 K, $\Delta\rho$ starts to deviate from the equilibrium lines and reaches a maximum around $T_{dep} \sim 300$ K (green region) for both compounds, with a much broader trend in stability in α,α-A compared to α,α-Phen. At $T_{dep} < 300$ K (blue region), the $\Delta\rho_{-A}$ of α,α-A films remain high, and SGs are formed for the entire window of our experiments, consistent with our previous report[129]. However, in the same region, $\Delta\rho_{-Phen}$ rapidly drops, and the films are no longer stable below $T_{dep} \sim$ 264 K.

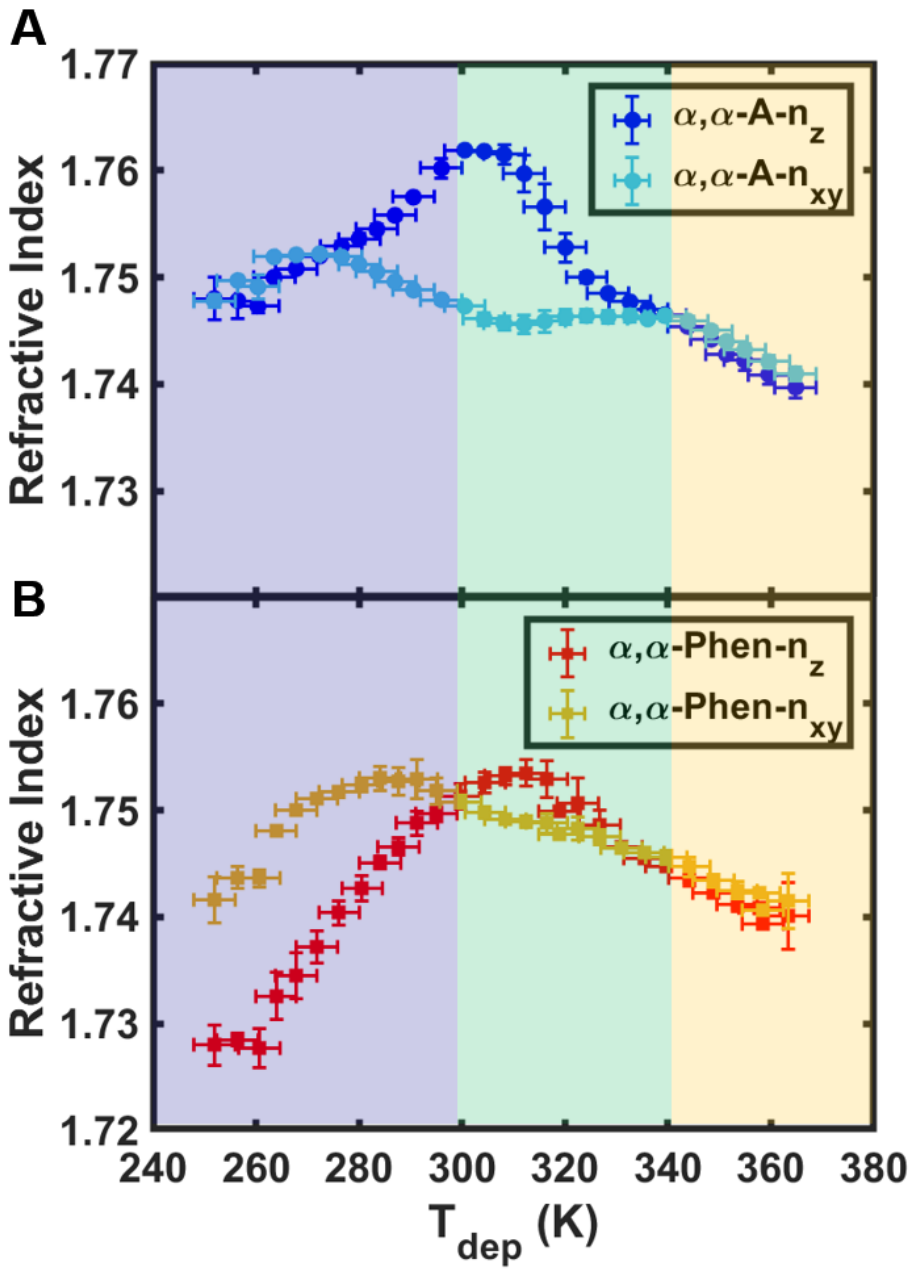

Figure 5.9: (A)/(B) Out-of-plane (n_z, solid blue circle/red square) and in-plane (n_{xy}, empty blue circle/red square) index of refraction at $\lambda = 632.8$ nm for ~1-micron-thick α,α-A/α,α-Phen PVD glasses as a function of deposition temperature. Data are measured on temperature gradient samples. The error bars are calculated as explained in Experimental Details section.

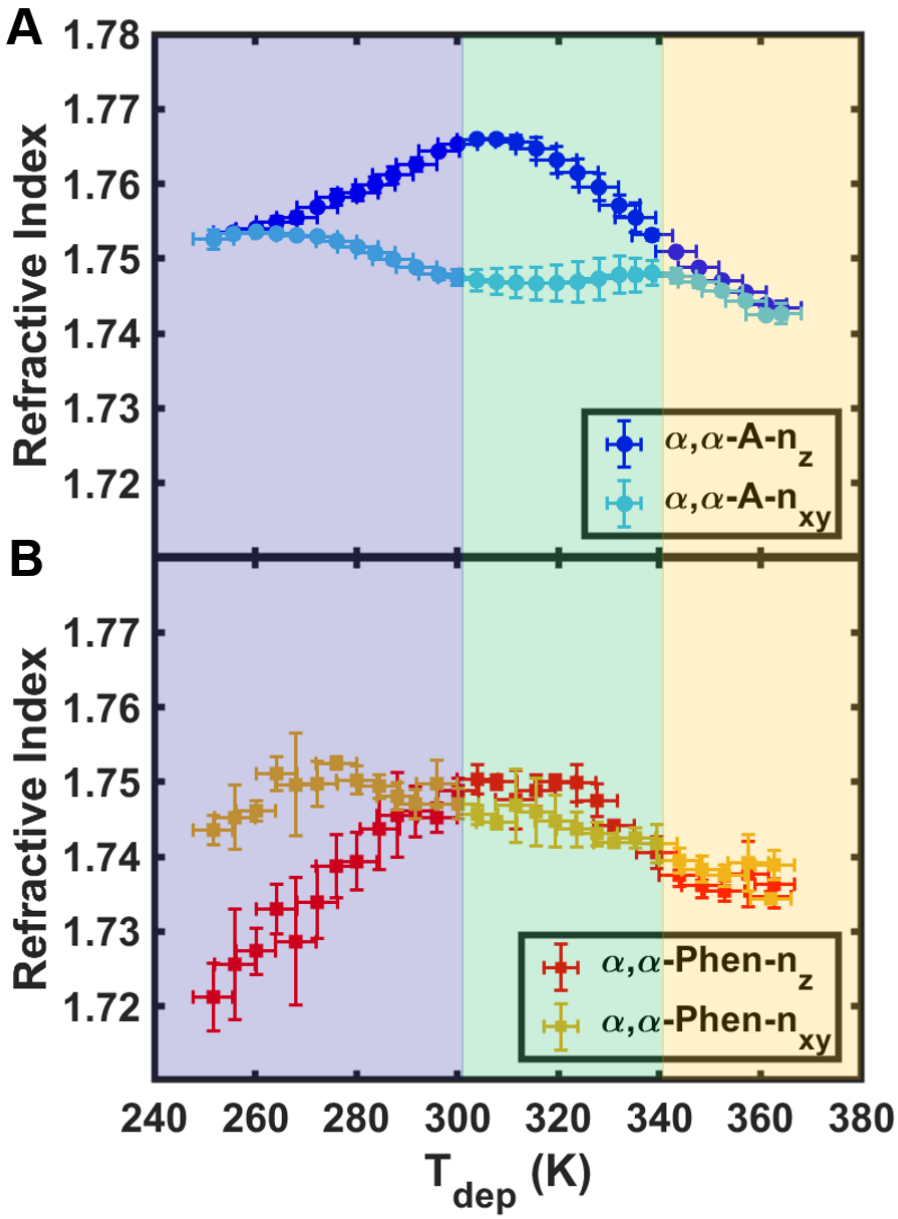

Figure 5.10: (A)/(B) Out-of-plane (n_z, solid blue circle/red square) and in-plane (n_{xy}, empty blue circle/red square) index of refraction at $\lambda = 632.8$ nm for α,α-A/α,α-Phen PVD glasses with thicknesses between 150 to 240 nm as a function of deposition temperature. Data are measured on temperature gradient samples. The error bars are calculated as explained in Experimental Details section.

Figure 5.9&5.10 show the indices of refraction measured on α,α-A and α,α-Phen SGs for 1-micron and ~200 nm films, respectively. The indices collected on 1-micron-thick samples

and ∼240 nm-thick samples are qualitatively similar. However, thinner α,α-A PVD glass shows positive birefringence in a broader T_{dep} range. In the orange region where 340 K $< T_{dep} <$ 368 K, both α,α-A and α,α-Phen SGs are isotropic, with $n_{xy} = n_z$. Within the temperature range between 300 K to 340 K (green region), α,α-A SG has a much larger n_z compared to n_{xy}. Because there is no molecular orientation detected in α,α-A SGs, birefringence in α,α-A SGs are attributed to a closer packing in z direction[129]. When T_{dep} is lower than 300 K, α,α-A SGs gradually become isotropic again (purple region). As for α,α-Phen SGs, their optical birefringence is in general less prominent than α,α-A SGs, with a turning point from positive to negative birefringence around 300 K, and their optical birefringence becomes strongly negative at lower T_{dep}. Negative birefringence is usually found in SGs that adopts in-plane molecular orientation at low T_{dep}s[10, 233]. Since α,α-Phen is a ellipsoid-shape molecule with a small aspect ratio, we hypothesis the -Phen moiety could potentially be aligned in parallel to the substrate at low T_{dep}s, due to the constraints at free surface. Some evidences of this in-plane packing can be found in Figure 5.5D ($T_{dep} = 251 \pm 4$ K), which has a different scattering intensity between xy and z directions at $q \sim 1.6\mathring{A}$. Meanwhile, the same peak appear to be isotropic in Figure 5.5E&F ($T_{dep} = 298 \pm 4$ K and 365±4 K). The molecular orientation (or substituent orientation) inα,α-Phen PVD glasses requires more investigation in the future.

5.4.2. GIWAXS Characterization of α,α-A and α,α-Phen PVD Glasses

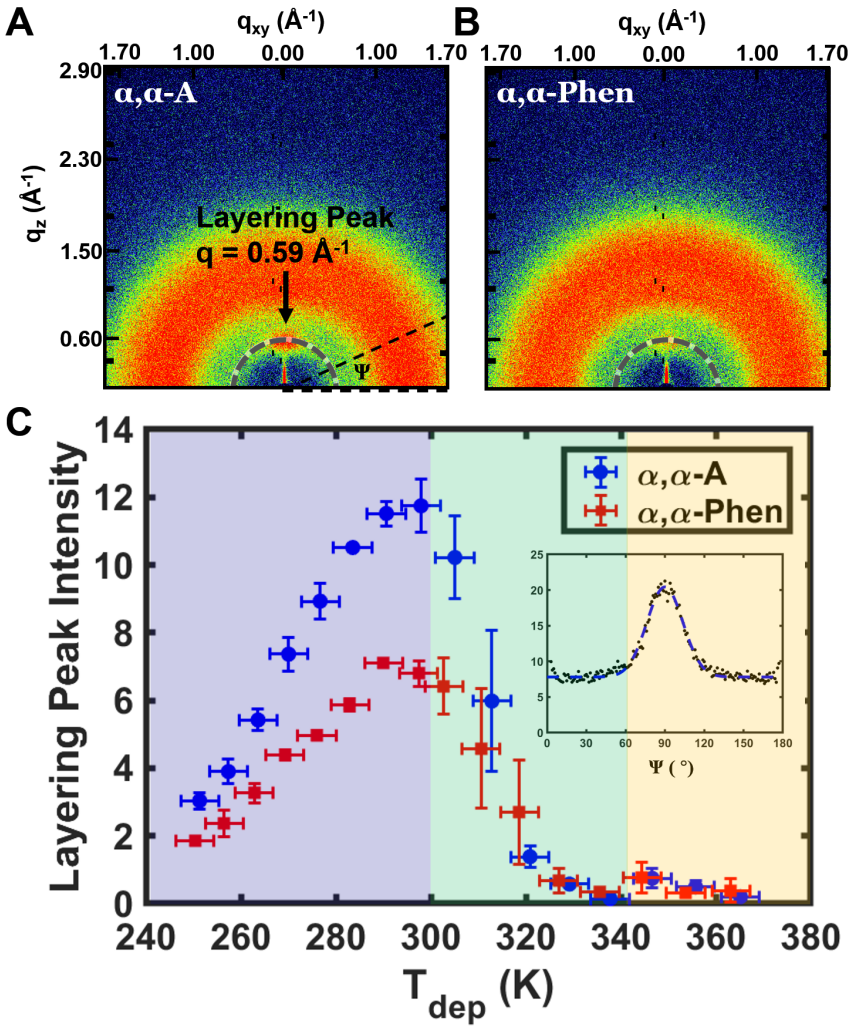

Figure 5.11: (A)/(B) 2D GIWAXS patterns for a 1-micron-thick α,α-A/α,α-Phen SG sample deposited at the temperature where the maximum layering peak intensity is measured. The deposition temperature of α,α-A SG sample is T_{dep}= 298±2 K. And the deposition temperature of α,α-Phen SG sample is T_{dep}= 289±2 K. These two images are displayed under the same color scale. It is clear to see that α,α-A SG has a larger maximum layering intensity than α,α-Phen SG. The variable, azimuthal integration angle Ψ, is defined as the angle between the bottom right of the detection limit and the line of integration, as indicated in (A). The dashed arc in (A)/(B) is the area where the intensity of layering peak is integrated as a function of Ψ, within the region of $q = 0.59\pm0.03$ Å^{-1}. (C) Layering peak intensity of α,α-A and α,α-Phen SGs calculated in the way shown in the inset as a function of deposition temperature. The intensity here are normalized by the background scattering intensity (the baseline of the Gaussian curve). Data are measured on temperature gradient samples. The error bars are calculated as explained in Experimental Details section.

Similar to what is reported previously on other organic SG systems, α,α-A and α,α-Phen SGs exhibit both packing anisotropy and molecular layering. The packing anisotropy is characterized by the difference in scattering intensity between in-plane integration and out-of-plane integration around $q \sim$ 1 - 1.7 Å^{-1} (0.37 - 0.63 nm), as what can be seen from Figure 5.4&5.5. In terms of α,α-A, its packing anisotropy appears to be the most prominent when 285 K $< T_{dep} <$ 315 K, with a higher scattering intensity in xy direction. Since there was no molecular orientation detected in α,α-A SGs, as what has been reported earlier[129], the higher scattering intensity in xy direction may indicate a more regular in-plane packing than out-of-plane. While in α,α-Phen PVD glasses, between 250 K $< T_{dep} <$ 300 K, the integrated out-of-plane scattering intensity is larger at the peak around $q \sim$ 1.5 Å^{-1} ($\sim$ 0.42 nm).

In both α,α-A and α,α-Phen SGs, a distinct layering peak can be observed in z direction, at $q_z = 0.59$ Å^{-1} (see Figure 5.11A&B), within the purple and green regions (T_{dep} <340 K). $q_z = 0.59$ Å^{-1} corresponds to the distance measured across α,α-A or α,α-Phen optimized molecular structure obtained by DFT ($\sim$1.2 - 1.4 nm, Figure 5.6). The intensity of this layering peak is shown to vary as T_{dep} changes along the gradient sample (Figure 5.11 C).

Besides the T_{dep} dependence of the layering peak intensity, SGs formed by the two molecules also exhibit different extent of layering. Figure 5.11A&B plot the 2D scattering patterns for α,α-A and α,α-Phen PVD glasses deposited at the temperatures where the maximum layering peak intensity are detected, respectively. It can be seen that α,α-A has a higher tendency to form layered structure compared to α,α-Phen, with a stronger layering peak. The magnitudes of the Gaussian curves obtained by fitting the accumulated scattering intensity between $q = 0.56$ Å^{-1} to 0.62 Å^{-1} at different T_{dep} are plotted in Figure 5.11C, where the inset shows an example of the accumulated scattering intensity plotted in the range of $0° < \Psi < 180°$ for α,α-A SG displayed in Figure 5.11 A, with the dashed curve in the plot indicating the fitting. As can be seen from Figure 5.11 C, when T_{dep} is above 340 K (orange region), there is no evidence of layering for both α,α-A and α,α-Phen PVD

glasses. As T_{dep} is decreased below 340 K, layering grows. The maximum layering intensity is measured at T_{dep}= 289±2 K for α,α-Phen, and at T_{dep}= 298±2 K for α,α-A, with its peak intensity being almost twice as much as what is measured in α,α-Phen PVD glasses.

5.4.3. α,α-A Exhibits Slower Surface Relaxation Than α,α-Phen

In order to understand the differences between α,α-A and α,α-Phen PVD glasses in terms of optical and packing anisotropy, as well as their ability to form SGs, we need to understand their surface relaxation and EL structures. While direct measurements of surface mobility are beyond this study, indirect data can be obtained from dewetting experiments, similar to our previous works[188]. It has been demonstrated previously that the characteristic time derived from isothermal dewetting experiments can be used as a measurement of thin film relaxation, which in turn provides an estimate of surface mobility and the range of mobility gradient[254].

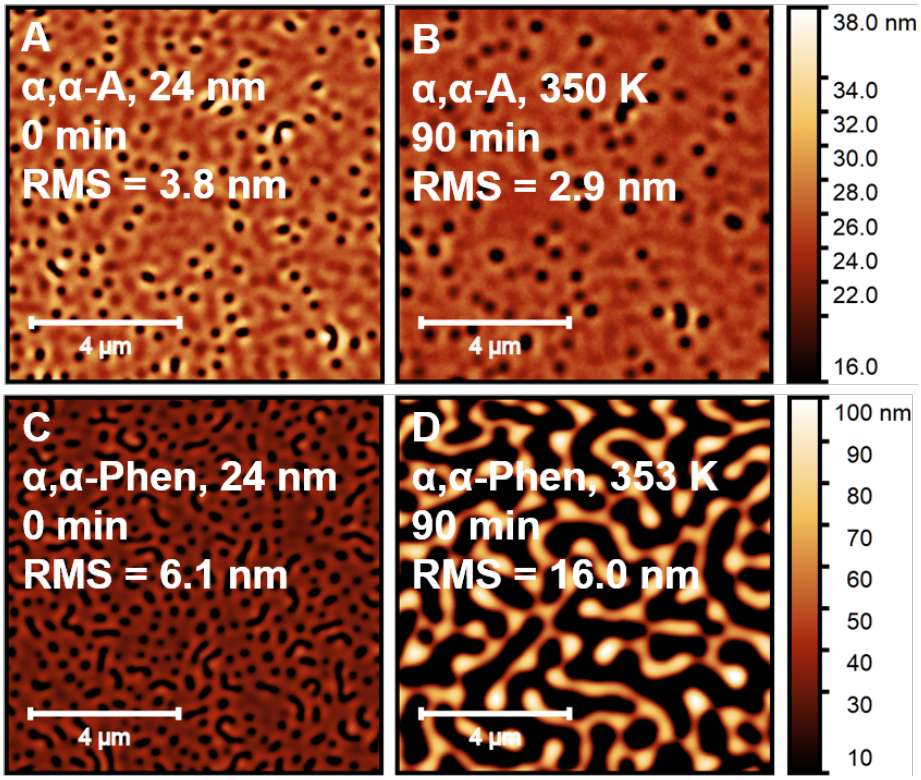

Figure 5.12: (A)/(C) Initial Atomic Force Microscopy (AFM) morphology of a 24 nm α,α-A/ α,α-Phen film deposited at its T_g (364 K for α,α-A and 366 K for α,α-Phen). (B)/(D) AFM Morphology of the same area after 90 min of isothermal annealing at $0.92T_g$ (350 K for α,α-A and 353 K for α,α-Phen). Grain wise mean square roughness (RMS) is labeled in each figure.

When α,α-A and α,α-Phen thin films with the same thickness are deposited at T_g, α,α-A thin films appear smoother than α,α-Phen thin films (Figure 5.12A&B) and have a smaller dewetted area (exposed substrate). When the two partially dewetted films are annealed at a temperature just below T_g (T_{anneal} = 350 K for α,α-A and 353 K for α,α-Phen), as can be seen from Figure 5.12C&D, the surface morphology of a 24 nm α,α-A thin film barely changes after a 90 min of annealing, while in contrast, the dewetted area on a α,α-Phen thin film grows rapidly and the film roughness increases drastically after the same annealing period. The results here suggest that, on average, a 24 nm α,α-Phen film has larger mobility than a α,α-A film with the same thickness. Considering a previous report on a 10±1 nm α,α-A film exhibiting substantial mobility[188], and the observation that

24 nm as-deposited α,α-A films are smoother than α,α-Phen films, we conclude enhance relaxations still exist at α,α-A surface, but its depth of surface mobility gradients is very likely to be smaller than that of α,α-Phen[254].

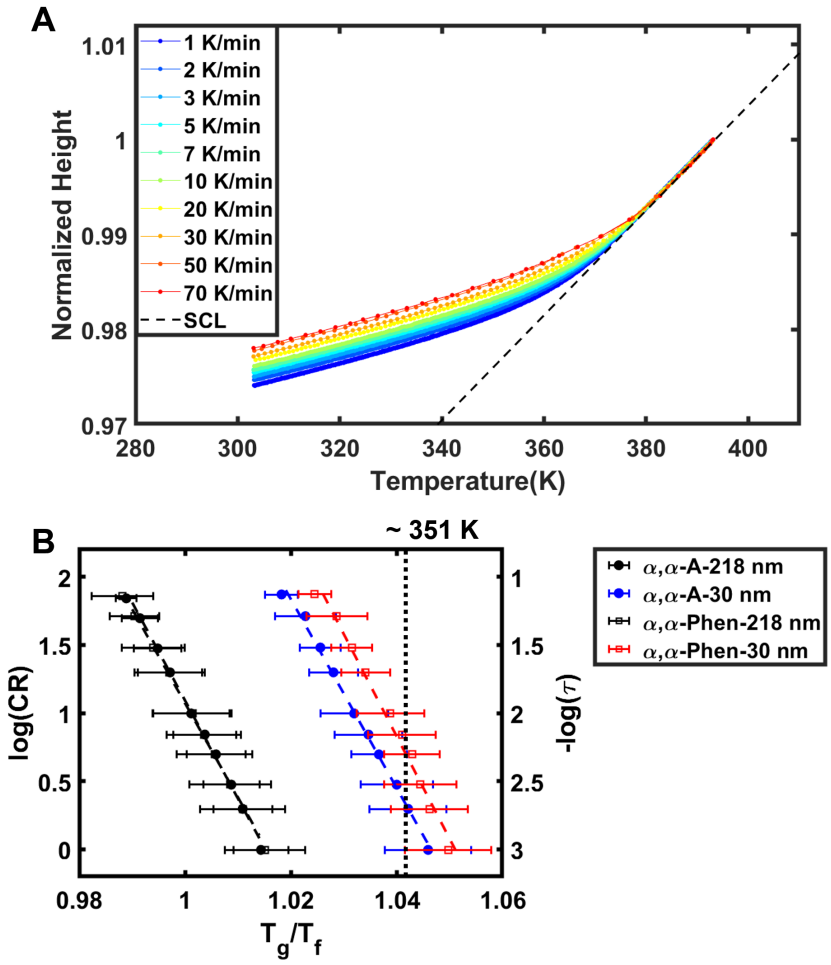

Figure 5.13: (A) An example of the cooling-rate-dependent-T_g ($\mathrm{CRT_g}$) experiment performed on 225 nm α,α-Phen film. 10 cooling rates are shown here. Film thicknesses are normalized at 393 K. Dashed line on the graph is a fitting to the SCL region. (B) log(cooling rate) (left axis) and extrapolated relaxation time (right axis) plotted against T_g/T_f for α,α-A and α,α-Phen films of thicknesses ~218 nm (black) and 30 nm (blue and red). T_g refers to the glass transition temperature of 218 nm (bulk) α,α-A and α,α-Phen film, respectively. T_f is the glass transition temperature obtained from cooling-rate-dependent-T_g ($\mathrm{CRT_g}$) experiment. Dashed lines represent the fitting to experimental data points using the equation shown on bottom right, which is the definition of fragility m. Dotted line on the graph indicates at which temperature the dewetting experiments are performed approximately.

To further validate these conclusions, cooling-rate-dependent-T_g ($\mathrm{CRT_g}$) experiments were also performed[127, 254, 70]. Full sets of α,α-A and α,α-Phen $\mathrm{CRT_g}$ data on a collection of films with different thicknesses can be found in Supplementary Information section 5.6.4, while only the thinnest and thickest films measured are plotted in Figure 5.13. From Figure 5.13, we notice the bulk α,α-A and α,α-Phen films show similar behavior as the cooling rate is varied. While for 30 nm films, even though their fragility remain the same, the curves are shifted to lower T_g value, indicating that thinner films have smaller glass transition temperature. If we compare the thin film relaxation times ($\tau_\alpha \propto \frac{1}{\mathrm{CR}}$) at the temperature where dewetting experiments were conducted (dotted line in Figure 5.13), we see that α,α-A thin films indeed have slower averaged relaxation times (shown by higher T_g value) than α,α-Phen, which agrees with our deduction from dewetting experiments.

5.4.4. Discussions

Molecular layering has been observed previously in many vapor deposited glasses. For rod-like molecules, smectic liquid crystal-like structures were reported under specific deposition conditions. The GIWAXS pattern for these smectic liquid crystal-like structures were featured with a broad anisotropic peak on q_{xy} direction between 1.2 - 1.5 $\mathrm{Å}^{-1}$, originated from the intermolecular distancing between aligned molecules, and one isolated peak (or several separate peaks) on q_z direction at $q_z < 1$ $\mathrm{Å}^{-1}$, which correlates to the length (or integer multiples of the length) of the deposited molecules[75, 21, 22]. Moreover, in a sphere-like molecular system, this layering peak was also detected, while no other anisotropic peaks were observed in their GIWAXS patterns[9].

In this study, we observed a slight structural anisotropy and difference in the intensity of molecular layering between α,α-A and α,α-Phen SGs. These effects have strong T_{dep} dependence. When looking at the T_{dep} dependence of molecular layering and index of refraction together, we find lots of similarities. Since we have confirmed there is no preferred molecular orientations in α,α-A PVD glass down to T_{dep} ~260 K in our previous publication[129], and we have more understanding on α,α-A surface relaxation[188], it is easier to start from

α, α-A PVD glass, to understand the process of vapor deposition and the origin of layering.

As illustrated above, when T_{dep} decreases from T_g, the intensity of layering peak goes through three regimes. When 340 K $< T_{dep} <$ 368 K, there is no significant layering detected. We observe an increase in the layering intensity between 300 K $< T_{dep} <$ 340 K, followed by a decrease after it reaches a maximum at T_{dep} ~300 K. The three regimes are color-coded differently in Figure 5.11. Correspondingly, the indices of refraction of α, α-A PVD glass can be divided into three regimes too. Within the range of 340 K $< T_{dep} <$ 360 K, $n_{xy} = n_z$, there is no optical birefringence. n_z starts to increase when $T_{dep} <$ 340 K and reaches a maximum at T_{dep} ~300 K, while n_{xy} remains almost constant. Below T_{dep} ~300 K, n_z decreases and α, α-A SGs become isotropic again.

We note that when placed in an external electrical field and only linear response is invoked, the relative permittivity of a dielectric can be related to the polarizability of its molecular components via Clausius-Mossotti relationship[186]. Moreover, if the dielectric is deformed geometrically in its lattice packing, a correction to the local field, which is resulted from the long-range effects from the asymmetric packing, should be applied based on the lattice distortion[130]. In our case, α, α-A molecules have induced dipole moments under external electrical field. Given the fact that there is no molecular alignment in α, α-A PVD glasses[129], the polarizability of α, α-A molecules should be spatially uniform, and the structural anisotropy of within α, α-A PVD glass should be relatively small compared to the effect of layering.

A schematic diagram of the three T_{dep} regimes in deposition process is shown in Figure 5.14, when T_{dep} is close to T_g, between 340 K $< T_{dep} <$ 360 K for α, α-A SGs, the surface molecules have sufficient mobility and the depth of surface mobility gradient is relatively larger, on the order of several nanometers presumably (Figure 5.14(c)). Molecules within the fast relaxing surface region can optimize their configuration in directions both in parallel and perpendicular to the substrate simultaneously. For α, α-A SGs deposited in this T_{dep} range, their indices of refraction increase simultaneously in the in-plane and out-of-plane

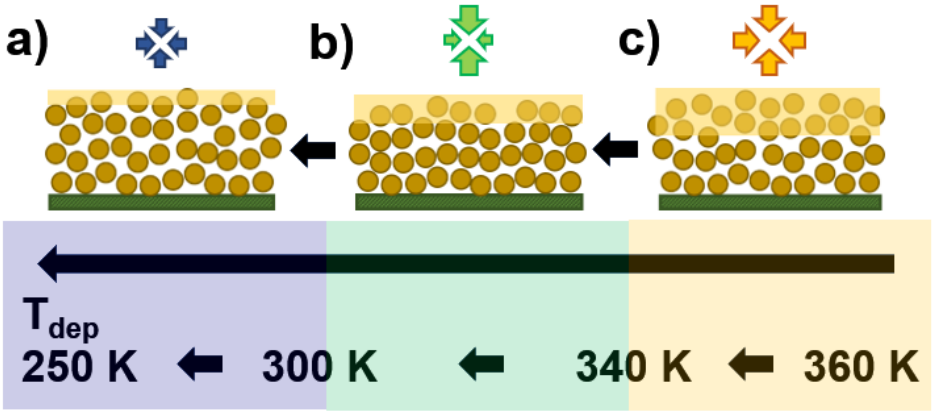

Figure 5.14: Schematic diagrams for the three deposition temperature regimes. As deposition temperature decreases, the molecules lose their in-plane and out-of-plane mobility consecutively and the surface mobile region on a glass shrinks.

directions and there is no signature of molecular layering, meaning the glasses are densified uniformly. The phenomenon observed here is also consistent with lower deposition rates yielding more isotropic glass[22]. In this regime, the density of α,α-A SGs increases rapidly as T_{dep} decreases.

When T_{dep} enters the second regime, between 300 K $< T_{dep} <$ 340 K, α,α-A molecules loss its diffusive mobility on top of the surface[188]. Meanwhile, the depth of surface mobility gradient reduces to be comparable with one or two molecular sizes. This inference was made based on the experiments done by Richert's group, where the depth of surface mobility gradient was measured to be 2.5 nm for 2-methyltetrahydrofuran around $0.82T_g$[220], which corresponds to ~300 K in the case of α,α-A(Figure 5.14(b)). Equilibrating in the out-of-plane direction is more accessible in this regime compared to in-plane diffusion, accounting for the different behaviors between n_z and n_{xy} in α,α-A SGs. The deposited glass ended up to be denser in z direction than in xy direction, following the aforementioned Clausius-Mossotti relationship. The differentiation in packing efficiency also gives rise to the molecular layering. Layering happens because the molecules are encountering confinement in xy direction but more freedom localized in z.

In the third regime, which is the kinetically arrested regime, 250 K $< T_{dep} <$ 300 K, as soon as the molecules arrived at the deposited glass surface, they are trapped in both in-plane and out-of-plane directions (Figure 5.14(a)). This is because the relaxation time of α,α-A molecules becomes so long that the time allowed for the molecules to equilibrate is not sufficient, given that the depth of surface mobility gradient shrinks to the size of one molecules (or smaller) at very low T_{dep}s[220]. As a result, the differences between the in-plane and out-of-plane indices of refraction are diminished, glasses become isotropic again with less layering. $\Delta\rho$ of α,α-A SGs formed in this T_{dep} region is smaller than what are formed in the second regime where the molecules on surface are less kinetically trapped.

How α,α-Phen molecule being different from α,α-A is on a substituent attached to the diarylbenzene moiety. Based on a discrete stepped Density-functional Theory (DFT) calculation, the rotation barrier in α,α-A molecule is estimated to be ∼30 kcal/mol (∼50 kT), while the rotation barrier for α,α-Phen molecule is only ∼13 kcal/mol (∼22 kT, Figure 5.7). At room temperature, the Phen–diarylbenzene bond is able to rotate almost freely but the A–diarylbenzene bond has quite a small dihedral angle range to vibrate (Figure 5.6). The constraint placed by the rotation barrier of a single substituent has induced a dramatic decrease of the configurations that can be adopted by α,α-A molecule during the equilibration process, which places barriers for α,α-A's surface relaxation, accounting for the slowing down of α,α-A thin film mobility, as confirmed by the dewetting and $\mathrm{CRT_g}$ experiments.

The differences between the anisotropy of α,α-A and α,α-Phen SGs are originated from the differences in their surface relaxation times and the depth of surface mobility gradient, as well as their molecular shapes. Due to the faster relaxation within α,α-Phen top surface layers and larger penetration depth of its surface mobility gradient, which allow the molecules to equilibrate better upon vapor deposition, α,α-Phen glasses have smaller optical birefringence and less prominent layering peak, compared to α,α-A glasses deposited under the same condition. Earlier works demonstrated by lowering the deposition rate,

molecules on the surface can end up with a more isotropic packing at low T_{dep}s[22]. What we presented here is that a small variation in molecular structure can have the same result as changing the deposition rate by orders of magnitude.

5.5. Summary and Outlook

Previous studies on SGs' structures and properties were mainly focused on the influence of molecular shape (rod-like, disc-like and sphere-like) and the presence of certain functional groups (hydroxyl group and halo group). In this work, we investigated the role of intra-molecular degrees of freedom in SG formation by looking into two carefully designed molecules which have the same molecular weight but a little variation on their chemical structures. The anthracene group on the diarylbenzene moiety in α,α-A molecule has created a much larger rotation barrier compared to the phenanthrene-diarylbenzene combination in α,α-Phen, which results in a reduction in its accessible configurations during equilibration. The loss in α,α-A's configurational entropy slows down α,α-A's surface relaxation and reduces its depth of surface mobility gradient, which consequently generates glasses with smaller optical birefringence and structural anisotropy, compared to α,α-Phen. Taking advantage of a custom-built temperature gradient setup, we are able to produce and characterize samples with a 120 K temperature difference across efficiently and reliably. When considering the SE (optical) and GIWAXS (structural) results together, we conclude that there are three regimes where the molecules have different strength of relaxations in-plane and out-of-plane in the PVD process while T_{dep} is decreased from T_g to T_g - 120 K.

We take α,α-A SGs as an example to illustrate the three T_{dep} regimes and define T_{dep} $\sim$340 K and $\sim$300 K to be the temperatures when α,α-A molecules loss their in-plane and out-of-plane mobility on the glass surface consecutively. α,α-A's out-of-plane motion shows weaker temperature dependence because it has more freedom than the confined in-plane mobility. Additionally, the depth of surface mobility gradient becomes shallower when T_{dep} decreases, as shown by previous reports[160, 220]. Layered structure forms in vapor deposited glass

when the depth of surface mobility gradient is about one or two molecule sizes and when there is asymmetric reduction of the in-plane and out-of-plane molecular mobility within the surface layer. The formation of layering, densification in z direction and positive optical birefringence in α,α-A SGs are self-consistent via Clausius-Mossotti relationship. The case of α,α-Phen SGs is similar to α,α-A except that their more feasible intra-molecular relaxation allows less deviation between their in-plane and out-of-plane molecular relaxation when T_{dep} decreases, which results in smaller optical birefringence and molecular layering in α,α-Phen PVD glasses. Additionally, as α,α-Phen being an ellipsoid-shaped molecule, it is likely to adopt in-plane orientation, decided by surface constraints, resulting in negative optical birefringence at low T_{dep}s. Despite the extensive research we performed here, question remains why α,α-A PVD glass has higher $\Delta\rho$ in the kinetically trapped regime, which may be hypothetically related to the sub-surface rearrangement during deposition, which is easier within α,α-Phen surface layers, given their high mobility. The existence of sub-surface rearrangement has been observed through both simulations[148] and experiments[220]. More direct evidences can be provided by *in-situ* ellipsometry measurement while depositing in the future.

5.6. Supplementary Information

5.6.1. Synthesis and Characterization of the Compounds Used in This Study

The two compounds used in this study were synthesized using the Suzuki cross-coupling method. The synthesis and characterization of 9-(3,5-di(naphthalen-1-yl)phenyl)anthracene (α,α-A) was reported in our previous publication[127]. To synthesize 9-(3,5-di(naphthalen-1-yl)phenyl)phenanthrene (α,α-Phen), 9-Phenanthracenylboronic acid (Sigma-Aldrich) was used instead of 9-Anthraceneboronic acid (Sigma-Aldrich) in the standard synthesis route.

Synthesis and NMR Characterization of α,α*-Phen* 1,1'-(5-Chloro-1,3-phenylene)dinaphthalene (0.547 g, 1.5 mmol, 1.0 equiv), 9-Phenanthracenylboronic acid (0.533 g, 2.4 mmol, 1.6 equiv), $Pd(OAc)_2$ (15 mg, 0.067 mmol, 2.5 mol %), DavePhos (54 mg, 0.137 mmol, 5 mol %), K_3PO_4 (0.64 g, 3.0 mmol, 2.0 equiv), THF (7.5 mL), and H_2O (1.50 mL) were added in

a dry round bottom flask equipped with a stir bar under nitrogen atmosphere. The reaction was completed after 10 h at 333 K. After the mixture was cooled to room temperature, the organic and aqueous layers were separated, and the aqueous layer was extracted with ethyl acetate three times. Then organic layers were combined, including the reaction mixture and extractions, dried over $MgSO_4$ and concentrated. And the residue was chromatographed on silica gel using hexanes to afford α,α-Phen in 60% yield (0.45 g, 0.9 mmol).

^{1}H and ^{13}C NMR characterization of α,α-Phen in $CDCl_3$: ^{1}H NMR ($\Psi\Delta\Psi\lambda_3$, 500 MHζ): δ 8.80 (δ, Ξ = 8.0 Hζ, 1H), 8.73 (δ, Ξ = 8.5 Hζ, 1H), 8.26-8.22 (μ, 3H), 7.94-7.92 (μ, 3H), 7.90 (σ, 1H), 7.89 (δ, Ξ = 7.0 Hζ, 2H), 7.82 (δ, Ξ = 2.0 Hζ, 2H), 7.79 (τ, Ξ = 2.0 Hζ, 1H), 7.71-7.62 (μ, 6H), 7.62 (τ, Ξ = 5.0 Hζ, 1.5 Hζ, 2H), 7.61-7.60 (μ, 4H). ^{13}C{H} NMR ($CDCl_3$, 125 MHz): δ 141.1, 140.0, 138.6, 134.2, 131.8, 131.3, 131.0, 131.0, 130.9, 130.3, 128.9, 128.6, 128.2, 128.1, 127.5, 127.1, 126.9, 126.9, 126.8, 126.5, 126.2, 126.1, 125.7, 123.2, 122.8 (Some peaks are overlapped due to similar chemical shifts). The data is shown in Figure 5.15

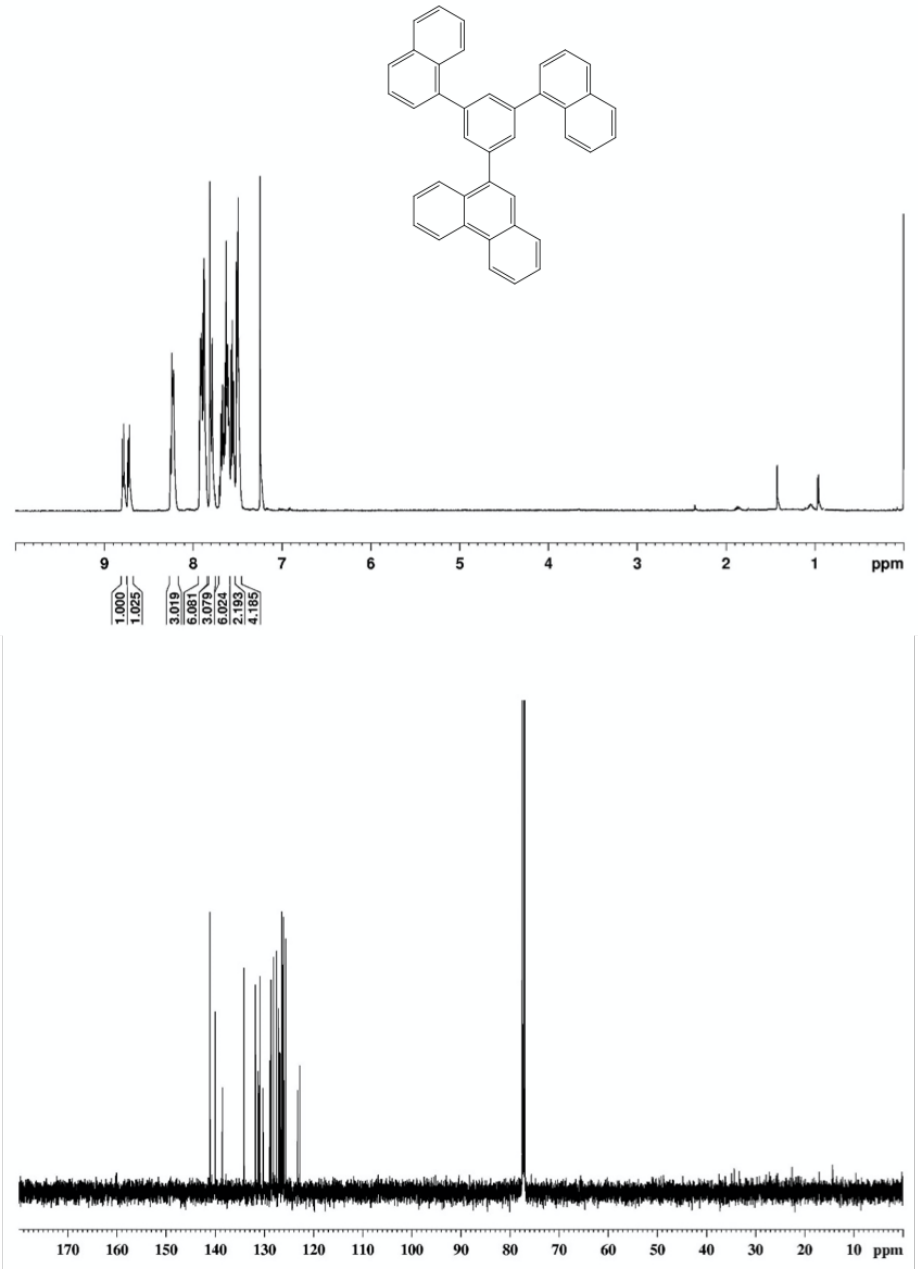

Figure 5.15: ^{1}H and ^{13}C NMR spectra of α,α-Phen in $CDCl_3$.

The glass transition temperatures (T_gs) of α,α-A and α,α-Phen were measured using *in-situ* Spectroscopic Ellipsometry (SE) upon cooling, after transformation from the as deposited state. The cooling curve of the liquid quenched (LQ) states of the two compounds can be found in Figure 5.7. Cooling rates were kept at 10 K/min. By fitting lines to the

cooling curves between 383 K to 393 K for the super-cooled liquid region (SCL) and 310 K to 330 K for the glass region (GL), T_gs were determined to be $T_{g,A} = 364 \pm 1$ K and $T_{g,Phen} = 366 \pm 1$ K. When normalized to the thicknesses at 393 K, the thermal expansion coefficients (α) for α,α-A were determined as $\alpha_{SCL,A} = (5.6 \pm 0.1) \times 10^{-4}$ K^{-1} and $\alpha_{GL,A} = (1.4 \pm 0.1) \times 10^{-4}$ K^{-1}. For α,α-Phen, these values were determined as $\alpha_{SCL,Phen} = (5.5 \pm 0.05) \times 10^{-4}$ K^{-1} and $\alpha_{GL,Phen} = (1.4 \pm 0.05) \times 10^{-4}$ K^{-1}.

5.6.2. Validation of Temperature Determination Along T-grad Samples

Since we applied no correction to endpoint temperature when making T-grad samples, in order to validate the temperatures calculated on T-grad samples, N,N'-Bis(3-methylphenyl)-N,N'-diphenylbenzidine (TPD) PVD glasses with different ranges of T_{dep} maintained across the gradient were made. Figure 5.16 shows the optical birefringence (difference between out-of-plane and in-plane indices of refraction) as a function of T_{dep} collected on three independent samples, which overlapped pretty well when considering the error in location determination. The birefringence values we measured are also consistent with the previous reports for this molecule[75]. When considering the error in location determination and temperature measurement, we decided our uncertainty in calculating T_{dep} to be 4 K.

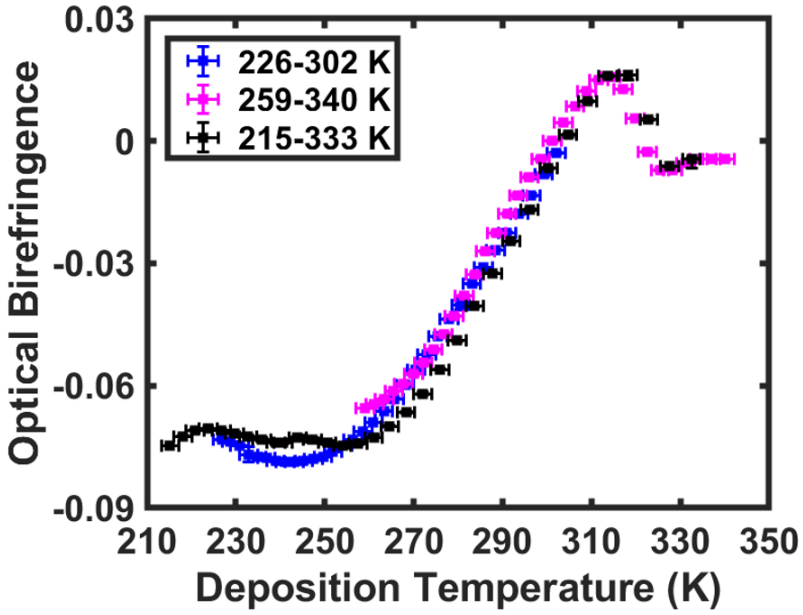

Figure 5.16: Optical birefringence of three TPD (chemical structure shown in the inset) PVD T-grad samples deposited with different temperature spans.

5.6.3. Supplementary Data for Thin Film Dewetting Experiments

Besides what is shown in the Result and Discussion section, the temperature dependence of characteristic dewetting time for 24 nm α,α-Phen thin film is measured. Figure 5.17A&B shows the initial and final surface topography of a 24 nm α,α-Phen film dewetted at 343 K for 1337 min. A 25% height threshold is applied when extrapolating the dewetted area ($A(t)$) at time t(s). Then the dewetted area is fitted with an empirical equation to get characteristic dewetting time τ_{dewet}:

$$A(t) - A(0) = A(\infty)(1 - \exp(-t/\tau_{dewet})), \tag{5.9}$$

with $A(0)$ being the initial dewetted area and $A(\infty)$ being the equilibrium value[254] (Figure 5.17C). τ_{dewet} for 24 nm α,α-Phen films dewetted at different temperatures from 333 K to

358 K are plotted in Figure 5.17D, and subsequently fitted with:

$$\log(\tau_{dewet}) = \frac{E_{a,dewet}}{1000k_B}\frac{1000}{T} + \log A. \tag{5.10}$$

The apparent activation energy $E_{a,dewet}$ for a 24 nm α,α-Phen thin film dewetting is determined to be 49±8 kJ/mol.

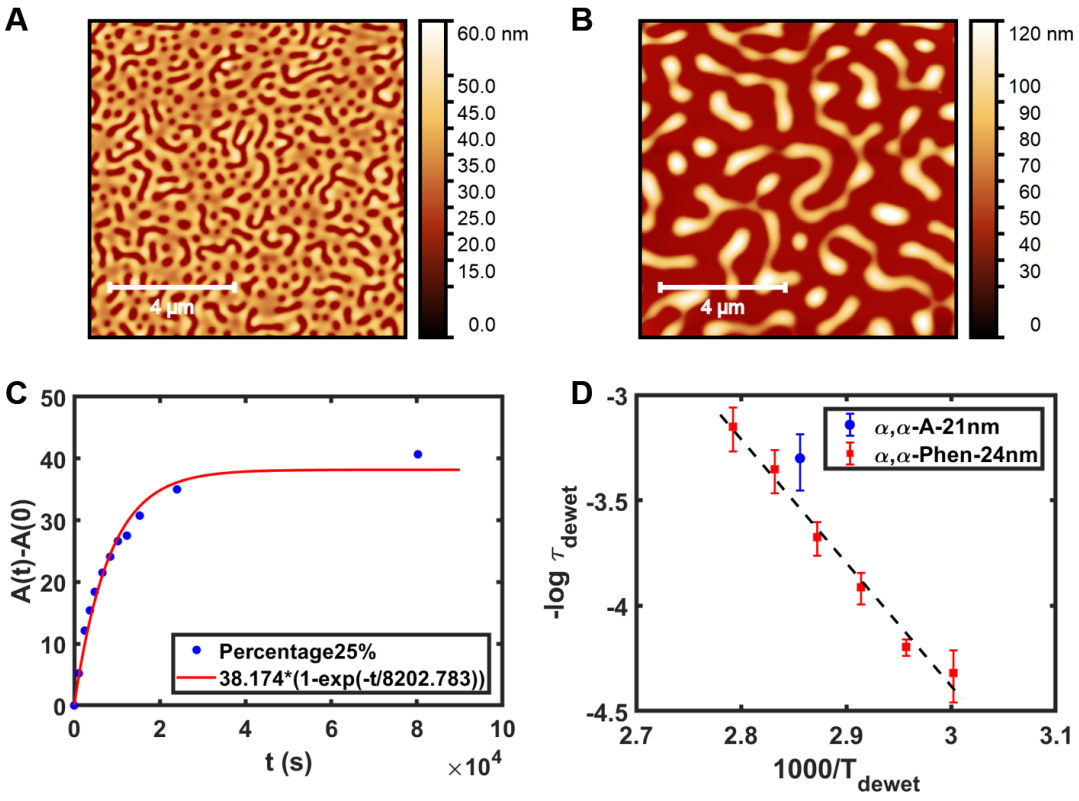

Figure 5.17: (A) Initial topography of a 24 nm α,α-Phen film deposited at T_g = 366 K with a 25% height threshold applied. (B) Surface topography of the same area as (A) after 1337 min annealing at 343 K with a 25% height threshold applied. (C) Example of a fitting to the dewetting profile. Red solid line indicates the fitting to determine characteristic dewetting time, which is τ_{dewet} = 8203 s for a 24 nm α,α-Phen film dewetting at 343 K. (D) -log (characteristic dewetting time) plotted against 1000/(dewetting temperature) for 24 nm α,α-Phen and 21 nm α,α-A thin films. The apparent activation energy can be derived by linear fitting of this plot. Error bars come from the uncertainty when fitting dewetting profiles.

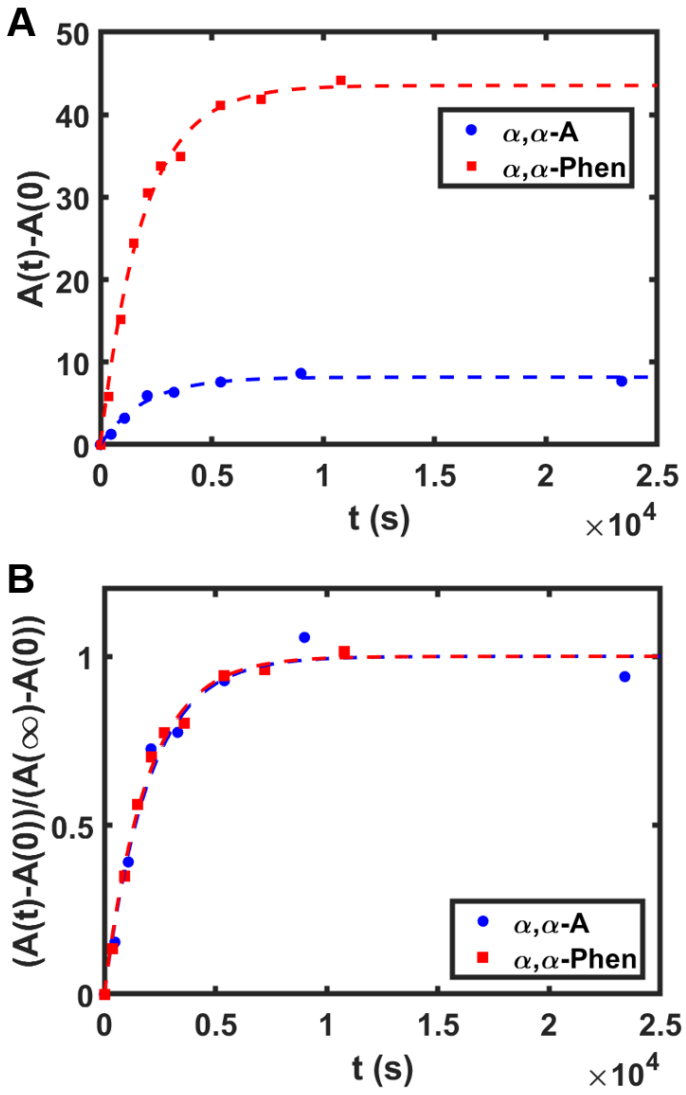

Figure 5.18: (A) Dewetting profiles $(A(t) - A(0))$ for a 21 nm α,α-A film dewetted at 350 K and a 24 nm α,α-Phen film dewetted at 353 K. (B) Normalized dewetting profiles against $(A(\infty) - A(0))$ for the same sets of data in (A).

As for α,α-A thin films, even though it was shown in the Result and Discussion section (Figure 5.12) that 24 nm α,α-A film surface topography evolved super slowly when annealed at 350 K ($0.96T_g$), a slightly thinner film, 21 nm, did show some fluidity when dewetted at the same temperature. The dewetting profiles of a 21 nm α,α-A film dewetted at 350 K and a 24 nm α,α-Phen film dewetted at 353 K are plotted together in Figure 5.18. And

they appear to have very similar τ_{dewet}, which can be seen more clearly when they are normalized against $(A(\infty) - A(0))$ in Figure 5.18B. We note that due to the limited data points collected for 21 nm α,α-A dewetting before it reached equilibrium value, the τ_{dewet} we calculated here is perhaps an upper bound. Nevertheless, the result here supports our statement that α,α-A indeed has enhanced surface mobility, but with a smaller length scale in terms of the depth of surface mobility gradient.

5.6.4. Supplementary Data for Cooling-rate-dependent-T_g Experiments

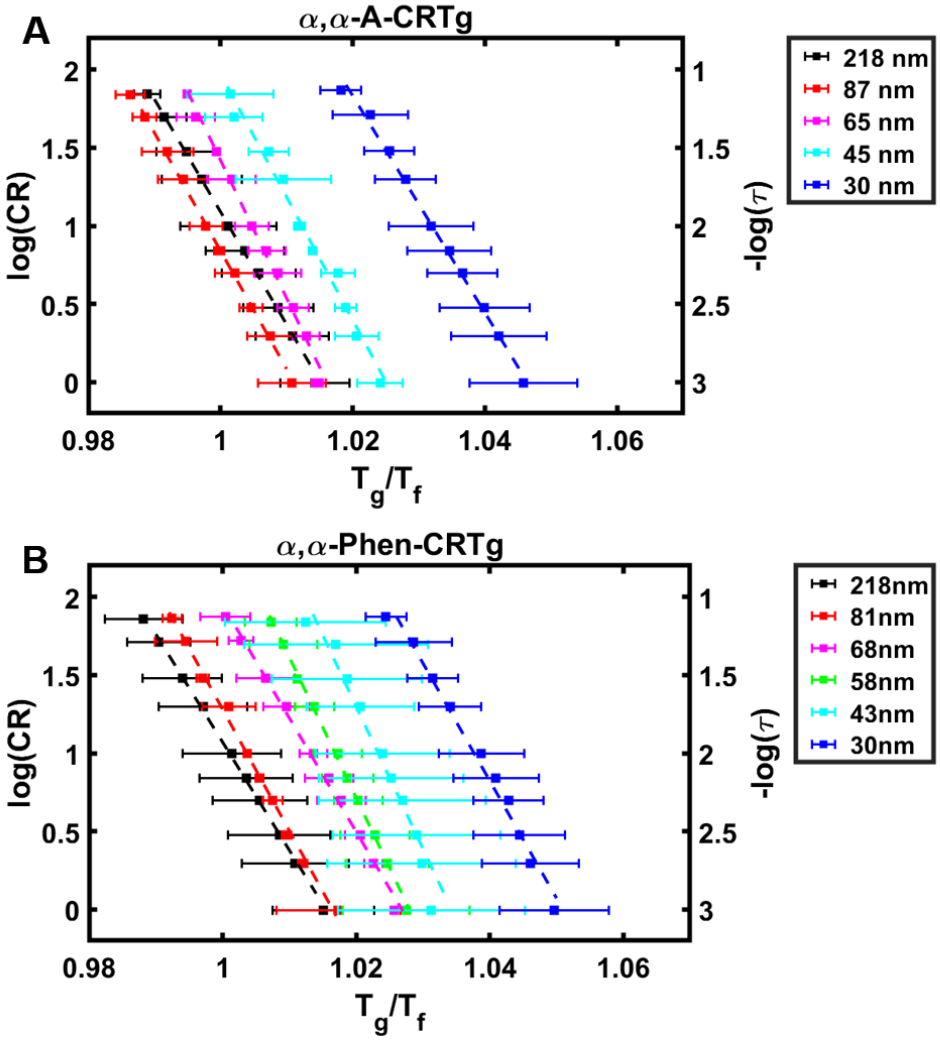

Figure 5.19:]
(A)/(B) log(cooling rate) (left axis) and extrapolated relaxation time (right axis) plotted against T_g/T_f for α,α-A/α,α-Phen films with different thicknesses between 218 nm to 30 nm. T_g refers to the glass transition temperature of 218 nm (bulk) α,α-A and α,α-Phen film, respectively. T_f is the glass transition temperature obtained from cooling-rate-dependent-T_g ($\mathrm{CRT_g}$) experiment. Dashed lines represent the fitting to experimental data points to calculate fragility m.

Cooling-rate-dependent-T_g experiments ($\mathrm{CRT_g}$) are conducted on a variety of α,α-A and α,α-Phen films with different thicknesses. The result is shown in Figure 5.19. Dashed lines

in the figure represent linear fitting to experimental data points to calculate fragility m:

$$m = \frac{\mathrm{d}\log\tau}{\mathrm{d}(T_g/T_f)} \simeq \frac{-\mathrm{d}\log(CR)}{\mathrm{d}(T_g/T_f)}. \tag{5.11}$$

Basically, the fragility of α,α-A and α,α-Phen films with different thicknesses are very similar as each other. All of them land within the range between $69 < m < 91$. No clear dependent on film thickness was observed, which is distinctly different from the previous reports on polymers and N,N'-Bis(3-methylphenyl)-N,N'-diphenylbenzidine (TPD) molecular glass[254, 70]. More experiments on thinner films are needed to explore the length scale for α,α-A and α,α-Phen fast surface dynamics, namely below what thickness the film fragility becomes thickness dependent.

5.6.5. Correlation Between Stable Glass Density and Averaged Indices of Refraction

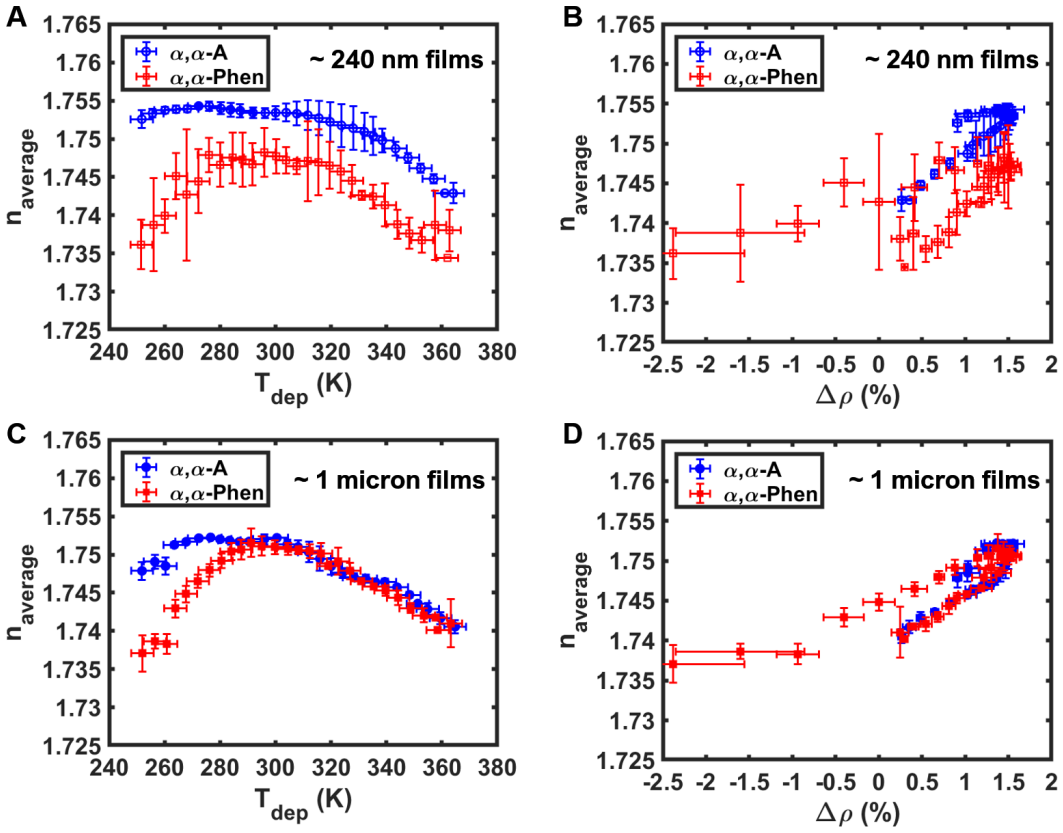

Figure 5.20: (A)/(C) Averaged indices of refraction ($n_{average}$) plotted against T_{dep} for ~240 nm/1 μm samples. (B)/(D) Correlation between the PVD glass $\Delta\rho$ measured on ~240 nm T-grad samples and the $n_{average}$ for ~240 nm/1 μm samples.

In Figure 5.20, we report the averaged indices of refraction ($n_{average}$) measured on α,α-A and α,α-Phen PVD glasses of different thicknesses. The $n_{average}$ was calculated as:

$$n_{average} = \left(\frac{{n_x}^2 + {n_y}^2 + {n_z}^2}{3}\right)^{1/2} = \left(\frac{{n_{xy}}^2 \times 2 + {n_z}^2}{3}\right)^{1/2}. \tag{5.12}$$

$n_{average}$ can be viewed as a scale of averaged number density in PVD glasses. From Figure 5.20A&C, we notice the T_{dep} dependence of $n_{average}$ is very similar to that of $\Delta\rho$. The

correlation plot of $n_{average}$ and $\Delta\rho$ can be found in Figure 5.20B&D.

Comparing the absolute value of $n_{average}$ for α,α-A and α,α-Phen PVD glasses, we see for ~240 nm films, α,α-A's $n_{average}$ is systematically higher than α,α-Phen's, even for the glasses deposited close to T_g, indicating a higher number density, but it is not the case for ~1 μm films. Future studies are needed to understand the observations here, which may suggest some kind of sub-surface molecular rearrangement as the deposition continues.

5.6.6. α,α-A and α,α-Phen UV-Vis Absorption Spectra and Fluorescence Spectra

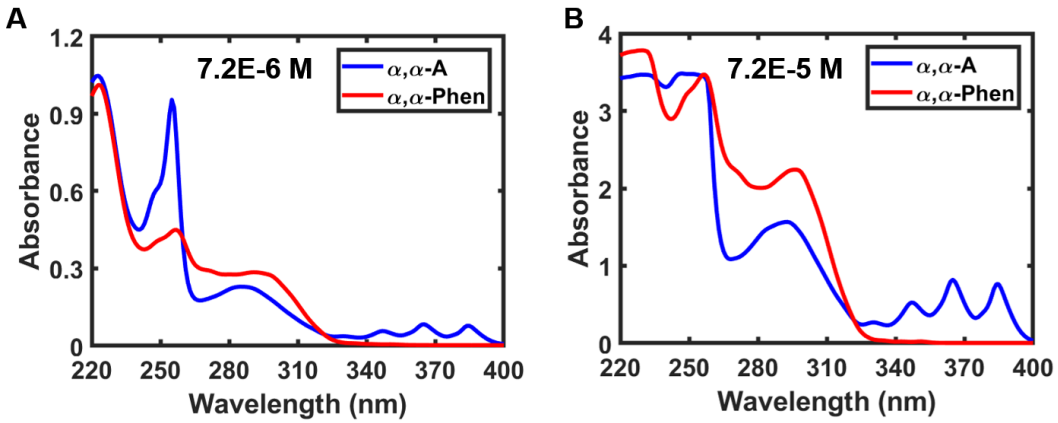

Figure 5.21: (A) UV-Vis absorption spectra of α,α-A (blue) and α,α-Phen (red) dissolved in n-hexane with a concentration of 7.2×10^{-6} M. (B) UV-Vis absorption spectra of α,α-A (blue) and α,α-Phen (red) dissolved in n-hexane with a concentration of 7.2×10^{-5} M. Absorbance value higher than 3 are not reliable due to the instrumental detection limit.

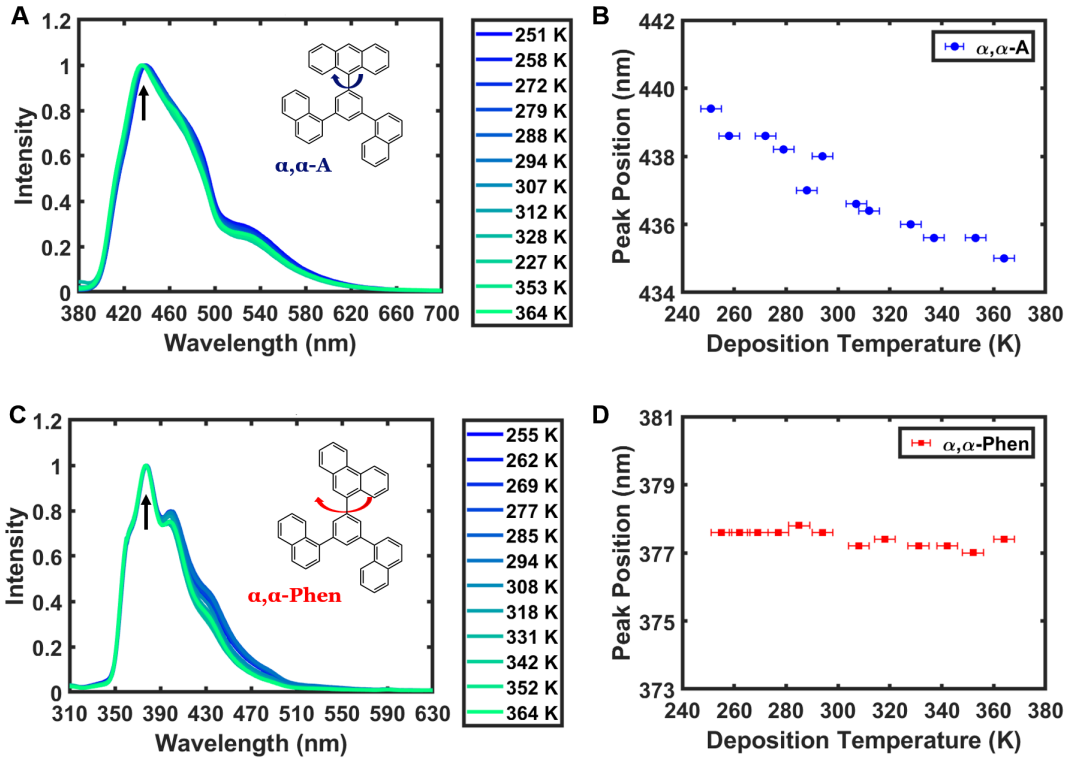

Figure 5.22: (A)/(C) Fluorescence spectra measured on α,α-A/α,α-Phen 1-micron SGs deposited at a series of deposition temperatures. Spectra are normalized by the largest emission intensity. Inset shows the molecule structure and the arrow is pointing at the largest emission peak whose position is plotted in (B)/(D). (B)/(D) Position of the largest emission peak in α,α-A/α,α-Phen Fluorescence spectra as a function of deposition temperature.

UV-Vis Absorption Spectra of α,α-A and α,α-Phen were measured at two solution concentrations (Figure 5.21). 0.00094±0.00001 g α,α-A/α,α-Phen was dissolved in 25.00 mL hexane (Fisher Scientific) to make a solution of 7.2×10^{-5} M. Then, 2.50 mL of the 7.2×10^{-5} M solution was diluted into 25.00 mL, to make a solution of 7.2×10^{-6} M. UV-Vis spectra were measured between 190 to 600 nm with a Jasco V-650 Spectrophotometer at a resolution of 1 nm. Absorbance value higher than 3 are not reliable due to the instrumental detection limit.

Fluorescence Spectra were collected on α,α-A and α,α-Phen 1-micron SG samples with

Jasco 8300 Spectroflurometer at 0.2 nm resolution. Excitation wavelength for α,α-A is 361 nm, while it is 295 nm for α,α-Phen. It can be seen from Figure 5.22B&D that the position of the largest emission peak shifted to lower wavelength as deposition temperature increases for α,α-A but stayed relatively constant for α,α-Phen, demonstrating a stronger $\pi-\pi$ interaction in α,α-A SGs at higher T_{dep}.

5.7. Acknowledgments

I acknowledge the use of the Dual Source and Environmental X-ray Scattering facility operated by the Laboratory for Research on the Structure of Matter at the University of Pennsylvania (NSF-MRSEC DMR-1720530) and Prof. Paul Heiney. The equipment purchase was made possible by an NSF MRI grant (17-25969), an ARO DURIP grant (W911NF-17-1-0282), and the University of Pennsylvania. Additionally, I would like to thank Dr. Mikhail Zhernenkov and Dr. Guillaume Freychet at Brookhaven National Lab for their kind assistance when we were collecting preliminary GIWAXS data for this work. More importantly, special thank is given to Haoqiang Zhao and Prof. Patrick J. Walsh for compound synthesis, Pengfei Jin and Prof. David M.Chenoweth for UV-Vis measurements, Sarah Wolf, Shivajee Govind and Dr. Yi Jin for maintenance of the deposition chamber, and Alex R. Moore and Prof. Zahra Fakhraai for valuable discussions.

CHAPTER 6: Experimental Data on the Effect of Inter-molecular Interaction on Stable Glass Properties and Structures

6.1. Abstract

This chapter describes the experiments studying the effect of inter-molecular interaction on stable glass properties and structures. Molecules that consist of a phenyl "body" group with either one fluorocarbon (1-tail) or eight fluorocarbons "tail" (8-tail) are vapor deposited. Structural characterizations of the PVD glasses formed by the two molecules exhibit distinctly different features. Due to the difference in interactions between the phenyl "body" group and the F-rich "tail" group, the vapor deposited glasses of the 8-tail molecule were characterized to be micro-phase separated and optically isotropic, with lower relative densities, compared to 1-tail PVD glasses. X-ray scattering experiments of the 1-tail molecule show an anisotropic peak at low q which can be attributed to molecular layering. While for 8-tail molecule, a peak at a lower q value turns out to be an isotropic structural peak due to micro-phase separation, corresponding to the size of fluorocarbon clusters.

These experimental data are consistent with previous simulation results. To our knowledge, this is the first experimental report of micro-phase separated stable glasses.

6.2. Introduction

The formation of stable glasses have been attributed to fast surface dynamics[259, 246, 124, 188] on glassy materials and the surface mediated equilibrium (SME) process[133, 18]. Previous investigations on systems that contain hydrogen bonding demonstrate that hydrogen bonding formed between molecules can slow down surface diffusion[35, 36], which will in turn inhibit the molecules' ability to form stable glasses[118]. Simulation studies by Moore *et al.* on coarse grained molecules made up of a phenyl "body" group and fluorocarbon tails of various lengths predicted that the phenyl and the fluorocarbon groups in these molecules tend to micro-phase separate during physical vapor deposition (PVD), with the effects most prominently observed in the case of the molecule with the longest tail.

With increasing fluorocarbon tail length, the stability of the PVD glasses also decreases. This work provides characterizations on the relative density and structures of PVD glasses made of molecules with one and eight fluorocarbons, showing experimental evidence of micro-phase separation during PVD, consistent with theoretical predictions.

6.3. Experimental Details

The two compounds used in this study are: 1,1'-(4'-(trifluoromethyl)-[1,1'-biphenyl]-3,5-diyl)dinaphthalene and 1,1'-(4'-(perfluorooctyl)-[1,1'-biphenyl]-3,5-diyl)dinaphthalene, for simplicity termed "1-tail" and "8-tail", respectively (Figure 6.1A). Their synthesis and NMR characterization can be found in Reference [88]. Glass transition temperatures (T_g) of the two compounds were measured on liquid quenched glass states using spectroscopic ellipsometry (SE) at a 10 K/min cooling rate. Fitting the super-cooled liquid (SCL) and glass (GL) regions of 1-tail and 8-tail normalized thickness *vs.* temperature with lines, T_g were determined to be 332±1 K for 1-tail molecule and 309±2 K for 8-tail molecule. The thermal expansion coefficients (α) were also measured to be $\alpha_{SCL,1-tail} = (6.1 \pm 0.1) \times 10^{-4}$ K^{-1} and $\alpha_{GL,1-tail} = (1.7 \pm 0.1) \times 10^{-4}$ K^{-1} for 1-tail molecule, and $\alpha_{SCL,8-tail} = (7.2 \pm 0.1) \times 10^{-4}$ K^{-1} and $\alpha_{GL,8-tail} = (2.5 \pm 0.1) \times 10^{-4}$ K^{-1} for 8-tail molecule.

1-tail and 8-tail PVD glasses of ∼150 nm thickness were prepared in the custom-built high vacuum chamber with the temperature gradient stage (T-grad) as described in section 5.3.1. 1-tail PVD glass was made between 233 K (0.70 T_g) < T_{dep} < 340 K (1.02 T_g). And 8-tail PVD glass was made between 243 K (0.79 T_g) < T_{dep} < 313 K (1.01 T_g). The deposition rate was 0.2±0.02 nm/s. The relative density ($\Delta\rho$) and indices of refraction of PVD glasses were measured by SE. Refer to section 5.3.3 for the detailed transformation process.

For the structural characterization, Grazing Incidence Wide Angle X-ray Scattering (GIWAXS) was used. GIWAXS experiments were conducted at Brookhaven National Lab (BNL) using Beamline 12-ID with a Pilatus 300K-W detector. Beam energy used in this study was 18.2 keV, corresponding to an X-ray wavelength of 0.681 $\mathring{A}$. The incidence angle was set to be 0.1°. A Python-based package provided by BNL was used to perform post

acquisition data analysis. Out-of-plane scattering intensity was calculated by integrating the full range of q from 0 - 3 $Å^{-1}$ in the z direction, but limiting the integrated q range in xy direction to be 0 - 0.25 $Å^{-1}$. In-plane scattering intensity was calculated in the reversed manner by limiting the integrated q range in the z direction.

6.4. Result and Discussion

6.4.1. Experimental Results

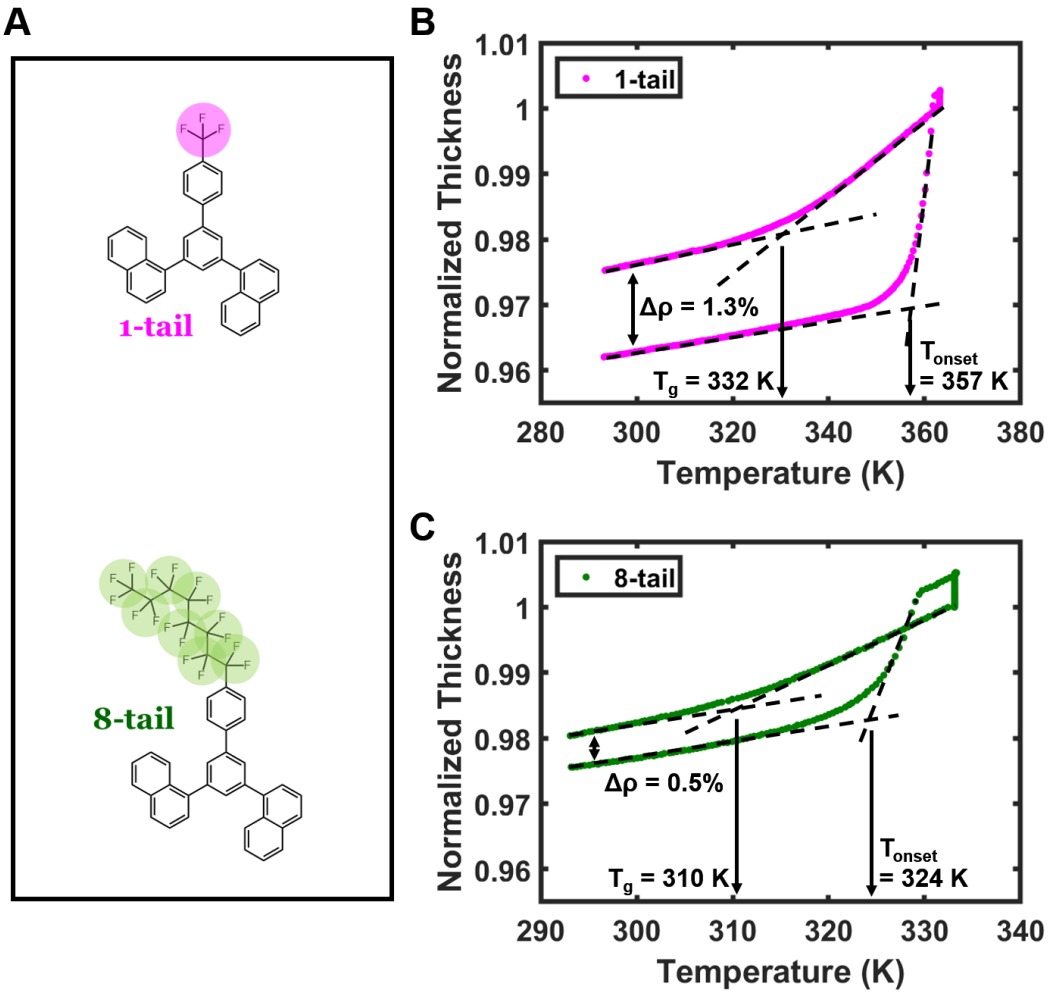

Figure 6.1: (A) Chemical structure of the 1-tail and 8-tail molecule. (B) Normalized thickness vs. temperature when transforming a ∼150 nm 1-tail SG deposited at T_{dep} = 282±2 K (0.85T_g). As-deposited films were heated from 293 K to 363 K and held isothermally for 30 min, then cooled to 293 K, transforming into LQG. The heating/cooling rates were 10 K/min. $T_{g,1-tail}$ = 332±1 K, indicated by a black arrow. Relative density increase, $\Delta\rho_{1-tail}$ = 1.3±0.1%. $T_{onset,1-tail}$ = 357 K (T_g+25 K). (C) Normalized thickness vs. temperature when transforming a ∼150 nm 8-tail SG deposited at T_{dep} = 274±2 K (0.89T_g). As-deposited films were heated from 293 K to 333 K and held isothermally for 30 min, then cooled to 293 K, transforming into LQG. $T_{g,8-tail}$ = 309±2 K. $\Delta\rho_{8-tail}$ = 0.5±0.1%. $T_{onset,8-tail}$ = 324 K (T_g+15 K).

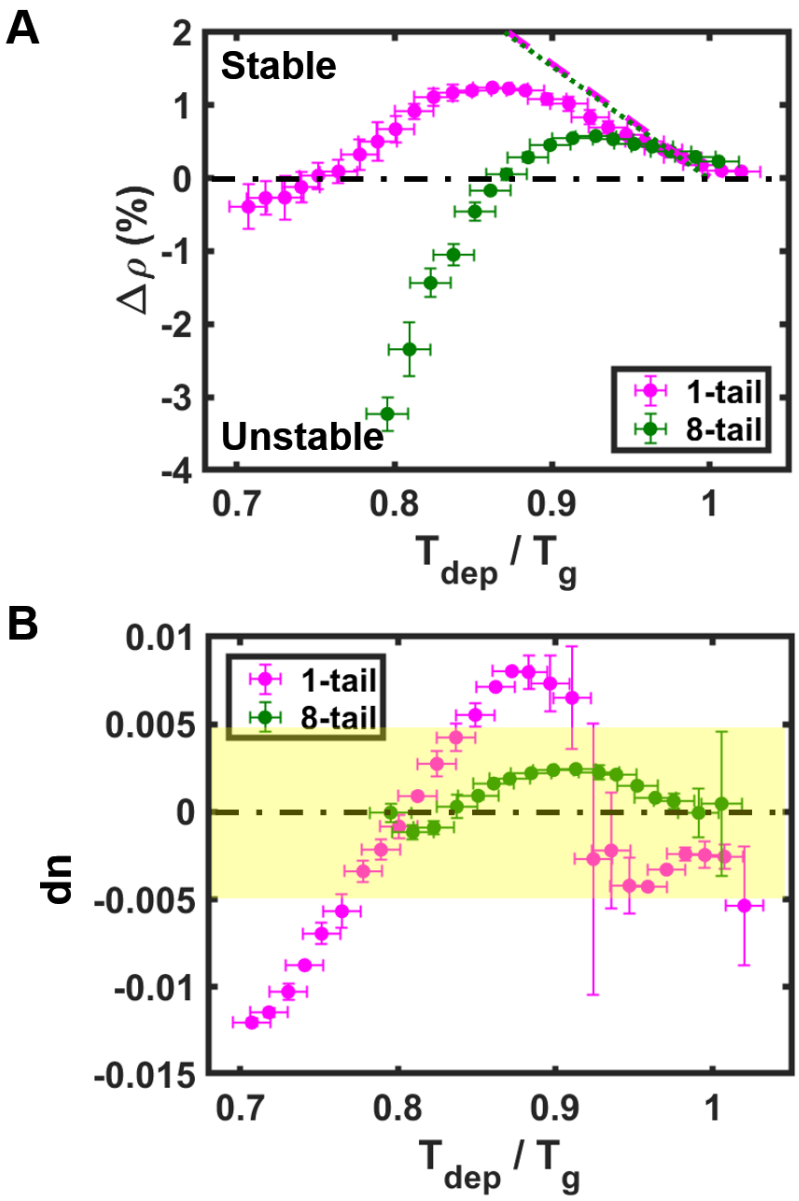

Figure 6.2: (A) $\Delta\rho$ *vs.* T_{dep}/T_g for 1-tail (magenta) and 8-tail (green) PVD glasses. Dashed and dotted lines are the extrapolated equilibrium lines for 1-tail and 8-tail PVD glasses, defined by the extrapolation of their SCL line, respectively. (B) Optical birefringence measured on 1-tail and 8-tail PVD glasses *vs.* T_{dep}/T_g. Shaded region in yellow is the uncertainty when measuring index of refraction with SE (± 0.005). Horizontal error bars show the uncertainty when determining temperatures on T-grad samples. Vertical error bars are from the standard error of each data points.

As what are shown in Figure 6.1A, the chemical structure of 1-tail and 8-tail molecules are distinguished by the length of their fluorocarbon substituent. From Figure 6.2A, we see the relative density of PVD glasses made by these two molecules exhibit different T_{dep} dependence, where the 1-tail molecule can form SGs in a larger T_{dep} range between 0.77 - 1.0 T_g. While, 8-tail molecule can only form PVD glasses denser than LQG at $T_{dep} >$ 0.88 T_g. The most stable glass made by 1-tail molecule thermodynamically (the densest glass) was achieved around 0.86 T_g, being $\Delta\rho$ $\sim$1.3$\pm$0.1 % denser than LQG. However, the largest density gain for the 8-tail PVD glasses was measured to be $\Delta\rho$ $\sim$0.5$\pm$0.1 %, obtained around T_{dep} $\sim$0.92 T_g. The transformation curves of the SGs deposited close to their optimal T_{dep}s are plotted in Figure 6.1B&C. It is clear that the 1-tail molecule can make glasses both thermodynamically and kinetically more stable than the 8-tail PVD glasses, consistent with simulation results.

The indices of refraction of the 1-tail and 8-tail PVD glasses were also measured by SE (Figure 6.2B & 6.6). Optical birefringence (dn) is defined as the difference between a glass's out-of-plane (n_z) and in-plane (n_{xy}) index of refraction ($dn = n_z - n_{xy}$). As can be seen from Figure 6.2A, the dn of 1-tail PVD glasses is initially close to 0 when $T_{dep} > 0.92T_g$ (305 K). (The small optical birefringence between 320 K $< T_{dep} <$ 340 K ($0.96T_g < T_{dep} < 1.02T_g$) is possibly due to the systematic error in measurements and modelings of $\sim$150 nm organic thin films.) As T_{dep} decreases, it becomes positive, going through a maximum, and starts to decrease from $T_{dep} > 0.87T_g$ (290 K), being strongly negative at $T_{dep} \sim 0.7T_g$ (235 K). While as for 8-tail molecular glasses, they have almost negligible dn and form nearly optically isotropic PVD glasses throughout the range of $0.8Tg < T_{dep} < 1.0T_g$ (243 K $< T_{dep} <$ 313 K).

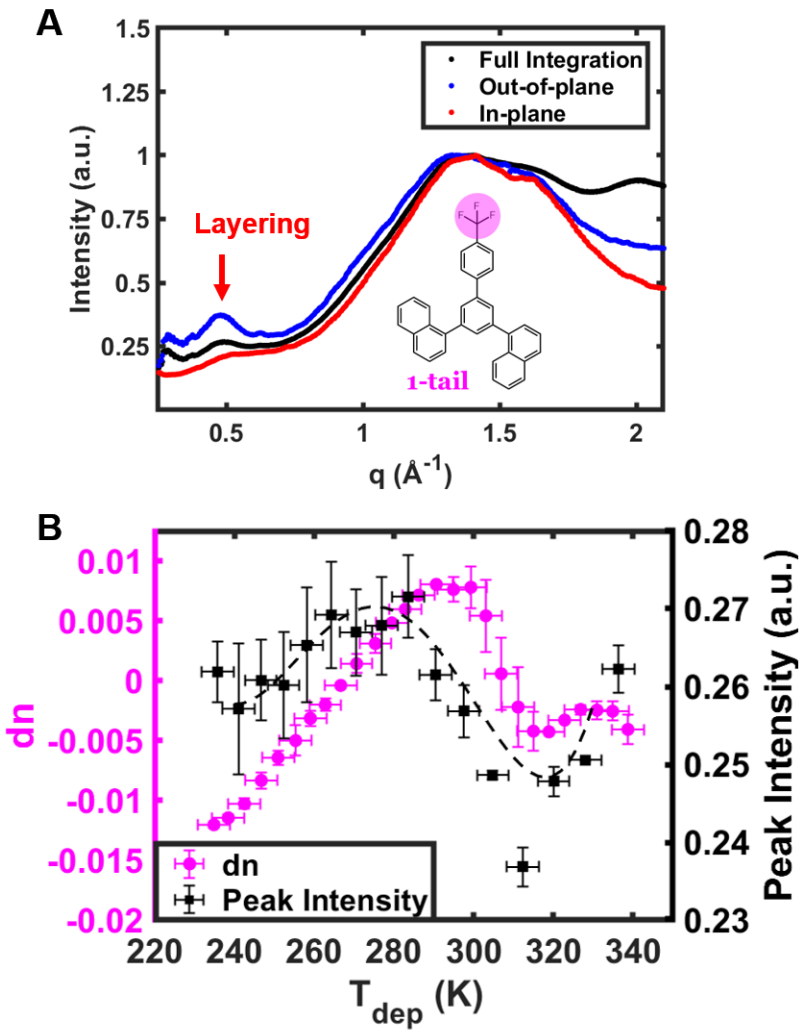

Figure 6.3: (A) Full (black), out-of-plane (blue) and in-plane (red) integration for the 2D GIWAXS scattering intensity of a 1-tail PVD glass deposited at T_{dep} = 284±2 K. The integration method is explained in the Experimental Details section. The red arror indicates the layering peak. (B) Optical birefringence (*dn*, magenta, left axis) and the intensity of layering (black, right axis) plotted *vs.* T_{dep} for 1-tail PVD glasses. Dashed line is the trend line for layering intensity.

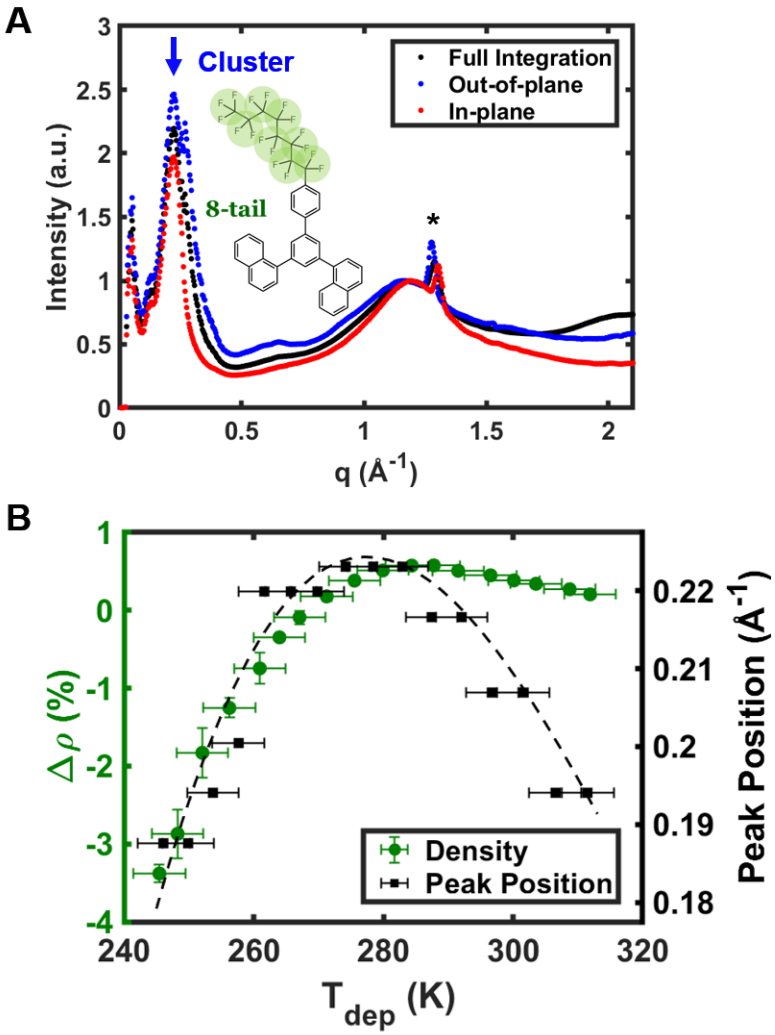

Figure 6.4: (A) Full (black), out-of-plane (blue) and in-plane (red) integration for the 2D GIWAXS scattering intensity of a 8-tail PVD glass deposited at T_{dep} = 274±2 K. The integration method is explained in the Experimental Details section. The blue arror indicates the peak due to fluorocarbon cluster formation. The peak with a asterisk on top is attributed to grease contamination, and not a feature of the 8-tail PVD glass. (B) Relative density ($\Delta\rho$, green, left axis) and the position of the cluster peak (black, right axis) *vs.* T_{dep} for 8-tail PVD glasses. Dashed line is the trend line for fluorocarbon cluster peak position.

GIWAXS experiments were conducted to characterize the packing of 1-tail and 8-tail molecules upon PVD. As for the integrated scattering intensities of 1-tail PVD glasses, they consist of a layering peak at $q \sim 0.5$ Å^{-1}, featured by a higher intensity in the out-of-plane (q_z) direction and corresponding to the size of 1-tail molecules, as well as structural peaks around

1 $Å^{-1} < q < 1.7$ $Å^{-1}$ (Figure 6.3A). As shown in Figure 6.3B, the intensity of the layering peak is correlated with the optical birefringence (dn) of the 1-tail PVD glasses within a wide range of T_{dep}, suggesting a close relationship between the glass packing and dn, which is consistent with our results in other molecular glass systems in Chapter 5.

However, in the case of 8-tail molecule, from Figure 6.4A, we see its scattering peak at the lowest $q \sim 0.2Å^{-1}$ appears to be almost isotropic with very strong intensities, compared to the layering peak in 1-tail PVD glasses. With its q value corresponding to ~3.1 nm and being almost twice of the size of 8-tail molecules, we attribute this peak to the length scale of the fluorocarbon clusters, which are predicted to vastly exist in PVD glasses formed by long-fluorocarbon-tailed molecules by the simulations[148]. In addition, as can be seen in Figure 6.4B, the position of this cluster peak is related to the film's relative density in 8-tail PVD glasses, indicating that larger fluorocarbon cluster size or larger micro-phase seperation domain size (corresponding to lower q) has larger effect on prohibiting the glass from forming denser packing. In that way, 8-tail PVD glasses reach their maximum relative density at where the smallest domain size is measured, which is the largest in q.

6.4.2. Discussions

Coarse grained simulations have predicted that the molecules with longer tails can aggregate and become trapped by tail segregation on the top free surface layer. This in turn slows down the surface relaxation, resulting in reduced stability. This phenomenon is comparable with the observation that hydrogen bonding molecules generally form less stable glasses upon PVD[118]. Similar results were found in our experiments, where the 8-tail molecule generally form less stable glasses, both thermodynamically and kinetically, compared to 1-tail molecules.

In addition, it was observed in coarse grained simulation that within the layers below the free surface, F-tailed molecules still have enough mobility to reorient, forming a disordered structure with the phenyl groups and fluorocarbon groups micro-phase separated. The micro-phase separation ability and the cluster sizes were predicted to increase as the

molecule's fluorocarbon tail length was increased[148]. Indeed, we observed scattering peaks corresponding to the size of fluorocarbon clusters only in 8-tailed molecules, where in 1-tail PVD glasses, an isotropic layering peak was found instead. The formation of fluorocarbon clusters has so strong a driving force with lower potential energy for long-fluorocarbon-tailed molecules, that it suppressed the effect of preferred molecular orientation, patterned by the equilibrated surface structure, upon PVD. That attributes to we seeing cluster peak in 8-tail PVD glasses at low q region but layering peak in 1-tail PVD glasses, where molecular orientation dominates the packing. This is the first experimental demonstration that micro-phase separation happens in SG systems.

The micro-phase separations would also explain the observation in Figure 6.2B, where the 8-tail PVD glasses appear to be nearly optically isotropic, but 1-tail PVD glasses have T_{dep} dependent optical birefringence. Optical birefringence can be originated from either anisotropic packing or molecular orientation[242, 39, 42]. Because the fluorocarbon clusters in 8-tail PVD glasses are disordered and isotropic in nature, as seen in the simulations[148], 8-tail molecules have almost no packing anisotropy or orientation when vapor deposited. This can be further confirmed by the GIWAXS experiments shown in Figure 6.4A. While for 1-tail PVD glasses, where the surface mediated equilibration decides the molecular orientation and packing, their structure are largely affected by the equilibrated surface structure at various T_{dep}. Therefore, T_{dep} dependent indices of refraction are found in 1-tail PVD glasses.

6.5. Summary and Outlook

In this chapter, we discussed the experimental results of 1-tail and 8-tail PVD glasses' relative density, optical birefringence and GIWAXS structural characterization. We demonstrate that our experimental data are consistent with the simulation result reported earlier, with the 8-tail molecules forming glasses less dense and kinetically less stable than the 1-tail molecules when vapor deposited. Additionally, we observed distinct optical and structural features in the glasses formed by these two molecules, which the coarse grained simulations

can provide us insights on. The 1-tail PVD glasses were measured to have T_{dep} dependent optical birefringence and closely correlated molecular layering. The relationship between them is a result of surface mediated molecular orientation during PVD. While in the case of 8-tail molecules, they form fluorocarbon clusters whose size is related to their relative density and stability. Micro-phase separation, for the first time, has been confirmed using GIWAXS in PVD glasses experimentally. It was shown to form more readily in the 8-tail glasses, as such it suppressed the effect of molecular orientation, making the glass isotropic in packing and indices of refraction.

6.6. Supplementary Information

6.6.1. Synthesis and Characterization of the Compounds Used in This Study

Synthesis and NMR Characterization of 1-tail Molecule

The synthesis and purification of 1,1'-(5-Chloro-1,3-phenylene)dinaphthalene can be found in Reference[127].

1,1'-(5-Chloro-1,3-phenylene)dinaphthalene (0.547 g, 1.5 mmol, 1.0 equiv), (4-(trifluoromethyl)phenyl)boron acid (0.380 g, 2.0 mmol, 1.3 equiv), $Pd(OAc)_2$ (8.4 mg, 0.037 mmol, 2.5 mol %), DavePhos (29.5 mg, 0.075 mmol, 5 mol %), K_3PO_4 (0.64 g, 3.0 mmol, 2 equiv), THF (7.5 mL), and H_2O (1.5 mL) were added in a dry round bottom flask equipped with a stir bar under nitrogen atmosphere. The reaction was completed after 16 h at 323 K. After the mixture was cooled to room temperature, the aqueous and organic layers were separated. The aqueous layer was extracted with ethyl acetate three times. The extraction was combined with the initial organic layer, dried over $MgSO_4$ and concentrated. The residue was chromatographed on silica gel using hexanes to afford 1,1'-(4'-(trifluoromethyl)-[1,1'-biphenyl]-3,5-diyl)dinaphthalene in 65% yield (463 mg).

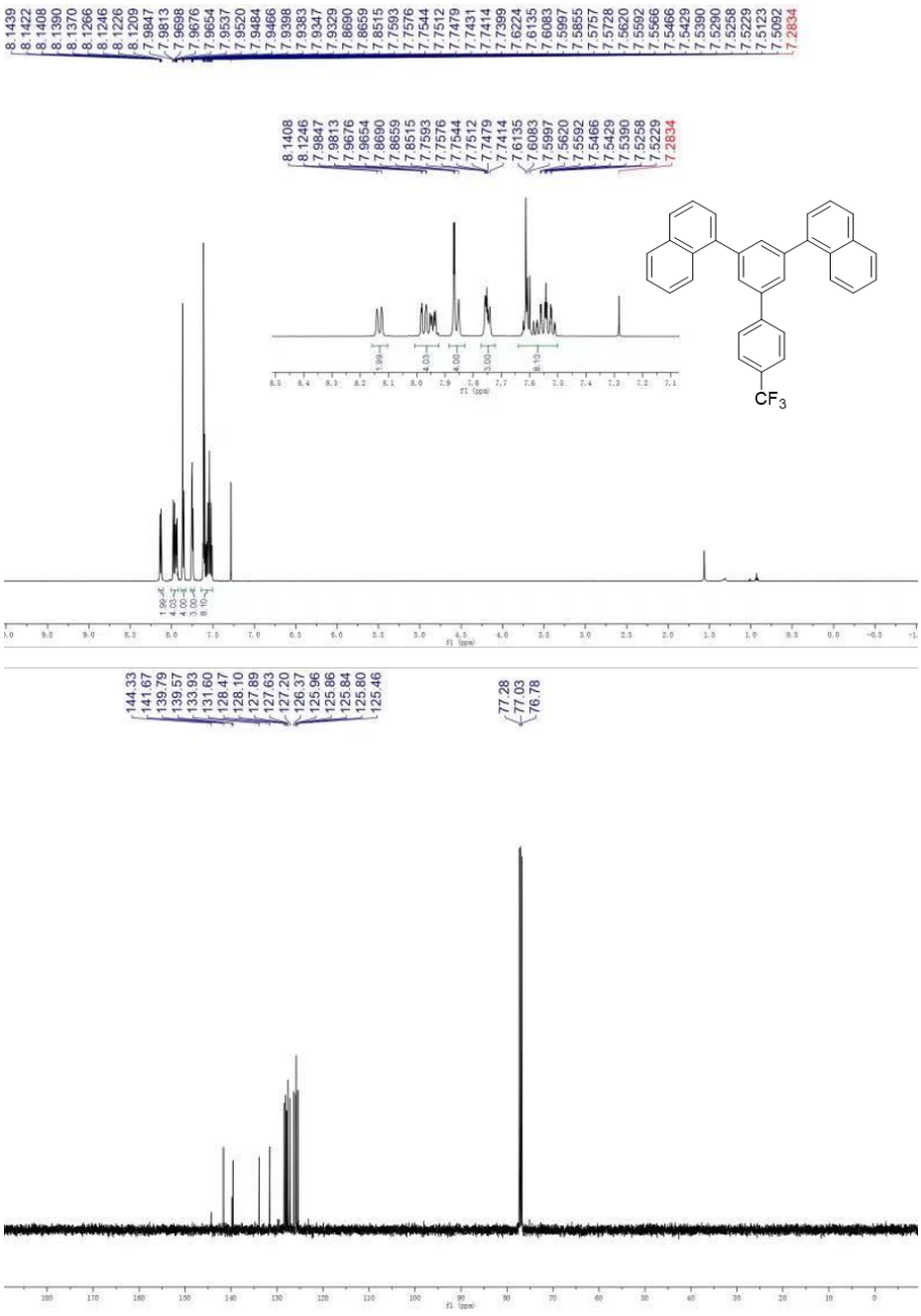

Figure 6.5: ^{1}H and ^{13}C NMR spectra of 1-tail molecule in $CDCl_3$.

Synthesis of 8-tail Molecule

1,3,5-tribromobenzene (0.622 g, 2 mmol, 1 equiv) and 1-naphthyl boronic acid (0.757 g, 4.4 mmol, 2.2 equiv) were added into a dry round bottom flast with a stir bar before purging the

flask with nitrogen. Toluene (40.7 mL), ethanol (25 mL), Na_2CO_3 (64 mL, 2 M solution in H_2O, 0.13 mol) and $Pd(PPh_3)_4$ (0.139 g, 0.12 mmol, 6 mol %) were then added to the flask in sequence. The reaction mixture was heated to 363 K and reacted for 48 h. Upon completion, the reaction was cooled to RT, and the organic layer was separated from the aqueous layers. Then the aqueous layer was extracted with Et_2O for three times. Organic portions were combined and dried over $MgSO_4$. The filtrate was then concentrated and the residue was chromatographed on silica gel to afford 1,1'-(5-Bromo-1,3-phenylene)dinaphthalene in 69% yield (560 mg).

In the second step, 1,1'-(5-Bromo-1,3-phenylene)dinaphthalene (0.500 g, 1.22 mmol, 1 equiv) and anhydrous tetrahydrofuran were added into an oven-dried 250-mL Schlenk tube with a stir bar under nitrogen atmosphere. The reaction was placed in acetone/dry ice cold bath (∼195 K), before n-butyllithium (d 0.68, 1.0 mL, 2.44 mmol, 2 equiv) was injected dropwisely. The reaction was further stirred in the acetone/dry ice bath for 3 h. Then trimethyl borate (d 0.932, 0.3 mL, 2.44 mmol, 2 equiv) in anhydrous tetrahydrofuran (5 mL) solution was added. The mixture was left to react at room temperature for 16h. Upon completion, the reaction was quenched with 2 M hydrochloric acid (d 0.073, 3 mL, 6 mmol) and dried under reduced pressure. Dichloromethane (3 mL) was added to dissolve the residue. More 2 M hydrochloric acid were added slowly to the solution until the its pH reached 1. Then the reaction was left to stir for 30 minutes. Organic and aqueous layers were separated and the aqueous layer was extracted by dichloromethane for 3 times. The organic layers were combined, dried over Na_2SO_4, and concentrated. The product, (3,5-dinaphthyl)boronic acid, was yielded in 62% yield (359 mg) after chromatography using a solvent mixture of hexanes:ethyl acetate = 1:1.

In the last step, (3,5-dinaphthyl)boronic acid (350 mg, 0.94 mmol, 1 equiv), 1-bromo-4-(perfluorooctyl)benzene (862.5 mg, 1.5 mmol, 1.5 equiv), $Pd(PPh_3)_4$ (115.6 mg, 0.10 mmol, 10 mol %), K_2CO_3 (276.4 mg, 2 mmol, 2 equiv), THF (7.7 mL), and H_2O (1.54 mL) were added in a dry round bottom flask with a stir bar under nitrogen atmosphere.

The reaction mixture was heated to 353 K, reacting for 16 h. Then, the mixture was cooled to room temperature. The organic and aqueous layers were separated. The aqueous layer was extracted with ethyl acetate three times. The combined organic layers, including the initial reaction mixture and ethyl acetate extractions, were dried over $MgSO_4$ and concentrated. The residue was chromatographed on silica gel using hexanes to afford 1,1'-(4'-(perfluorooctyl)-[1,1'-biphenyl]-3,5-diyl)dinaphthalene in 41% yield (317 mg).

More synthetic details and NMR characterization can be found in Reference [88].

6.6.2. In-plane and Out-of-plane Indices of Refraction of 1-tail and 8-tail PVD Glasses

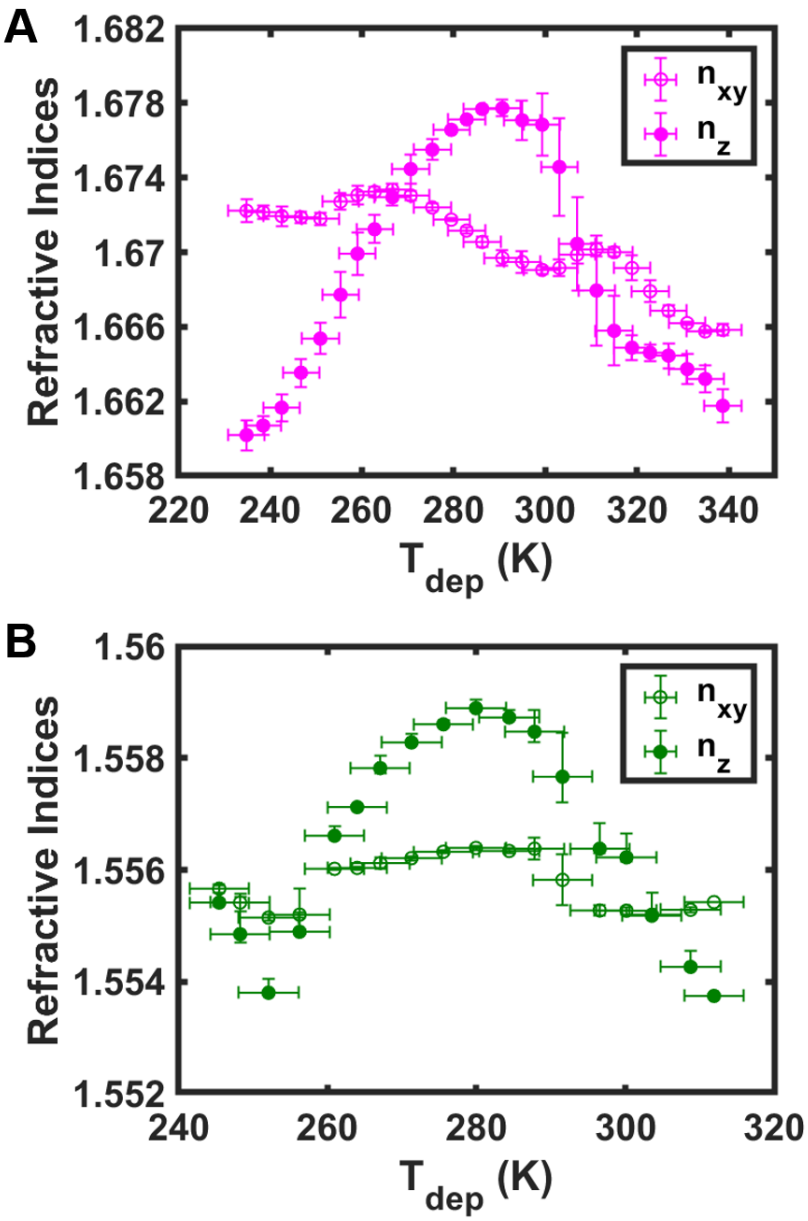

Figure 6.6: (A)/(B) In-plane (n_{xy}) and out-of-plane (n_z) indices of refraction measured on 1-tail (magenta)/8-tail (green) PVD glasses as a function of T_{dep}.

6.7. Acknowledgments

I acknowledge the use of Brookhaven National Lab Beamline 12-ID and the assistance from Dr. Mikhail Zhernenkov and Dr. Guillaume Freychet in thin film GIWAXS characterization. Moreover, the author would like to thank Dr. Gui Gao, Haoqiang Zhao and Prof. Patrick J. Walsh for compound synthesis, Sarah Wolf, Shivajee Govind and Dr. Yi Jin for sample preparation, Alex R. Moore for data analysis, and Prof. Zahra Fakhraai for guidance.

BIBLIOGRAPHY

[1] E. V. Aleksandrovich, A. N. Aleksandrovich, and G. M. Mikheev. Laser-induced modification of optical properties of glassy selenium films synthesized by vacuum thermal evaporation. *Journal of Non-Crystalline Solids*, 545:120249, oct 2020. doi: 10.1016/j.jnoncrysol.2020.120249.

[2] C. Angell. Perspective on the glass transition. *Journal of Physics and Chemistry of Solids*, 49(8):863–871, jan 1988. doi: 10.1016/0022-3697(88)90002-9.

[3] C. Angell. Relaxation in liquids, polymers and plastic crystals — strong/fragile patterns and problems. *Journal of Non-Crystalline Solids*, 131-133:13–31, jun 1991. doi: 10.1016/0022-3093(91)90266-9.

[4] C. A. Angell. Formation of glasses from liquids and biopolymers. *Science*, 267(5206): 1924–1935, mar 1995. doi: 10.1126/science.267.5206.1924.

[5] C. A. Angell. The fragility of glassforming liquids: thermal vs athermal systems, and kinetic vs thermodynamic origins. In *Fragility of Glass-Forming Liquids*, volume 13. Hindustan Book Agency New Delhi, India, 2014.

[6] A. Annamareddy, Y. Li, L. Yu, P. M. Voyles, and D. Morgan. Factors correlating to enhanced surface diffusion in metallic glasses. *The Journal of Chemical Physics*, 154 (10):104502, mar 2021. doi: 10.1063/5.0039078.

[7] A. Annamareddy, P. M. Voyles, J. Perepezko, and D. Morgan. Mechanisms of bulk and surface diffusion in metallic glasses determined from molecular dynamics simulations. *Acta Materialia*, page 116794, mar 2021. doi: 10.1016/j.actamat.2021.116794.

[8] K. Bagchi and M. D. Ediger. Controlling structure and properties of vapor-deposited glasses of organic semiconductors: Recent advances and challenges. *The Journal of Physical Chemistry Letters*, 11(17):6935–6945, jul 2020. doi: 10.1021/acs.jpclett.0c01682.

[9] K. Bagchi, N. E. Jackson, A. Gujral, C. Huang, M. F. Toney, L. Yu, J. J. de Pablo, and M. D. Ediger. Origin of anisotropic molecular packing in vapor-deposited alq3 glasses. *The Journal of Physical Chemistry Letters*, pages 164–170, dec 2018. doi: 10.1021/acs.jpclett.8b03582.

[10] K. Bagchi, A. Gujral, M. F. Toney, and M. D. Ediger. Generic packing motifs in vapor-deposited glasses of organic semiconductors. *Soft Matter*, 15(38):7590–7595, 2019. doi: 10.1039/c9sm01155b.

[11] R. R. Baglay and C. B. Roth. Communication: Experimentally determined profile of local glass transition temperature across a glassy-rubbery polymer interface with a tg difference of 80 k. *The Journal of Chemical Physics*, 143(11):111101, sep 2015. doi: 10.1063/1.4931403.

[12] J. Barták, J. Málek, K. Bagchi, M. D. Ediger, Y. Li, and L. Yu. Surface mobility in amorphous selenium and comparison with organic molecular glasses. *The Journal of Chemical Physics*, 154(7):074703, feb 2021. doi: 10.1063/5.0041273.

[13] C. Bauer, R. Böhmer, S. Moreno-Flores, R. Richert, H. Sillescu, and D. Neher. Capacitive scanning dilatometry and frequency-dependent thermal expansion of polymer films. *Physical Review E*, 61(2):1755–1764, feb 2000. doi: 10.1103/physreve.61.1755.

[14] R. K. Bay and A. J. Crosby. Uniaxial extension of ultrathin freestanding polymer films. *ACS Macro Letters*, pages 1080–1085, aug 2019. doi: 10.1021/acsmacrolett.9b00408.

[15] M. S. Beasley, C. Bishop, B. J. Kasting, and M. D. Ediger. Vapor-deposited ethylbenzene glasses approach "ideal glass" density. *The Journal of Physical Chemistry Letters*, jul 2019. doi: 10.1021/acs.jpclett.9b01508.

[16] K. Bernatz, I. Echeverría, S. Simon, and D. Plazek. Characterization of the molecular structure of amorphous selenium using recoverable creep compliance measurements. *Journal of Non-Crystalline Solids*, 307-310:790–801, sep 2002. doi: 10.1016/s0022-3093(02)01522-3.

[17] L. Berthier and M. D. Ediger. Facets of glass physics. 2015. doi: 10.1063/PT.3.3052.

[18] L. Berthier, P. Charbonneau, E. Flenner, and F. Zamponi. Origin of ultrastability in vapor-deposited glasses. *Physical Review Letters*, 119(18), nov 2017. doi: 10.1103/physrevlett.119.188002.

[19] R. Böhmer, K. L. Ngai, C. A. Angell, and D. J. Plazek. Nonexponential relaxations in strong and fragile glass formers. *The Journal of Chemical Physics*, 99(5):4201–4209, sep 1993. doi: 10.1063/1.466117.

[20] G. Biroli and J. P. Bouchaud. The random first-order transition theory of glasses: a critical assessment.

[21] C. Bishop, J. L. Thelen, E. Gann, M. F. Toney, L. Yu, D. M. DeLongchamp, and M. D. Ediger. Vapor deposition of a nonmesogen prepares highly structured organic glasses. *Proceedings of the National Academy of Sciences*, page 201908445, sep 2019. doi: 10.1073/pnas.1908445116.

[22] C. Bishop, Y. Li, M. F. Toney, L. Yu, and M. D. Ediger. Molecular orientation for vapor-deposited organic glasses follows rate-temperature superposition: The case of posaconazole. *The Journal of Physical Chemistry B*, 124(12):2505–2513, mar 2020. doi: 10.1021/acs.jpcb.0c00625.

[23] C. Bishop, Z. Chen, M. F. Toney, H. Bock, L. Yu, and M. D. Ediger. Using deposition rate and substrate temperature to manipulate liquid crystal-like order in a vapor-

deposited hexagonal columnar glass. *The Journal of Physical Chemistry B*, mar 2021. doi: 10.1021/acs.jpcb.0c11564.

[24] C. W. Brian, L. Zhu, and L. Yu. Effect of bulk aging on surface diffusion of glasses. *The Journal of Chemical Physics*, 140(5):054509, feb 2014. doi: 10.1063/1.4863556.

[25] E. Bussmann, I. Ermanoski, P. J. Feibelman, N. C. Bartelt, and G. L. Kellogg. Buried pd slows self-diffusion on cu(001). *Physical Review B*, 84(24), dec 2011. doi: 10.1103/physrevb.84.245440.

[26] C. R. Cao, Y. M. Lu, H. Y. Bai, and W. H. Wang. High surface mobility and fast surface enhanced crystallization of metallic glass. *Applied Physics Letters*, 107(14): 141606, oct 2015. doi: 10.1063/1.4933036.

[27] C. R. Cao, L. Yu, and J. H. Perepezko. Surface dynamics measurement on a gold based metallic glass. *Applied Physics Letters*, 116(23):231601, jun 2020. doi: 10.1063/5.0007838.

[28] X. Cao, H. Zhang, and Y. Han. Release of free-volume bubbles by cooperative-rearrangement regions during the deposition growth of a colloidal glass. *Nature Communications*, 8(1), aug 2017. doi: 10.1038/s41467-017-00428-4.

[29] S. Capponi, S. Napolitano, N. R. Behrnd, G. Couderc, J. Hulliger, and M. Wübbenhorst. Structural relaxation in nanometer thin layers of glycerol. *The Journal of Physical Chemistry C*, 114(39):16696–16699, sep 2010. doi: 10.1021/jp108151p.

[30] R. Casalini and C. M. Roland. Communication: Effect of density on the physical aging of pressure-densified polymethylmethacrylate. *The Journal of Chemical Physics*, 147 (9):091104, sep 2017. doi: 10.1063/1.4995567.

[31] A. Cavagna. Supercooled liquids for pedestrians. *Physics Reports*, 476(4-6):51–124, jun 2009. doi: 10.1016/j.physrep.2009.03.003.

[32] E. P. Chan, K. A. Page, S. H. Im, D. L. Patton, R. Huang, and C. M. Stafford. Viscoelastic properties of confined polymer films measured via thermal wrinkling. *Soft Matter*, 5(23):4638, 2009. doi: 10.1039/b916207k.

[33] D. Chandler and J. P. Garrahan. Dynamics on the way to forming glass: Bubbles in space-time. *Annual Review of Physical Chemistry*, 61(1):191–217, mar 2010. doi: 10.1146/annurev.physchem.040808.090405.

[34] L. Chen, C. Cao, J. Shi, Z. Lu, Y. Sun, P. Luo, L. Gu, H. Bai, M. Pan, and W. Wang. Fast surface dynamics of metallic glass enable superlatticelike nanostructure growth. *Physical Review Letters*, 118(1), jan 2017. doi: 10.1103/physrevlett.118.016101.

[35] Y. Chen, W. Zhang, and L. Yu. Hydrogen bonding slows down surface diffusion of molecular glasses. *The Journal of Physical Chemistry B*, 120(32):8007–8015, aug 2016. doi: 10.1021/acs.jpcb.6b05658.

[36] Y. Chen, M. Zhu, A. Laventure, O. Lebel, M. D. Ediger, and L. Yu. Influence of hydrogen bonding on the surface diffusion of molecular glasses: Comparison of three triazines. *The Journal of Physical Chemistry B*, 121(29):7221–7227, jul 2017. doi: 10.1021/acs.jpcb.7b05333.

[37] Y. Z. Chua, M. Ahrenberg, M. Tylinski, M. D. Ediger, and C. Schick. How much time is needed to form a kinetically stable glass? AC calorimetric study of vapor-deposited glasses of ethylcyclohexane. *The Journal of Chemical Physics*, 142(5):054506, feb 2015. doi: 10.1063/1.4906806.

[38] R. H. Colby, L. J. Fetters, and W. W. Graessley. The melt viscosity-molecular weight relationship for linear polymers. *Macromolecules*, 20(9):2226–2237, sep 1987. doi: 10.1021/ma00175a030.

[39] S. S. Dalal and M. D. Ediger. Molecular orientation in stable glasses of indomethacin. *The Journal of Physical Chemistry Letters*, 3(10):1229–1233, apr 2012. doi: 10.1021/jz3003266.

[40] S. S. Dalal, A. Sepúlveda, G. K. Pribil, Z. Fakhraai, and M. D. Ediger. Density and birefringence of a highly stable α,α,β-trisnaphthylbenzene glass. *The Journal of Chemical Physics*, 136(20):204501, may 2012. doi: 10.1063/1.4719532.

[41] S. S. Dalal, Z. Fakhraai, and M. D. Ediger. High-throughput ellipsometric characterization of vapor-deposited indomethacin glasses. *The Journal of Physical Chemistry B*, 117(49):15415–15425, aug 2013. doi: 10.1021/jp405005n.

[42] S. S. Dalal, D. M. Walters, I. Lyubimov, J. J. de Pablo, and M. D. Ediger. Tunable molecular orientation and elevated thermal stability of vapor-deposited organic semiconductors. *Proceedings of the National Academy of Sciences*, 112(14):4227–4232, Mar. 2015. doi: 10.1073/pnas.1421042112.

[43] C. R. Daley, Z. Fakhraai, M. D. Ediger, and J. A. Forrest. Comparing surface and bulk flow of a molecular glass former. *Soft Matter*, 8(7):2206, 2012. doi: 10.1039/c2sm06826e.

[44] K. Dalnoki-Veress, B. Nickel, C. Roth, and J. Dutcher. Hole formation and growth in freely standing polystyrene films. *Physical Review E*, 59(2):2153–2156, feb 1999. doi: 10.1103/physreve.59.2153.

[45] S. Dash, P. Chen, and P. Boolchand. Molecular origin of aging of pure se glass: Growth of inter-chain structural correlations, network compaction, and partial ordering. *The Journal of Chemical Physics*, 146(22):224506, jun 2017. doi: 10.1063/1.4983480.

[46] K. Dawson, L. A. Kopff, L. Zhu, R. J. McMahon, L. Yu, R. Richert, and M. D. Ediger. Molecular packing in highly stable glasses of vapor-deposited tris-naphthylbenzene isomers. *The Journal of Chemical Physics*, 136(9):094505, mar 2012. doi: 10.1063/1.3686801.

[47] K. J. Dawson, K. L. Kearns, M. D. Ediger, M. J. Sacchetti, and G. D. Zografi. Highly stable indomethacin glasses resist uptake of water vapor. *The Journal of Physical Chemistry B*, 113(8):2422–2427, feb 2009. doi: 10.1021/jp808838t.

[48] K. J. Dawson, K. L. Kearns, L. Yu, W. Steffen, and M. D. Ediger. Physical vapor deposition as a route to hidden amorphous states. *Proceedings of the National Academy of Sciences*, 106(36):15165–15170, jul 2009. doi: 10.1073/pnas.0901469106.

[49] K. J. Dawson, L. Zhu, L. Yu, and M. D. Ediger. Anisotropic structure and transformation kinetics of vapor-deposited indomethacin glasses. *The Journal of Physical Chemistry B*, 115(3):455–463, jan 2011. doi: 10.1021/jp1092916.

[50] J. C. Dyre, T. Hechsher, and K. Niss. A brief critique of the adam–gibbs entropy model. *Journal of Non-Crystalline Solids*, 355(10-12):624–627, may 2009. doi: 10.1016/j.jnoncrysol.2009.01.039.

[51] S. U. Dzhalilov and K. I. Rzaev. On the phenomenon of selenium vitrification. *physica status solidi (b)*, 20(1):261–266, 1967. doi: 10.1002/pssb.19670200123.

[52] M. D. Ediger. Perspective: Highly stable vapor-deposited glasses. *The Journal of Chemical Physics*, 147(21):210901, dec 2017. doi: 10.1063/1.5006265.

[53] M. D. Ediger, C. A. Angell, and S. R. Nagel. Supercooled liquids and glasses. *The Journal of Physical Chemistry*, 100(31):13200–13212, jan 1996. doi: 10.1021/jp953538d.

[54] C. J. Ellison and J. M. Torkelson. The distribution of glass-transition temperatures in nanoscopically confined glass formers. *Nature Materials*, 2(10):695–700, sep 2003. doi: 10.1038/nmat980.

[55] Y. S. Elmatad, D. Chandler, and J. P. Garrahan. Corresponding states of structural glass formers. *The Journal of Physical Chemistry B*, 113(16):5563–5567, apr 2009. doi: 10.1021/jp810362g.

[56] Y. S. Elmatad, D. Chandler, and J. P. Garrahan. Corresponding states of structural glass formers. II. *The Journal of Physical Chemistry B*, 114(51):17113–17119, dec 2010. doi: 10.1021/jp1076438.

[57] Y. Esaki, T. Komino, T. Matsushima, and C. Adachi. Enhanced electrical properties and air stability of amorphous organic thin films by engineering film density. *The Journal of Physical Chemistry Letters*, 8(23):5891–5897, nov 2017. doi: 10.1021/acs.jpclett.7b02808.

[58] C. M. Evans, H. Deng, W. F. Jager, and J. M. Torkelson. Fragility is a key parameter in determining the magnitude of tg-confinement effects in polymer films. *Macromolecules*, 46(15):6091–6103, jul 2013. doi: 10.1021/ma401017n.

[59] Z. Fakhraai and J. A. Forrest. Probing slow dynamics in supported thin polymer films. *Physical Review Letters*, 95(2), jul 2005. doi: 10.1103/physrevlett.95.025701.

[60] Z. Fakhraai and J. A. Forrest. Measuring the surface dynamics of glassy polymers. *Science*, 319(5863):600–604, feb 2008. doi: 10.1126/science.1151205.

[61] Z. Fakhraai and J. A. Forrest. Measuring the surface dynamics of glassy polymers. *Science*, 319(5863):600–604, feb 2008. doi: 10.1126/science.1151205.

[62] Z. Fakhraai, T. Still, G. Fytas, and M. D. Ediger. Structural variations of an organic glassformer vapor-deposited onto a temperature gradient stage. *The Journal of Physical Chemistry Letters*, 2(5):423–427, mar 2011. doi: 10.1021/jz101723d.

[63] E. Fontana and W. Plummer. A study of viscosity-temperature relationships in the geo2 and sio2 systems. *Phys. Chem. Glasses*, 7(4):139–146, 1966.

[64] J. Frischeisen, D. Yokoyama, C. Adachi, and W. Brütting. Determination of molecular dipole orientation in doped fluorescent organic thin films by photoluminescence measurements. *Applied Physics Letters*, 96(7):073302, feb 2010. doi: 10.1063/1.3309705.

[65] G. S. Fulcher. ANALYSIS OF RECENT MEASUREMENTS OF THE VISCOSITY OF GLASSES. *Journal of the American Ceramic Society*, 8(6):339–355, jun 1925. doi: 10.1111/j.1151-2916.1925.tb16731.x.

[66] Y. J. Gagnon and C. B. Roth. Local glass transition temperature tg(z) within polystyrene is strongly impacted by the modulus of the neighboring PDMS domain. *ACS Macro Letters*, 9(11):1625–1631, oct 2020. doi: 10.1021/acsmacrolett.0c00659.

[67] S. Gao, Y. P. Koh, and S. L. Simon. Calorimetric glass transition of single polystyrene ultrathin films. *Macromolecules*, 46(2):562–570, jan 2013. doi: 10.1021/ma3020036.

[68] J. P. Garrahan, R. L. Jack, V. Lecomte, E. Pitard, K. van Duijvendijk, and F. van Wijland. Dynamical first-order phase transition in kinetically constrained models of glasses. *Physical Review Letters*, 98(19), may 2007. doi: 10.1103/physrevlett.98.195702.

[69] S. Gayathri, Sridevi.S, and S. Asokan. Investigations on photo-mechanical and photo-thermo-mechanical strain variations in amorphous selenium using fiber bragg grating sensor. *Journal of Non-Crystalline Solids*, 477:7–11, dec 2017. doi: 10.1016/j.jnoncrysol.2017.09.027.

[70] E. C. Glor, R. J. Composto, and Z. Fakhraai. Glass transition dynamics and fragility of ultrathin miscible polymer blend films. *Macromolecules*, 48(18):6682–6689, sep 2015. doi: 10.1021/acs.macromol.5b00979.

[71] E. C. Glor, G. V. Angrand, and Z. Fakhraai. Exploring the broadening and the existence of two glass transitions due to competing interfacial effects in thin, supported

polymer films. *The Journal of Chemical Physics*, 146(20):203330, may 2017. doi: 10.1063/1.4979944.

[72] J. Gómez, A. Gujral, C. Huang, C. Bishop, L. Yu, and M. D. Ediger. Nematic-like stable glasses without equilibrium liquid crystal phases. *The Journal of Chemical Physics*, 146(5):054503, feb 2017. doi: 10.1063/1.4974829.

[73] R. Grosse, P. Krause, M. Meissner, and A. Tausend. The coefficients of thermal expansion and the gruneisen functions of trigonal and amorphous selenium in the temperature range between 10k and 300k. *Journal of Physics C: Solid State Physics*, 11(1):45–53, jan 1977. doi: 10.1088/0022-3719/11/1/016.

[74] Y. Gueguen, T. Rouxel, P. Gadaud, C. Bernard, V. Keryvin, and J.-C. Sangleboeuf. High-temperature elasticity and viscosity of GexSe1-xglasses in the transition range. *Physical Review B*, 84(6), aug 2011. doi: 10.1103/physrevb.84.064201.

[75] A. Gujral, K. A. O'Hara, M. F. Toney, M. L. Chabinyc, and M. Ediger. Structural characterization of vapor-deposited glasses of an organic hole transport material with x-ray scattering. *Chemistry of Materials*, 27(9):3341–3348, apr 2015. doi: 10.1021/acs.chemmater.5b00583.

[76] A. Gujral, L. Yu, and M. Ediger. Anisotropic organic glasses. *Current Opinion in Solid State and Materials Science*, dec 2017. doi: 10.1016/j.cossms.2017.11.001.

[77] D. B. Hall and J. M. Torkelson. Small molecule probe diffusion in thin and ultrathin supported polymer films. *Macromolecules*, 31(25):8817–8825, dec 1998. doi: 10.1021/ma9812128.

[78] P. Z. Hanakata, J. F. Douglas, and F. W. Starr. Local variation of fragility and glass transition temperature of ultra-thin supported polymer films. *The Journal of Chemical Physics*, 137(24):244901, dec 2012. doi: 10.1063/1.4772402.

[79] J. L. Hartke. Drift mobilities of electrons and holes and space-charge-limited currents in amorphous selenium films. *Physical Review*, 125(4):1177–1192, feb 1962. doi: 10.1103/physrev.125.1177.

[80] J. L. Hartke and P. J. Regensburger. Electronic states in vitreous selenium. *Physical Review*, 139(3A):A970–A980, aug 1965. doi: 10.1103/physrev.139.a970.

[81] H. Hasegawa, T. Ohta, K. Ito, and H. Yokoyama. Stress-strain measurement of ultra-thin polystyrene films: Film thickness and molecular weight dependence of crazing stress. *Polymer*, 123:179–183, aug 2017. doi: 10.1016/j.polymer.2017.07.018.

[82] J. Hegedüs, K. Kohary, D. G. Pettifor, K. Shimakawa, and S. Kugler. Photoinduced volume changes in amorphous selenium. *Physical Review Letters*, 95(20), nov 2005. doi: 10.1103/physrevlett.95.206803.

[83] F. Hellman. Surface-induced ordering: A model for vapor-deposition growth of amorphous materials. *Applied Physics Letters*, 64(15):1947–1949, apr 1994. doi: 10.1063/1.111751.

[84] H. Heyuan and A. Shiva. Recent development of amorphous selenium-based x-ray detectors: A review. *IEEE Sensors Journal*, pages 1–1, 2019. doi: 10.1109/jsen.2019.2950319.

[85] K. Hinrichs and K.-J. Eichhorn, editors. *Ellipsometry of Functional Organic Surfaces and Films*. Springer Berlin Heidelberg, 2014. doi: 10.1007/978-3-642-40128-2.

[86] L. Hong, V. Novikov, and A. Sokolov. Is there a connection between fragility of glass forming systems and dynamic heterogeneity/cooperativity? *Journal of Non-Crystalline Solids*, 357(2):351–356, jan 2011. doi: 10.1016/j.jnoncrysol.2010.06.071.

[87] D. Huang and G. B. McKenna. New insights into the fragility dilemma in liquids. *The Journal of Chemical Physics*, 114(13):5621–5630, apr 2001. doi: 10.1063/1.1348029.

[88] G. Huang. *Synthesis of 1-aryl-3,5-di(1-naphthyl) Benzenes for Engineering Stable Thin Glass Films*. PhD thesis, 2018.

[89] L.-F. Huang and Z. Zeng. Roles of mass, structure, and bond strength in the phonon properties and lattice anharmonicity of single-layer mo and w dichalcogenides. *The Journal of Physical Chemistry C*, 119(32):18779–18789, aug 2015. doi: 10.1021/acs.jpcc.5b04669.

[90] X. Huang and C. B. Roth. Changes in the temperature-dependent specific volume of supported polystyrene films with film thickness. *The Journal of Chemical Physics*, 144(23):234903, jun 2016. doi: 10.1063/1.4953855.

[91] Y. Ikeda and K. Shimakawa. Real-time in situ measurements of photoinduced volume changes in chalcogenide glasses. *Journal of Non-Crystalline Solids*, 338-340:539–542, jun 2004. doi: 10.1016/j.jnoncrysol.2004.03.037.

[92] M. Ilton, D. Qi, and J. A. Forrest. Using nanoparticle embedding to probe surface rheology and the length scale of surface mobility in glassy polymers. *Macromolecules*, 42(18):6851–6854, sep 2009. doi: 10.1021/ma901057b.

[93] J. Jiang, D. M. Walters, D. Zhou, and M. D. Ediger. Substrate temperature controls molecular orientation in two-component vapor-deposited glasses. *Soft Matter*, 12(13):3265–3270, 2016. doi: 10.1039/c6sm00262e.

[94] Y. Jin. *The Effect of Thickness and Interface Interactions on Stability of Molecular Glasses*. PhD thesis, 2020. URL `https://proxy.library.upenn.edu/login?url=https://www-proquest-com.proxy.library.upenn.edu/dissertations-theses/effect-thickness-interface-interactions-on/docview/2480256091/se-2?accountid=14707`.

[95] G. Juška and K. Arlauskas. Impact ionization and mobilities of charge carriers at high electric fields in amorphous selenium. *Physica Status Solidi (a)*, 59(1):389–393, may 1980. doi: 10.1002/pssa.2210590151.

[96] S. Kasap, J. B. Frey, G. Belev, O. Tousignant, H. Mani, L. Laperriere, A. Reznik, and J. A. Rowlands. Amorphous selenium and its alloys from early xeroradiography to high resolution x-ray image detectors and ultrasensitive imaging tubes. *physica status solidi (b)*, 246(8):1794–1805, aug 2009. doi: 10.1002/pssb.200982007.

[97] Y. Katayama and K. Tsuji. X-ray structural studies on elemental liquids under high pressures. *Journal of Physics: Condensed Matter*, 15(36):6085–6103, aug 2003. doi: 10.1088/0953-8984/15/36/302.

[98] Y. Katayama, T. Mizutani, W. Utsumi, O. Shimomura, M. Yamakata, and K. ichi Funakoshi. A first-order liquid–liquid phase transition in phosphorus. *Nature*, 403 (6766):170–173, jan 2000. doi: 10.1038/35003143.

[99] W. Kauzmann. The nature of the glassy state and the behavior of liquids at low temperatures. *Chemical Reviews*, 43(2):219–256, oct 1948. doi: 10.1021/cr60135a002.

[100] S. Kawana and R. Jones. Effect of physical ageing in thin glassy polymer films. *The European Physical Journal E*, 10(3):223–230, mar 2003. doi: 10.1140/epje/i2002-10111-4.

[101] S. Kawana and R. A. L. Jones. Character of the glass transition in thin supported polymer films. *Physical Review E*, 63(2), jan 2001. doi: 10.1103/physreve.63.021501.

[102] K. L. Kearns, S. F. Swallen, M. D. Ediger, T. Wu, and L. Yu. Influence of substrate temperature on the stability of glasses prepared by vapor deposition. *The Journal of Chemical Physics*, 127(15):154702, oct 2007. doi: 10.1063/1.2789438.

[103] K. L. Kearns, S. F. Swallen, M. D. Ediger, T. Wu, Y. Sun, and L. Yu. Hiking down the energy landscape: progress toward the kauzmann temperature via vapor deposition. *The Journal of Physical Chemistry B*, 112(16):4934–4942, apr 2008. doi: 10.1021/jp7113384.

[104] J. L. Keddie, R. A. L. Jones, and R. A. Cory. Size-dependent depression of the glass transition temperature in polymer films. *Europhysics Letters (EPL)*, 27(1):59–64, jul 1994. doi: 10.1209/0295-5075/27/1/011.

[105] A. S. Keys, L. O. Hedges, J. P. Garrahan, S. C. Glotzer, and D. Chandler. Excitations are localized and relaxation is hierarchical in glass-forming liquids. *Physical Review X*, 1(2), nov 2011. doi: 10.1103/physrevx.1.021013.

[106] J.-H. Kim, A. Nizami, Y. Hwangbo, B. Jang, H.-J. Lee, C.-S. Woo, S. Hyun, and T.-S. Kim. Tensile testing of ultra-thin films on water surface. *Nature Communications*, 4 (1), oct 2013. doi: 10.1038/ncomms3520.

[107] S. Kim, S. A. Hewlett, C. B. Roth, and J. M. Torkelson. Confinement effects on glass transition temperature, transition breadth, and expansivity: Comparison of ellipsometry and fluorescence measurements on polystyrene films. *The European Physical Journal E*, 30(1), sep 2009. doi: 10.1140/epje/i2009-10510-y.

[108] J. G. Kirkwood. Critique of the free volume theory of the liquid state. *The Journal of Chemical Physics*, 18(3):380–382, mar 1950. doi: 10.1063/1.1747635.

[109] W. Kob and L. Berthier. Probing a liquid to glass transition in equilibrium. *Physical Review Letters*, 110(24), jun 2013. doi: 10.1103/physrevlett.110.245702.

[110] A. V. Kolobov, M. Kondo, H. Oyanagi, R. Durny, A. Matsuda, and K. Tanaka. Experimental evidence for negative correlation energy and valence alternation in amorphous selenium. *Physical Review B*, 56(2):R485–R488, jul 1997. doi: 10.1103/physrevb.56.r485.

[111] A. V. Kolobov, H. Oyanagi, K. Tanaka, and K. Tanaka. Structural study of amorphous selenium by in situ EXAFS: Observation of photoinduced bond alternation. *Physical Review B*, 55(2):726–734, jan 1997. doi: 10.1103/physrevb.55.726.

[112] A. V. Kolobov, M. Kondo, H. Oyanagi, A. Matsuda, and K. Tanaka. Negative correlation energy and valence alternation in amorphous selenium: Anin situoptically induced ESR study. *Physical Review B*, 58(18):12004–12010, nov 1998. doi: 10.1103/physrevb.58.12004.

[113] A. V. Kolobov, H. Oyanagi, A. Roy, and K. Tanaka. A nanometer scale mechanism for the reversible photostructural change in amorphous chalcogenides. *Journal of Non-Crystalline Solids*, 232-234:80–85, jul 1998. doi: 10.1016/s0022-3093(98)00397-4.

[114] M. Kotkata, F. Abdel-Wahab, and M. Al-Kotb. Effect of in-content on the optical properties of a-se films. *Applied Surface Science*, 255(22):9071–9077, aug 2009. doi: 10.1016/j.apsusc.2009.06.110.

[115] R. Kurita. Critical-like phenomena associated with liquid-liquid transition in a molecular liquid. *Science*, 306(5697):845–848, oct 2004. doi: 10.1126/science.1103073.

[116] T. Lan and J. M. Torkelson. Fragility-confinement effects: Apparent universality as a function of scaled thickness in films of freely deposited, linear polymer and its absence in densely grafted brushes. *Macromolecules*, 49(4):1331–1343, feb 2016. doi: 10.1021/acs.macromol.5b02489.

[117] W. T. Laughlin and D. R. Uhlmann. Viscous flow in simple organic liquids. *The Journal of Physical Chemistry*, 76(16):2317–2325, aug 1972. doi: 10.1021/j100660a023.

[118] A. Laventure, A. Gujral, O. Lebel, C. Pellerin, and M. D. Ediger. Influence of hydrogen bonding on the kinetic stability of vapor-deposited glasses of triazine derivatives. *The*

Journal of Physical Chemistry B, 121(10):2350–2358, mar 2017. doi: 10.1021/acs.jpcb.6b12676.

[119] E. Leon-Gutierrez, A. Sepúlveda, G. Garcia, M. T. Clavaguera-Mora, and J. Rodríguez-Viejo. Stability of thin film glasses of toluene and ethylbenzene formed by vapor deposition: an in situ nanocalorimetric study. *Phys. Chem. Chem. Phys.*, 12(44):14693–14698, 2010. doi: 10.1039/c0cp00208a.

[120] E. Leon-Gutierrez, A. Sepúlveda, G. Garcia, M. T. Clavaguera-Mora, and J. Rodríguez-Viejo. Correction: Stability of thin film glasses of toluene and ethylbenzene formed by vapor deposition: an in situ nanocalorimetric study. *Physical Chemistry Chemical Physics*, 18(11):8244–8245, 2016. doi: 10.1039/c6cp90023b.

[121] J. Li, X. Zhu, Q. Xie, G. Pu, and D. Yang. Deposition time effects on optical gap, dark conductivity and x-ray photoresponse properties of thermal evaporated a-se thin films. *Journal of Materials Science: Materials in Electronics*, sep 2018. doi: 10.1007/s10854-018-0052-7.

[122] J. Li, X. Zhu, and D. Yang. Evaporation time effects on structural, optical and x-ray photoresponse properties of thermal evaporated a-se thin films at low vacuum degree. *AIP Advances*, 8(9):095304, sep 2018. doi: 10.1063/1.5047832.

[123] J. Li, X. Zhu, D. Yang, P. Gu, and H. Wu. Investigations on structural, optical and x-radiation responsive properties of a-se thin films fabricated by thermal evaporation method at low vacuum degree. *Materials*, 11(3):368, mar 2018. doi: 10.3390/ma11030368.

[124] Y. Li, W. Zhang, C. Bishop, C. Huang, M. D. Ediger, and L. Yu. Surface diffusion in glasses of rod-like molecules posaconazole and itraconazole: effect of interfacial molecular alignment and bulk penetration. *Soft Matter*, 16(21):5062–5070, 2020. doi: 10.1039/d0sm00353k.

[125] Y. Z. Li, Y. T. Sun, Z. Lu, M. Z. Li, H. Y. Bai, and W. H. Wang. Size effect on dynamics and glass transition in metallic liquids and glasses. *The Journal of Chemical Physics*, 146(22):224502, jun 2017. doi: 10.1063/1.4984977.

[126] J. E. G. Lipson and S. T. Milner. Local and average glass transitions in polymer thin films. *Macromolecules*, 43(23):9874–9880, dec 2010. doi: 10.1021/ma101099n.

[127] T. Liu, K. Cheng, E. Salami-Ranjbaran, F. Gao, E. C. Glor, M. Li, P. J. Walsh, and Z. Fakhraai. Synthesis and high-throughput characterization of structural analogues of molecular glassformers: 1,3,5-trisarylbenzenes. *Soft Matter*, 11(38):7558–7566, 2015. doi: 10.1039/c5sm01044f.

[128] T. Liu, K. Cheng, E. Salami-Ranjbaran, F. Gao, C. Li, X. Tong, Y.-C. Lin, Y. Zhang, W. Zhang, L. Klinge, P. J. Walsh, and Z. Fakhraai. The effect of chemical structure on

the stability of physical vapor deposited glasses of 1,3,5-triarylbenzene. *The Journal of Chemical Physics*, 143(8):084506, aug 2015. doi: 10.1063/1.4928521.

[129] T. Liu, A. L. Exarhos, E. C. Alguire, F. Gao, E. Salami-Ranjbaran, K. Cheng, T. Jia, J. E. Subotnik, P. J. Walsh, J. M. Kikkawa, and Z. Fakhraai. Birefringent stable glass with predominantly isotropic molecular orientation. *Physical Review Letters*, 119(9), aug 2017. doi: 10.1103/physrevlett.119.095502.

[130] C. Lo, J. T. Wan, and K. Yu. Geometric anisotropic effects on local field distribution: Generalized clausius–mossotti relation. *Computer Physics Communications*, 142(1-3): 453–456, dec 2001. doi: 10.1016/s0010-4655(01)00388-5.

[131] V. Lubchenko and P. G. Wolynes. Theory of structural glasses and supercooled liquids. doi: 10.1146/annurev.physchem.58.032806.104653.

[132] P. Luo, C. R. Cao, F. Zhu, Y. M. Lv, Y. H. Liu, P. Wen, H. Y. Bai, G. Vaughan, M. di Michiel, B. Ruta, and W. H. Wang. Ultrastable metallic glasses formed on cold substrates. *Nature Communications*, 9(1), apr 2018. doi: 10.1038/s41467-018-03656-4.

[133] I. Lyubimov, L. Antony, D. M. Walters, D. Rodney, M. D. Ediger, and J. J. de Pablo. Orientational anisotropy in simulated vapor-deposited molecular glasses. *The Journal of Chemical Physics*, 143(9):094502, sep 2015. doi: 10.1063/1.4928523.

[134] J. Málek, R. Svoboda, P. Pustková, and P. Čičmanec. Volume and enthalpy relaxation of a-se in the glass transition region. *Journal of Non-Crystalline Solids*, 355(4-5):264–272, feb 2009. doi: 10.1016/j.jnoncrysol.2008.11.014.

[135] J. H. Mangalara, M. D. Marvin, and D. S. Simmons. Three-layer model for the emergence of ultrastable glasses from the surfaces of supercooled liquids. *The Journal of Physical Chemistry B*, 120(21):4861–4865, may 2016. doi: 10.1021/acs.jpcb.6b04736.

[136] M. Marple, J. Badger, I. Hung, Z. Gan, K. Kovnir, and S. Sen. Structure of amorphous selenium by 2d 77 se NMR spectroscopy: An end to the dilemma of chain versus ring. *Angewandte Chemie International Edition*, 56(33):9777–9781, jul 2017. doi: 10.1002/anie.201704323.

[137] L.-M. Martinez and C. A. Angell. A thermodynamic connection to the fragility of glass-forming liquids. *Nature*, 410(6829):663–667, apr 2001. doi: 10.1038/35070517.

[138] M. D. Marvin, R. J. Lang, and D. S. Simmons. Nanoconfinement effects on the fragility of glass formation of a model freestanding polymer film. *Soft Matter*, 10(18): 3166, 2014. doi: 10.1039/c3sm53160k.

[139] J. C. Mauro and R. J. Loucks. Selenium glass transition: A model based on the enthalpy landscape approach and nonequilibrium statistical mechanics. *Physical Review B*, 76(17), nov 2007. doi: 10.1103/physrevb.76.174202.

[140] J. D. McGraw, T. S. Chan, S. Maurer, T. Salez, M. Benzaquen, E. Raphaël, M. Brinkmann, and K. Jacobs. Slip-mediated dewetting of polymer microdroplets. *Proceedings of the National Academy of Sciences*, 113(5):1168–1173, jan 2016. doi: 10.1073/pnas.1513565113.

[141] J. C. Meredith, A. P. Smith, A. Karim, and E. J. Amis. Combinatorial materials science for polymer thin-film dewetting. *Macromolecules*, 33(26):9747–9756, dec 2000. doi: 10.1021/ma001298g.

[142] M. Merolle, J. P. Garrahan, and D. Chandler. Space-time thermodynamics of the glass transition. *Proceedings of the National Academy of Sciences*, 102(31):10837–10840, jul 2005. doi: 10.1073/pnas.0504820102.

[143] A. Mikaeili, T. Matsushima, Y. Esaki, S. A. Yazdani, C. Adachi, and E. Mohajerani. The origin of changes in electrical properties of organic films fabricated at various vacuum-deposition rates. *Optical Materials*, 91:93–100, may 2019. doi: 10.1016/j.optmat.2019.03.012.

[144] S. Mirigian and K. S. Schweizer. Unified theory of activated relaxation in liquids over 14 decades in time. *The Journal of Physical Chemistry Letters*, 4(21):3648–3653, oct 2013. doi: 10.1021/jz4018943.

[145] S. Mirigian and K. S. Schweizer. Elastically cooperative activated barrier hopping theory of relaxation in viscous fluids. i. general formulation and application to hard sphere fluids. *The Journal of Chemical Physics*, 140(19):194506, may 2014. doi: 10.1063/1.4874842.

[146] S. Mirigian and K. S. Schweizer. Elastically cooperative activated barrier hopping theory of relaxation in viscous fluids. II. thermal liquids. *The Journal of Chemical Physics*, 140(19):194507, may 2014. doi: 10.1063/1.4874843.

[147] O. Mishima and Y. Suzuki. Propagation of the polyamorphic transition of ice and the liquid–liquid critical point. *Nature*, 419(6907):599–603, oct 2002. doi: 10.1038/nature01106.

[148] A. R. Moore, G. Huang, S. Wolf, P. J. Walsh, Z. Fakhraai, and R. A. Riggleman. Effects of microstructure formation on the stability of vapor-deposited glasses. *Proceedings of the National Academy of Sciences*, 116(13):5937–5942, mar 2019. doi: 10.1073/pnas.1821761116.

[149] C. T. MOYNIHAN and U. E. SCHNAUS. Heat capacity and equilibrium polymerization of vitreous se. *Journal of the American Ceramic Society*, 54(3):136–140, mar 1971. doi: 10.1111/j.1151-2916.1971.tb12240.x.

[150] S. V. Muley, C. Cao, D. Chatterjee, C. Francis, F. P. Lu, M. D. Ediger, J. H. Perepezko, and P. M. Voyles. Varying kinetic stability, icosahedral ordering, and

mechanical properties of a model zr-cu-al metallic glass by sputtering. *Physical Review Materials*, 5(3), mar 2021. doi: 10.1103/physrevmaterials.5.033602.

[151] W. W. Mullins. Flattening of a nearly plane solid surface due to capillarity. *Journal of Applied Physics*, 30(1):77–83, jan 1959. doi: 10.1063/1.1734979.

[152] Y. Noguchi, Y. Miyazaki, Y. Tanaka, N. Sato, Y. Nakayama, T. D. Schmidt, W. Brütting, and H. Ishii. Charge accumulation at organic semiconductor interfaces due to a permanent dipole moment and its orientational order in bilayer devices. *Journal of Applied Physics*, 111(11):114508, jun 2012. doi: 10.1063/1.4724349.

[153] P. A. O'Connell. Rheological measurements of the thermoviscoelastic response of ultrathin polymer films. *Science*, 307(5716):1760–1763, mar 2005. doi: 10.1126/science.1105658.

[154] P. A. O'Connell and G. B. McKenna. Arrhenius-type temperature dependence of the segmental relaxation below tg. *The Journal of Chemical Physics*, 110(22):11054–11060, jun 1999. doi: 10.1063/1.479046.

[155] G. M. Odegard and A. Bandyopadhyay. Physical aging of epoxy polymers and their composites. *Journal of Polymer Science Part B: Polymer Physics*, 49(24):1695–1716, oct 2011. doi: 10.1002/polb.22384.

[156] M. Oh-e, H. Ogata, and F. Araoka. Randomization and constraint of molecular alignment and orientation: Temperature-dependent anisotropy and phase transition in vapor-deposited thin films of an organic cross-shaped molecule. *ACS Omega*, 4(1):39–47, jan 2019. doi: 10.1021/acsomega.8b02560.

[157] W. Oldekop. Theoretical discussion of the viscosity of glasses. *Glastech Ber*, 30:8–14, 1957.

[158] W. J. Orts, J. H. van Zanten, W. li Wu, and S. K. Satija. Observation of temperature dependent thicknesses in ultrathin polystyrene films on silicon. *Physical Review Letters*, 71(6):867–870, aug 1993. doi: 10.1103/physrevlett.71.867.

[159] K. Paeng and M. D. Ediger. Molecular motion in free-standing thin films of poly(methyl methacrylate), poly(4-tert-butylstyrene), poly(α-methylstyrene), and poly(2-vinylpyridine). *Macromolecules*, 44(17):7034–7042, sep 2011. doi: 10.1021/ma201266r.

[160] K. Paeng, S. F. Swallen, and M. D. Ediger. Direct measurement of molecular motion in freestanding polystyrene thin films. *Journal of the American Chemical Society*, 133(22):8444–8447, jun 2011. doi: 10.1021/ja2022834.

[161] A. D. Phan and K. S. Schweizer. Elastically collective nonlinear langevin equation theory of glass-forming liquids: Transient localization, thermodynamic mapping, and

cooperativity. *The Journal of Physical Chemistry B*, 122(35):8451–8461, aug 2018. doi: 10.1021/acs.jpcb.8b04975.

[162] A. D. Phan and K. S. Schweizer. Theory of spatial gradients of relaxation, vitrification temperature and fragility of glass-forming polymer liquids near solid substrates. *ACS Macro Letters*, 9(4):448–453, mar 2020. doi: 10.1021/acsmacrolett.0c00006.

[163] R. Pinchaipat, M. Campo, F. Turci, J. E. Hallett, T. Speck, and C. P. Royall. Experimental evidence for a structural-dynamical transition in trajectory space. *Physical Review Letters*, 119(2), jul 2017. doi: 10.1103/physrevlett.119.028004.

[164] V. V. Poborchii, A. V. Kolobov, and K. Tanaka. An in situ raman study of polarization-dependent photocrystallization in amorphous selenium films. *Applied Physics Letters*, 72(10):1167–1169, mar 1998. doi: 10.1063/1.121002.

[165] V. V. Poborchii, A. V. Kolobov, and K. Tanaka. Photomelting of selenium at low temperature. *Applied Physics Letters*, 74(2):215–217, jan 1999. doi: 10.1063/1.123297.

[166] J. E. Pye, K. A. Rohald, E. A. Baker, and C. B. Roth. Physical aging in ultrathin polystyrene films: Evidence of a gradient in dynamics at the free surface and its connection to the glass transition temperature reductions. *Macromolecules*, 43(19): 8296–8303, oct 2010. doi: 10.1021/ma101412r.

[167] D. Qi, M. Ilton, and J. A. Forrest. Measuring surface and bulk relaxation in glassy polymers. *The European Physical Journal E*, 34(6), jun 2011. doi: 10.1140/epje/i2011-11056-1.

[168] D. Qi, C. R. Daley, Y. Chai, and J. A. Forrest. Molecular weight dependence of near surface dynamical mechanical properties of polymers. *Soft Matter*, 9(37):8958, 2013. doi: 10.1039/c3sm51601f.

[169] Y. Qiu, L. W. Antony, J. J. de Pablo, and M. D. Ediger. Photostability can be significantly modulated by molecular packing in glasses. *Journal of the American Chemical Society*, 138(35):11282–11289, aug 2016. doi: 10.1021/jacs.6b06372.

[170] Y. Qiu, L. W. Antony, J. M. Torkelson, J. J. de Pablo, and M. D. Ediger. Tenfold increase in the photostability of an azobenzene guest in vapor-deposited glass mixtures. *The Journal of Chemical Physics*, 149(20):204503, nov 2018. doi: 10.1063/1.5052003.

[171] A. N. Raegen, J. Yin, Q. Zhou, and J. A. Forrest. Ultrastable monodisperse polymer glass formed by physical vapour deposition. *Nature Materials*, jul 2020. doi: 10.1038/s41563-020-0723-7.

[172] J. Ràfols-Ribé, M. Gonzalez-Silveira, C. Rodríguez-Tinoco, and J. Rodríguez-Viejo. The role of thermodynamic stability in the characteristics of the devitrification front of vapour-deposited glasses of toluene. *Physical Chemistry Chemical Physics*, 19(18): 11089–11097, 2017. doi: 10.1039/c7cp00741h.

[173] J. Ràfols-Ribé, A. Vila-Costa, C. Rodríguez-Tinoco, A. F. Lopeandía, J. Rodríguez-Viejo, and M. Gonzalez-Silveira. Kinetic arrest of front transformation to gain access to the bulk glass transition in ultrathin films of vapour-deposited glasses. *Physical Chemistry Chemical Physics*, 20(47):29989–29995, 2018. doi: 10.1039/c8cp06264a.

[174] H. Rau. Vapour composition and critical constants of selenium. *The Journal of Chemical Thermodynamics*, 6(6):525–535, jun 1974. doi: 10.1016/0021-9614(74)90039-1.

[175] D. R. Reichman and P. Charbonneau. Mode-coupling theory. *Journal of Statistical Mechanics: Theory and Experiment*, 2005(05):P05013, may 2005. doi: 10.1088/1742-5468/2005/05/p05013.

[176] G. Reiter. Probing properties of polymers in thin films via dewetting. In *Glass Transition, Dynamics and Heterogeneity of Polymer Thin Films*, pages 29–63. Springer Berlin Heidelberg, 2012. doi: 10.1007/12_2012_174.

[177] A. Reznik, S. D. Baranovskii, O. Rubel, G. Juska, S. O. Kasap, Y. Ohkawa, K. Tanioka, and J. A. Rowlands. Avalanche multiplication phenomenon in amorphous semiconductors: Amorphous selenium versus hydrogenated amorphous silicon. *Journal of Applied Physics*, 102(5):053711, sep 2007. doi: 10.1063/1.2776223.

[178] R. Richert. Heterogeneous dynamics in liquids: fluctuations in space and time. *Journal of Physics: Condensed Matter*, 14(23):R703–R738, may 2002. doi: 10.1088/0953-8984/14/23/201.

[179] B. Riechers, A. Guiseppi-Elie, M. D. Ediger, and R. Richert. Ultrastable and polyamorphic states of vapor-deposited 2-methyltetrahydrofuran. *The Journal of Chemical Physics*, 150(21):214502, jun 2019. doi: 10.1063/1.5091796.

[180] F. Ritort and P. Sollich. Glassy dynamics of kinetically constrained models. *Advances in Physics*, 52(4):219–342, jun 2003. doi: 10.1080/0001873031000093582.

[181] G. Robinson, S. B. Ross-Murphy, and E. R. Morris. Viscosity-molecular weight relationships, intrinsic chain flexibility, and dynamic solution properties of guar galactomannan. *Carbohydrate Research*, 107(1):17–32, sep 1982. doi: 10.1016/s0008-6215(00)80772-7.

[182] C. Rodríguez-Tinoco, M. Gonzalez-Silveira, J. Ràfols-Ribé, G. Garcia, and J. Rodríguez-Viejo. Highly stable glasses of celecoxib: Influence on thermo-kinetic properties, microstructure and response towards crystal growth. *Journal of Non-Crystalline Solids*, 407:256–261, jan 2015. doi: 10.1016/j.jnoncrysol.2014.07.031.

[183] C. Rodríguez-Tinoco, M. Gonzalez-Silveira, J. Ràfols-Ribé, A. F. Lopeandía, and J. Rodríguez-Viejo. Transformation kinetics of vapor-deposited thin film organic glasses: the role of stability and molecular packing anisotropy. *Physical Chemistry Chemical Physics*, 17(46):31195–31201, 2015. doi: 10.1039/c5cp04692k.

[184] C. B. Roth, B. Deh, B. G. Nickel, and J. R. Dutcher. Evidence of convective constraint release during hole growth in freely standing polystyrene films at low temperatures. *Physical Review E*, 72(2), aug 2005. doi: 10.1103/physreve.72.021802.

[185] C. P. Royall, F. Turci, and T. Speck. Dynamical phase transitions and their relation to structural and thermodynamic aspects of glass physics. *The Journal of Chemical Physics*, 153(9):090901, sep 2020. doi: 10.1063/5.0006998.

[186] P. V. Rysselberghe. Remarks concerning the clausius-mossotti law. *The Journal of Physical Chemistry*, 36(4):1152–1155, apr 1932. doi: 10.1021/j150334a007.

[187] J. M. Sallese, A. Ils, D. Bouvet, P. Fazan, and C. Merritt. Modeling of the depletion of the amorphous-silicon surface during hemispherical grained silicon formation. *Journal of Applied Physics*, 88(10):5751–5755, nov 2000. doi: 10.1063/1.1321024.

[188] S. Samanta, G. Huang, G. Gao, Y. Zhang, A. Zhang, S. Wolf, C. N. Woods, Y. Jin, P. J. Walsh, and Z. Fakhraai. Exploring the importance of surface diffusion in stability of vapor-deposited organic glasses. *The Journal of Physical Chemistry B*, 123(18): 4108–4117, apr 2019. doi: 10.1021/acs.jpcb.9b01012.

[189] K. S. Schweizer and D. S. Simmons. Progress towards a phenomenological picture and theoretical understanding of glassy dynamics and vitrification near interfaces and under nanoconfinement. *The Journal of Chemical Physics*, 151(24):240901, dec 2019. doi: 10.1063/1.5129405.

[190] T. Scopigno. Is the fragility of a liquid embedded in the properties of its glass? *Science*, 302(5646):849–852, oct 2003. doi: 10.1126/science.1089446.

[191] T. Scopigno, W. Steurer, S. Yannopoulos, A. Chrissanthopoulos, M. Krisch, G. Ruocco, and T. Wagner. Vibrational dynamics and surface structure of amorphous selenium. *Nature Communications*, 2:195, feb 2011. doi: 10.1038/ncomms1197.

[192] S. Sen, S. Gaudio, B. G. Aitken, and C. E. Lesher. Observation of a pressure-induced first-order polyamorphic transition in a chalcogenide glass at ambient temperature. *Physical Review Letters*, 97(2), jul 2006. doi: 10.1103/physrevlett.97.025504.

[193] U. Senapati and A. K. Varshneya. Viscosity of chalcogenide glass-forming liquids: an anomaly in the 'strong' and 'fragile' classification. *Journal of Non-Crystalline Solids*, 197(2-3):210–218, may 1996. doi: 10.1016/0022-3093(95)00628-1.

[194] A. Sepúlveda, E. Leon-Gutierrez, M. Gonzalez-Silveira, C. Rodríguez-Tinoco, M. T. Clavaguera-Mora, and J. Rodríguez-Viejo. Accelerated aging in ultrathin films of a molecular glass former. *Physical Review Letters*, 107(2), jul 2011. doi: 10.1103/physrevlett.107.025901.

[195] A. L. Shapiro, P. W. Rooney, M. Q. Tran, F. Hellman, K. M. Ring, K. L. Kavanagh, B. Rellinghaus, and D. Weller. Growth-induced magnetic anisotropy and clustering in

vapor-deposited co-pt alloy films. *Physical Review B*, 60(18):12826–12836, nov 1999. doi: 10.1103/physrevb.60.12826.

[196] J. S. Sharp, J. H. Teichroeb, and J. A. Forrest. The properties of free polymer surfaces and their influence on the glass transition temperature of thin polystyrene films. *The European Physical Journal E*, 15(4):473–487, dec 2004. doi: 10.1140/epje/i2004-10078-0.

[197] A. Shavit and R. A. Riggleman. Influence of backbone rigidity on nanoscale confinement effects in model glass-forming polymers. *Macromolecules*, 46(12):5044–5052, jun 2013. doi: 10.1021/ma400210w.

[198] H. W. Sheng, H. Z. Liu, Y. Q. Cheng, J. Wen, P. L. Lee, W. K. Luo, S. D. Shastri, and E. Ma. Polyamorphism in a metallic glass. *Nature Materials*, 6(3):192–197, feb 2007. doi: 10.1038/nmat1839.

[199] Z. Shi, P. G. Debenedetti, and F. H. Stillinger. Properties of model atomic free-standing thin films. *The Journal of Chemical Physics*, 134(11):114524, mar 2011. doi: 10.1063/1.3565480.

[200] M. Shibata, Y. Sakai, and D. Yokoyama. Advantages and disadvantages of vacuum-deposited and spin-coated amorphous organic semiconductor films for organic light-emitting diodes. *Journal of Materials Chemistry C*, 3(42):11178–11191, 2015. doi: 10.1039/c5tc01911g.

[201] D. Sidebottom. Fifty years of fragility: A view from the cheap seats. *Journal of Non-Crystalline Solids*, 524:119641, nov 2019. doi: 10.1016/j.jnoncrysol.2019.119641.

[202] D. L. Sidebottom. Connecting glass-forming fragility to network topology. *Frontiers in Materials*, 6, jun 2019. doi: 10.3389/fmats.2019.00144.

[203] S. Simon, J. Sobieski, and D. Plazek. Volume and enthalpy recovery of polystyrene. *Polymer*, 42(6):2555–2567, mar 2001. doi: 10.1016/s0032-3861(00)00623-6.

[204] L. Singh, P. J. Ludovice, and C. L. Henderson. Influence of molecular weight and film thickness on the glass transition temperature and coefficient of thermal expansion of supported ultrathin polymer films. *Thin Solid Films*, 449(1-2):231–241, feb 2004. doi: 10.1016/s0040-6090(03)01353-1.

[205] S. Singh, M. D. Ediger, and J. J. de Pablo. Ultrastable glasses from in silico vapour deposition. *Nature Materials*, 12(2):139–144, jan 2013. doi: 10.1038/nmat3521.

[206] R. S. Smith, R. A. May, and B. D. Kay. Probing toluene and ethylbenzene stable glass formation using inert gas permeation. *The Journal of Physical Chemistry Letters*, 6 (18):3639–3644, sep 2015. doi: 10.1021/acs.jpclett.5b01611.

[207] S. Sohn, K. H. Park, S.-K. Kwon, H.-K. Lee, H. Ahn, S. Jung, and Y.-H. Kim. Preferential orientation of tetrahedral silicon-based hosts in phosphorescent organic

light-emitting diodes. *ACS Omega*, 3(8):9989–9996, aug 2018. doi: 10.1021/acsomega.8b01358.

[208] C. M. Stafford, C. Harrison, K. L. Beers, A. Karim, E. J. Amis, M. R. VanLandingham, H.-C. Kim, W. Volksen, R. D. Miller, and E. E. Simonyi. A buckling-based metrology for measuring the elastic moduli of polymeric thin films. *Nature Materials*, 3(8):545–550, jul 2004. doi: 10.1038/nmat1175.

[209] C. M. Stafford, B. D. Vogt, C. Harrison, D. Julthongpiput, and R. Huang. Elastic moduli of ultrathin amorphous polymer films. *Macromolecules*, 39(15):5095–5099, jul 2006. doi: 10.1021/ma060790i.

[210] S. Stølen, T. Grande, and H.-B. Johnsen. Fragility transition in GeSe2–se liquids. *Physical Chemistry Chemical Physics*, 4(14):3396–3399, jun 2002. doi: 10.1039/b201396g.

[211] P. Strohriegl and J. Grazulevicius. Charge-transporting molecular glasses. *Advanced Materials*, 14(20):1439–1452, oct 2002. doi: 10.1002/1521-4095(20021016)14:20⟨1439::aid-adma1439⟩3.0.co;2-h.

[212] D. M. Sussman, S. S. Schoenholz, E. D. Cubuk, and A. J. Liu. Disconnecting structure and dynamics in glassy thin films. *Proceedings of the National Academy of Sciences*, 114(40):10601–10605, sep 2017. doi: 10.1073/pnas.1703927114.

[213] S. F. Swallen, K. L. Kearns, M. K. Mapes, Y. S. Kim, R. J. McMahon, M. D. Ediger, T. Wu, L. Yu, and S. Satija. Organic glasses with exceptional thermodynamic and kinetic stability. *Science*, 315(5810):353–356, jan 2007. doi: 10.1126/science.1135795.

[214] S. F. Swallen, K. Traynor, R. J. McMahon, M. D. Ediger, and T. E. Mates. Stable glass transformation to supercooled liquid via surface-initiated growth front. *Physical Review Letters*, 102(6), feb 2009. doi: 10.1103/physrevlett.102.065503.

[215] G. Tammann and W. Hesse. Die abhängigkeit der viscosität von der temperatur bie unterkühlten flüssigkeiten. *Zeitschrift für anorganische und allgemeine Chemie*, 156 (1):245–257, oct 1926. doi: 10.1002/zaac.19261560121.

[216] K. Tanaka and K. Shimakawa. Mechanisms of photoinduced fluidity in chalcogenide glasses: Molecular orbital analyses. *Journal of Non-Crystalline Solids*, 481:579–584, feb 2018. doi: 10.1016/j.jnoncrysol.2017.12.005.

[217] X.-P. Tang, U. Geyer, R. Busch, W. L. Johnson, and Y. Wu. Diffusion mechanisms in metallic supercooled liquids and glasses. *Nature*, 402(6758):160–162, nov 1999. doi: 10.1038/45996.

[218] C. Tangpatjaroen, K. Bagchi, R. A. Martínez, D. Grierson, and I. Szlufarska. Mechanical properties of structure-tunable, vapor-deposited TPD glass. *The Journal of Physical Chemistry C*, 122(48):27775–27781, nov 2018. doi: 10.1021/acs.jpcc.8b09718.

[219] J. Teichroeb and J. Forrest. Direct imaging of nanoparticle embedding to probe viscoelasticity of polymer surfaces. *Physical Review Letters*, 91(1), jul 2003. doi: 10.1103/physrevlett.91.016104.

[220] E. Thoms, J. P. Gabriel, A. Guiseppi-Elie, M. D. Ediger, and R. Richert. In situ observation of fast surface dynamics during the vapor-deposition of a stable organic glass. *Soft Matter*, 2020. doi: 10.1039/d0sm01916j.

[221] Thorlabs. Product specification sheet of LEDWE-15 - epoxy-encased white light LED. `https://www.thorlabs.com/drawings/980c9974da1daa2-D1A8DE62-E2C5-8C0F-1EBF3112880A1576/LEDWE-15-SpecSheet.pdf`, 2020.

[222] J. M. Torres, C. M. Stafford, and B. D. Vogt. Elastic modulus of amorphous polymer thin films: Relationship to the glass transition temperature. *ACS Nano*, 3(9):2677–2685, aug 2009. doi: 10.1021/nn9006847.

[223] J. M. Torres, N. Bakken, J. Li, and B. D. Vogt. Substrate temperature to control moduli and water uptake in thin films of vapor deposited n,n′-di(1-naphthyl)-n,n′-diphenyl-(1,1′-biphenyl)-4,4′-diamine (NPD). *The Journal of Physical Chemistry B*, 119(35):11928–11934, aug 2015. doi: 10.1021/acs.jpcb.5b05814.

[224] M. Tylinski, Y. Z. Chua, M. S. Beasley, C. Schick, and M. D. Ediger. Vapor-deposited alcohol glasses reveal a wide range of kinetic stability. *The Journal of Chemical Physics*, 145(17):174506, nov 2016. doi: 10.1063/1.4966582.

[225] M. Tylinski, M. S. Beasley, Y. Z. Chua, C. Schick, and M. D. Ediger. Limited surface mobility inhibits stable glass formation for 2-ethyl-1-hexanol. *The Journal of Chemical Physics*, 146(20):203317, may 2017. doi: 10.1063/1.4977787.

[226] F. Varnik, J. Baschnagel, and K. Binder. Reduction of the glass transition temperature in polymer films: A molecular-dynamics study. *Physical Review E*, 65(2), jan 2002. doi: 10.1103/physreve.65.021507.

[227] T. Vilmin and E. Raphaël. Dewetting of thin polymer films. *The European Physical Journal E*, 21(2):161–174, oct 2006. doi: 10.1140/epje/i2006-10057-5.

[228] I. Virginia Semiconductor. Basic mechanical and thermal properties of silicon. `http://www.virginiasemi.com/pdf/Basic%20Mechanical%20and%20Thermal%20Properties%20of%20Silicon.pdf`, 2020.

[229] H. VOGEL. Das temperaturabhangigkeitsgesetz der viskositat von flussigkeiten. *Phys. Z.*, 22:645–646, 1921. URL `https://ci.nii.ac.jp/naid/10004192038/en/`.

[230] G. Wahnström. Molecular-dynamics study of a supercooled two-component lennard-jones system. *Physical Review A*, 44(6):3752–3764, sep 1991. doi: 10.1103/physreva.44.3752.

[231] W. E. Wallace, J. H. van Zanten, and W. L. Wu. Influence of an impenetrable interface on a polymer glass-transition temperature. *Physical Review E*, 52(4):R3329–R3332, oct 1995. doi: 10.1103/physreve.52.r3329.

[232] D. M. Walters, R. Richert, and M. D. Ediger. Thermal stability of vapor-deposited stable glasses of an organic semiconductor. *The Journal of Chemical Physics*, 142 (13):134504, apr 2015. doi: 10.1063/1.4916649.

[233] D. M. Walters, L. Antony, J. J. de Pablo, and M. D. Ediger. Influence of molecular shape on the thermal stability and molecular orientation of vapor-deposited organic semiconductors. *The Journal of Physical Chemistry Letters*, 8(14):3380–3386, jul 2017. doi: 10.1021/acs.jpclett.7b01097.

[234] E. Williams and N. Lavery. Laser processing of bulk metallic glass: A review. *Journal of Materials Processing Technology*, 247:73–91, sep 2017. doi: 10.1016/j.jmatprotec.2017.03.034.

[235] Y. Xia, W. Zhu, M. Lockhart, B. Aitken, and S. Sen. Fragility and rheological behavior of metaphosphate liquids: Insights into their chain vs. network characters. *Journal of Non-Crystalline Solids*, 514:77–82, jun 2019. doi: 10.1016/j.jnoncrysol.2019.03.036.

[236] X. Xing, L. Zhong, L. Zhang, Z. Chen, B. Qu, E. Chen, L. Xiao, and Q. Gong. Essential differences of organic films at the molecular level via vacuum deposition and solution processes for organic light-emitting diodes. *The Journal of Physical Chemistry C*, 117(48):25405–25408, nov 2013. doi: 10.1021/jp410547w.

[237] Q. Xu, N. Zhu, H. Fang, X. Wang, R. D. Priestley, and B. Zuo. Decoupling role of film thickness and interfacial effect on polymer thin film dynamics. *ACS Macro Letters*, pages 1–8, dec 2020. doi: 10.1021/acsmacrolett.0c00760.

[238] Y. Xu, P. Grobelny, A. V. Allmen, K. Knudson, M. Pikal, J. F. Carpenter, and T. W. Randolph. Protein quantity on the air–solid interface determines degradation rates of human growth hormone in lyophilized samples. *Journal of Pharmaceutical Sciences*, 103(5):1356–1366, may 2014. doi: 10.1002/jps.23926.

[239] Z. Yang, Y. Fujii, F. K. Lee, C.-H. Lam, and O. K. C. Tsui. Glass transition dynamics and surface layer mobility in unentangled polystyrene films. *Science*, 328(5986):1676–1679, jun 2010. doi: 10.1126/science.1184394.

[240] S. N. Yannopoulos and K. S. Andrikopoulos. Raman scattering study on structural and dynamical features of noncrystalline selenium. *The Journal of Chemical Physics*, 121(10):4747–4758, sep 2004. doi: 10.1063/1.1780151.

[241] M. Yasaka. X-ray thin-film measurement techniques. *The Rigaku Journal*, 26(2):1–9, 2010.

[242] D. Yokoyama. Molecular orientation in small-molecule organic light-emitting diodes. *Journal of Materials Chemistry*, 21(48):19187, 2011. doi: 10.1039/c1jm13417e.

[243] D. Yokoyama, Y. Setoguchi, A. Sakaguchi, M. Suzuki, and C. Adachi. Orientation control of linear-shaped molecules in vacuum-deposited organic amorphous films and its effect on carrier mobilities. *Advanced Functional Materials*, 20(3):386–391, feb 2010. doi: 10.1002/adfm.200901684.

[244] H. Yoon and G. B. McKenna. Dynamic and temperature dependent response of physical vapor deposited se in freely standing nanometric thin films. *The Journal of Chemical Physics*, 144(18):184501, may 2016. doi: 10.1063/1.4948322.

[245] L. Yu. Amorphous pharmaceutical solids: preparation, characterization and stabilization. *Advanced Drug Delivery Reviews*, 48(1):27–42, may 2001. doi: 10.1016/s0169-409x(01)00098-9.

[246] L. Yu. Surface mobility of molecular glasses and its importance in physical stability. *Advanced Drug Delivery Reviews*, 100:3–9, may 2016. doi: 10.1016/j.addr.2016.01.005.

[247] C. Yuan, M. Ouyang, and J. T. Koberstein. Effects of low-energy end groups on the dewetting dynamics of poly(styrene) films on poly(methyl methacrylate) substrates. *Macromolecules*, 32(7):2329–2333, apr 1999. doi: 10.1021/ma980774o.

[248] A. Zhang, Y. Jin, T. Liu, R. B. Stephens, and Z. Fakhraai. Polyamorphism of vapor-deposited amorphous selenium in response to light. *Proceedings of the National Academy of Sciences*, 117(39):24076–24081, sep 2020. doi: 10.1073/pnas.2009852117.

[249] K. Zhang, Y. Li, Q. Huang, B. Wang, X. Zheng, Y. Ren, and W. Yang. Ultrastable amorphous sb2se3 film. *The Journal of Physical Chemistry B*, 121(34):8188–8194, aug 2017. doi: 10.1021/acs.jpcb.7b03408.

[250] W. Zhang and L. Yu. Surface diffusion of polymer glasses. *Macromolecules*, 49(2):731–735, jan 2016. doi: 10.1021/acs.macromol.5b02294.

[251] X. Zhang and D. A. Drabold. Direct molecular dynamic simulation of light-induced structural change in amorphous selenium. *Physical Review Letters*, 83(24):5042–5045, dec 1999. doi: 10.1103/physrevlett.83.5042.

[252] Y. Zhang and Z. Fakhraai. Decoupling of surface diffusion and relaxation dynamics of molecular glasses. *Proceedings of the National Academy of Sciences*, 114(19):4915–4919, apr 2017. doi: 10.1073/pnas.1701400114.

[253] Y. Zhang and Z. Fakhraai. Invariant fast diffusion on the surfaces of ultrastable and aged molecular glasses. *Physical Review Letters*, 118(6), feb 2017. doi: 10.1103/physrevlett.118.066101.

[254] Y. Zhang, E. C. Glor, M. Li, T. Liu, K. Wahid, W. Zhang, R. A. Riggleman, and

Z. Fakhraai. Long-range correlated dynamics in ultra-thin molecular glass films. *The Journal of Chemical Physics*, 145(11):114502, sep 2016. doi: 10.1063/1.4962734.

[255] Y. Zhang, R. Potter, W. Zhang, and Z. Fakhraai. Using tobacco mosaic virus to probe enhanced surface diffusion of molecular glasses. *Soft Matter*, 12(44):9115–9120, 2016. doi: 10.1039/c6sm01566b.

[256] Y. Zhang, C. N. Woods, M. Alvarez, Y. Jin, R. A. Riggleman, and Z. Fakhraai. Effect of substrate interactions on the glass transition and length-scale of correlated dynamics in ultra-thin molecular glass films. *The Journal of Chemical Physics*, 149 (18):184902, nov 2018. doi: 10.1063/1.5038174.

[257] J. Zhao and G. B. McKenna. Temperature divergence of the dynamics of a poly(vinyl acetate) glass: Dielectric vs. mechanical behaviors. *The Journal of Chemical Physics*, 136(15):154901, apr 2012. doi: 10.1063/1.3701736.

[258] J. Zhao, S. L. Simon, and G. B. McKenna. Using 20-million-year-old amber to test the super-arrhenius behaviour of glass-forming systems. *Nature Communications*, 4 (1), apr 2013. doi: 10.1038/ncomms2809.

[259] L. Zhu, C. W. Brian, S. F. Swallen, P. T. Straus, M. D. Ediger, and L. Yu. Surface self-diffusion of an organic glass. *Physical Review Letters*, 106(25), jun 2011. doi: 10.1103/physrevlett.106.256103.

[260] W. Zhu, B. G. Aitken, and S. Sen. Communication: Observation of ultra-slow relaxation in supercooled selenium and related glass-forming liquids. *The Journal of Chemical Physics*, 148(11):111101, mar 2018. doi: 10.1063/1.5022787.

[261] W. Zhu, B. G. Aitken, and S. Sen. Observation of a dynamical crossover in the shear relaxation processes in supercooled selenium near the glass transition. *The Journal of Chemical Physics*, 150(9):094502, mar 2019. doi: 10.1063/1.5086173.